2

# THE UNIVERSITY OF MICHIGAN
# RADIO ASTRONOMY OBSERVATORY

## DEPARTMENT OF ASTRONOMY

# ANALYSIS OF TYPE III SOLAR RADIO BURSTS

# OBSERVED AT KILOMETRIC WAVELENGTHS FROM

# THE OGO-V SATELLITE

Final Scientific Report

NASA Contract          NAS 5-9099

Submitted by:

Fred T. Haddock
Project Director

Written by:  Hector Alvarez

December 1971

The University of Michigan
Radio Astronomy Observatory
Department of Astronomy

## PROLOGUE

This report summarizes the major points of a doctoral dissertation submitted in partial fulfillment of the requirements for the Doctor of Philosophy degree, in the Horace H. Rackham School of Graduate Studies at The University of Michigan. Copies of the dissertation are available for study at the Library of Congress and the University Library.

# ACKNOWLEDGEMENTS

The direct or indirect contribution of many people have helped me to obtain this degree. I want to express my thanks and acknowledgements to them.

First of all to Professor Fred T. Haddock for his constant interest and support since I came to this country, for his suggestion to pursue and interdepartmental degree, for guiding my research with keen intuition, for working in close association with me, and for critically reading the drafts in their final stages. Honoring this recognition I chose to write this dissertation in the first person plural.

My recognition is also extended to the staff of the Radio Astronomy Laboratory that, under the direction of Professor Haddock, made possible the success of The University of Michigan radio astronomy space program. Mr. Wilbur J. Lindsay was responsible to Professor Haddock for all of the space program. Mr. Robert G. Peltzer had the overall supervision of the OGO Project from the prototype stage through flight. Dr. Lyman W. Orr developed the radiometer engineering design up to the prototype stage. He was assisted by Mr. Bobby G. Finch who completed the design, supervised the construction, and participated in the early stages of testing. Mr. Barry D. MacRae served as project engineer following the early testing through completion of the project. Mr. Ancil S. Zeitak built the prototype unit. Sally L. Breckenridge wrote the programs to process and analyze the data.

I profited from many useful conversations with Mr. Peltzer and Mr. MacRae regarding the operation of the radiometer and of the spacecraft, and with Mr. William H. Potter regarding general subjects related to the interpretation of the data. Mr. Peltzer also kindly read the first drafts on Chapters II and III.

I want to express my acknowledgements to the other members of my doctoral committee and especially to Co-Chairman Professor H. Weil who, besides entertaining many discussions, had the first encounter with the "English" of most of my early drafts. In particular, I discussed with Professor Mohler Section 4.5 on associations and Professor Tai made useful comments on the transformation of radiometer output into flux density.

Mr. Raymond L. Bantle did most of the drafting and Mrs. Wanita J. Rasey typed the final version.

TABLE OF CONTENTS

LIST OF TABLES

LIST OF ILLUSTRATIONS

LIST OF APPENDICES

CHAPTER I.  INTRODUCTION

## 1.1  Background

### 1.1.1  Solar Activity.

The sun is a restless star.  Its activity is manifested by multiple characteristics:  it may be as emission of particles or of electromagnetic waves, it may vary slowly or abruptly and violently, it may be very weak or extremely strong.

We can observe the efflux of matter from the Sun that ranges from the steady solar wind up to the explosively ejected packets of high-energy particles.  Also from the Sun we can observe the widest electro-magnetic spectrum of any celestial object.  It spans at least fourteen decades of wavelengths that range from about the $10^{-8}$ cm of hard X-rays up to $10^6$ cm of the Type III burst  radio emission.

These forms of activity exhibit different degrees of interdependence.

The solar radio emission can be classified according to frequency range and spectrum, to temporal characteristics, to polarization, or to morphology.  Commonly a mixture of these elements is used since they are not completely  related.

The broadest classification is based on intensity-time behavior:  (1) The emission of the undisturbed Sun and (2) the bursts.  The first is divided into two parts:  A background component which remains at a constant level for months or years, and a slowly varying component which changes gradually as the active centers are carried by the Sun's rotation.  The steady background is sometimes called the "quiet sun" and it corresponds to the thermal radiation of the Sun, it excludes the active centers or

other sources of transient perturbations; it changes with the solar cycle. The slowly varying component, or S-component, is also of thermal origin but it is associated with sunspots and chromospheric plages or active centers. Sometimes the designation of quiet sun seems to be used in a more general context in place of undisturbed sun. This radiation has been observed in the range between millimeter and meter wavelengths and it originates approximately between the lower chromosphere and one solar radius above it.

The second group in the broad classification of solar radio emission, the radio bursts, refers to the active sun. They are observed between millimeter and kilometer wavelengths and their characteristics depend on the region of the frequency spectrum where they are found; this in turn is related to the dominating mechanism of generation. In contrast with the quiet sun the bursts are primarily of non-thermal origin and they are usually associated with explosive events like flares.

The original burst classification started with three groups: the types I, II and III that were followed later by the types IV and V. At first all these types were observed in the meter range but later studies have revealed that the Type IV is present in the centimeter range while the Type III have now been observed at wavelengths in the kilometric range. Other bursts of a more uncertain classification are also observed in the centimeter range. This gave rise to a more loose grouping in terms of wavelength range (microwave, meter wave, etc.).

Review articles on solar bursts have been published, for example by Wild, Smerd and Weiss (1963), Maxwell (1965) and Boischot (1967a). The whole subject of solar radio emission is covered at an elementary level by

A. G. Smith (1967) and exhaustively at an advanced level in books by Kundu (1965) and by Zheleznyakov (1970).

The radio bursts occur in the mass of gas that surround the Sun. Several names for this gas are found in the literature for example solar atmosphere, solar corona, solar plasma and solar wind; we will use them indifferently. Sometimes the term corona or inner corona is used to designate the part within probably ten solar radii while the terms outer or super corona refer to the part beyond that approximate limit.

The important characteristics of the solar bursts are: (a) the frequency range in which they are observed during their lifetime, (b) the instantaneous bandwidth, that is, the frequency range in which they are observed at any instant, (c) the spectral structure that shows whether the emission is concentrated in certain frequencies (harmonics) or in a continuous range, (d) the type and degree of polarization of the radiation, (e) the time of start at the different frequencies, (f) the time structure at the different frequencies, (g) the peak intensity, (h) the size, position and motion of the emitting region.

Which characteristics can be measured depends on the observing instrument. Basically the receiver may be tuned to one or more fixed frequencies or its bandpass may be swept rapidly and continuously in frequency. In the first case, we obtain bursts profiles (plots of intensity versus time), in the second, we obtain dynamic radio spectrograms (plots of frequency versus time, modulated by intensity). The antenna may be a simple antenna or an array. A large array is required to measure size and position of the source.

The sequence of Roman numerals used to designate burst types does not bear any generic relationship, however Types IV and V are usually

observed after Types II and III respectively. While I, II and IV have a well defined spectral structure, IV and V belong to the continuum class.

Bursts of Type I are short lived (tenths of seconds), occur in rapid succession and are superimposed on a more or less steady background that may last for hours or days. The bursts themselves are confined to a narrow band of frequencies while the background emission is a broad continuum. The combination of the two phenomena has been called "noise storm." They are often 100% circularly polarized and their emission mechanism is not yet definitely identified. They are not associated with flares but with active centers. Their existence has been reported at frequencies as low as 0.2 MHz (Fainberg and Stone, 1971b).

A very useful concept in dealing with Type II and III bursts is that of frequency drift rate (FDR). It is the rate of change of burst arrival time at the different frequencies and it is expressed in MHz $sec^{-1}$. In the classical Types II and III bursts the FDR is negative, that is, the lower the frequency the later the time of arrival. In what follows this sign will be implicitly understood.

This driftrate is a direct consequence of the emission mechanism of these kinds of bursts: a perturbation originating on the sun that travels outward through the solar atmosphere producing radio waves at frequencies related to the fundamental or the second harmonic of the local plasma frequency. Since the density of the solar plasma decreases with increasing distance the bursts exhibit a negative frequency drift rate. The magnitude of the FDR depends, among other things, on the velocity of the perturbation and on the gradient of electron density distribution along the path of the exciter.

The Type II bursts are characterized by a low FDR, the highest being of the order of 1 MHz sec$^{-1}$ at about 200 MHz. For this reason they have also been called "slow drift" bursts. Their detection has been claimed at frequencies as low as 0.2 MHz (Slysh, 1967c) but without convincing supporting facts. The exciting perturbation is believed to be plasma shock waves emanating from flares and with speeds of a few thousand km sec$^{-1}$. The spectral characteristic is a well-defined frequency structure prominent at the fundamental and, often, at the second harmonic. The radiation is unpolarized or very weakly polarized. In the meter range they last for about 10 minutes.

1.1.2 Type III Bursts. These are the most common of all the solar phenomena. They constitute the only type that is observed at frequencies as low as 0.050 MHz covering a range of at least four decades, Haddock and Alvarez, (1969). Their principal characteristic is a high FDR in the meter range, of about 30 MHz sec$^{-1}$ at 300 MHz, decreasing with increasing wavelength. They are called "fast drift" bursts.

Since the Type III bursts span a large frequency range it is not surprising that their characteristics vary drastically with frequency. For example, between a few hundred MHz and 0.050 MHz the duration of the bursts increases from tenths of a second to thousands of seconds, the intensity of one burst may increase by a factor of $10^5$ or $10^6$, the frequency drift rate decreases from approximately $10^2$ to $10^{-4}$ MHz sec$^{-1}$.

The first report in the scientific literature on solar radio emission is that of Reber (1944). The discovery of solar radio emission was made during World War II by Hey in 1942 but for military security reasons it was not reported until later, Hey (1946). Also in the same year

and independently Southworth observed quiet sun radio emission that he did not report until 1945. Before this many reports were made during the sunspot maximum of the previous decade by ham operators, in Q.S.T., etc. The history of the pre-discovery period has been summarized by A. G. Smith (1967). During the rest of that decade many papers were published; for example by Appleton (1945), Shklovskii (1946), Pawsey, Payne-Scott and McCready (1946), Denisse (1946), Khaikin and Chikachev (1947), Allen (1947b),Hey, Parsons and Phillips (1948), Payne-Scott (1949), etc. These workers recognized the existence of sudden short enhancements that were called bursts or outbursts. Of special importance was the observation of Payne-Scott, Yabsley and Bolton (1947), confirming Bowen's verbal report that there were "successive delays between the onset of the burst on 200, 100 and Mc/s..."

The decade of the 50's was very prolific in solar work. This was carried out especially by the Australian scientists and it started with a series of fundamental papers by Wild and McCready (1950) and Wild (1950a, 1950b). The first paper defines the Types I, II and III; the second is related mainly to Type II and the third to Type III. They constitute the first comprehensive study of solar bursts. These studies were performed between 70 and 130 MHz that is a very small fraction of the frequency range covered by these bursts; nevertheless many of the approximate formulas found by Wild to represent some of their characteristics have been shown by us to be valid in the kilometer wavelength range. The success of Wild's observations was due to a large extent to the introduction of the "panoramic receiver" or dynamic spectrograph.

The discovery of the delays in the arrivals of a burst at different frequencies aroused interest in the mechanism of excitation. Payne-Scott,

Yabsley and Bolton (1947) wrote "the successive delays . . . suggest that the outburst was related to some physical agency passing from high-frequency to lower-frequency levels. If we assume, following ideas suggested by Martyn, that the radiation at any frequency originates near the level where the coronal density reduces the refractive index to zero, we can derive a rough estimate of these heights from electron-density data given by Baumbach." They derived velocities between 500 and 750 Km sec$^{-1}$ and they noticed that they "are of the same order as those of prominence material . . . and auroral particles . . ." Because of the magnitude of the speeds we can infer that they observed Type II bursts.

It is interesting to notice that earlier Shklovskii (1946), apparently without knowing about the observed frequency delays, had proposed that "these proper oscillations can be excited by the streams of charged particles moving through the corona with a velocity larger than the velocity of sound." This paper seems to have been unknown to Payne-Scott, Yabsley and Bolton and has remained almost unnoticed.

Wild (1950b) examined these ideas and concluded that "the explanation of the frequency drift of Type III bursts in terms of the motion of exciting agencies is consistent with observational evidence. With the assumed electron density distribution, [Baumbach-Allen] velocities of between about $2 \times 10^4$ and $10^5$ Km sec$^{-1}$ would be required to account for the observed drift rates."

The presence of double peaks on single-frequency observations was recognized as early as 1949 by Payne-Scott, and it was interpreted as due to an echo of the original burst (from the characteristics of the data we have inferred that she observed Type III bursts). This was probably

the same phenomenon that Wild, Roberts and Murray (1954) interpreted later as harmonic pairs in Type III bursts. It was to them the justification of the application of the critical frequency hypothesis to this kind of bursts. This hypothesis has been called the Local Plasma Hypothesis and we have accepted it in this work.

The second harmonic has had important implications in the theoretical studies of the emission mechanisms. One of the main results of this work is the unexpected discovery that the relative amount of second harmonic radiation observed at the Earth increases as the frequency decreases. We have called this the second harmonic phenomenon or second harmonic prevalence.

Two other mechanisms have been proposed besides the local plasma hypothesis. The first, by Slysh (1967), postulates that the bursts are emitted at a frequency that is higher than the local plasma frequency and that it is sensitive to the local temperature. Slysh's paper contains some errors that were partially corrected by Papagiannis (1971). A version completely corrected by us still is inconsistent with our results. Our discovery of the second harmonic phenomenon certainly affects Slysh's argument against the local plasma hypothesis.

A second alternative to the local plasma hypothesis has been offered by Kuckes and Sudan (1969, 1971). They propose that the emission is related to coherent synchrotron deceleration of 100-keV electrons that excite radio waves at the electron cyclotron frequency and its harmonics. A possible weakness of this theory rests in the magnitude of the required magnetic field, that may exceed the observed values. The second harmonic phenomenon found by us, that places the origin of most hectometric and kilometric wavelength bursts further out than was previously thought, may also effect this theory.

According to the local plasma hypothesis fast particles excite plasma waves that in turn produce radio waves. An important and influential theoretical paper is that of Ginzburg and Zheleznyakov (1958a). According to these authors the plasma waves are produced by a Cherenkov-type process and are amplified by the two-stream instability resulting from the interaction of the fast charged particles with the ambient plasma. The mechanism by which the longitudinal waves couple into transverse waves with the observed characteristics is not completely understood. The same theoreticians proposed that the conversion of energy from plasma to electromagnetic waves is achieved by the scattering of "coherent" plasma waves on small-scale inhomogeneities of the background plasma. The slow thermal motion of the heavy ions produces quasi-neutral random fluctuations $\delta N'$ of the plasma density while the light and mobile electrons produce spatial electric charge fluctuations $\delta N''$. "Since the variation of plasma density occurs rather slowly, scattering by $\delta N'$ does not result in any significant change in the wave frequency . . . so that the electromagnetic waves formed by this scattering have the same frequency as the incident plasma wave. This scattering process is called Rayleigh scattering. The radiation in this case is emitted incoherently and mainly in the forward direction" (Kundu 1965, p. 59). The space-charge fluctuations $\delta N''$ of the electron density can be plasma waves present in the background plasma with frequencies close to the plasma frequency, waves with other frequencies are more strongly damped. The interaction of coherent plasma waves set up by the exciting particles with the space-charge fluctuations produces an electromagnetic wave at twice the plasma frequency. This process is called combination scattering. According to Ginzburg and

Zheleznyakov, the fundamental of Type III bursts is generated by Rayleigh scattering and the second harmonic by combination scattering. This theory does not require a magnetic field. But is was considered later by them in connection with noncoherent mechanisms (Ginzburg and Zheleznyiakov, 1961). They conclude, among other things, that solar bursts of Types II and III may not be related to the "noncoherent" emission of plasma waves in an isotropic plasma. The conversion of plasma waves into electromagnetic waves in a strong magnetic field was further studied by Tsytovich and Kaplan (1969).

Type III bursts are elliptically polarized. This phenomenon has been treated theoretically by Yip (1970c).

During the last few years several theoretical contributions have been made, for example, by Yip (1970a, b and c), Melrose (1970), D. F. Smith (1969, 1970), Zheleznyakov and Zaitsev (1970a and b). All these authors adopt scattering as the basic process of energy conversion. A radical departure from these ideas was taken by Kuckes and Sudan (1971) who invoke coherent synchrotron deceleration of high-energy electrons.

Reviews on the mechanisms of solar radio bursts have been given by Wild, Smerd and Weiss (1963), and by Takakura (1966, 1967).

As a direct consequence of the local plasma hypothesis it is expected that the relaxation of the plasma oscillations set up by the passage of the exciter particles is governed by the physical condition of the local plasma. For this reason the study of the time of decay of Type III bursts is of special interest.

The importance of Type III bursts lies in the fact that they can be used to study "in situ" some properties of the solar plasma at different

levels. Except for deep-space probes this may be one of the few methods which can do this. Other radio methods to study the solar plasma involve the observations of the scattering of radio waves from extra-solar radio sources, Hewish (1955), Baseylan and Sinitsin (1971) or from space probes, Stelzried et al. (1970). Also other techniques have been used, radar observations, James (1970), and the observation of dispersion of pulsar pulses, Hollweg (1968), Goldstein and Meisel (1969). The usefulness of these methods has been limited in determining the electron density distribution because they give only integrated densities along the line of the sight. Some of the techniques can give information about the size of density inhomogeneities.

Another radio method of studying solar plasma, recently proposed by Ferencz and Tarcsai (1970) consists of the observation of an anomalous frequency decrease of the 21-cm emission of Taurus A when it passes close to the Sun.

The earliest radio method was suggested by Vitkevich in 1951. It consists of the observation of the occultation of a radio source by the solar corona. The method would allow the determination of electron density, electron temperature and magnetic fields of the corona. The observation of changes in the apparent angular size of the radio source would permit the study of coronal inhomogeneities. Later that year, and independently of Vitkevich, Machin and Smith (1951) proposed a similar but less comprehensive method.

The Type III bursts can be used as "depth probes" because the frequency of observation determines the electron density of the emission level, provided that the mode is known to be fundamental or second harmonic.

The height of the level above the photosphere is undetermined; however, because of the negative density gradient, the lower the frequency the higher the level.

The early observations of Type III bursts were performed in the meter-wavelength range. This corresponds to sources a few solar radii from the Sun. Interferometric observations made by Wild, Sheridan and Neylan (1959) showed that the exciters velocities ranged between 0.2 and 0.8 of the velocity of light in vacuum, and that the deduced electron densities were about one order of magnitude larger than the standard Baumbach-Allen model. Similar results by other workers led to the idea that the bursts are produced in dense streamers.

High-frequency observations of the early workers revealed also that the time decay of the bursts was nearly exponential, Williams, (1948); Payne-Scott, (1949) . The last author was aware that this phenomenon could lead to determination of the temperature of the solar plasma, however she only mentioned it. As far as we know the first calculations of temperature using this property were carried out by Boischot, Lee and Warwick (1960). The values derived by them were in agreement with those determined by optical means.

1.1.3 Observations from Spacecraft. Because of the shielding effects of the Earth ionosphere on the waves at frequencies below approximately 5 MHz, the ground-based radio observations of Type III bursts yielded information from levels not higher than that reached by optical means. The advent of Earth artificial satellites permitted observations at longer wavelengths. The solar radio observations from space were initiated by Hartz (1964) who obtained information down to

1.5 MHz. Since then lower and lower frequencies have been reached. Table 1.1 shows a complete list of solar radio astronomy instruments aboard artificial satellites or space probes and some of their characteristics. They are presented in order of decreasing lowest frequency of observation.

Very low frequency observations from spacecraft have to overcome many problems. Among them we should mention the low directivity attainable with electrically short antennas and its impedance matching over a wide range of frequencies. The matching difficulties result from the change in the antenna electrical parameters with electrical length as well as from the modifications of these parameters by the surrounding plasma.

The extension of the observations to successively lower frequencies has allowed the possibility to probe further and further out into the solar corona. Our discovery of the second harmonic phenomenon about doubles the distance associated with Type III bursts below approximately 1 MHz. Up to the advent of space observations, and particularly by OGO-V, there was a large distance gap that extended between 20 to 215 solar radii between the realm of the optical observations and that of the Earth neighborhood spacecraft observations. This gap was filled by the radio observations of Type III bursts from satellites.

As the lowest frequency of observation was lowered some discrepancies with the measurements made of the solar atmosphere by other means began to stand out. Ground-based radio observations indicated that the electron densities along the exciters' path was about one order of magnitude larger than predicted by the current solar wind models. This was explained by assuming that the sources of the bursts occurred within dense streamers. The existence of these streamers at distances larger than about 100 solar

Table 1.1

Solar Radio Astronomy Instruments on Spacecraft

| Spacecraft | Designed Frequency Band (MHz) | Lowest Frequency of Detected Bursts (MHz) | Type of Receiver | Antenna | Burst Type Observed | Reference |
|---|---|---|---|---|---|---|
| OGO-III | 4.0 - 2.0 | 2.0 | Sweep | Monopole | III,V | Haddock, F.T. & Graedel, T.E. (1969) |
| Alouette-I | 10 - 1.5 | 1.5 | Sweep | Two orthogonal dipoles | III | Hartz, T.R. (1964) |
| ATS-II | 3.0 - 0.45 | 0.45 | Discrete | Dipole | III | Alexander, J.K., et al. (1969) |
| RAE-I | 5.4 - 0.2<br>9 - 0.245 | 0.2 | Sweep | Two V's | III storms | Fainberg, J. & Stone, R.G., (1970) |
| | | | | | Continuum | Fainberg, J. & Stone, R.G. (1971b) |
| Alouette II | 15 - 0.1 | 0.7 | Sweep | Two dipoles? | III | Hartz, T.R. (1969) |
| OGO-V | 3.5 - 0.050 | 0.050 | Discrete | Dipole | III | Haddock, F.T. & Alvarez, H. (1969) |
| Venus 2 | 0.985 - 0.03 | 0.985 | Discrete | Dipole | III | Slysh, V.I. (1967b) |
| Luna 11 & 12 | 1.0 - 0.03 | 0.2 | Discrete | Dipole | III | Slych, V.I. (1967a) |
| IMP-VI | 3.5 - 0.050 | 0.050 | Discrete | Dipole | III | Haddock, F.T. (1971) |
| IMP-VI | 9.9 - 0.030 | ~0.030 | Sweep | Dipole | III | Brown, L.W. as quoted by R.G. Stone (1971) |
| ZOND 3 | 2 - 0.02 | 0.21 | Discrete | Dipole | II | Slysh, V.I. (1967c) |

radii had to be invoked in order to interpret the very low frequency

bursts in the usual way. Our interpretation based on the second harmonic

phenomenon has removed this condition for distances larger than a few

tens of solar radii at the same time that it maintains the constancy of

the velocity of the exciters at values in agreement with those obtained

from direct observations.

Another important discrepancy refers to the temperature of the

solar corona. The values deduced from the decay time of the bursts

observed by Hartz in 1964, assuming collisional damping, were lower than

those expected from solar wind models. This discrepancy increased as

lower frequency data became available. The closing of the gap between

the Sun and the Earth has permitted us to demonstrate quantitatively that

this temperature discrepancy is the same that solar wind theoreticians have

found in the last few years between theory and experiment near the Earth.

The reason for this discrepancy is still unexplained.

Low-frequency observations have also allowed Fainberg and Stone

(1971a) to measure inhomogeneities in the ambient plasma, and the solar

wind speed.

Observations in this range have brought the need to consider the

shape of the exciters' path and its orientation with respect to the Sun-

Earth direction. Ground-based measurements studied levels so close to the

Sun that it was a good assumption to make that the path of the common

Type III burst exciters is radial. In working at distances larger than

100 solar radii the assumption may not be justified. Though we have no

definite evidence against the radial trajectory we have chosen a spiral

path determined by the shape imparted to the interplanetary magnetic field

by the Sun's rotation. Preliminary data from IMP-VI look very promising
to elucidate this and other important aspects of Type III bursts, such
as the size of the sources, Haddock (1971).

The very low frequency observations will allow the study of the
associations between the Type III exciters and the high-energy particles that
are being ejected from flares and passing by the Earth. In this way the
controversial identity of the exciters may be revealed.

Finally, since the Earth is affected so directly by the Sun's
activity, the study of Type III bursts may be of practical importance in
obtaining a better understanding of the solar-terrestrial relationships.

## 1.2 Outline of the Research

The data of the OGO-V satellite give plots of intensity versus time
at the eight frequencies of observation and with a time resolution of
9 seconds. Of the many bursts observed we selected 64 that
drifted down to and below 0.35 MHz. From them we measured:

(a) Time of occurrence,

(b) Amplitude and

(c) Time of decay.

The basic assumptions in the analysis of these data are:

(A) Local plasma hypothesis,

(B) The exciter particles travel with a constant speed along an
Archimedes spiral situated on the plane of the ecliptic,

(C) The radio waves travel from the source to the Earth as in vacuum,

(D) The fundamental and second harmonic emission are generated
simultaneously and in the same small region and

(E) Except for their role in guiding the exciter particles we do not consider the effect of magnetic fields.

In Chapter 2 we describe the instrumentation of the OGO-V radio astronomy experiment. We discuss the receiver preflight and inflight characteristics. Attention is given to the study of the spacecraft-antenna system in order to perform approximate analysis of the burst intensities. We examine the data acquisition system and how, together with the receiver transfer characteristics, it affects the large signals that will be of special importance to us. At the end of this chapter we describe the satellite orbit and discuss the effect of orbit and spacecraft motion on the orientation of the antenna pattern.

Chapter 3 deals with the presentation and characteristics of the data. These, plus scientific considerations, lead us to establish a selection criterion. We emphasize throughout the whole work that the validity of some of our results may be limited by this selection.

Chapter 4 is devoted to the data analysis proper and it is divided into five parts. In the first part we discuss what can be measured and learned from the data supplied by our OGO-V experiment. The second part presents the analysis of the bursts' start time. The delays in the arrivals at the different frequencies are expressed as drift rates. We combine the results from OGO-V bursts with as many results as we could find in the literature and we obtain a simple law of FDR versus frequency valid at least between 550 and 0.075 MHz. By using this law, the basic assumptions and the electron densities measured near the Sun and near the Earth we derive an expression of electron density versus distance. This is used as an intermediate step to arrive at a simple semi-empirical formula in

agreement with the electron densities observed near the Sun and near the Earth, consistent with the observation of drift rates of Type III bursts and that is not in conflict with theoretical solar wind models. Other applications of the formula are discussed.

We describe a new technique devised to study the bursts' time of arrival. This consists in predicting the arrival times at the Earth, for the fundamental and second harmonic emission. A comparison with the observations shows unexpectedly that at approximately 1 MHz the mode of the observed radiation changes from predominately fundamental to predominately second harmonic. This preponderance of second harmonic increases with decreasing frequency and at 0.05 MHz most of the emission appears to be harmonic. Extrapolation of these results to higher frequencies agrees with ground-based data. Next, we make direct use of this phenomenon to determine velocities of the exciters. By assuming a density model as thin as the solar wind we find that we can deduce values similar to those obtained from direct ground-based observations. We discuss the effects of the basic assumptions on the derived velocities.

The third part of Chapter 4 contains the study of the burst amplitudes. The absolute quantitative aspect relies on the validity of the antenna model discussed in Chapter 2. The power spectrum is usually double or single peaked. We suspect that the double peak may be related to the second harmonic emission. The power level of the burst maximum is found to be several orders of magnitude larger than at frequencies observed from ground. The power spectrum may peak at frequencies as low as 0.05 MHz. We study also energy spectra and find results similar to those obtained for the power spectra.

We approximate an average energy spectrum by a rather simple
mathematical formula that, at the high frequencies, reduces to that found
by Wild in 1950. We discuss possible implications of our results on the
theory of the mechanisms of Type III burst emission.

In the fourth part of Chapter 4 we analyze the times of decay. We
explain the technique used and its limitations. Combining our observations
with all of those we could find at other frequencies we obtain a simple
formula to express decay times versus frequency. We compare the observations
with the Coulomb-collisional decay times computed from theoretical solar
wind models and conclude the complete failure of the simple collisional
damping hypothesis to explain the decay time of Type III bursts. Combining
observations and theory we derive an approximate relationship for the ratio
of observed to computed decay times as a function of distance. Because this
function is derived from radio observations it is valid in a continuous
range of distances. This relationship is equivalent to the one that solar
wind theoreticians found while fitting the theory to temperature observations
near the Earth. When these relationships are expressed in terms of the
same parameters they become practically equal.

In the last part of Chapter 4 we examine the association of the
observed kilometric-wave bursts with other solar phenomena: $H\alpha$ and
X-ray flares, energetic particles and radio bursts detected from ground.
By assuming that the origin of the bursts coincides with the center of the
$H\alpha$ flares we find that the distribution of the kilometric-wave bursts
is heavily biased toward the western solar hemisphere while the distribution
found by ground based observers at higher frequencies is the opposite. Using
unpublished data by Lin (1971) we find that all the kilometric-wave

bursts associated with high-energy solar electrons also occurred on the western solar hemisphere as do our Type III bursts.

Chapter 5 contains a summary of the results achieved in this work. In Chapter 6 we make recommendations for future experiments.

In the course of this research we concentrated not only on the properties of the kilometric-wave bursts but also we tried to combine them with the results of other workers in as many frequencies as it was possible to find. This turned out to be a rewarding approach because it unveiled general trends across four frequency decades. Often this allowed us to write fairly approximate but simple formulas to describe the characteristics in question.

Numbers of equations, tables or figures included in the appendices are preceded by the letter A.

# CHAPTER II.  THE OGO-V RADIO ASTRONOMY EXPERIMENT

## 2.1  Description of the Instrumentation

The radiometer consists of a 9.15-m monopole antenna and a stepping-frequency superheterodyne receiver tunable through the eight frequencies of 0.050, 0.100, 0.200, 0.350, 0.600, 0.900, 1.800 and 3.500 MHz in 9.2 seconds.  This instrument has been described in detail by MacRae, (1968) and will only be described briefly below.

The Radio Astronomy Experiment package is located in the Solar Oriented Experiment Package No. 1 (SOEP-1) of the Orbital Geophysical Observatory V (OGO-V) spacecraft with the monopole antenna extended in the -X direction that is perpendicular to the Earth-spacecraft-Sun plane. (See Fig. 2.1.)

### 2.1.1  The Antenna.

The antenna unit consists of a 5.08-cm wide and 9.15-m long beryllium-copper ribbon wound on a spool before deployment. The beryllium-copper ribbon is heat-treated in such a way that in the free state it forms a cylindrical tube of approximately 1.27 cm in diameter.  A ground command releases a restraining strap and allows the ribbon to unwind (by virtue of the stored energy in the wound condition) and to form a cylindrical boom.  A plating of silver on top of gold is deposited on the outer surface of the beryllium-copper strip to improve its thermal properties.  The inboard 3.05 m of the ribbon are coated with Dupont "Kapton" to insulate the boom from the plasma sheath surrounding the spacecraft.
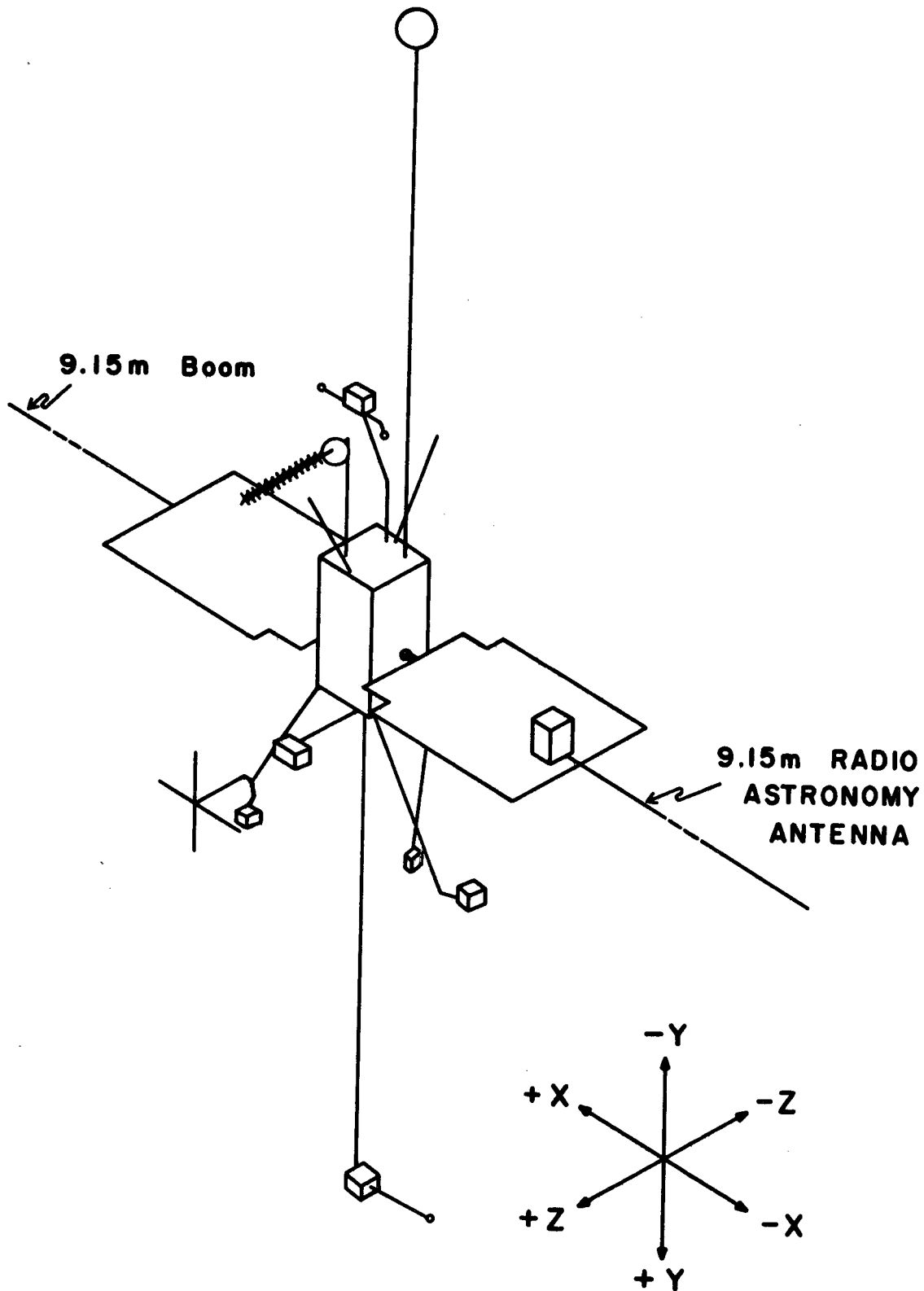
FIG. 2.1  OGO-V CONFIGURATION.

The electrical length of the boom ranges between 0.017 and 0.0015 wavelengths at the frequencies of operation.

The antenna equivalent circuit used in the engineering phase of the work is shown in Fig. 2.2 where

$C_A$ = antenna capacitance,

$R$ = antenna radiation resistance,

$C_B$ = equivalent stray capacitance,

$V^2$ = $4 \, k \, T \, R \, \Delta f$ = mean squared noise voltage,

$T$ = antenna temperature,

$\Delta f$ = bandwidth and

$k$ = Boltzmann's constant, $1.38 \times 10^{-23}$ joule $K^{-1}$.

The determination of the exact values of these parameters is not possible because of the complex configuration of the monopole-spacecraft structure, and also because the spacecraft is not in vacuum. However estimates can be obtained by adopting models for the structure and by assuming it to be in vacuum.

Because of the shape of the spacecraft we considered two simple models. In the first we assumed that the Radio Astronomy antenna is fed against an infinite and perfectly conducting plane. In the second we considered that our antenna and the rest of the spacecraft behave like a center-fed short dipole. In spite of the fact that neither structure is an exact representation we felt that the above approximations probably represent limits to the actual situation. From them we computed the parameters involved and found that the monopole and dipole results differ at most by a factor of two. We believe that the dipole model is better therefore we adopted it.

$$C_A$$
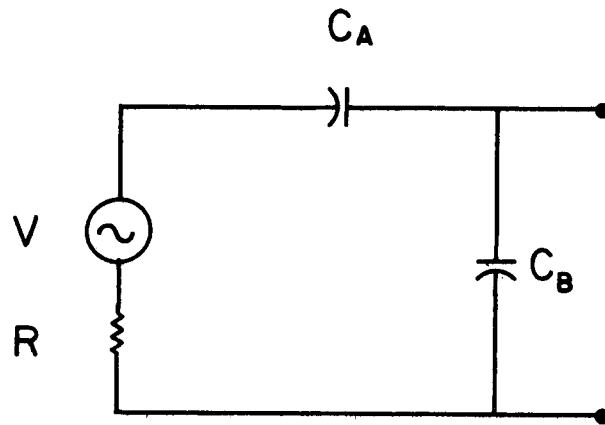
FIG. 2.2  ANTENNA EQUIVALENT CIRCUIT.

The radiation resistance of an electrically short dipole is given by the well known formula:

$$R = 80 \left[ \frac{\pi h}{\lambda} \right]^2 , \qquad (2.1)$$

where h = dipole half-length and

    $\lambda$ = free space wavelength.

The capacitance derived from transmission line analogy and valid for an electrically short antenna is (Jordan, 1950, p. 465):

$$C_A = \frac{\varepsilon_o \pi h}{\left[ \ln \frac{h}{a} - 1 - \frac{1}{2} \ln \frac{2h}{\lambda} \right]} , \qquad (2.2)$$

where $\varepsilon_o$ = permittivity of free space and

    a = antenna radius.

The other parameters are the same as in Eq. (2.1).

In Fig. 2.2, $C_B$ is the stray capacitance due to the proximity to the antenna of grounded surfaces and due to the connecting leads. Careful preflight measurements of the configuration gave a value of 7.5 pF for the base capacitance of the antenna unit itself. The contribution of the connecting leads was estimated as 7.5 pF that gives $C_B$ = 15 pF.

    2.1.2 The Receiver. As mentioned earlier, the receiver is of the superheterodyne type, with a center frequency tunable in eight steps. The discrete frequencies are 0.05, 0.1, 0.2, 0.35, 0.6, 0.9, 1.8, and 3.5 MHz.

The system block diagram is shown in Fig. 2.3. The antenna signal is amplified by a low-noise, broadband preamplifier. A low-pass filter in the preamplifier rejects undesired frequencies above 3.5 MHz and additional notch filters are located at the preamplifier input to prevent telemetry signals from entering the radiometer. The preamplifier output is mixed with signals from a crystal-controlled local oscillator that is stepped in frequency to achieve the eight discrete frequencies across the band.

The 6-dB bandwidth of the I.F. amplifier is 10 KHz, and is determined by the crystal filter in the mixer output. Frequency stepping is in synchronism with the spacecraft data system. The I.F. stage has automatic gain control with a useful dynamic range of 44 dB. The output of the detector is filtered with a time constant of 0.21 seconds.

An analog voltage is generated in the oscillator circuitry which identifies the operating frequency.

A solid-state four-level noise calibrator is connected in place of the antenna for inflight calibration every 9.85 minutes. Approximately 37 seconds are required for a calibration, after which the antenna is restored to the radiometer input.

2.1.3 The Timing. The system can operate in two modes. In the normal mode of operation the preamplifier output is stepped through the eight discrete frequencies already mentioned and is called the stepping mode. In the other mode, nonstepping, the local oscillator frequency is selected to give an output at only one of the eight frequencies.
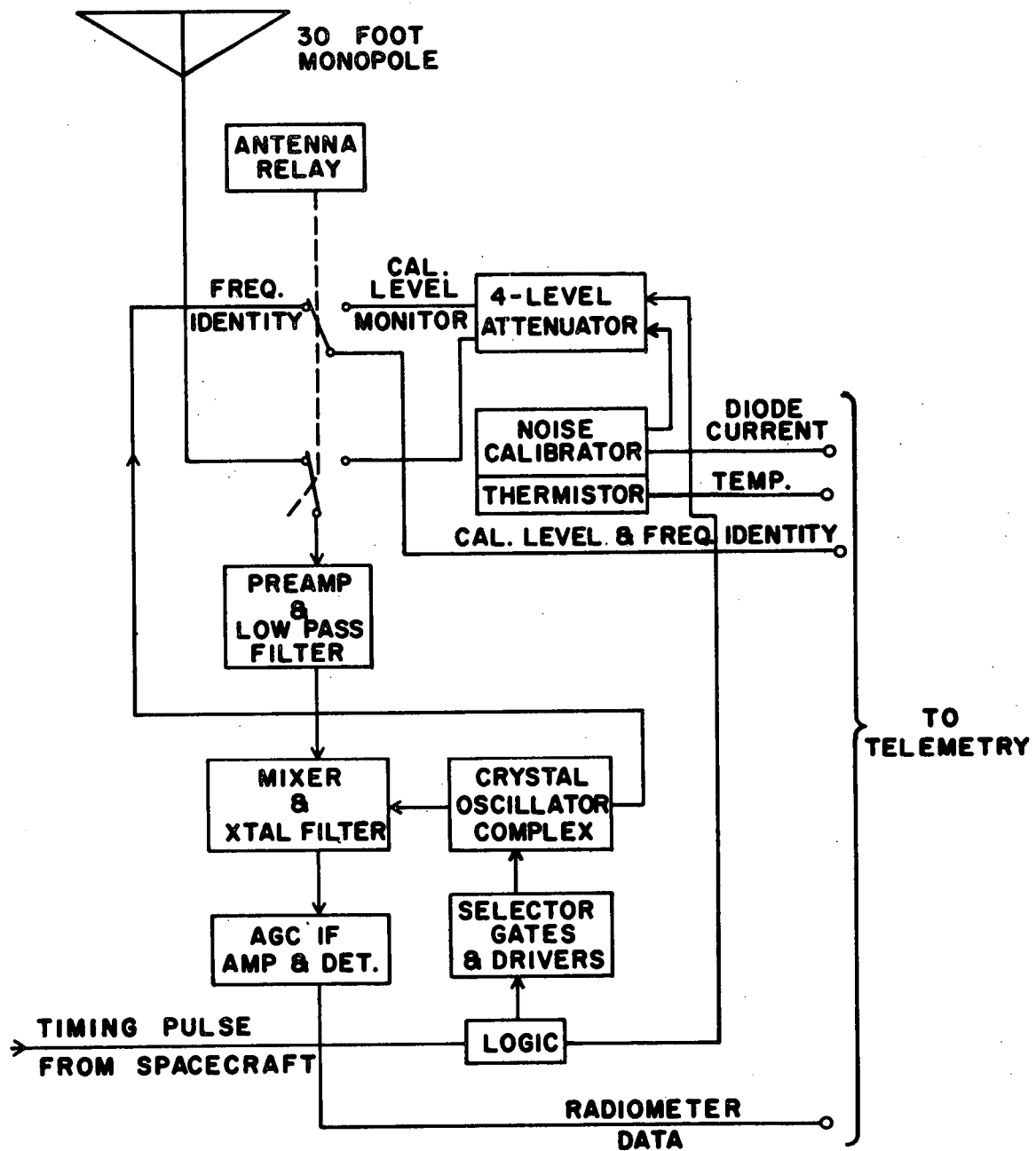
FIG. 2.3  SYSTEM BLOCK DIAGRAM.

The sequence of events in the radiometer when it operates in the normal mode is illustrated in Fig. 2.4. The train of timing pulses furnished by the spacecraft to the receiver at intervals of 1.152 seconds is shown in Fig. 2.4a. Each pulse causes the radiometer frequency to change as shown in Fig. 2.4b. The eight frequency steps, $f_1$ through $f_8$, constitute a subcycle of approximately 9.2-seconds duration.

During each frequency step when the spacecraft telemetry rate is 1 kb/sec (1000 bits per sec) three data samples are taken, the first is the sample containing the frequency identification voltage and the last two are the radiometer output data samples. The radiometer data samples are taken at time intervals of 3.31 and 4.37 postdetector time constants, measured from the timing pulse. This is illustrated in Fig. 2.4c. See also Section 2.1.6.

The subcycle repeats continuously except when a ground command is sent to disable the frequency stepping.

The calibration cycle consists of four subcycles of eight frequency steps each as shown in Fig. 2.4d, similar to 2.4c, but drawn to a smaller time scale. The calibrator level, as shown in 2.4e, is held constant during the first subcycle. Thus all eight frequencies are calibrated at the same levels. This is repeated for the remaining three subcycles at successively increased calibrator power levels. At the end of the 36.9-second calibration cycle , the calibrator is disconnected and the antenna is reconnected to the radiometer input. A calibration cycle occurs once during a main cycle which consists of 64 subcycles of 9.83 min each. Four of them are devoted to calibration
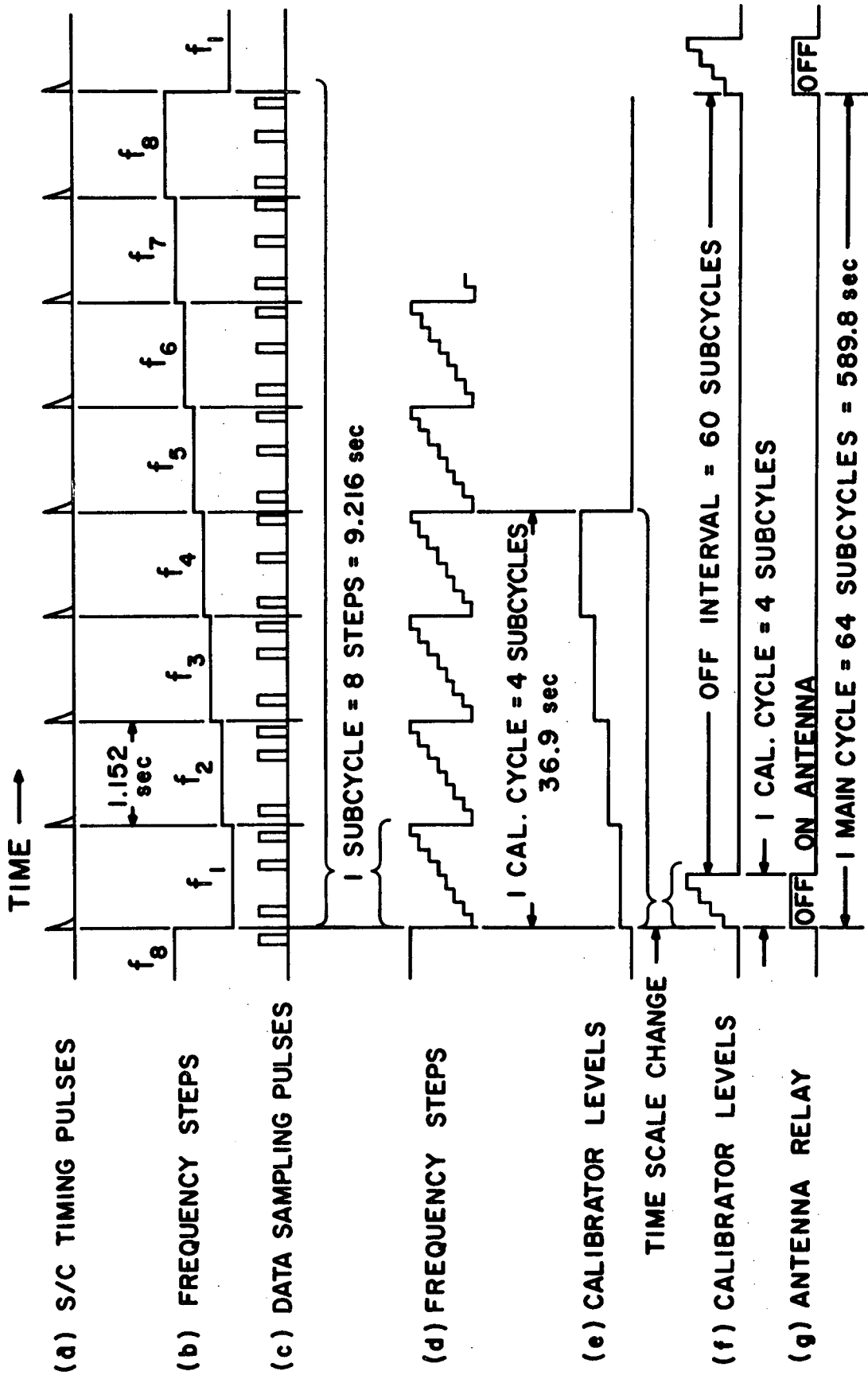
FIG. 2.4 TIMING DIAGRAM.

as shown in 2.4f.  The antenna is connected to the receiver approximately
94 percent of the time.  The action of the antenna relay is illustrated
in 2.4g.

2.1.4  Preflight Calibration.  The preflight calibration of the
receiver involved several operations but only the final result concerns
us here, i.e., the measurement of the overall system response over the
anticipated ranges of operating temperatures and input signal levels.

Plots of the radiometer output versus noise input  signals were
obtained at each frequency of operation.  As is usual in dealing with
noise power, the input is measured in units of the product RT (ohm K),
where T is the effective receiver input noise temperature and R is the
antenna radiation resistance.  When the operating temperature was varied
between -20°C and +45°C there was insignificant variation in receiver
output.  We adopted an average curve at each frequency.  The corresponding
values are shown in Table 2.1.  As an example, the curve for 3.5 MHz
is shown in Fig. 2.5.  Notice the saturation knee that has important
implications and that will be discussed later.

For frequencies from 3.5 MHz to 0.2 MHz the power transfer curves
are practically the same over the entire range of signal levels.  For
0.1 and 0.05 MHz the curves differ from the others in the small-signal
region, below 1.5 volts output, because of a higher receiver noise
temperature.

In the laboratory calibration the antenna was replaced by a
dummy equivalent circuit configured as in Fig. 2.2 using the parameters
shown in Table 2.2 for all eight frequencies.
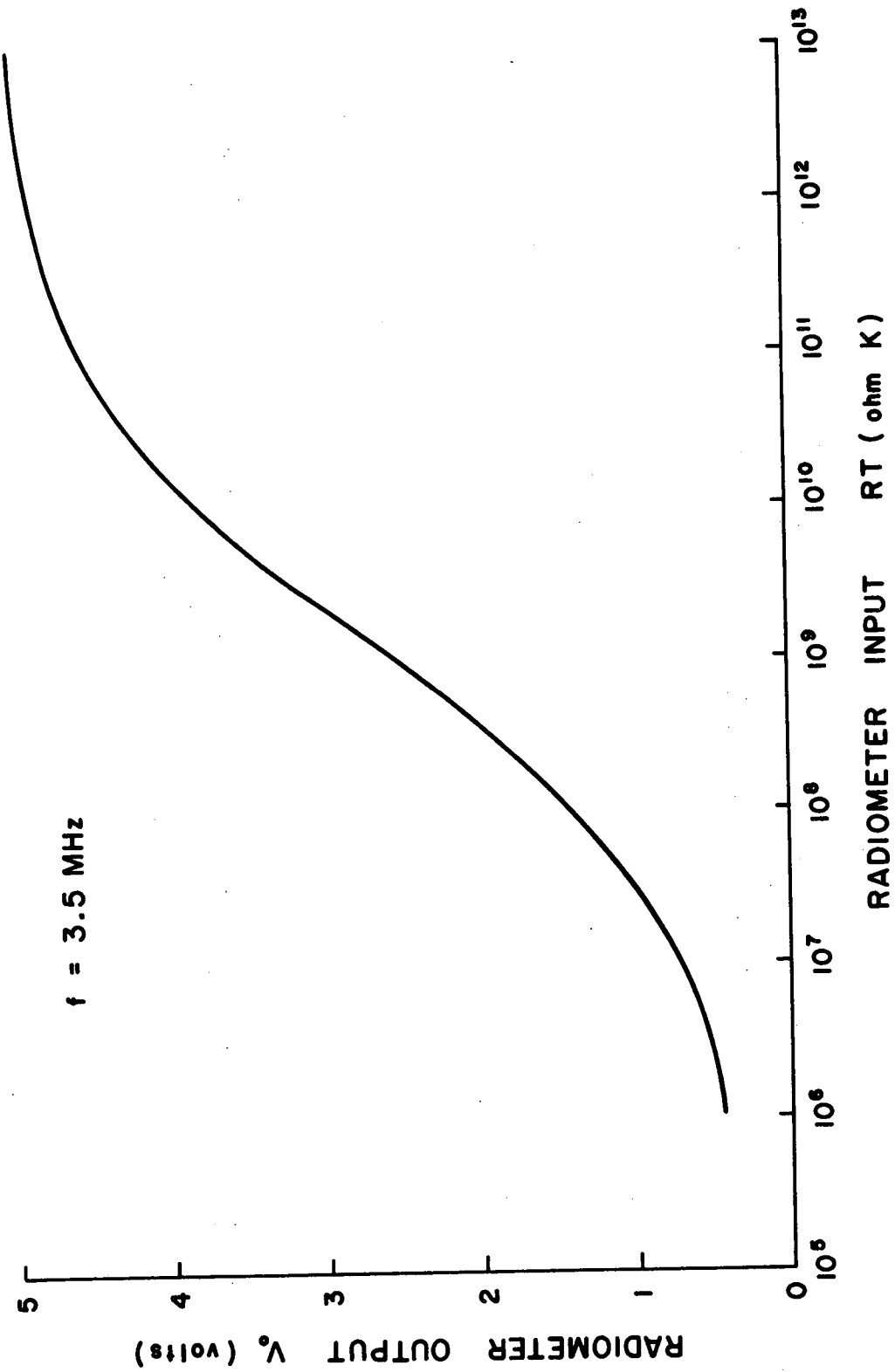
FIG. 2.5 EXAMPLE OF RADIOMETER RESPONSE CURVE.

Table 2.1

Radiometer Output Voltages Preflight Calibration

| RT(ohm K) | f(MHz) | | | | | | | |
|---|---|---|---|---|---|---|---|---|
| | 0.05 | 0.1 | 0.2 | 0.35 | 0.6 | 0.9 | 1.8 | 3.5 |
| $4 \times 10^{13}$ | 5.00 | 5.00 | 5.00 | 5.00 | 5.00 | 5.00 | 5.00 | 5.00 |
| $10^{13}$ | 4.98 | 4.98 | 4.98 | 4.98 | 4.98 | 4.98 | 4.98 | 4.98 |
| $4 \times 10^{12}$ | 4.96 | 4.96 | 4.96 | 4.96 | 4.96 | 4.96 | 4.96 | 4.96 |
| $10^{12}$ | 4.91 | 4.91 | 4.91 | 4.91 | 4.92 | 4.92 | 4.92 | 4.91 |
| $4 \times 10^{11}$ | 4.80 | 4.82 | 4.82 | 4.85 | 4.82 | 4.82 | 4.83 | 4.81 |
| $10^{11}$ | 4.53 | 4.58 | 4.59 | 4.61 | 4.60 | 4.60 | 4.60 | 4.55 |
| $4 \times 10^{10}$ | 4.29 | 4.36 | 4.36 | 4.39 | 4.35 | 4.38 | 4.40 | 4.35 |
| $10^{10}$ | 3.75 | 3.86 | 3.85 | 3.91 | 3.85 | 3.88 | 3.90 | 3.80 |
| $4 \times 10^{9}$ | 3.28 | 3.39 | 3.40 | 3.46 | 3.42 | 3.45 | 3.45 | 3.35 |
| $2 \times 10^{9}$ | 2.90 | 3.02 | 3.00 | 3.09 | 3.02 | 3.05 | 3.10 | 2.95 |
| $10^{9}$ | 2.52 | 2.62 | 2.60 | 2.70 | 2.62 | 2.65 | 2.67 | 2.55 |
| $4 \times 10^{8}$ | 2.06 | 2.10 | 2.10 | 2.15 | 2.11 | 2.12 | 2.16 | 2.05 |
| $10^{8}$ | 1.49 | 1.52 | 1.43 | 1.47 | 1.45 | 1.45 | 1.50 | 1.40 |
| $4 \times 10^{7}$ | 1.24 | 1.24 | 1.11 | 1.15 | 1.10 | 1.12 | 1.15 | 1.10 |
| $10^{7}$ | 1.02 | 0.96 | 0.72 | 0.72 | 0.65 | 0.73 | 0.78 | 0.75 |
| $4 \times 10^{6}$ | 0.96 | 0.80 | 0.54 | 0.52 | 0.45 | 0.52 | 0.60 | 0.60 |
| $10^{6}$ | 0.92 | 0.65 | 0.42 | 0.32 | 0.27 | 0.30 | 0.40 | 0.45 |

Table 2.2

Different Parameters of the Antenna Equivalent Circuit Shown in Fig. 2.2

| Circuit | R (ohm) | $C_A$ (pF) | $C_B$ (pF) |
| --- | --- | --- | --- |
| Laboratory calibration | 25 | 160 | 22.3 |
| This study | Eq. (2.1) | Eq. (2.2) | 15 |

### 2.1.5 Interference, Radiometer Stability and Sensitivity.

Inspection of the data shows the presence of spurious signals which can be classified as impulsive or nonimpulsive interference. Impulsive interference is manifested simultaneously in the eight channels as a sudden increase in the output level followed by equally sudden decrease to the original level. The signals are very strong and last from minutes to hours. The four lower frequency channels are usually affected by this type of interference. They are not observed in the other channels. Since we found no coincidence with spacecraft ground commands we concluded that it was due to other experiments onboard. No obvious repetitive pattern was found. The fact that this type of interference occurs simultaneously in different channels provides a means to discriminate it from the Type III solar bursts which show a drift in frequency with time.

The nonimpulsive interference is manifested as permanent high levels of the eight outputs, higher than the preflight receiver noise. This is especially true in the case of the 1.8 and 0.35 MHz channels as can be seen in Fig. 2.6 where the typical system noise level of the radiometer output is shown. The output is measured in terms of the
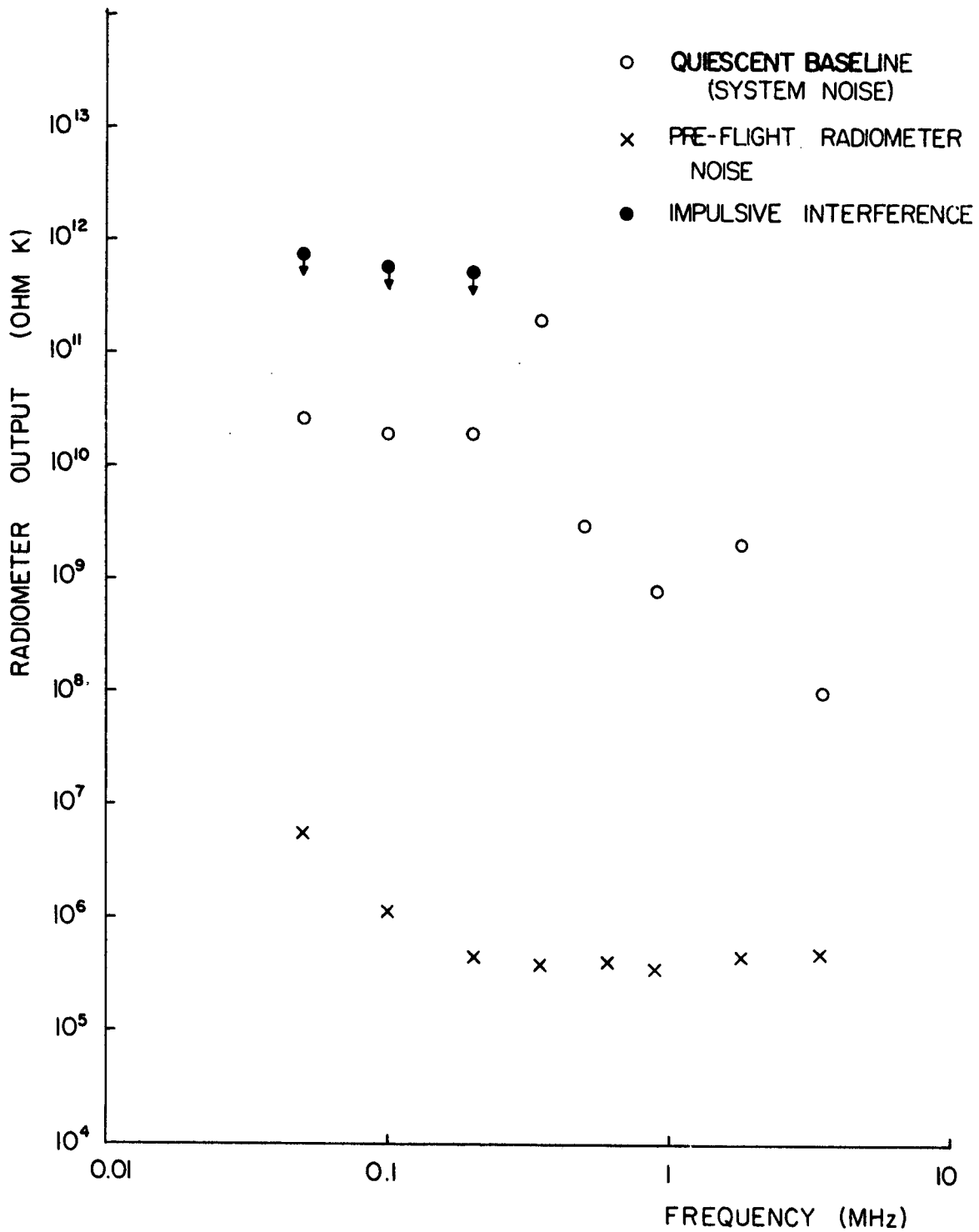
FIG. 2.6  TYPICAL AVERAGE NOISE LEVELS OF THE RADIOMETER.

RT product of the antenna radiation resistance and the antenna temperature. Figure 2.7 shows that the amplitude of the noise fluctuations in the same two channels are much larger than those of the adjacent channels.

The stability of the radiometer gain was checked by examining the inflight calibration approximately every two months between March 1968 and December 1969. We found that the output voltage corresponding to the four calibration levels stayed constant in all channels within a few percent during this period. (Alvarez, 1971)

To study the sensitivity of the system, we examined the radiometer output when the spacecraft was close to apogee, near 147,000 km, at times in which the baselines of the eight frequency channels seemed to be fairly steady and free from solar bursts or impulsive interference. Figure 2.6 shows typical values of the baseline levels. Their peak-to-peak fluctuations are shown in Fig. 2.7. The measurements were made during the first 103 orbital revolutions of the spacecraft. We observe that the baseline levels of the system noise increase steadily as the frequency decreases, except for the 1.8 and 0.35 MHz channels that obviously are abnormally high. The arrows indicate typical impulsive interference levels that most of the time affect the low frequency channels.

Transformation of RT Product into Flux Density. In Section 2.1.1 we considered a balanced dipole as a simple approximation of the monopole-spacecraft system. By using this model we can estimate the order of magnitude of the received flux densities.

The collecting area A and the gain G of a loaded antenna are related by the formula, (Tai, 1961):
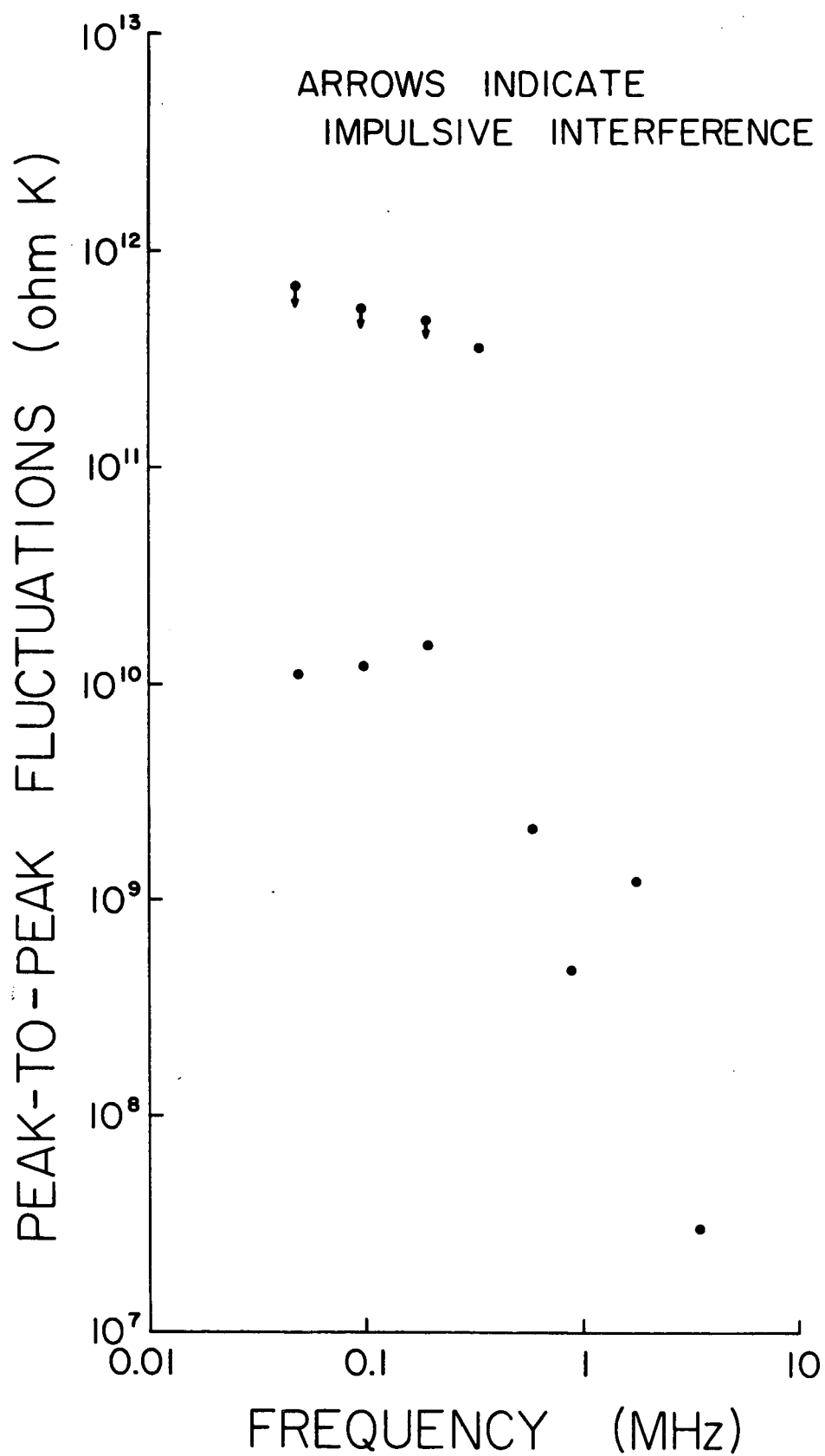
FIG. 2.7 TYPICAL PEAK-TO-PEAK NOISE LEVELS OF THE RADIOMETER.

$$A = q_1 q_2 G \frac{\lambda^2}{4\pi} \quad , \tag{2.3}$$

where $q_1$ is the impedance mismatching factor defined as

$$q_1 = \frac{\text{power delivered to the load}}{\text{power delivered to a matched load}} \quad ,$$

$$= \frac{4 R_A R_L}{(R_A + R_L)^2 + (X_A + X_L)^2} \quad , \tag{2.4}$$

also

$$Z_L = R_L + jX_L = \text{load impedance,}$$

$$Z_A = R_A + jX_A = \text{antenna impedance defined at the load terminals and}$$

$$q_2 = \text{polarization mismatch factor.}$$

If the incident field is randomly polarized, the average value of $q_2$ is

$$q_2 = 0.5 \quad . \tag{2.5}$$

In what follows we will assume this condition and in Section 4.3 we will discuss further the state of polarization of Type III bursts. We will further assume that the antenna terminals are directly connected to the receiver input therefore $R_A = R$ and $X_A = 1/2\pi f C_A$.

The total flux density of randomly polarized radiation incident on an antenna is related to the antenna temperature T by the formula:

$$S_f = \frac{kT}{A} \quad , \quad \text{w m}^{-2} \text{ Hz}^{-1} \quad , \tag{2.6}$$

where k = Boltzmann's constant.

Inserting Eqs. (2.1), (2.3) and (2.5) into Eq. (2.6) we get

$$S_f = \frac{k(RT)}{10 \, q_1 G \pi h^2} \; , \qquad\qquad (2.7)$$

where the product (RT) is the measured quantity. This formula is numerically the same for the antenna model consisting of a monopole perpendicular to an infinite and perfectly conducting plane.

Equation (2.7) assumes that the antenna is a balanced dipole but the (RT) scale in which our data are expressed were obtained from a calibration using a different antenna model. See Table 2.2. Therefore, to be consistent, we should define a new calibration curve appropriate for the dipole parameters. To compute the correction factor that will take this into account let us call $P_R$ the power measured at the receiver output. Also let $P_1'$ and $P_1$ be the power collected by the antenna as deduced by assuming the laboratory calibration model and by a balanced dipole model, respectively. Finally, let $q_1'$ and $q_1$ be the corresponding mismatching factors. If $G_R$ is the receiver power gain and there are no ohmic losses then

$$P_1' = \frac{P_R}{q_1' \, G_R}$$

and

$$P_1 = \frac{P_R}{q_1 \, G_R} \; .$$

Therefore:

$$P_1 = \frac{q_1'}{q_1} \, P_1'$$

It is straightforward to compute $q_1'$ and $q_1$ from Eq. (2.4). In computing $Z_L$, $C_B$ should be added to $C_S$. The radiometer input shunt parameters were measured by Yorks (1968) and are shown in Table 2.3. The results of the calculations are shown in Table 2.4. Practically the same quantities are obtained for the monopole-infinite plane model. We observe that the corrections are large.

### Table 2.3

### Parameters of the Radiometer Input Impedance

| Frequency (MHz) | $R_S$ (ohm) | $C_S$ (pF) |
| --- | --- | --- |
| 3.5 | $10 \times 10^5$ | 25.0 |
| 1.8 | $5.60 \times 10^5$ | 24.2 |
| 0.9 | $1.02 \times 10^5$ | 24.2 |
| 0.6 | $9.23 \times 10^4$ | 24.2 |
| 0.35 | $8.77 \times 10^4$ | 24.2 |
| 0.2 | $8.82 \times 10^4$ | 24.4 |
| 0.1 | $1.22 \times 10^5$ | 27.2 |
| 0.05 | $1.05 \times 10^5$ | 33.8 |

Table 2.4

Correction Factor for Antenna-Receiver Mismatching

| f (MHz) | $q'_1$ | $q_1$ | $q'_1/q_1$ |
|---------|--------|-------|------------|
| 3.5 | $6.0 \times 10^{-5}$ | $8.2 \times 10^{-6}$ | 7.2 |
| 1.8 | $1.1 \times 10^{-4}$ | $3.8 \times 10^{-6}$ | 29.0 |
| 0.9 | $5.9 \times 10^{-4}$ | $4.9 \times 10^{-6}$ | $1.2 \times 10^2$ |
| 0.6 | $6.5 \times 10^{-4}$ | $2.3 \times 10^{-6}$ | $2.8 \times 10^2$ |
| 0.35 | $6.8 \times 10^{-4}$ | $8.0 \times 10^{-6}$ | $8.5 \times 10^2$ |
| 0.2 | $6.8 \times 10^{-4}$ | $2.4 \times 10^{-7}$ | $2.8 \times 10^3$ |
| 0.1 | $4.8 \times 10^{-4}$ | $3.8 \times 10^{-8}$ | $1.3 \times 10^4$ |
| 0.05 | $5.1 \times 10^{-4}$ | $7.9 \times 10^{-9}$ | $6.5 \times 10^4$ |

We can write Eq. (2.7) as

$$S_f = \frac{k}{10 \, G \, \pi h^2} \left( \frac{q'_1}{q_1} \right) (RT) \quad , \tag{2.8}$$

for the dipole G = 1.5. The length of the OGO-V boom is h = 9.15 m. Then we can write Eq. (2.8) as

$$S_f = 3.5 \times 10^{-27} \left( \frac{q'_1}{q_1} \right) (RT) \quad , \quad \text{w m}^{-2} \text{ Hz}^{-1} \quad . \tag{2.8a}$$

We will use this equation in Section 4.3.

The mean sky brightness temperature over the sky is equal to the antenna temperature T. The Rayleigh-Jeans approximation, valid in our cases, gives the specific intensity

$$I_f = \frac{2kT}{\lambda^2} \quad . \tag{2.9}$$

Using Eq. (2.1) and introducing the correction factor $(q_1'/q_1)$, we have

$$I_f = \frac{k}{40\,\pi^2 h^2} \left( \frac{q_1'}{q_1} \right) (RT) \quad , \quad \text{w m}^{-2} \text{ Hz}^{-1} \text{ sr}^{-2} \tag{2.9a}$$

or, for our antenna,

$$I_f = 4.15 \times 10^{-24} \left( \frac{q_1'}{q_1} \right) (RT) \quad .$$

Using $(RT) = 9.5 \times 10^7$ ohm-K from Fig. 2.6 we obtain at 3.5 MHz the following specific intensity:

$$I_f = 3.0 \times 10^{-19} \quad , \quad \text{w m}^{-2} \text{ Hz}^{-1} \text{ sr}^{-2} \quad .$$

Values obtained by other observers range between $8 \times 10^{-21}$ and $6 \times 10^{-20}$, R. R. Weber et al. (1969); therefore the OGO-V values are higher than the measured upper limit by a factor of 5. This means that either the system noise has contributions other than the cosmic noise or that our representation of the antenna by a dipole is incorrect. Figure 2.6 shows that the system noise increases with decreasing frequency. This leads us to assume that the high values of $I_f$ obtained are due to a contribution in excess of the cosmic background.

2.1.6 Data Acquisition. The data received from the spacecraft telemetry system consists not only of the radiometer output but also of

other parameters related to the radiometer operation, for example,

currents, voltages, temperatures, etc. The information is collected

by the operation of a main commutator (main frame) and two sub-commutators.

The main commutator has words numbered from 1 to 128. Each consists

of 9 bits. Eight bits are used for analog data. The lowest repetition

rate of the main commutator is 1.152 sec which corresponds to 1000

bits/sec (1 kb/sec.). Of special interest is the word No. 13, that

corresponds to the frequency identification voltage and Nos. 77 and

125 which are the two samples of the radiometer output. Since the

sampling the radiometer output at each of the eight frequencies lasts

1.152 sec, consecutive samples at any frequency are separated by 9.2 sec.

At the 1 kb/sec rate this interval constitutes the limitation in <u>time</u>

<u>resolution</u> of the instrument, not the postdetector time constant of

0.21 sec. This fact accounts for one of the reasons that our data time

profiles are not as precise as we would like.

The repetition rate of the main commutator can be increased by

a factor of 8 or 64. At the rates of 8 and 64 kb/sec the time between

samplings, at each frequency, in consecutive main cycles is only 0.69

and 0.08 post-detection time constants. However the frequency-stepping

rate is always 1.152 sec per channel so the time resolution is not

improved by using higher bit rates.

The data from the OGO-V satellites are collected by Goddard Space

Flight Center (GSFC) ground stations and sent to GSFC where the

decommutated data tapes are prepared for each experimenter. The data

are of two types, real time and playback. Real time transmissions

are at 1, 8 and 64 kb/sec data rates whereas the playback data obtained

from onboard tape recorders are recorded at 1 kb/sec.

2.1.7 Telemetry Quantization. The telemetry uses 8 bits in
a binary system allowing 256 discrete levels in the analog-to-digital
conversion of an analog voltage between 0 and 5.12 volts. Since the
output of the radiometer ranges between 0.0 and 5.1 volts, it is
divided into 256 steps of 0.020 volts each. The design of the system
is such that an incoming signal that has a value lying between discrete
steps, is truncated to the adjacent lower discrete voltage level. This
produces telemetry quantization that combined with radiometer saturation
results in further limitation in time resolution and in signal amplitude
resolution.

The simple diagram of Fig. 2.8 shows the history of a fictitious
input signal. The strength of the input signal is expressed in (RT) units
and the receiver output $V_o$ in volts. The telemetry voltage steps $V_T$
are indicated. Figure 2.8 applies to any of the eight frequencies.
The input signal (a) drives the receiver (b) to saturation. The dashed
line follows a particular point (4). The signal is sampled, (c)
and then the samples are transmitted by telemetry to ground. These
samples are corrected by a computer using the radiometer response curve
(d) and are finally plotted (e). It is seen that the incoming signal
is changed by the telemetry quantization, especially in the nonlinear
portions of the response curve. The time-of-start of the signal is
modified and the amplitude is reduced.

To assess the effect of this problem on the actual observations
we measured the amplitude of the discrete levels in the range of
strong signals. The range of interest in the (RT) product was above
$10^{10}$ ohm-K. We measured many strong signals of different amplitudes so
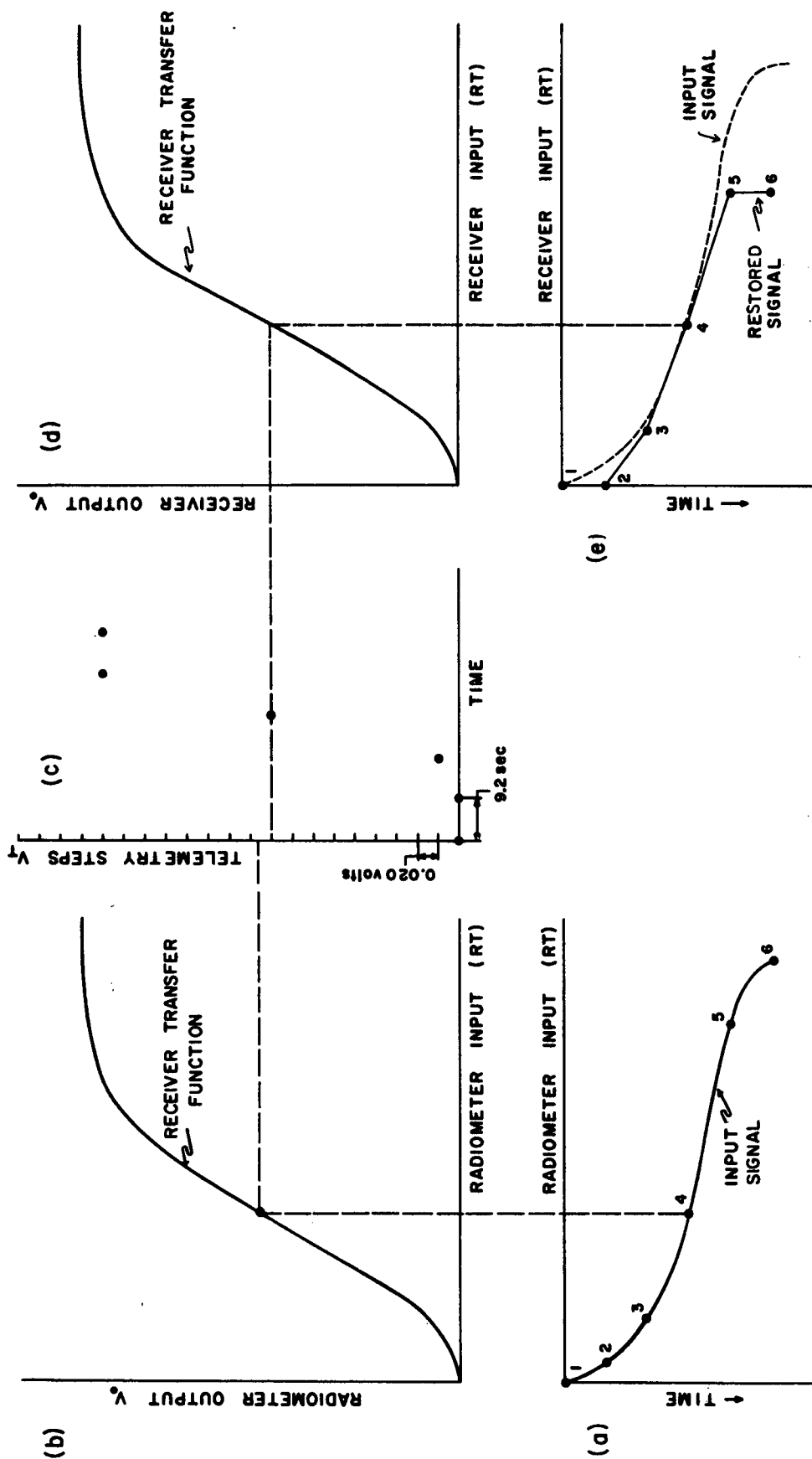
FIG. 2.8  PICTURE OF SATURATION AND TELEMETRY QUANTIZATION EFFECTS
ON LARGE INPUT SIGNALS.

C.2

that we believe that the list of levels shown in Table 2.5 is fairly complete. We prepared a diagram of discrete output levels, for each frequency, whose practical objective was to determine the uncertainty in the amplitude of very strong solar bursts. The effect on time is negligible in the four upper channels because the system noise in flight is in the linear part of the power transfer curve of the receiver. The combined effects of saturation and telemetry quantization can be appreciated in Fig. 3.2a (Section 3.1) for the event of Nov. 18, 1968. Saturation produces the horizontal upper parts of the profiles. The staircase-shaped discontinuities in the upper parts are due to the discrete voltage steps of the telemetry system. Tick marks on the right- and left-hand sides indicate the zero levels.

## 2.2 The Spacecraft

2.2.1 History and Orbit. The OGO-V satellite was launched on March 4, 1968 from the Eastern Test Range at Cape Kennedy, Florida. The initial orbital parameters were approximately the following: height of perigee 292 km, height of apogee 147,000 km, inclination to the equator 31°, and period of 63 hr 25 min. We notice that the orbit is highly elliptical and that the height of apogee is 0.38 of the Earth-Moon distance. The Radio Astronomy Experiment was turned on 19 hours after liftoff. The antenna was deployed on the fourth revolution at 1825 U.T., 14 March 1968. During the time covered in this study (March 1968 to February 1970), the radiometer was in the normal stepping mode except for the following three periods: 25 April to 18 June 1968, 12-14 September 1969, and 15-17 December 1969. The modes were nonstepping

Table 2.5

Radiometer Discrete Outputs for Large Signals.  Units (ohm-K) Should Be

Multiplied by $10^9$

| 3.5 MHz | 1.8 MHz | 0.9 MHz | 0.6 MHz | 0.35 MHz | 0.2 MHz | 0.1 MHz | 0.05 MHz |
|---|---|---|---|---|---|---|---|
| 6.5 | 8.2 | 4.7 | 7.6 | 7.8 | 9.3 | 9.2 | 11.6 |
| 15.0 | 11.5 | 5.2 | 8.9 | 9.3 | 11.7 | 13.3 | 16.2 |
| 17.6 | 12.1 | 6.0 | 9.2 | 13.0 | 13.0 | 15.6 | 17.1 |
| 22.5 | 12.7 | 7.2 | 11.2 | 13.6 | 13.5 | 21.2 | 26.8 |
| 30.0 | 14.0 | 8.7 | 13.2 | 21.7 | 15.8 | 24.0 | 30.2 |
| 33.2 | 14.5 | 10.5 | 14.0 | 24.3 | 16.7 | 25.2 | 32.0 |
| 41.8 | 19.2 | 12.2 | 16.2 | 25.6 | 21.6 | 30.2 | 38.8 |
| 45.2 | 21.1 | 15.3 | 17.0 | 30.7 | 24.2 | 32.2 | 41.5 |
| 64.8 | 22.4 | 20.5 | 22.6 | 32.8 | 25.8 | 40.0 | 50.8 |
| 90.0 | 26.5 | 22.7 | 25.0 | 40.0 | 30.7 | 43.0 | 54.5 |
| 95.0 | 28.2 | 24.0 | 26.5 | 43.0 | 32.7 | 53.5 | 75.0 |
| 128 | 34.3 | 28.7 | 32.0 | 52.4 | 40.0 | 75.0 | 97.0 |
| 140 | 36.8 | 30.3 | 34.2 | 72.0 | 43.0 | 82.0 | 104 |
| 187 | 40.0 | 37.2 | 41.3 | 78.7 | 52.3 | 120 | 150 |
| 372 | 47.0 | 40.0 | 43.9 | 93.0 | 56.3 | 165 | 155 |
| 426 | 53.5 | 49.8 | 52.5 | 104 | 72.0 | 185 | 203 |
| 460 | 66.7 | 53.5 | 55.8 | 138 | 79.0 | 340 | 226 |
| 1260 | 73.8 | 68.2 | 69.8 | 150 | 103 | 437 | 402 |
| 2070 | 74.7 | 74.0 | 75.7 | 245 | 117 | 472 | 443 |
| | 110 | 74.7 | 100 | 353 | 160 | 1240 | 1240 |
| | 160 | 100 | 111 | 450 | 180 | 2060 | 2060 |
| | 172 | 111 | 154 | 1250 | 348 | | |
| | 313 | 155 | 172 | 2080 | 437 | | |
| | 426 | 175 | 341 | 40000 | 472 | | |
| | 440 | 194 | 422 | | 1250 | | |
| | 1000 | 343 | 1000 | | 2080 | | |
| | 1860 | 424 | 1860 | | | | |
| | | 1000 | 42000 | | | | |

at 3.5, 0.6 and 0.6 MHz, respectively. During the last two periods
the spacecraft was intentionally rotated around the Y-Y axis in a spin
mode with an average period of 38 minutes.

Between March 1968 and February 1970, the height of perigee
increased from 6,800 to 21,800 km and the height of apogee decreased
from 153,000 to 138,000 (geocentric distances).

Since the spacecraft orbit is approximately fixed with respect
to the stars it rotates relative to the Sun-Earth direction as the Earth
moves around the Sun.

Predictions of the spacecraft position and other related parameters
are published in advance by GSFC to the experimenters in separate
magnetic tapes along with the data tapes. The commands sent to the
spacecraft are published in the Revolution Report Bulletins. Other
information pertaining to the spacecraft is also published monthly in
the Operation Summary Reports. The UCLA Fluxgate Magnetometer Group
has generated OGO-V Orbital Plots available in microfilm form.

2.2.2 <u>Relative</u> <u>Motion</u> <u>of</u> <u>the</u> <u>Antenna</u> <u>Pattern</u>. Referring to
Fig. 2.1, the radio astronomy antenna is contained in the plane of
the solar paddles which are always normal to the Sun-spacecraft line,
therefore, the antenna is normal to that direction. On the other hand,
the Z-axis always points to the Earth, therefore the antenna is normal
also to the Earth-spacecraft line. Thus the antenna is always
perpendicular to the plane Sun-Earth-spacecraft.

The plane of the orbit of the spacecraft is inclined about 31°
with respect to the Earth's equator, and it is also inclined with
respect to the ecliptic. In Fig. 2.9, (P) is the plane of the ecliptic
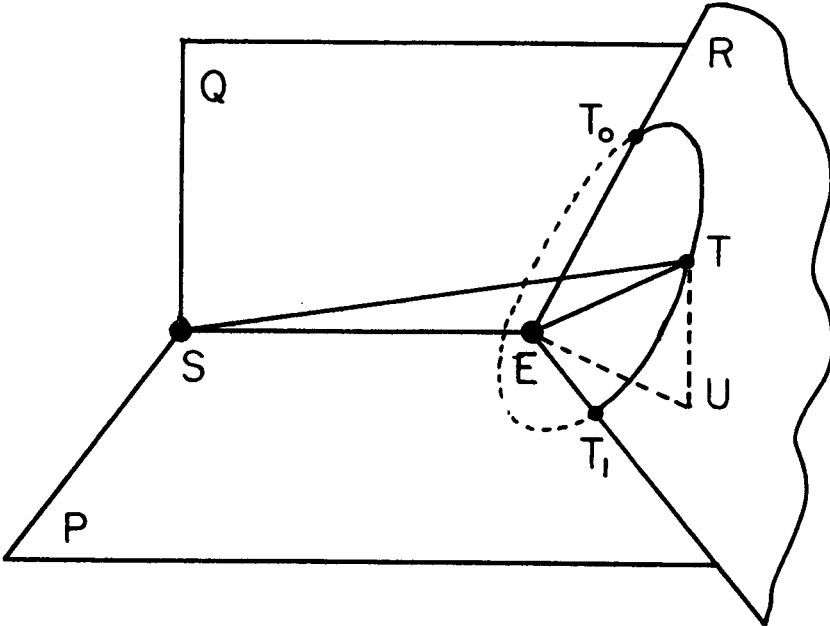
FIG. 2.9  ORIENTATION OF THE OGO-V ORBIT.

and (R) is the plane of the spacecraft orbit. Plane (Q) is normal to (P). S and E are the positions of the Sun and Earth, respectively. T represents the spacecraft. Thus, the antenna at T is always perpendicular to the plane (SET). As the spacecraft moves along its orbit the plane (SET) hinges about the intersection SE and it goes from a position in the plane (P) when T is at $T_1$, to a position normal to (P) when T is at $T_0$. If we accept that the antenna pattern is that of a short dipole, then when the spacecraft is in $T_1$ the direction of the nulls is normal to the plane of the ecliptic (P), and when the spacecraft is in $T_0$ the direction of the nulls is parallel to plane (P) and therefore is perpendicular to (Q). For practical purposes it can be considered that the Sun-Earth direction coincides with the Sun-spacecraft line because the size of the OGO-V orbit is small compared with 1 Astronomical Unit (A.U.) Then we can say that the direction of the nulls rotates in a plane perpendicular to the Sun-Earth line and that it coincides with the plane of the ecliptic twice during each spacecraft revolution of 63.4 hours. The time between successive coincidences are not equal because the speed of the spacecraft changes along the orbit. Due to the motion of the Earth the spacecraft orbit plane (R) rotates about an axis perpendicular to (P) at E completing a rotation in about a year.

CHAPTER III.  THE DATA

## 3.1  The Presentation of the Data

The data can be presented in several forms, the two most useful
being 35-mm Monitoring film and CalComp plots.  The purpose of the
Monitoring film is to display as much data as possible in a semi-processed
stage in order to look for special events that can then be fully processed
in the form of CalComp plots.  All of the processing of the data was done
at the Radio Astronomy Laboratory on the XDS-930 Computer and the associated
special equipment designed and built by the UM/RAO Laboratory staff.  A
detailed description of the data processing has been given elsewhere by
Breckenridge (1969).

The Monitoring Film.  In this format the output voltages of the
eight frequency channels are displayed simultaneously in 35-mm film.  See
Fig. 3.1.  The time axis runs from left to right along the length of the
film.  The outputs of the eight channels are staggered across the width
of the film.  The 3.5-MHz channel is at the top and the seven remaining
channels are displayed below it in order of decreasing frequency.  The
eight tracings have the same time reference, that is, a line perpendicular
to the length of the film corresponds to the same time in all of the
channels.

The zero voltage levels of the channels are equally spaced across
the width of the film except for the 1.8-MHz channel.  In this case,
and for unknown reasons, the background noise level is very high; presumably
because of spacecraft interference.  In order to avoid overlap with the
tracing of the 3.5-MHz output, the 1.8 MHz output level was lowered by 1.0
volt.
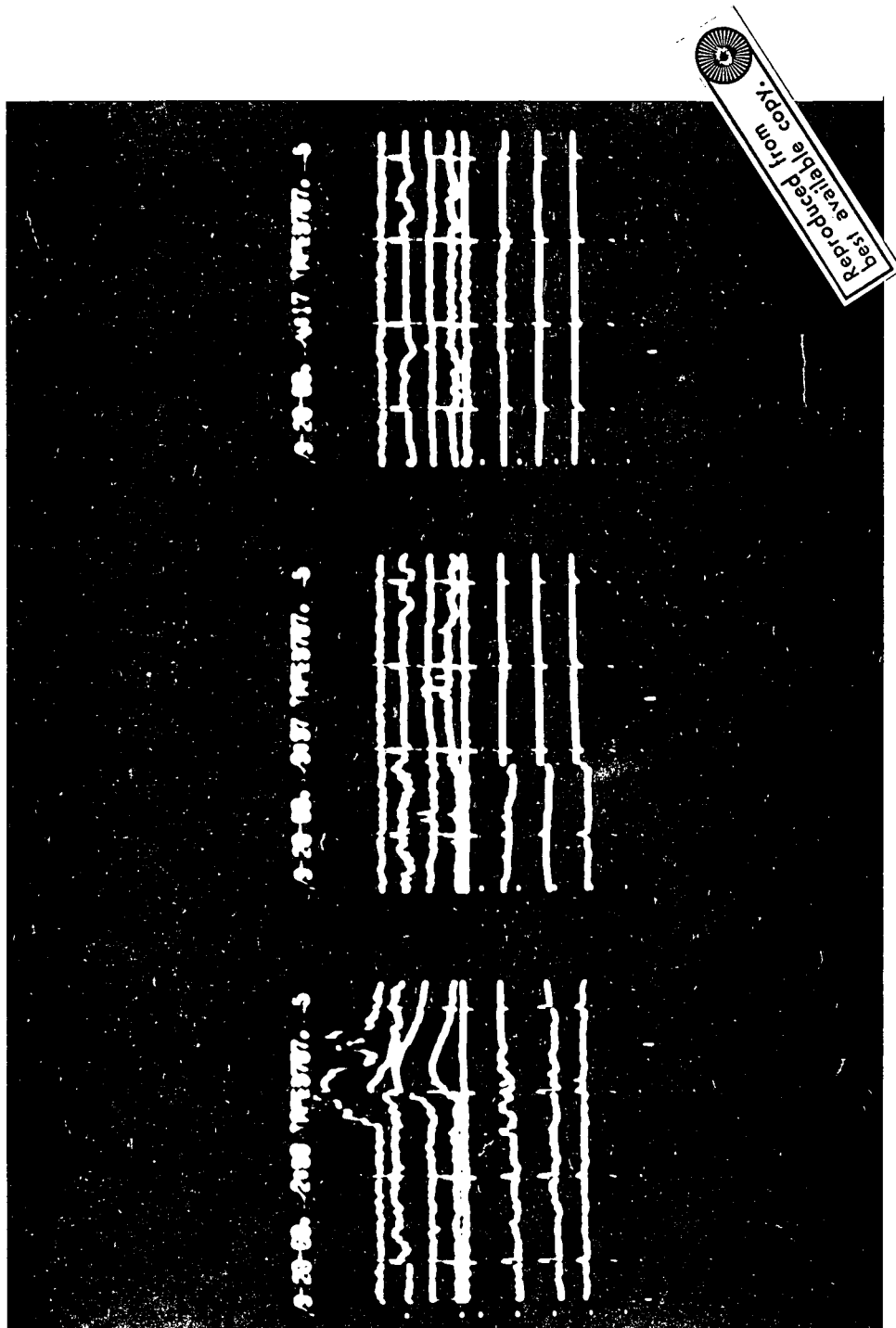
FIG. 3.1  SAMPLE OF 35-mm MONITORING FILM.

The time axis (in U.T.) runs continuously. During the periods of data gaps the computer generates fill data equivalent to a 40.96 volts signal; these are not plotted. Each frame of film contains 39.0 minutes of data. It is important to notice that the blank spaces between frames are not time gaps but are due to the advancing mechanism of the film. The top of each frame contains the following labels: (a) the data and time for the start of the frame, (b) the number of the input data tape and (c) the number of the file in the input tape. Tic marks along the left side across the film indicate the zero voltage level for each of the eight outputs; tic marks along the time axis indicate half hours. Because of the compressed time scale, the inflight calibration signals are seen as vertical short lines about 10 minutes apart.

If the Attitude Orbit (A/O) tape was available at the time of processing the Monitoring Film, some of this information was incorporated into the film. This included, among others, time marks for apogee and perigee passes.

The software to handle the data is called the Monitoring Program. There are programs to process 1 kb/sec and 8 kb/sec data. The program reads the GSFC data tape, unpacks each of the eight outputs, converts them into display coordinates, transfers the data to the buffer core and then to the photographic cathode ray tube where all eight output voltages are plotted simultaneously and are photographed on-line by a 35-mm automatic camera.

Of the two output samples taken during each main commutator cycle, only the second one (word 125) is used in 1 kb/sec data. In the 8 kb/sec data we use the word 125 of the eighth main commutator cycle. In both

cases the sample is taken 5.37 post-detector time constants after the
frequency is changed. This criterion was adopted in order to arrive
at 1% of the steady-state value. There is no program for the 64 kb/sec
data because the effort involved is not compensated by the small amount
of information recorded at this data rate.

The CalComp Plots. The periods of time of special interest found
in the Monitoring Film, or otherwise, are processed in a CalComp Model
565 plotter. Separate plots are made for each frequency channel. The
computer corrects the output voltage for the transfer curve corresponding
to the frequency channel being processed, and then displays it in units
of RT (ohm - K) product. See Fig. 3.2. Because of the high intensity of
the solar bursts selected in this study, scales of about $10^{10}$ or $10^{11}$
(ohm - K) per inch are necessary in order to have the burst time profile
within the limits of the paper, 8 inches maximum. The time scale used
was 3 minutes per inch because in so doing, 0.1 inch contain two consecutive
sample points of the radiometer output and so the samples are readily
identifiable. This is relevant in measuring the time of start of a burst.
The pen of the plotter connects the points by straight line segments in
such a way that the curve intensity versus time is continuous. The CalComp
plots are conveniently labeled with the pertinent information. The
calibration cycles are not plotted and their time is filled with a straight
segment.

## 3.2 Data Coverage in Time

The Monitoring film that was scanned in search of solar bursts
included data between 14 March 1968 (the day the Radio Astronomy antenna
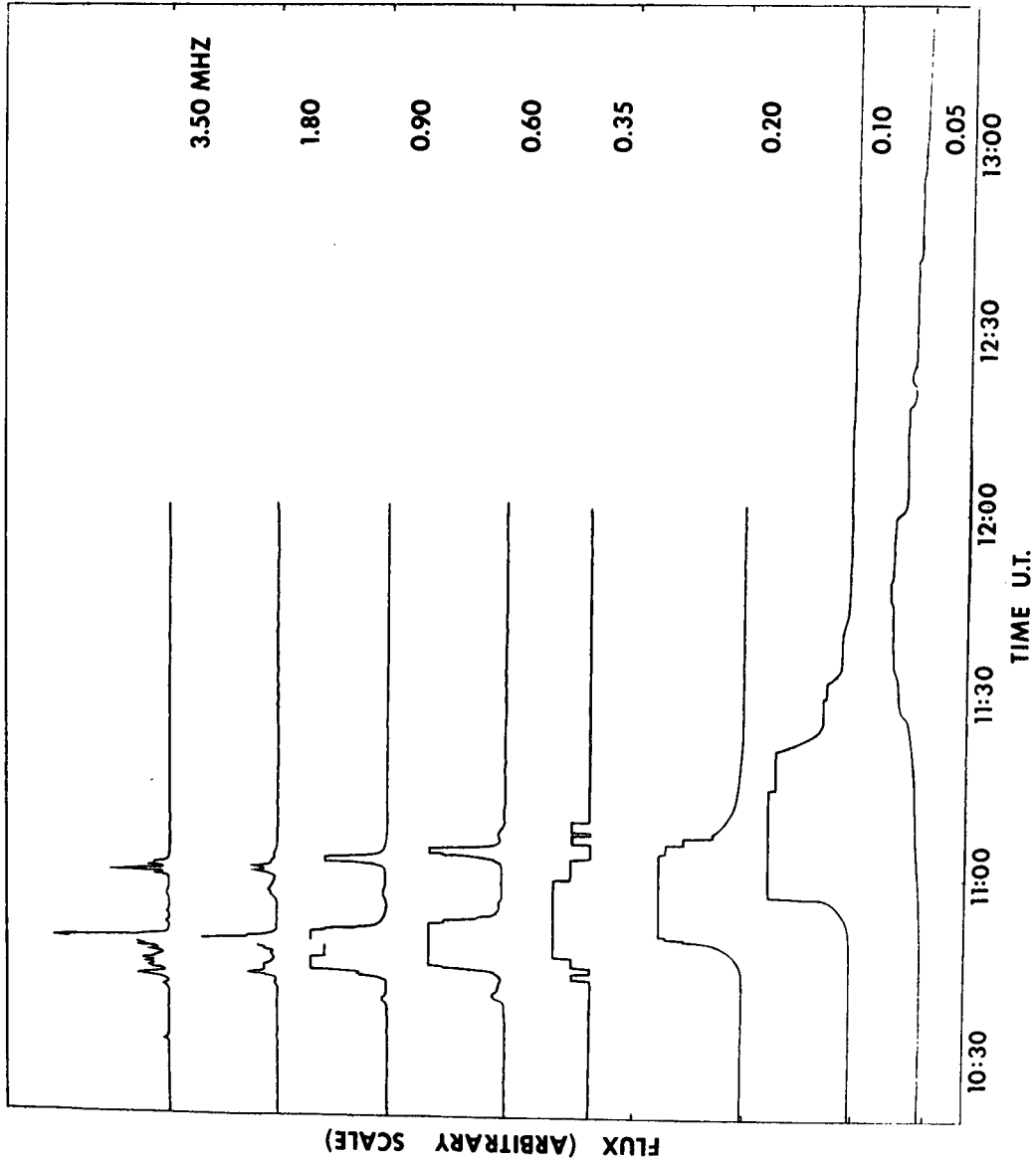
FIG. 3.2a  CALCOMP TRACINGS FOR THE 18 NOVEMBER 1968 EVENT

AFTER IMPULSIVE INTERFERENCE HAS BEEN REMOVED.  THE

FLUX DENSITY SCALE AT 3.5 MHz IS ENLARGED 10 TIMES.
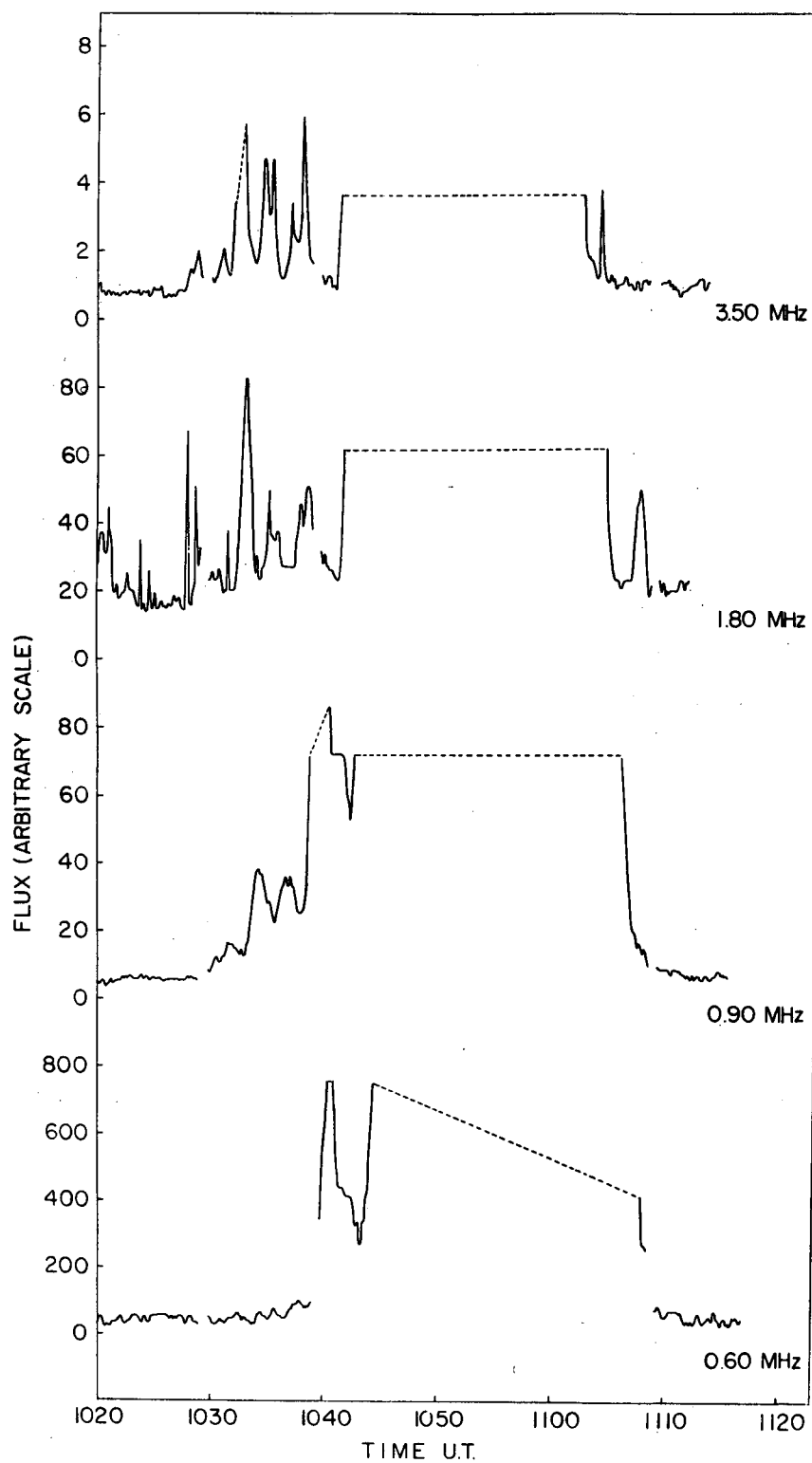
FIG. 3.2b   TRACING FOR THE 18 NOVEMBER 1968 EVENT.   ENLARGEMENT
OF THE UPPER FOUR CHANNELS.   THE DOTTED LINES CORRESPOND
TO OFF-SCALE VALUES.

was deployed) and February 1970. For the period from March 1968 through June 1969, the data time coverage was fairly complete with a total of about 7212 hours. Table 3.1. The data between 24 April 1968 - 18 June 1968, during which time the radiometer was in the non-stepping mode, was not processed. When it was decided to stop searching for bursts with the purpose of analysis, only sparse data had been received for the period between July 1969 - February 1970. The data for this time period probably did not cover more than 2000 hours.

## 3.3  Characteristics of the Data

The data may have been marred by any of the following reasons:

(a)  Inflight Calibrations. These last for 36.9 sec and repeat every 9.83 minutes and affect all frequency channels simultaneously. Sometimes they would occur at the beginning or the middle of an important burst.

(b)  Data Gaps in Time Coverage. These had the same effect as (a) except that they can be longer but they rarely coincided with important bursts.

(c)  Sporadic Spacecraft Interference. This permanently affects the 0.35-MHz channel and, most of the time, the rest of the lower ones.

(d)  Ionospheric noise. Strong noise is detected, especially in the higher frequency channels, when the spacecraft goes through perigee. It may be due to drastic changes in the antenna impedance or to noise produced by the ionosphere itself, or induced by the spacecraft. During the period scanned for this study the geocentric height of perigee increased from 6800 to 21800 km and the geocentric height of apogee decreased from 153000 to 138000 km.

Table 3.1

Total Amount of OGO-V Data Searched

| | Hours of Data | Total Coverage in Month (%) |
|---|---|---|
| 1968 | | |
| March | 609.3* | 95.20* |
| April | 371.0 | 51.53 |
| May | 10.3 | 1.38 |
| June | 290.6 | 40.36 |
| July | 711.0 | 95.57 |
| August | 691.7 | 92.98 |
| September | 511.3 | 71.02 |
| October | 552.0 | 74.19 |
| November | 552.0 | 76.67 |
| December | 507.0 | 68.15 |
| 1969 | | |
| January | 519.0 | 69.76 |
| February | 348.3 | 51.83 |
| March | 476.5 | 64.05 |
| April | 411.5 | 57.15 |
| May | 401.3 | 53.95 |
| June | 460.7 | 63.99 |
| July | 364.0 | 48.92 |
| August | 445.6 | 59.90 |
| September | 253.0 | 35.14 |
| October | 503.0 | 67.68 |
| November | 223.8 | 31.08 |
| December | 33.8 | 4.55 |
| 1970 | | |
| January | 365.0 | 49.1 |
| February | 336 ** | 50 |

---

* This is measured from the 5th of the month, the time at which we first received data. The antenna was deployed on the 14th.

** Estimated.

We may expect some ionospheric frequency cut-off when the spacecraft is near perigee. Typical values of electron densities in the ionosphere are shown in Table 3.2 (Bowles, 1963; Slysh, 1965). Also shown are the corresponding plasma frequencies. The distances are measured from the center of the Earth.

With good approximation, we can compute the effect of the Earth's ionosphere, assumed spherically symmetric, on our data. Let us consider the revolution No. 117 (31 December 1968 - 2 January 1969) as an example. Taking the data of the OR 3/A predictions, mentioned in Section 2.2.1, and that of Table 3.2, we found that the spacecraft spent 96.9% of the period (62.4 hours) outside the 0.1-MHz level and 87.2% of the period outside the 0.05-MHz level. Since the 0.05-MHz bursts occur rarely, we concluded that the ionosphere had very little effect on the observing capability of the radiometer. In fact, we found only one case of a strong event in which the 0.6-MHz burst must have occurred just after the spacecraft penetrated the corresponding critical level in the ionosphere because there was no indication of it in the 0.6-MHz channel while the 0.9-MHz burst was very strong. (3 April 1969)

The amount of time during which the spacecraft was eclipsed by the Earth from the Sun is negligible.

## 3.4 Selection of the Data

It became clear at an early stage in the scanning of the monitoring film that the quality of the data, as determined by the impulsive inter-ference, would impose the following logical division: the data from the highest four frequency channels (the high-frequency range) constitute

Table 3.2

Typical Ionospheric Electron Densities

| $\frac{N}{(cm^{-3})}$ | $\frac{f}{(MHz)}$ | $\frac{R}{(km)}$ |
|---|---|---|
| $1.5 \times 10^5$ | 3.5 | 7200 |
| $4 \times 10^4$ | 1.8 | 8200 |
| $10^4$ | 0.9 | 9800 |
| $4.4 \times 10^4$ | 0.6 | 11000 |
| $1.5 \times 10^3$ | 0.35 | 13500 |
| $5 \times 10^2$ | 0.2 | 14900 |
| $1.2 \times 10^2$ | 0.1 | 21400 |
| $31^{(*)}$ | 0.05 | 53700 |

(*) Extrapolated from Slysh (1965, Fig. 2)

one group and the data from the lowest four frequencies (the low-frequency range) constitute the other. As we saw in paragraph 2.1.5, only those bursts having a flux density of the order of $10^{10}$ ohm-K (see Fig. 2.6), at and below 0.2 MHz, would exceed the limits set by the noise background of the system. In the same range of requencies, the requirement on minimum flux density rises to about $5 \times 10^{11}$ ohm-K when the burst occurs during the presence of impulsive interference. Since the four low-frequency channels are affected by this type of noise most of the time, it turns out that only a few extremely strong solar bursts were observed by our radiometer in that range. There is a large number of strong bursts that are just below the intensity limit. These bursts are usually very well developed in the range of 3.5-0.6 MHz. We estimate that their number may be about ten times larger than that of the very low frequency bursts.

Since the OGO-V radiometer has at least two channels below the lowest frequency of observation of Type III solar bursts reported in the literature, we decided that the most important area of study was that of the very low frequencies, down to and below 0.35 MHz. As a direct consequence the observed events would be affected, in general, by the problem of saturation combined with telemetry quantization.

It is important to realize that the way in which the data have been chosen may introduce a selection effect on the final conclusions drawn from this study. A study of the hundreds of bursts in the range between 3.5 and 0.6 MHz would shed light on this matter. The amount of data scanned is approximately that shown in Table 3.1 and it covers about 9000 hours. In these data we found 64 events that satisfied the

selection criterion. Inspection of data processed after the 64 bursts were selected indicates that there were 15 more bursts in the period extending from July 1969 through middle February 1970. These 15 bursts were not included in this analysis. The 64 selected events that we could properly call kilometric-wave bursts are listed in Appendix 1, Table A.1.

CHAPTER IV.  ANALYSIS OF THE SELECTED EVENTS

## 4.1  Measurable Parameters

In the last section of the previous chapter we stated the criterion

adopted to select the radio events for further study.  They should be

observed down to or below 0.35 MHz.  Since the noise system level of the

four lowest channels is usually high because of radio interference, a

burst to be observed in these channels needed to be extremely strong.

We found that a characteristic inherent to all these events was a very

complex time structure.  We have implied that a very strong event is also

very complex.

For discussion it is appropriate to establish some definitions.

We will call EVENT the complete radio phenomenon from the time it starts

in our records until it ends.  This definition may be used in a more

restrictive sense when it refers to only one frequency.  The objective

of the definition is to distinguish the whole complex time profile, EVENT,

from its individual COMPONENTS, or BURSTS components.  Because of

limitations in time resolution due to sampling rate or to saturation

effects already discussed, the number of identifiable components

constitutes a lower limit of the actual number.

The profiles of intensity versus time that the radiometer provides

at each frequency allows us to measure the following parameters of interest:

(a)  Time of start of an event and of its components at the different

frequencies,

(b)  Rise time, defined as the time it takes a burst to rise within

certain fractions of its peak value,

(c) Decay time, defined as the time it takes a burst to decrease from its peak to 37 percent of that value ($e^{-1}$),

(d) Duration of an event or its components,

(e) Peak intensity.

## 4.2 Time of Start

As it has been explained in Section 2.1.6, the maximum accuracy with which we can measure a starting time is 9.2 sec. We can reach this accuracy in the 3.5, 0.9, and 0.6 MHz channels. Since the 1.8-MHz channel is usually noisy the accuracy is reduced. The accuracy is always poor in the 0.35-MHz channel and it varies between good and poor in the 0.2-, 0.1- and 0.05-MHz channels, depending on the presence of impulsive interference. This is usually present at the times of occurrence of the selected bursts. However, this does not render our data useless because the delay in the times of arrival of the bursts increases rapidly with decreasing frequency and the accuracy in the measurement becomes less critical.

The times of start of the components of an event were plotted in graphs displaying frequency versus time. The scale used was 2 inches/MHz in the ordinate and 3 min/inch in the abscissa. We plotted not only the time of start of well identifiable components but also those times at which a discontinuity in either the rising or decaying part of a burst profile suggested a buried component. Very often in the case of strong events and because of the quantization-saturation effect, the peak becomes a horizontal trace of up to several minutes of duration. In those cases it is impossible to guess how many components are hidden.

The uncertainties in the times of arrival were represented in the plots by horizontal segments. The inaccuracies in frequency are not noticeable in the chosen scale. The time of start of the 3.5-MHz leading component was used as reference. An example is shown in Fig. 4.1.

Sometimes a few or all points corresponding to a frequency channel may be missing because of gaps in the data, or interference, or just because the burst was weak.

4.2.1 Observed Frequency Drift Rates. A direct result from the measurements of the arrival time of a burst is its frequency drift rate (FDR). The first step in the technique used to determine the FDR consisted in drawing a smooth curve through the observed points corresponding to a certain component in the plot of frequency versus time of arrival. The second step was to measure the slope of the curve thus obtained at a certain number of points. The advantage of the method is that it handles graphically the uncertainties in the time of arrival. It is equivalent to a weighted graphical averaging. Whenever it was possible two extreme smooth curves compatible with the data would be drawn. The slope measured at a certain frequency in these two curves would give the upper and lower limits of the FDR at that frequency. Because we had obtained a continuous curve in frequency versus time we could measure the slope at any frequency. In each case we selected the two extreme frequencies in the following way: the highest frequency was midway between the first and the second present, the lowest frequency was midway between the last one present and the one before the last. The intermediate points were usually selected at the frequencies of observation except in special cases where more points were needed. The values of FDR so obtained were plotted on log-log paper
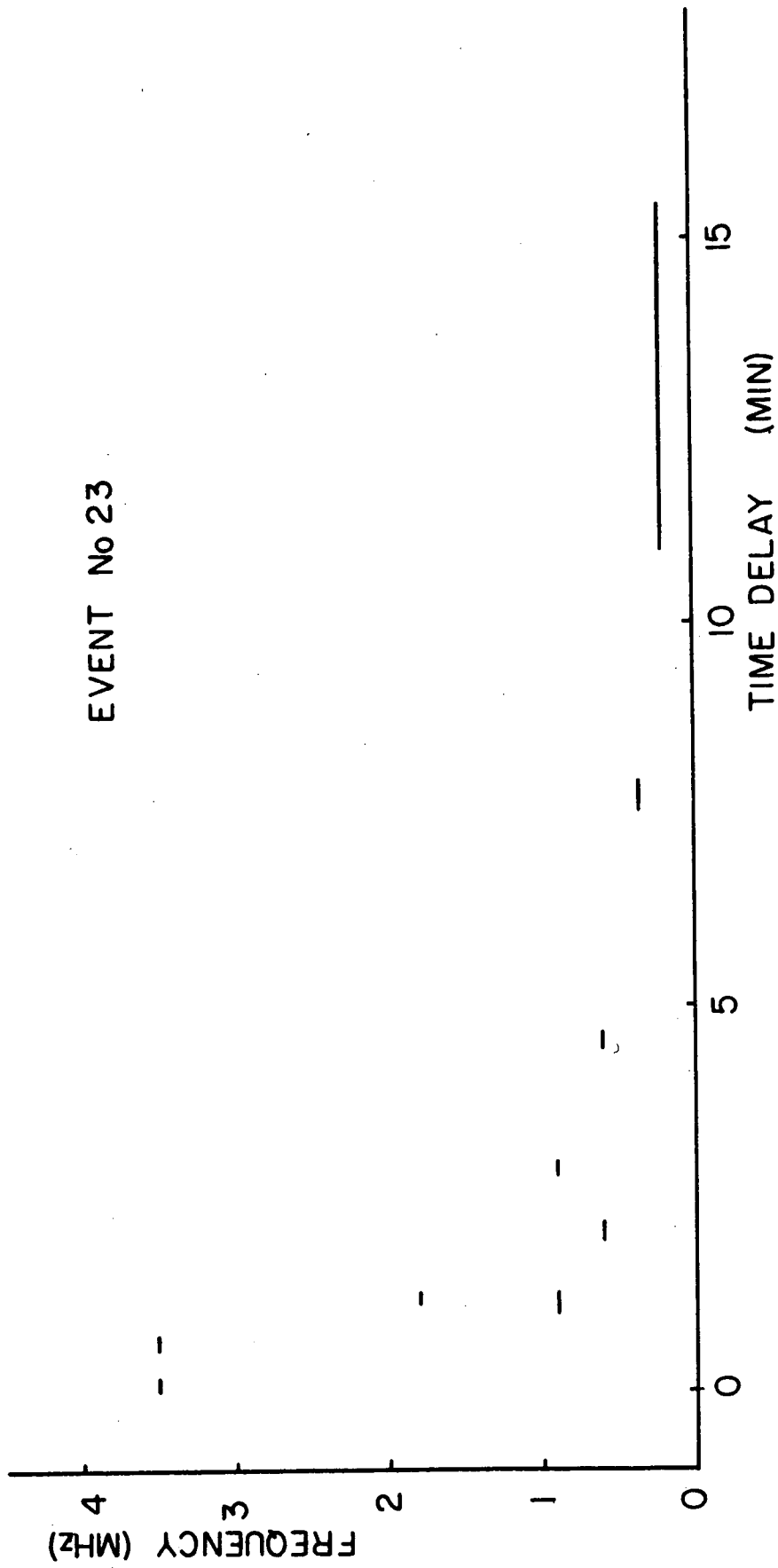
FIG. 4.1  EXAMPLE OF FREQUENCY VERSUS OBSERVED ARRIVAL TIMES.

LEADING COMPONENTS.

with df/dt as ordinate and f as abscissa. The points were then connected by straight segments with an approximate best fit.

The validity of the method depends on the unmistakable identification of one and the same component at each of the frequencies of observation. This limited the applicability of the technique because of the extreme complexity of the selected events, plus the lack of time resolution. We thought of two cases in which the method would be applicable. In the first case the criterion adopted was to use the time of start of the event and assume that at each frequency this corresponds to the time of start of the first component of the complex. In the second case, whenever an event contained a component several times stronger than the rest it was assumed that this component could be followed without too much ambiguity at lower frequencies. As we will see shortly the assumption involved in the two cases were not always found to be valid. Those events in which the assumptions were correct permitted us to extend the knowledge of FDR of Type III bursts down to 0.075 MHz. The others led to the discovery of the unexpected prevalence of second harmonic emission below about 1 MHz. (Section 4.2.5).

By using the above technique we obtained FDR curves for the first 52 selected events. (Of the rest, 11 were selected from the raw data after we found problems in interpreting the results and therefore we did not process them in this way, and one was useless for this purpose.) We found that, based on their shapes, we could classify the curves into several groups that we designated as A, B, C, D, E, and Unclassified. See Fig. 4.2. Haddock and Alvarez, (1970). The FDR's of the bursts in the last group were not amenable to the drawing of any meaningful curve. It
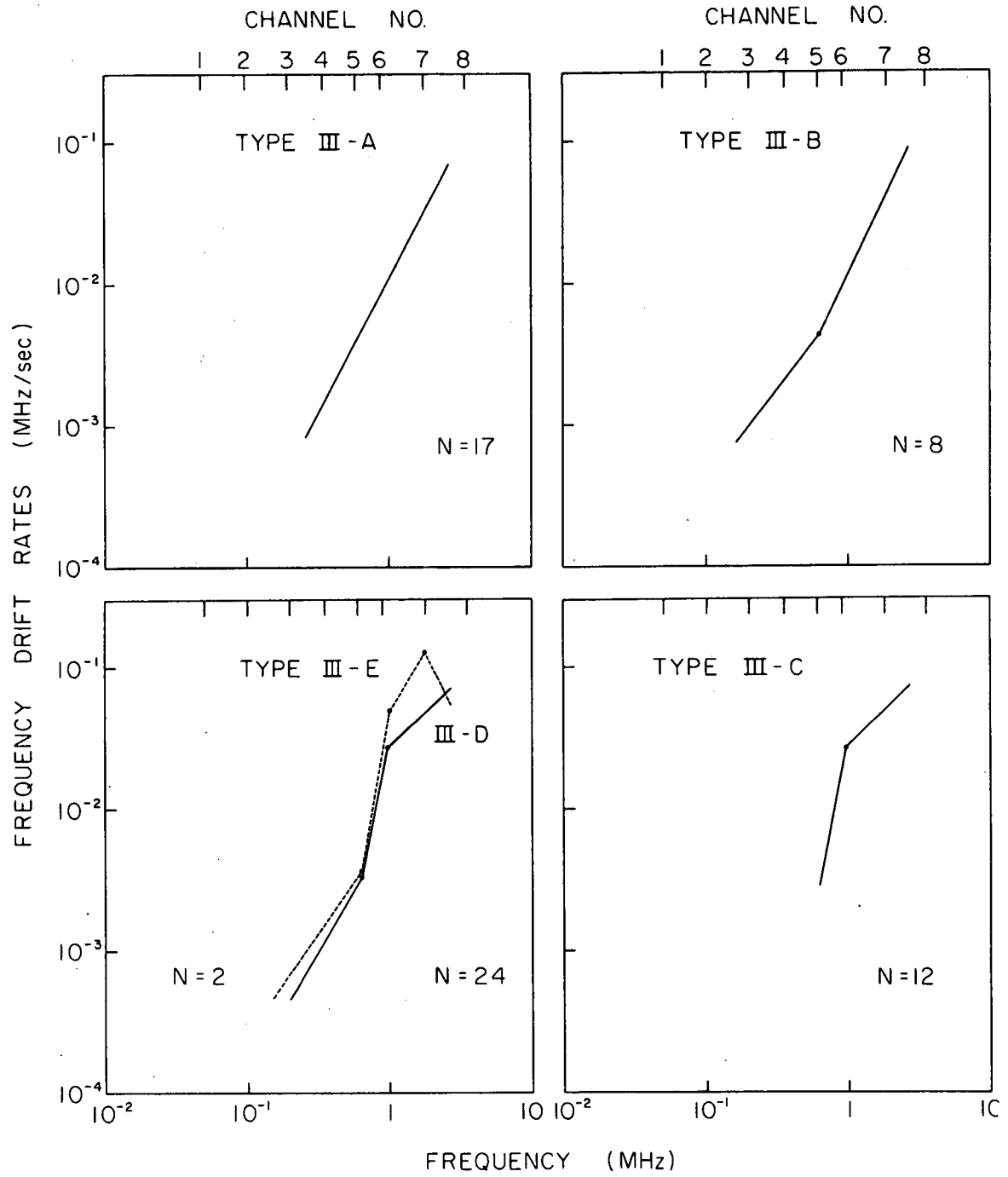
FIG. 4.2  TYPES OF APPARENT FREQUENCY DRIFT RATE CURVES.

turns out, as we will see later, that the only cases for which the curves really represent FDR are those in group A. The peculiar shapes of the other groups are artifacts produced by a technique that does not discriminate between fundamental and second harmonic emission.

Fortunately the first bursts selected for analysis were those in group A. They were chosen because of the simplicity of their FDR curves: a straight line. The technique to be described in Section 4.2.5 revealed that the emission of these bursts at the different frequencies was mostly at the fundamental or at the second harmonic, to the extent that this could be determined. The FDR curves were obtained for 17 of the 53 bursts. (The number is 53 and not 52 because in event No. 62 we could measure two components.) The numbers of the corresponding events, as given in Table A.1 of Appendix 1, are: 6, 13, 16, 18, 19, 20, 22, 24, 25, 27, 29, 30, 31, 34, 62.

A straight line can be characterized by its slope, $\alpha$, and by its intercept with the ordinate axis, a. We can thus write the equation of a straight line in a log-log plot as:

$$\log \left| \frac{df}{dt} \right| = a + \alpha \log f \ . \tag{4.1}$$

In our plots we expressed f in MHz and t in seconds. The parameter "a" is the logarithm of the FDR at 1 MHz. The slope of the line is positive, $\alpha > 0$.

Equation (4.1) can be written:

$$\frac{df}{dt} = -10^a f^\alpha \ , \tag{4.2}$$

where the negative sign has been added because as the time increases
the frequency drifts from high to low values. The form of this equation
suggests defining $\alpha$ as the FDR Index. Within the accuracy of our
measurement this relationship is valid at least between 2.65 MHz, the
mid frequency between the two highest channels, and 0.075 MHz, the
mid frequency between the two lowest channels. We will see very soon
that its validity holds up to 550 MHz. (Haddock and Alvarez, 1969).

The measured values of a and $\alpha$ are given in Table 4.1 and their
frequency distributions are presented in Fig. 4.3.

Figure 4.3a shows that the spread in the distribution of "a" is
not too large while Fig. 4.3b shows that the spread in $\alpha$ is larger.
It is interesting to observe that $\alpha$ does not become less than 1.0.
We will refer to this point in Sections 4.2.3 and 4.2.4. The distri-
butions have the following values of average and standard deviation:

$$\bar{\alpha} = 1.92 \quad , \quad \bar{a} = -1.93 \quad , \quad \sigma_\alpha = 0.38 \quad , \quad \sigma_a = 0.13 \quad . \quad (4.3)$$

Table 4.1 does not contain observations below 0.1 MHz. In fact,
the only event observed down to 0.05 MHz is the event No. 21. The
characteristics of its FDR curve are those of a straight line except
close to the higher frequencies where the points lie somewhat above the
extrapolated straight line. Because of this closeness and because of the
uniqueness of this event it was included in our calculations but it
was treated in a different approach. This consisted in averaging, at
each of the frequencies selected for FDR measurements, the values of
FDR obtained for the 18 different bursts. These averages
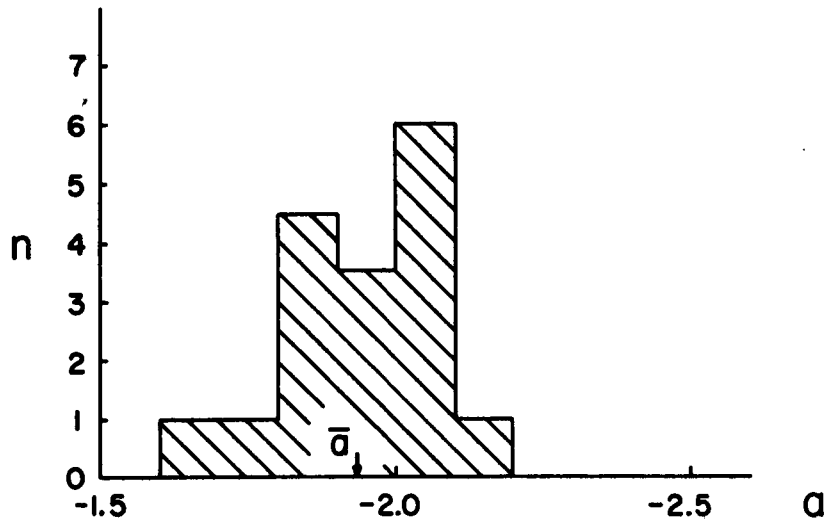
(a)
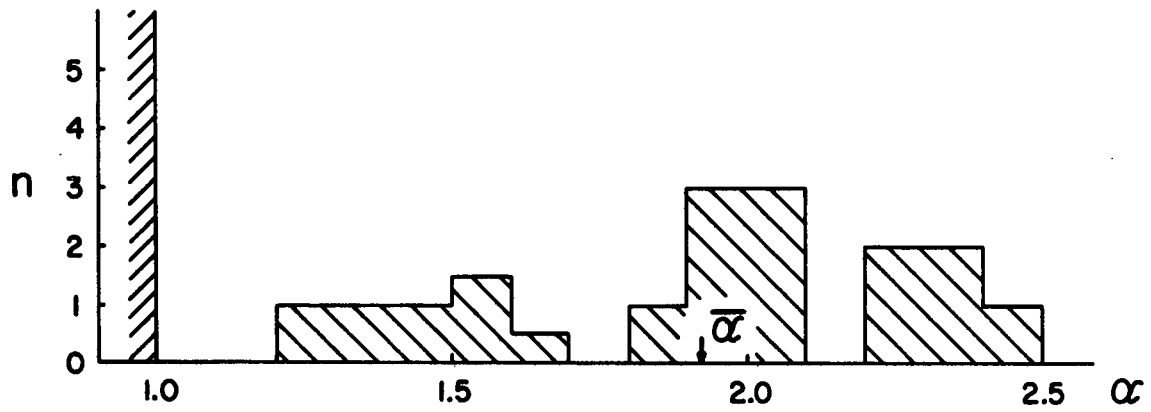


(b)

FIG. 4.3   DISTRIBUTION OF THE PARAMETERS a AND $\alpha$ IN THE TYPE A

BURSTS.

## Table 4.1

Parameters of Frequency Drift Rate Curves for Bursts of Group A(*)

| Event No. | a | α |
|---|---|---|
| 6 | - 1.92 | 1.42 |
| 13 | - 1.75 | 2.05 |
| 16 | - 1.90 | 1.98 |
| 18 | - 1.90 | 1.31 |
| 19 | - 2.18 | 2.24 |
| 20 | - 1.96 | 2.01 |
| 22 | - 1.84[**] | 2.27[**] |
| 24 | - 1.83 | 1.97 |
| 25 | - 2.02 | 1.83 |
| 27 | - 2.01 | 1.59 |
| 29 | - 1.83 | 2.48 |
| 30 | - 2.04 | 2.03 |
| 31 | - 1.90 | 2.34 |
| 34 | - 1.65 | 1.21 |
| 42 | - 2.03 | 1.93 |
| 62 | - 2.03 | 1.60 |
| 62 | - 2.08 | 2.32 |

(*) These measurements were made from graphs in which f was expressed in MHz and time in seconds.

(**) Averages.

were plotted against frequency in a log-log graph and a straight line
fitted by the least-squares method. The frequencies used and the
averaged FDR obtained are presented in Table 4.2. The least-square
fitting of a straight line gave the following parameters:

$$\alpha = 1.93 \; , \quad a = -1.89 \; , \quad \sigma = 0.08 \; , \quad (4.4)$$

where $\sigma$ is the standard deviation of the dispersion in ordinates of
the data points with respect to the fitted line. The line and the
data of Table 4.2 are shown in Fig. 4.4.

We see that the values of a and $\alpha$ found by the two methods are
not significantly different. For describing an average FDR curve we
have chosen the second procedure because it is the one consistent with
the form in which the data at other frequencies, that we will soon use,
are given in the literature.

The next step in the study of FDR of Type III solar bursts was
to find the extent of the validity of the empirical law described by
Eq. (4.2). For this we collected some of the data on FDR published in
the literature. These data are shown in Fig. 4.5 that also shows the
OGO-V points listed in Table 4.2. The least squares fit of a straight
line through the points other than OGO-V's gave the following parameters:

$$\alpha = 1.88 \; , \quad a = -2.07 \; , \quad \sigma = 0.13 \; . \quad (4.5)$$

The least square fit to a straight line of all the points
contained in Fig. 4.5 except Young et al., gave the following results:

Table 4.2

Average Frequency Drift Rate for 18 Bursts

| f (MHz) | $\log \left\|\overline{\dfrac{df}{dt}}\right\|$ | $\sigma$ (*) | $\left\|\overline{\dfrac{df}{dt}}\right\|$ MHz sec$^{-1}$ |
|---|---|---|---|
| 2.70 | - 1.07 | 0.16 | $8.5 \times 10^{-2}$ |
| 1.80 | - 1.44 | 0.10 | $3.7 \times 10^{-2}$ |
| 0.90 | - 1.90 | 0.19 | $1.3 \times 10^{-2}$ |
| 0.75 | - 1.98 | 0.23 | $1.0 \times 10^{-2}$ |
| 0.60 | - 2.36 | 0.17 | $4.4 \times 10^{-3}$ |
| 0.48 | - 2.48 | 0.22 | $3.3 \times 10^{-3}$ |
| 0.35 | - 2.86 | 0.11 | $1.4 \times 10^{-3}$ |
| 0.275 | - 3.08 | 0.15 | $8.4 \times 10^{-4}$ |
| 0.20 | - 3.28 | 0.12 | $5.3 \times 10^{-4}$ |
| 0.15 | - 3.47 | 0.14 | $3.4 \times 10^{-4}$ |
| 0.10 | - 3.79 | 0.13 | $1.6 \times 10^{-4}$ (**) |
| 0.075 | - 4.01 | 0.15 | $9.8 \times 10^{-5}$ (**) |

(*) This is the standard deviation corresponding to the values in the second column.

(**) These two values come from only one observation. The error quoted corresponds to the maximum and minimum values compatible with the observation.
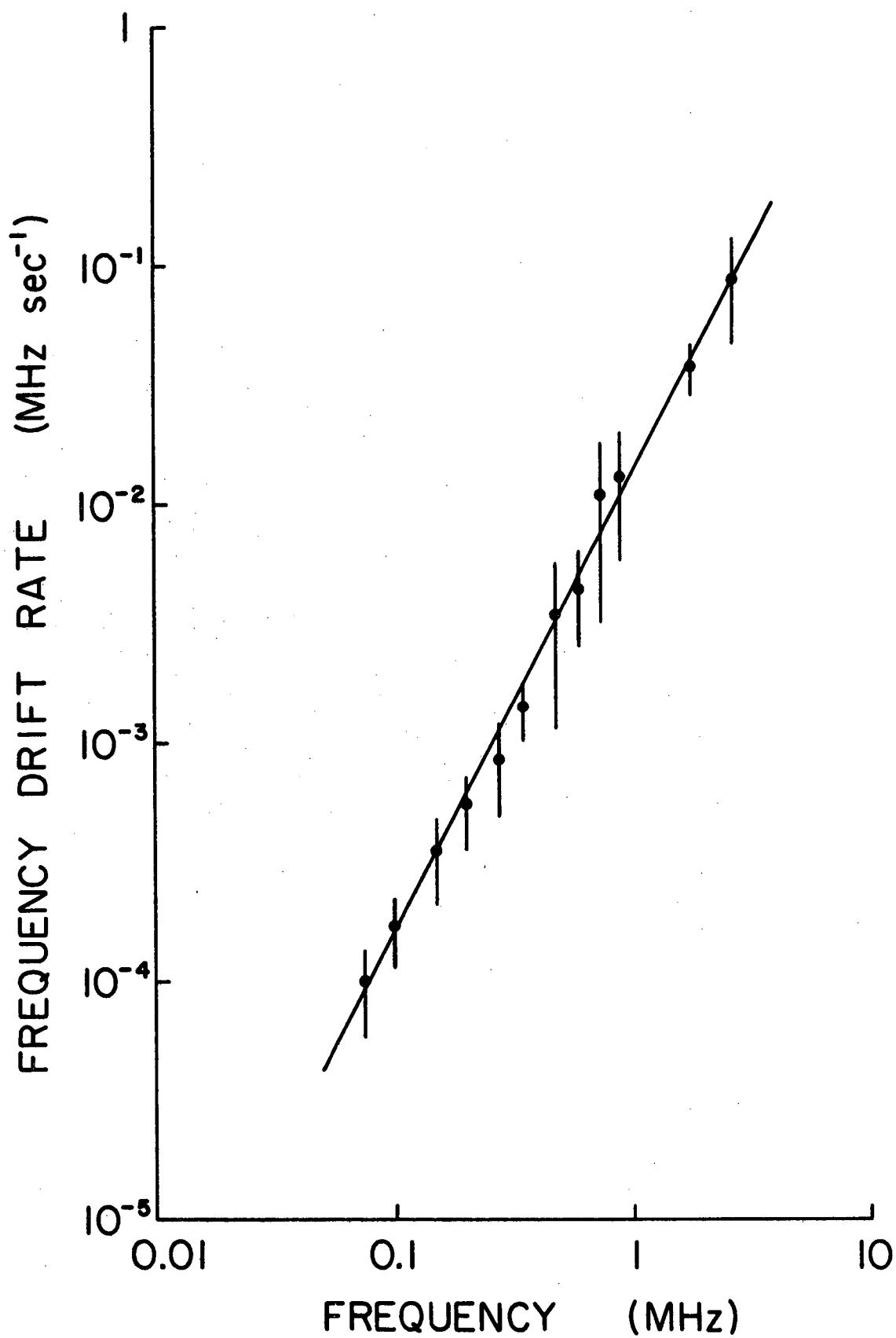
FIG. 4.4  AVERAGE FREQUENCY DRIFT RATES FOR 18 BURSTS OBSERVED

BY OGO-V.
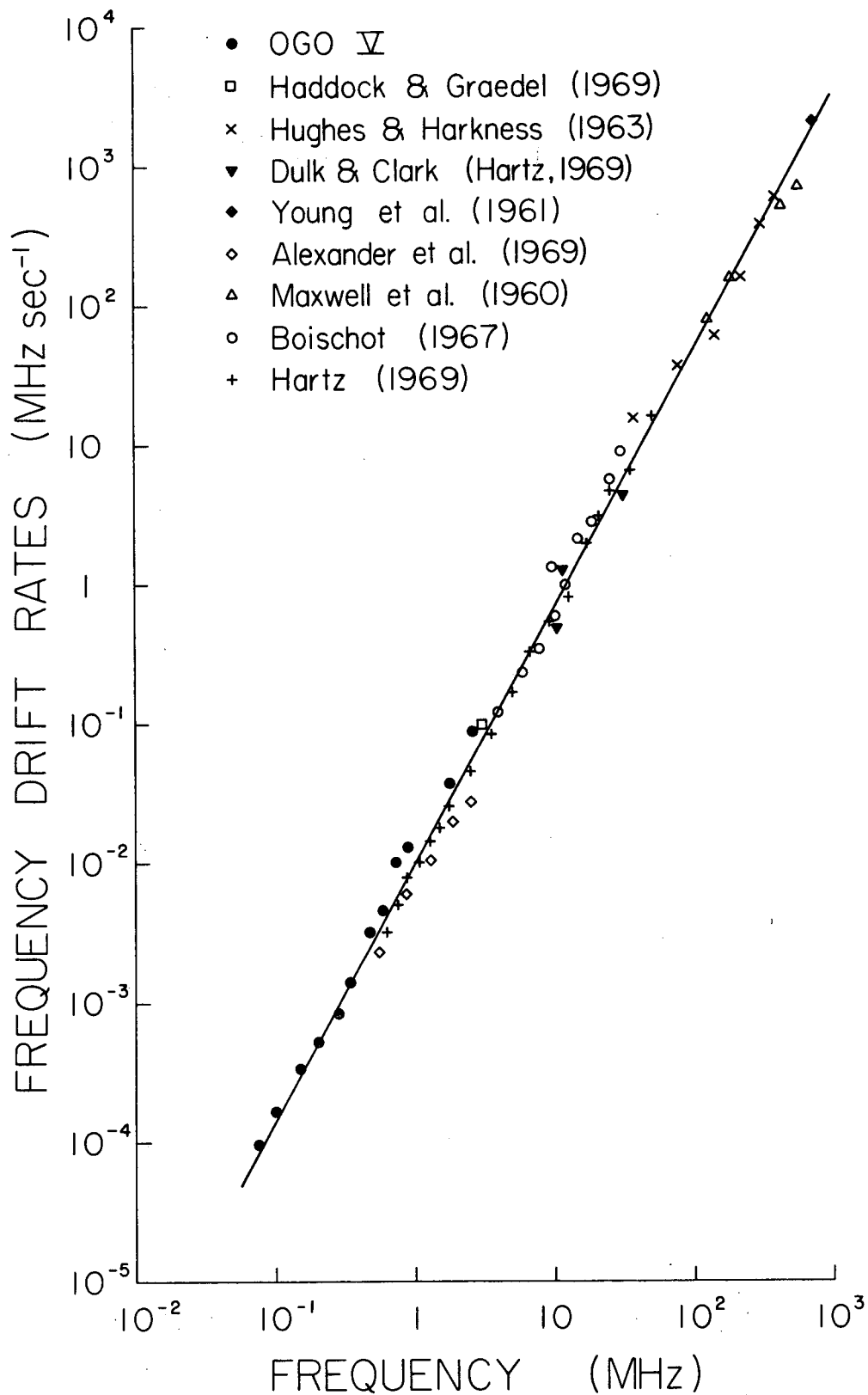
FIG. 4.5 FREQUENCY DRIFT RATES FOR TYPE III BURSTS.

$$\alpha = 1.84 \quad , \quad a = -2.00 \quad , \quad \sigma = 0.13 \quad . \qquad (4.6)$$

A line with the parameters of Eq. (4.6) is shown in the same figure.
The summary of all these data is presented in Table 4.3.

<div align="center">Table 4.3</div>

<div align="center">Least Square Fit of the Line $\log \left| \dfrac{df}{dt} \right| = a + \alpha \log f$</div>

| Data | $\alpha$ | $a$ | $\sigma$ |
|---|---|---|---|
| OGO-V.  Table 4.2 | 1.93 | - 1.89 | 0.08 |
| Other than OGO-V's | 1.88 | - 2.06 | 0.13 |
| All | 1.84 | - 2.00 | 0.13 |

In order to represent the variation of the frequency drift rate
with frequency we will adopt the parameters derived from "all" the
data. The error that we will make by using this line to represent the
OGO-V data is several times less than $\sigma_a$ and $\sigma_\alpha$. We can conservatively
state that Eq. (4.2) is valid between 550 and 0.075 MHz and can be
written

$$\frac{df}{dt} = - 0.01 \, f^{-1.84} \text{ MHz sec}^{-1} \quad .$$

The data of Young et al. (1961) between 500 and 940 MHz were not used
because it is not certain that the bursts are of the classical Type III,
(Kundu et al. 1961). However they agree with the values expected from
an extrapolation of the computed line. Young et al. found that the frequency
drift rate is $\gtrsim 2000$ MHz sec$^{-1}$.

The line that fits all the observations in Fig. 4.5 deserves special attention because it is remarkable that such a good linear fit can be obtained over seven decades in frequency drift rate with observations made in such a variety of circumstances. For example, the earliest observations included are from Maxwell et al. (1960) and were taken close to the sunspot maximum of 1958.25. On the other hand, the OGO-V data was obtained at the next sunspot maximum, in 1968. The data contained in Fig. 4.5 span 80 percent of an 11-year cycle, from peak to peak. The positions of the associated flares are not known, except for OGO-V data, and we can expect them to cover a wide range of values. The velocities of the exciter particles also are known to have an appreciable distribution of values. Finally, the coronal electron densities as well as the emission mode (fundamental or second harmonic) associated with each measurement may have been different. In spite of all this, the standard deviation in the spread of the points in $\log |df/dt|$ from the best fit line is only 0.13.

Attempts have been made in the past to find a mathematical expression for the FDR as a function of frequency. Wild (1950) found in the range 70 to 130 MHz:

$$\frac{df}{dt} = -\frac{f}{4.5} \, , \quad \text{MHz sec}^{-1} \, .$$

In fact, he started with the same relationship as Eq. (4.2) and he then used $\alpha = 1$.

There was early recognition that the plot of $\log |df/dt|$ versus $\log f$ was a straight line (for example, Hartz 1969). Graedel (1969) wrote an expression in the form of Eq. (4.1) that he used to compute

electron density gradients in the solar corona. The form Eq. (4.2) simplifies mathematical manipulation and retains the sign.

We can summarize this section as follows:

(a) We have developed a technique for measuring the FDR of Type III bursts. Its indiscriminate use in cases where it is not applicable led to the disclosure of an unexpected prevalence of second harmonic components, as will be explained in Section 4.2.5.

(b) We established that a plot of frequency drift rate versus frequency in a log-log scale can be well represented by a straight line down to 0.075 MHz.

4.2.2 **Basic Assumptions.** The analysis of the frequency drift rates of Type III bursts depends on a knowledge about the following subjects:

(a) Electron density of the solar corona,

(b) Mechanisms of emission of Type III bursts,

(c) Trajectory of the exciter particles,

(d) Velocity of the exciter particles,

(e) Propagation of the electromagnetic radiation through the solar corona to the Earth's environs,

(f) Other subjects.

The purpose of this section is to obtain models of the electron density distribution that are consistent primarily with observation and, if possible, with theory. These models will be based on assumptions regarding the last five subjects. We will start by discussing these subjects.

(a)  Electron Density Distribution of the Solar Corona

The only ranges of distance studied experimentally before the OGO-V observations were near the Sun and near the Earth.

Optical observations have provided information to distances out to 20 solar radii ($R_\odot$). Some of the optical studies were done by Baumbach (1937), van de Hulst (1950), Michard (1954), Blackwell (1956), Blackwell and Petford (1966), Gillet et al. (1964), Newkirk et al. (1969), Hansen et al. (1969), Newkirk et al. (1970) and Schmidt (1953).

The electron density N of the solar wind near the Earth has been determined mainly by experiments onboard spacecraft. Montgomery et al. (1968), Koehler (1968), Neugebauer and Snyder (1966a, 1966b), Wolfe et al. (1967), Bonetti et al. (1969), Stelzried et al. (1970), and by the group at Stanford University headed by V. R. Eshleman (see Staff, 1966).

A determination of N at 1 A.U. using observations of the zodiacal light was done by Blackwell and Ingham (1961), by Ney et al. (1961) and also by Elsasser (1963). Radar techniques have also been used involving reflections from Venus (Campbell and Muhleman, 1969; Brandt, 1964; Smith et al. 1968), from the Moon (Howard et al. 1965) and from several spacecrafts (Howard and Koehler, 1967; Howard, 1968).

Measurements near Venus were made by Mariner V and were reported by Bridge et al. (1967). It is not clear however if the measurement actually represents the solar wind electron density because of the nearness of the spacecraft to the Venus shock front.

Other radio techniques to study the solar corona are based on the observation of the scintillation of radio sources, on the occulation of radio sources by the solar corona and on the observation of pulsars.

Care has to be exercised however in selecting electron density values near the Earth because many of them are inferred through the use of a particular model. This is the case of the results, for example, of Stelzried et al. (1970), Blackwell and Ingham (1961), Campbell and Muhleman (1969), Brandt (1964) and Smith et al. (1968).

Very near the sun N varies typically between $10^8$ and $10^9$ cm$^{-3}$ for the corona and up to more than $10^9$ cm$^{-3}$ for coronal streamers.

Near the Earth there is also a wide range of values that go from 1 cm$^{-3}$ to 100 cm$^{-3}$, or more. However the average is generally accepted as lying between 5 and 30 cm$^{-3}$.

We have recognized the fact that the electron densities depend on the phase of the solar cycle in which they were measured, however we did not consider this effect in our models.

(b) Mechanism of Emission

There is little doubt that the radio bursts originate in plasma oscillations set up by the passage of exciter particles through the solar corona. These oscillations represent longitudinal waves which can couple into transverse electromagnetic waves by mechanisms which are not well understood. This is the so-called Plasma Hypothesis. As was mentioned in Section 1.1.2 the original idea was suggested independently by Shklovskii (1946) and by Payne-Scott et al. (1947) but it was developed primarily by Wild (1950).

Our observations and others have revealed the existence of the fundamental emission as well as the second harmonic, at twice the fundamental frequency. The identification of harmonics in Type III bursts was made at least in 1954 by Wild , Murray, and Rowe (1954).

The well-known plasma frequency equation is:

$$f = j \; 9 \; \sqrt{N} \; , \tag{4.7}$$

where $f$ = frequency, Hz,

$N$ = electron density, $m^{-3}$,

$j$ = 1, for the fundamental,

$j$ = 2, for the second harmonic.

The solar corona has a negative electron density gradient. Any of our single-frequency channels, let us say centered at frequency $f_0$, can receive indiscriminately burst radiation emitted as fundamental from a coronal level whose plasma frequency is $f_0$, or/and emitted as second harmonic from an outer level whose plasma frequency is $1/2 \; f_0$. It will be important then to distinguish between fundamental emission at a frequency $f_0$, its second harmonic at frequency $2f_0$, and the emission at frequency $f_0$ generated as second harmonic.

In this study, we have assumed that a fundamental frequency $f$ and its second harmonic at $2f$ are produced simultaneously and in the same general region.

(c) Trajectory of Exciter Particles

In the past it has been sufficient for observers to consider that the exciter particles were ejected along a straight path. The distances from the Sun to the plasma levels corresponding to the lowest frequencies of observation then available were not large enough to require a

discrimination between the shapes of the trajectories. We realized that the source of our 0.05 MHz burst could be placed at 100 $R_\odot$, or beyond. This made it necessary to choose a path for the particles.

The two obvious choices were a straight line coming radially out from the center of the Sun and an Archimedes spiral as suggested by the solar wind studies. In the first case the particles would not be influenced by the solar magnetic field, except perhaps very close to the Sun, therefore the trajectory would be presumably along the radius joining the center of the Sun with the center of the associated optical flare. This would lead to a simple three dimensional geometry. In the second case, the exciter particles would be guided by the interplanetary magnetic field along an Archimedes spiral.

We expected that the observations would permit us to decide which trajectory was a better assumption.

The Spiral Trajectory. Parker (1958) based on studies made by Alfvén proposed that the interplanetary magnetic field would be frozen-in to the solar plasma and dragged by this plasma as it streams continuously out from the Sun. The magnetic field lines would be shaped into Archimedes spirals whose characteristics would depend on the rate of rotation of the Sun and on the velocity of flow of the solar plasma. Experimental studies made first by McCracken (1962) proved Parker's prediction. Observations performed later have confirmed McCracken's findings. (Dessler, 1967; Kavanagh et al., 1970). Because the plasma outflow is mainly in the equatorial plane of the Sun the magnetic field may be expected to be parallel and close to it except perhaps near the

Sun, (Gold, 1958; Jager, 1960, Sturrock and Smith, 1968). For simplicity we assumed the spiral trajectories to be contained in the plane of the ecliptic in spite of the fact that it is actually inclined about 7.5 degrees with respect to the solar equator. In general this will result in an underestimation of the exciter velocity because the introduction of the third dimension makes the distances larger. Figure 4.6 shows the geometry involved. The plane of the ecliptic coincides with the plane of the paper. S represents the Sun and E the Earth.

$\theta_F$ $\approx$ heliocentric longitude of the associated flare and

$\ell$ = one astronomical unit (A.U.)

The equation of the spiral shown in Fig. 4.6 is

$$\theta = \theta_F - \varepsilon \frac{r}{\ell} , \qquad (4.8)$$

where $\varepsilon$ is the tightness of the spiral which can be shown to be:

$$\varepsilon = \tan \phi_E = \ell \frac{\Omega}{V_S} , \qquad (4.9)$$

where $\phi_E$ is the angle at which the spiral intersects the radius vector at 1 A.U. Also, $\varepsilon$ is directly proportional to the Sun's angular rotation $\Omega$ and inversely proportional to the solar wind velocity $V_S$. At the solar equator $\Omega = 2.7 \times 10^{-6}$ rad sec$^{-1}$. Typical values of $V_S$ at the Earth range between 300 and 400 km sec$^{-1}$. (Dessler, 1967; Parker, 1969). In this study we assumed $V_S$ to be constant and independent of distance. Some values of $\phi_E$ measured and predicted are presented in Table 4.4. After approximating $\theta = \theta_F$ at $r = 1$, we adopted in this study $\varepsilon = \pi/2$ or $\phi_E = 57.5$ degrees. Thus, exciter particles originating on the west limb will pass through the Earth.
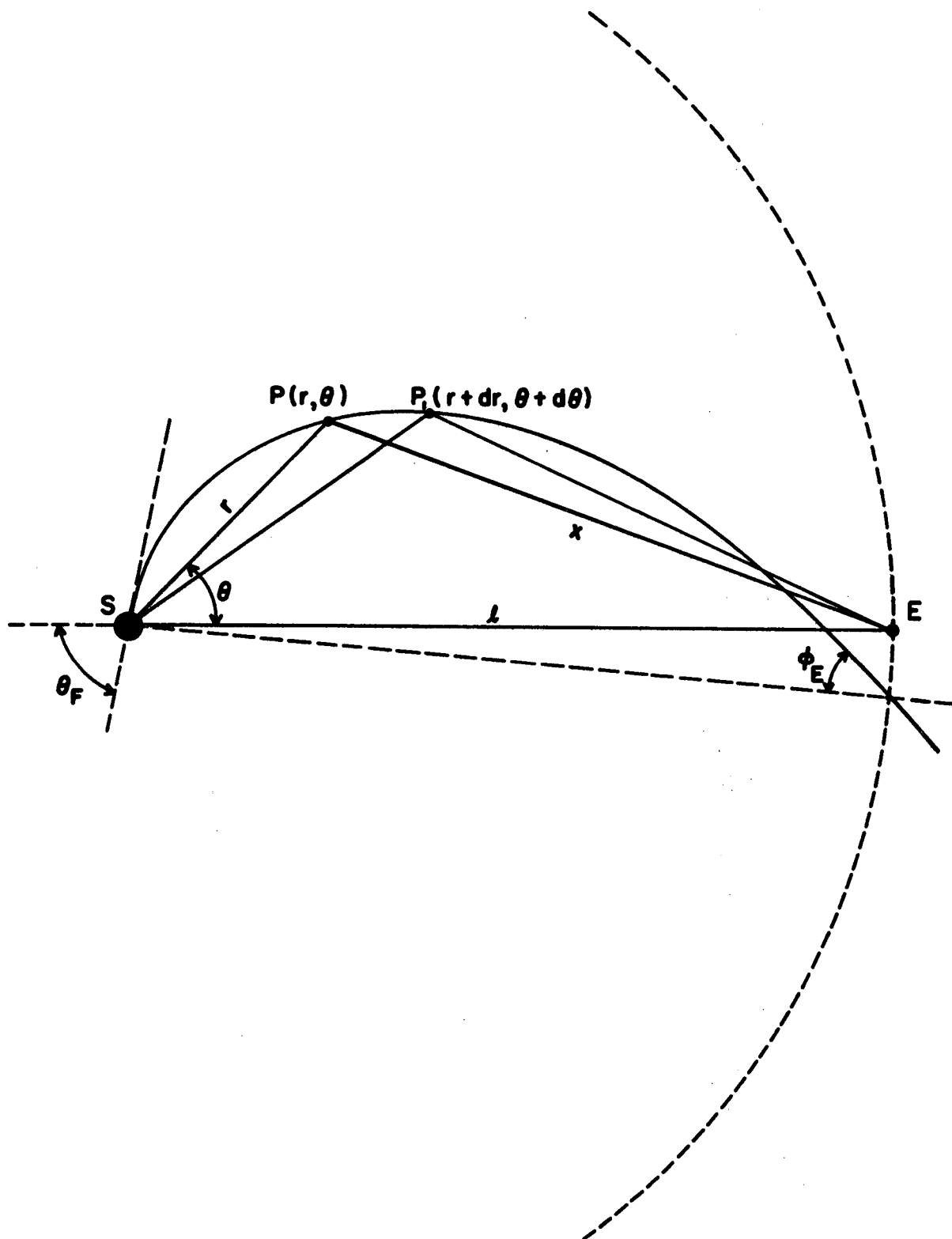
FIG. 4.6  GEOMETRY OF THE TRAJECTORY OF THE EXCITER PARTICLES.

Table 4.4

Characteristics of the Solar Wind Spiral Structure

| $\phi_E^\circ$ | $\theta_F^\circ$ | Author |
|---|---|---|
| 45 | 57 | Parker (1964) |
| ~55 | ~90 | McCracken (1962) |
| 30-40 | ~50 | Fan et al. (1968) |
| 55 | | Wolff et al. (1971) |
| 46 | 60 | Wilcox (1968) |
| 57.5 | 90 | This Study |

The Radial Trajectory. The three-dimensional form of this geometry was not used. Instead we made some use of radial paths contained in the plane of the ecliptic. These results were obtained directly from Eq. (4.8), making $\varepsilon = 0$.

(d) The Velocity of the Exciter Particles

Following the local plasma hypothesis, we have accepted that the bursts are produced by a group of very fast particles traversing the solar corona with certain velocity v. The original hypothesis assumed that the velocity was constant during the motion of the particles. This matter has not been settled. Stewart (1965) has accepted the constancy of v. Malville (1972a) observed a burst whose velocity seems to decrease from 0.45c in the 180-50 MHz range to 0.18c in the 19-9 MHz range, where c is the velocity of light in vacuum. However we believe that his evidence is inconclusive because in the light of our findings, discussed

in Section 4.2.5, the same velocity pattern could be given by a burst

with a velocity 0.40c radiating at the fundamental frequency in the

high-frequency range but then radiating, at the same frequency but as

second harmonic, in the low-frequency range. The "switch" in mode

prevalence from fundamental to second harmonic produced by a constant

exciter velocity could be observed as an apparent reduction in velocity

by a factor slightly less than two.

Boischot (1967b) working in the range from 40 to 8 MHz found that

the velocities derived from the bursts radiating in the fundamental mode

decreases with increasing distance from the Sun and he also found the

same trend for the velocities derived from the second harmonic.

Close to the Sun we could think that some ion-electron collisional

effects and magnetic effects are strong enough to produce deceleration,

for example, by energy losses, however at distance larger than a few

tens of solar radii we can suggest no obvious cause to reduce the velocity

of the particles. Small-scale inhomogeneities in the electron density

and small-scale structure in the interplanetary magnetic field may

certainly cause fluctuations in the velocity, however the timing accuracy

of our observations may be unable to resolve them.

Considering the above discussion we decided to use a constant

velocity. Referring to Fig. 4.6 we have:

$$\text{arc } PP_1 = ds$$

and

$$v = \frac{ds}{dt} . \qquad (4.10)$$

We will also use the velocity parameters $\beta$ defined by

$$\beta = \frac{v}{c} \, , \tag{4.11}$$

where c is the velocity of light in vacuum. The observations will give information about the velocity of the particles associated with each burst.

(e) Propagation of the Electromagnetic Radiation

In a plasma the trajectory of a ray traveling at an angle to a direction in which there is a density gradient is not a straight line. In connection with the solar corona this problem has been treated by several authors (Smerd and Westfold, 1949; Jaeger and Westfold, 1950; Link, 1951; Reule, 1952; Bracewell and Preston, 1956; J. C. James, 1966). The results achieved by these authors are valid only in the high frequency range where the distances of the plasma levels to the Sun are small. For example, Jaeger and Westfold, and also Bracewell and Preston used Baumbach's model of the solar corona modified by Allen; Link used an inverse power law distribution and Reule used the original Baumbach model.

Since they considered rays originating (or reflecting) at points close to the Sun, the work of these authors was simplified because they could assume that all the rays observed at the Earth came parallel to the Sun-Earth direction. (See Fig. 4.7a). But for a burst at a very low frequency originating at a distance that is an appreciable fraction of 1 A.U. the situation is different, as we can see in Fig. 4.7b. Accordingly, the approach has to be different also.
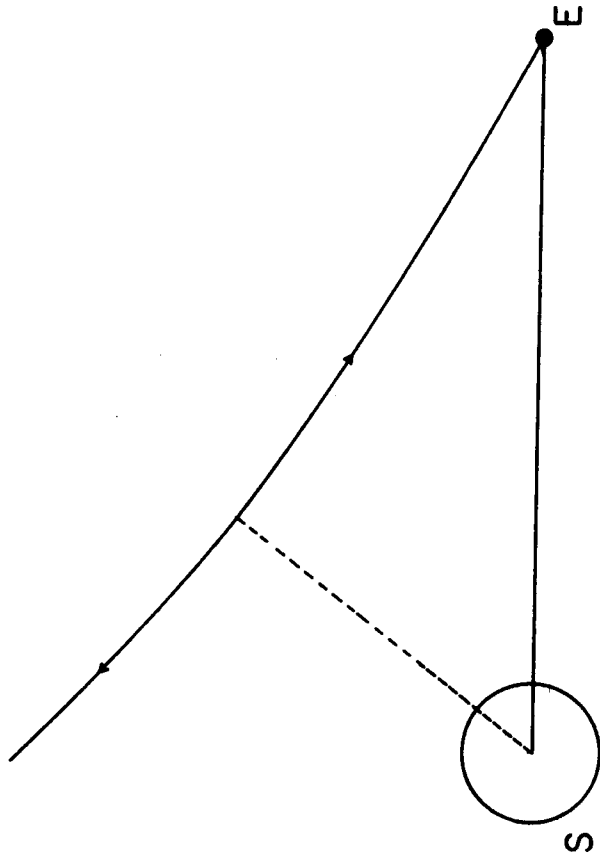
LOW FREQUENCY

(b)
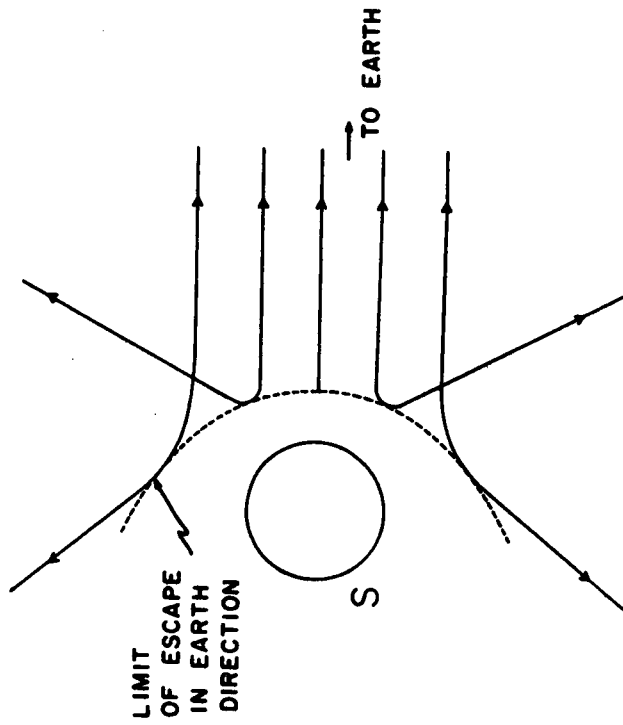
HIGH FREQUENCY

(a)

FIG. 4.7  RAY PATHS IN THE CORONA FOR HIGH AND FOR LOW FREQUENCIES.

At the time we did this work our expression for the electron density distribution was complicated (see Eq. A.14) and it was not appropriate for analytical manipulation that could lead to a simple answer. We considered it premature to use more involved numerical methods.

Because of the complications mentioned above we decided to assume in this study that the electromagnetic energy propagates along a straight line to the Earth, travelling with the velocity of light in vacuum.

There are several implications involved in this assumption. First, if we assume a spherically symmetric corona with a negative electron density gradient then, strictly speaking, we could not see the bursts ocurring within the surface of escape of radiation defined for the frequencies of observation and for the Sun-Earth direction. (See Fig. 4.7a). At lower frequencies this restriction is more limiting because the lower the frequency the larger the proportion of the ray path that will be in a region where the index of refraction is near zero, and this is the region of appreciable refractive effects. The geometry of the trajectory of the exciter particles also has a bearing on this problem, as it can be realized by thinking of particles ejected from a west limb flare along either a straight line or a spiral. The nature of the radiation, whether fundamental or second harmonic, is also related to this problem because a frequency emitted as second harmonic originates at a level where its index of refraction is $\approx 1$. (Wild, Sheridan and Neylan, 1959).

The problem of escape of the radiation has received attention by Shain and Higgins (1959), who proposed a solution based on the existence of small-scale irregularities in the solar atmosphere from where the radiation would be scattered to the Earth.

The alternative to a spherically symmetric corona is a corona containing large scale enhancements like long streamers. The concept of solar streamers became necessary in radio work because since the early studies, the models of electron densities that were required to fit the observations were found to be about 10 times as dense as the typical coronal models (Shain and Higgins, 1959; Wild, Sheridan and Neylan, 1959). The critical level of a certain plasma frequency is higher in the streamer than in the homogeneous corona. We will come back to this subject when we discuss the results.

Second, the assumption that the electromagnetic waves travel in a straight path implies that the velocities obtained for the exciter particles are underestimated.

Third, the assumption of propagation as in vacuum conditions ignores group retardation effects which will also result in an underestimation of the velocities (Wild, Sheridan and Neylan, 1959).

The problem of the effect of a plasma on the propagation of electromagnetic waves is closely related to the mode of emission. Stewart (1962) found that the second harmonic precedes its fundamental and he attributed it to group retardation effects. Smerd et al. (1962) observed that in some cases the second harmonic arrives from a direction closer to the center of the disk than that of the fundamental at the same frequency. Elgaroy and Rodberg (1963) have also dealt with the problem

of the delay between fundamentals and second harmonics at the <u>same</u>
frequency. The theory of Type III bursts developed by Smith (1969)
and based on these observations succeeds in predicting the early arrival
of the second harmonic with respect to its fundamental.

With the simple equation discussed later for the electron density
distribution it should be easier to refine our calculations by introducing
some of the effects discussed in this paragraph.

(f) <u>Other Factors</u>

In the derivation of the electron density distribution no
temperature effects were considered; no magnetic field influence was
considered either except for the guiding of the exciter particles along
a spiral.

4.2.3 <u>Electron Density Distribution--Form 1</u>. In our study of
the distribution of electron density in the corona we arrived at two
mathematical expressions that we will call Forms 1 and 2. In spite of
the fact that we consider only Form 2 as being important we will discuss
briefly Form 1 because it led to Form 2 and also because some results
presented later were based on it.

The Eq. (4.2) represents a differential equation that together with
the relationship between the plasma frequency and electron density suggested
that we could go one step further beyond obtaining electron density
gradients, and by integration solve for the electron density distribution
itself. This was done using Eqs. 4.2, 4.7, 4.8 and 4.10 plus the
assumptions discussed in the previous section. The details are given in
the Appendix No. 2. The final result is Eq. (A.14) that represents Form 1.

Conceptually there are objections to this expression because the electron density distribution depends on the velocity parameter $\beta$ and on the position of the associated optical flare.  In order to determine the constant of integration we used the value of the electron density at an arbitrary distance.  Equation (A.14) permits us to impose arbitrary conditions at the base of the corona but not at the orbit of the Earth because the function may become ill-behaved  at shorter distances.

On different grounds we may expect the Eq. (A.14) to be invalid for large distances, say $r \gtrsim 1$ A.U.  We recall that by hypothesis particles travelling through a density distribution given by Eq. (A.14), under the assumptions made, give a frequency drift rate curve expressed by Eq. (4.1), that is, a straight line in a log-log plot that extends from an infinite frequency down to zero frequency.  This is not physically reasonable.

In spite of the above deficiencies we found that, using some reasonable values for the parameters involved, Eq. (A.14) gives quantitative results that are consistent with the observations (electron densities and frequency drift rates) within the orbit of the Earth. Figures 4.15 and 4.17 in Section 4.2.5 show examples of models based on Form 1.

4.2.4  Electron Density Distribution--Form 2.  These deficiencies of the function, Eq. (A.14), led to search for another one that would eliminate the unwanted features while keeping the desirable ones.  This function should give results in agreement with the observations of frequency drift rates and with observations of electron densities.  If possible it should also be simpler.  The form of the new expression, suggested by Eq. (A.14) itself, is:

$$N = \frac{A}{(r - b)^p} \ . \tag{4.12}$$

We will refer to this as electron density distribution Form 2.

In order to arrive at acceptable models based on this expression we need to adopt values for the three parameters and to test the models against observations.

We will express $r$ and $b$ in units of solar radii and $A$ in $cm^{-3}$. The radial distance $r$ will be measured from the center of the Sun.

We will adopt the exponent $p$ found in Eq. (A.14) and whose expression is given by Eq. (A.11), reproduced below:

$$p = \frac{2}{\alpha - 1} \ . \tag{A.11}$$

As before $\alpha$ is the frequency drift rate index. Using the value of $\alpha = 1.84$ obtained from data over all the range of frequencies as shown in Table 4.3 we arrive at

$$p = 2.38 \ . \tag{4.13}$$

It is interesting to compare the values of $p$ derived from the radio data in this manner with those obtained either from observations or theories. Table 4.5 presents some values at distances at which the curve log N versus log r is very close to a straight line and therefore $p$ could be measured easily.

We notice that the radio determinations agree well with the observations and with the theory of either solar wind or streamers models.

Table 4.5

Values of p Measured from the Work of Several Authors

| p | Range of r ($R_\odot$) | Source |
|---|---|---|
| 2.38 | ≈1 - ≈200 | OGO-V observations plus others (Table 4.3, third row) |
| 2.16 | ≈4 - ≈200 | OGO-V Group A. Eq. (4.3) |
| 2.3 | 5 - 16 | Blackwell and Petford's Observations (1966) |
| 2.57 | $\gtrsim 40$ | Newkirk's presentative corona (1967) |
| 2.28 | $\gtrsim 70$ | Whang et al., solar wind model (1966) |
| 2.09 | $\gtrsim 100$ | Cuperman and Harten's solar wind model. (1971 Fig. 2,) |
| 2.12 | $\gtrsim 300$ | Hartle and Sturrock's solar wind model. (1968, Fig. 7) |
| 2.25 | $\gtrsim 100$ | Noble and Scarf's solar wind model (1963) |
| 2.09 | $\gtrsim 200$ | Neuman and Kopps' streamer model (1969?, 1970?) |
| ~3 | 153 - 214 | Neugebauer and Snyder's Observations (1966b) |
| 7 | 1.2 - 2.2 | Gillet et al., Observations (1964) |
| 1.94 | 5 - 70 | Erickson's Observations (1964) |

Most theories, if not all, predict something close to an inverse power law at distances larger than about 100 $R_\odot$.

From Table 4.1 we can compute the extreme values of p deduced from OGO-V observations. They are 1.35 and 9.52 derived from events No. 29 and No. 34, respectively. We consider that the last is too high, possibly due to an error in the determination of $\alpha$. More meaningful are the p values corresponding to the values of $\alpha$ that are one standard deviation from the mean index given in the relations, Eq. (4.3); the resulting values of p are 1.55 and 3.70. We see that they cover the range shown in Table 4.5. The exception is given by the observations of Gillet et al., probably because they correspond to distances very close to the Sun.

As we noticed before, the measured $\alpha$ is never $\lesssim 1$. (See Fig. 4.3). This should be expected because, examining the Eqs. (A.11) and (A.12), we see that p and D approach infinity as $\alpha$ approaches 1 and that Eq. (A.14) is undeterminate at that value. For $\alpha = 1$ Eq. (4.12) gives N = 0 and for $\alpha \lesssim 1$ the electron density increases with increasing distance, all of which is absurd.

In order to study further Form 1 we attempted to fit Eq. (4.12) to some observations and models by selecting three points from the data and determining the parameters A, b, p such that the curve would pass through those three points.

We obtained the solution by computing the functions $Q_1(b)$ and $Q_2(b)$ derived from Eq. (4.12) and defined below:

$$Q_1(b) = \frac{\log\left(\frac{N_1}{N_2}\right)}{\log\left(\frac{r_2 - b}{r_1 - b}\right)}$$

and

$$Q_2(b) = \frac{\log\left(\frac{N_2}{N_3}\right)}{\log\left(\frac{r_3 - b}{r_2 - b}\right)} \quad ,$$

where $N_1$ is the density at distance $r_1$, etc.

The solution for both b and p was found graphically by plotting $Q_1$ and $Q_2$ as functions of b, and by finding the intersection:

$$Q_1(b) = Q_2(b) = p \quad .$$

Table 4.6 shows sets of values of A, b and p that fit the results of several authors with different degrees of precision. Except for Whang et al. model the rest were done by the method explained above. The selection of the three points was by visual inspection and we did not attempt to optimize the fitting. In order to have an estimate of the quality of the fitting we calculated at different distances the ratio N/N', of the electron density obtained from the fitted model to that of the original data. Table 4.7 shows these ratios for some of the data included in Table 4.6. The fitting to observational data is usually good, for example, that of Newkirk (1969), Newkirk (1970), Blackwell and Petford (1966), van de Hulst (1950). The fitting to models in the range

Table 4.6

Fitting of $N = A/(r - b)^p$

| p | b | log A | Authors | Remarks |
|---|---|---|---|---|
| 2.55 | 0.89 | 6.33 | Newkirk (1967) | Composite **representative** corona. Equator min. |
| 4.66 | 0.52 | 8.34 | Newkirk (1969) | Average active enhancement plus quiet component. |
| 2.86 | 0.60 | 6.87 | Newkirk (1970) | Southwest streamer. |
| 3.31 | 0.41 | 7.32 | Newkirk (1970) | Southeast streamer. |
| 5.35 | 0.06 | 7.83 | Newkirk (1970) | Equatorial excluding streamer. |
| 2.23 | 0.02 | 6.11 | Blackwell and Petford (1966) | Corona, $r < 20 R_\odot$ |
| 2.27 | 1.72 | 5.77 | Pneuman and Kopp (1969?, 1970?) | Streamer core model $r \geq 2 R_\odot$ . |
| 2.33 | 0.93 | 6.27 | Whang et al. (1966) | Solar wind model. |
| 3.51 | 0.68 | 6.87 | van de Hulst (1950) | Equator max. |
| 2.25 | 0.79 | 6.33 | Hartle and Sturrock (1968, Fig. 1) | Solar wind model. |

Table 4.7

Values of N/N' Representing the Quality of Fitting [†]

| r (R☉) | Models from Observations | | | | | Models from Theory | | |
|---|---|---|---|---|---|---|---|---|
| | Newkirk (1967) | Newkirk (1969) | Newkirk (1970) S.W.Str. | Blackwell-Petford (1966) | van de Hulst (1950) | Whang et al. (1966) | Pneuman-Kopp (1969,? 1970?) | Hartle-Sturrock (1968) |
| 1.00 | | | | | 1.00 * | | | 2.34 |
| 1.02 | 1.00 * | | | | | 1.15 | | |
| 1.12 | | 1.00 * | | | | | | |
| 1.25 | | 1.00 | | | | | | |
| 1.37 | | 0.95 | | | | | | |
| 1.50 | | 1.00 * | | | | | | |
| 1.6 | 0.51 | | | | | | | |
| 1.66 | | | 1.00 * | | | | | |
| 1.75 | | 0.95 | | | | | | |
| 1.98 | | | 1.03 | | | | | |
| 2.00 | | 1.00 * | | | 1.00 * | 0.48 | 10.00 | 1.00 * |
| 2.36 | | | 1.00 * | | | | | |
| 2.56 | | | 1.10 | | | | | |
| 3.00 | | | | | 1.12 | | 1.41 | |
| 3.16 | | | | | | | | 1.00 |
| 3.17 | | | 1.00 * | | | | | |
| 4 | 1.00 * | | | | 1.00 | 0.89 | 1.00* | |
| 5 | | | | 1.00 * | 1.00 * | | | |
| 6 | 1.09 | | | | 0.73 | | | |
| 7 | | | | 0.98 | | | | |
| 10 | 1.02 | | | 1.00 * | | 1.12 | 1.00* | 1.00 * |
| 13 | | | | 1.01 | | | | |
| 16 | | | | 1.00 * | | | | |
| 31.6 | | | | | | | | 1.00 |
| 40 | 0.84 | | | | | | 1.16 | |
| 100 | 0.86 | | | | | | | 0.99 |
| 200 | | | | | | 0.89 | 1.00* | 1.00 * |
| 215 | 1.00 * | | | | | | | |
| 1000 | | | | | | 0.63 | | 0.63 |

[†] N = electron densities computed from models using A, b and p listed in Table 4.6

N' = electron densities from authors listed in Table 4.6

\* = Indicates the points used in the fitting

from 1 to 215 $R_\odot$ is usually poor at small distances but, in general, for

r greater than 2 or 4 $R_\odot$ the agreement is satisfactory. For theoretical

models, such as those of Whang et al. (1966) and Hartle and Sturrock

(1968), no attempt was made to have a good fit beyond 215 $R_\odot$. In fact,

we observed that the corresponding values of p in Table 4.5 and those

used in the fitting model, Table 4.6, are not the same, therefore we do

not expect a good fit at large distances. This suggests that an alternative

way to find the three parameters that will give a good fit to a theoretical

model is to adopt p as predicted from the model and then determine A

and b by a fit at two points. The agreement of Eq. (4.12) with obser-

vations and theory over a large part of the distance range, and its

simplicity makes it useful for analytical work.

Several authors have in the past fitted their observations to the

first few terms of a sequence of inverse power of r (Stelzried et al., 1970;

Baumbach, 1937; Hollweg, 1968; Blackwell and Petford, 1966;

Ingham, 1961; Saito, 1950; Newkirk et al., 1970; Newkirk et al., 1969;

Allen, 1947a)or else they have used other functions that are susceptible

of being expressed in that form (Bohlin and Simon, 1969; Newkirk, 1961;

Bohlin, 1970; Chapman, 1957; Wild et al., 1959). It seems that the

simplicity of the formula Eq. (4.12) and of the procedure for determining

the three parameters is advantageous even if the fitting is not so precise.

Electron Density Models. The next step in the study of Form 2 is

to adopt values for A and b that will lead to the formulation of some

numerical models.

Since we want to compare the computed values of drift rates with

the observed values, it seems natural to select an exponent p obtained

from the radio data. Since we also want our density model to cover the widest range of distance we should adopt the p derived from the largest range of frequency. Earlier we found it to be p = 2.38, Eq. (4.13).

After p has been chosen the values of A and b can be obtained by assigning electron densities at two distances. The obvious choices are 1 and 215 solar radii. From Table 4.6 we see that b is expected to be of the order of unity, therefore at 1 A.U. r >> b and A will be determined by N at the Earth, N(215). Consequently b will be effectively determined by N near the Sun, N(1).

Observational facts and the acceptance of the local plasma hypothesis impose some restrictions on the numerical values of N(1) and of N(215). Because Type III bursts have been observed at frequencies as high as 550 MHz (Maxwell et al., 1960) the electron density near the Sun cannot be smaller than $3.73 \times 10^9$ cm$^{-3}$. (See Table 4.8). The corresponding plasma level is not known and for simplicity we will take it at 1 $R_\odot$. Within the wide range of values of N measured near the Earth we choose two alternatives: one with N = 7.7 cm$^{-3}$ and the other with N = 30.9 cm$^{-3}$. The values are within accepted observational limits and they correspond to a plasma frequency of 0.05 MHz as second harmonic and fundamental, respectively.

The choice of the electron density at the Earth has implications regarding the homogeneity of the corona that we want to model. If we accept an homogeneous corona then the maximum electron density at the Earth compatible with the observation of a burst at 0.05 MHz is 30.9 cm$^{-3}$ because the Earth would be precisely in the plasma level. This is true in the case in which the burst is supposed to originate in the homogeneous

Table 4.8

Plasma Frequencies and Electron Densities

$$(f = 9 \times 10^{-3} \, jN^{1/2})$$

| f (MHz) | N (cm$^{-3}$) | |
|---------|---------------|---------------|
|         | j = 1         | j = 2         |
| 550     | $3.73 \times 10^9$ | $9.34 \times 10^8$ |
| 3.5     | $1.15 \times 10^5$ | $3.78 \times 10^4$ |
| 1.8     | $4.0 \times 10^4$  | $1.00 \times 10^4$ |
| 0.90    | $1.00 \times 10^4$ | $2.5 \times 10^3$ |
| 0.60    | $4.44 \times 10^3$ | $1.11 \times 10^3$ |
| 0.35    | $1.51 \times 10^3$ | $3.78 \times 10^2$ |
| 0.20    | $4.93 \times 10^2$ | $1.23 \times 10^2$ |
| 0.10    | 123.5              | 30.9 |
| 0.05    | 30.9               | 7.7 |

maximum-density corona itself or in the case of a denser streamer

embedded in that corona. Evidently in the first case there are more

stringent limitations in directionality due to refractive effects.

Some models based on the above conditions are shown in Table 4.9.

Model T (thin) is not dense enough at the base of the corona to give

a plasma frequency of 550 MHz, (see Table 4.6). The designation D stands

for Dense. Model C (Combination) is as dense as D at r = 1 and as

T at r = 215. D*2 corresponds to a model twice as dense as D. Because

of the above discussion model D*2 probably represent a denser

streamer. Figure 4.8 shows some of these models and some observational

data. On the frequency scale $f_F$ represents a fundamental at frequency f

emitted at level r(f) and $f_H$, a second harmonic at frequency f emitted

at the level r(f/2).

Table 4.9

Characteristics of Some Models. $N(r) = A/(r - b)^p$

| Model | N(1) $(cm^{-3})$ | N(215) $(cm^{-3})$ | log A | b | p |
|-------|------------------|--------------------|--------|------|------|
| T | $4.0 \times 10^8$ | 7.7 | 6.44 | 0.88 | 2.38 |
| C | $4.0 \times 10^9$ | 7.7 | 6.44 | 0.95 | 2.38 |
| D | $4.0 \times 10^9$ | 31 | 7.05 | 0.91 | 2.38 |
| C*2 | $8.0 \times 10^9$ | 15.4 | 6.75 | 0.95 | 2.38 |
| D*2 | $8.0 \times 10^9$ | 62 | 7.35 | 0.91 | 2.38 |

Direct determinations of the heights of the Type III sources have

been made by several authors. Table 4.10 shows the results found in the

literature, and Fig. 4.9 compares them with the predictions from several

of our models.
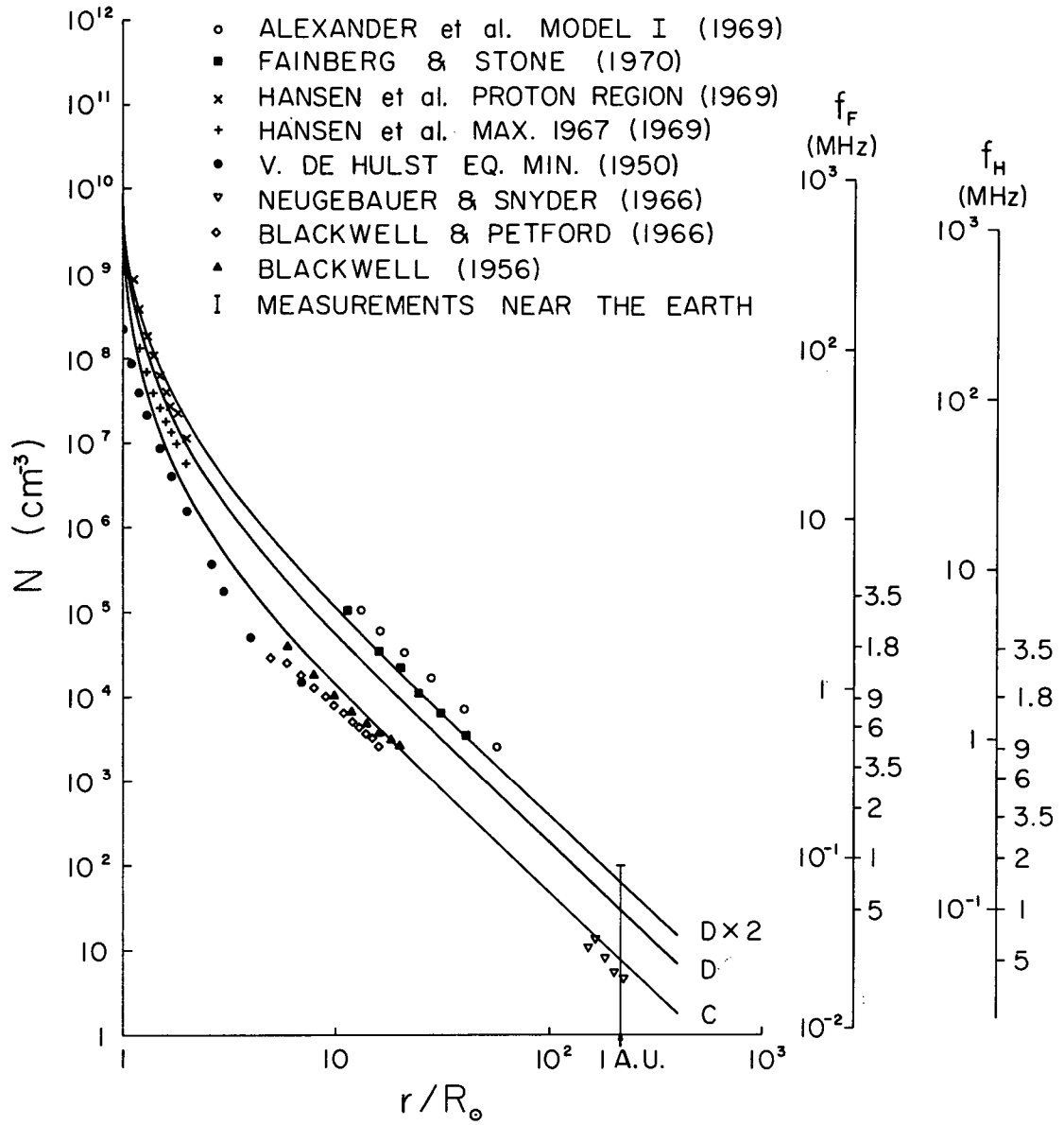
FIG. 4.8 COMPARISON OF ELECTRON DENSITY MODELS WITH VARIOUS

OBSERVATIONS.

C.3
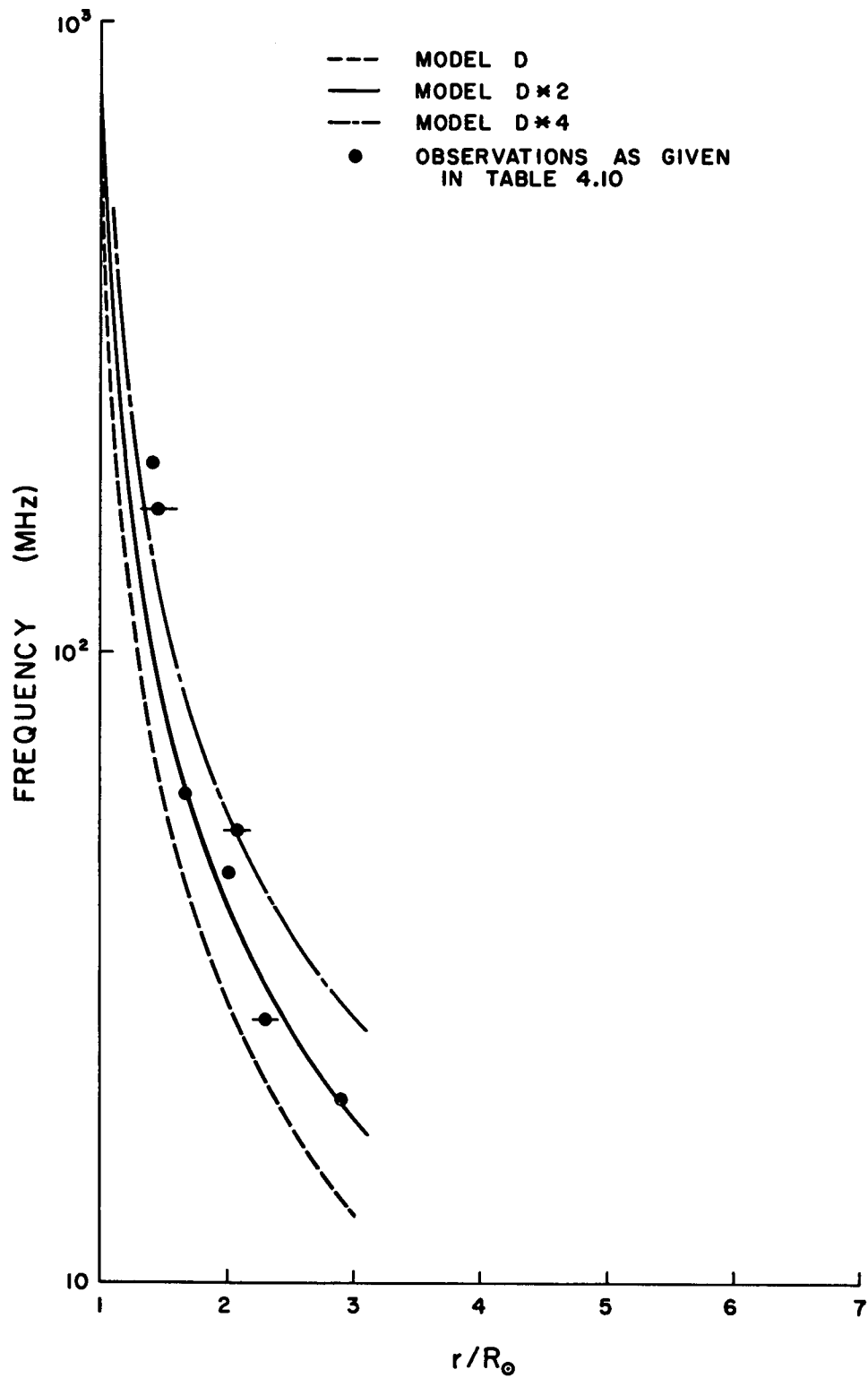
FIG. 4.9 OBSERVED AND PREDICTED HEIGHTS OF TYPE III SOURCES.

Table 4.10

Direct Measurements of the Height of Type III Solar Bursts Sources

| f (MHz) | R (R$_\odot$) | Author | Instrument[**] |
|---|---|---|---|
| 200 | 1.4 | Morimoto (1961) | I |
| 169 | 1.3 - 1.6 | Bourgeret et al. (1970) | R |
| 52.5 | 2.07 ± 0.10 | Morimoto (1964) | SFI |
| 50[*] | ~1.7 | Kundu et al. (1970) | SFI |
| 60 | ~1.66 | Wild et al. (1959) | SFI |
| 45 | ~2.0 | Wild et al. (1959) | SFI |
| 30[*] | ~2.3 | Kundu et al. (1970) | SFI |
| 26.3 | 2.4 ± 0.2 | Malitson & Erickson (1966) | I |
| 26.3 | 2.0 - 2.5 | Erickson (1963) | I |
| 19.7 | 2.9 | Shain & Higgins (1959) | I |

---

[*] Fundamental.

[**] I means interferometer, R means radio heliograph and SFI means sweep-frequency interferometer.

We can see that direct observations require a model with a distribution of density between two and four times that of model D. The last model corresponds probably to streamers. At the lower frequencies the observations fit the less dense model D*2 better, and we suspect that the higher frequency bursts may originate in local condensations which may disperse and blend into a homogeneous corona at greater distances.

It has been customary to refer coronal electron density distributions to a model considered as standard. Some of the reference models have

been Baumbach-Allen, van de Hulst (1950) and Newkirk (1967). We will

adopt the last one. In Table 4.11 we give an approximate equivalence

expressed in terms of the ratio of electron densities of the different

models (N) to that of Newkirk's ($N_N$).

Table 4.11

Approximate Equivalent of Some Electron Density Models

| Model | ($N/N_N$) Between 10-40 ($R_\odot$) | N (215) ($cm^{-3}$) | Plasma Level of 0.05 MHz Fundamental. ($R_\odot$) |
|---|---|---|---|
| Newkirk (1967) | 2 | 2.5 | 85 |
| T | 4 | 7.7 | 115 |
| C*2 | 4 | 15.4 | 155 |
| D | 8 | 31 | 215 |
| D*2 | 16 | 62 | 300 |
| Fainberg & Stone (1970) | 16 | 40[†] | 230 |
| Penuman & Kopp (1969?, 1970?) (Interstreamer) | 0.20 | 1.1 | 44 |
| Pneuman & Kopp (1979?, 1970?) (Streamer's core) | 0.20 | 3.1 | 71 |

[†]Extrapolated.

Prediction of Frequency Drift Rates (FDR). The next step in the

study of Form 2 is to investigate if it predicts results compatible with

radio observations. For this we will predict FDR and we will compare

them with the observations.

Due to the simplicity of Eq. (4.12) it is easy to derive an expression for the frequency drift rate observed at the Earth. The details are given in Appendix 3. The final expression for the drift rate given by Eq. (A.26) is:

$$\log \left| \frac{df}{dt} \right| = \log \left[ \frac{pc\beta}{2R_{\odot}(81j^2 \; 10^{-6} \; A)^{1/p}} \right]$$

$$+ \left[ \frac{p + 2}{p} \right] \log f - \log \left[ H(f, \, \epsilon, \, \theta_F) + \beta \; G(f, \, \epsilon, \, \theta_F) \right] \; . \qquad (A.26)$$

The terminology has the same meaning as before except for the functions H and G which are defined in Appendix 3. In general, H is related to the trajectory of the exciter particles and G is related to the trajectory of the electromagnetic waves. The frequency is expressed in MHz, the time in seconds and the distance is solar radii.

In order to compute numerical values for the frequency drift rates we need to adopt values for the rest of the parameters involved in Eq. (A.26).

The velocity $\beta$ and the mode of emission $j$ will be kept as variable parameters.

For the geometry of the plane trajectory we will consider two alternatives: a radial line and an Archimedes spiral with $\epsilon$ equal to 0 and $\pi/2$, respectively, in Eq. (4.8). The values of $\epsilon$ can be substituted directly into the Eq. (A.22) to compute the functions H and G. The position $\theta_F$ of the associated flare will be kept as an adjustable parameter.

To illustrate the effect of the orientation of the trajectory on the FDR curves we have chosen the following values for $\theta_F$: 90°, 30°, 0°, -90°. We recall that 90° corresponds to a west-limb flare. The angle of 30° was selected from the study of the distribution of the helio-centric longitudes of the flares associated with our bursts. As we will see in Section 4.5.1, the $\theta_F$ distribution of OGO-V bursts has an average of 30° with a standard deviation of 51°. We shall assume that this is the case also for the bursts outside the frequency coverage of OGO-V in order to use all the observations.

To summarize, the following elements were used to compute log $|df/dt|$ versus f from Eq. (A.26):

Models:  C, D and D*2  (see Table 4.9)

Trajectory:  radial ($\epsilon = 0$) and spiral ($\epsilon = \pi/2$)

Mode:  Fundamental ($j = 1$) and second harmonic ($j = 2$)

Position of associated flare:  $\theta_F = 30°$, also 0, 90° and -90°.

Figures from Figs. 4.10 to 4.14 show curves representative of the results. We should compare them with Fig. 4.5. In general we observe that the resulting curves are fairly straight down to about 0.2 MHz. In this range their slopes are equal or close to what is predicted, this means that the term $\Delta$ in Eq. (A.27) varies slowly. Special effects originating in $\Delta$ are predicted at frequencies below approximately 0.2 MHz and we will discuss them shortly.

In order to illustrate the effect of the different parameters on the FDR curves, only one parameter was changed in each of the figures.

Figure 4.10 shows the effect of varying $\theta_F$, i.e., the orientation of the trajectory with respect to the Sun-Earth direction. The curves
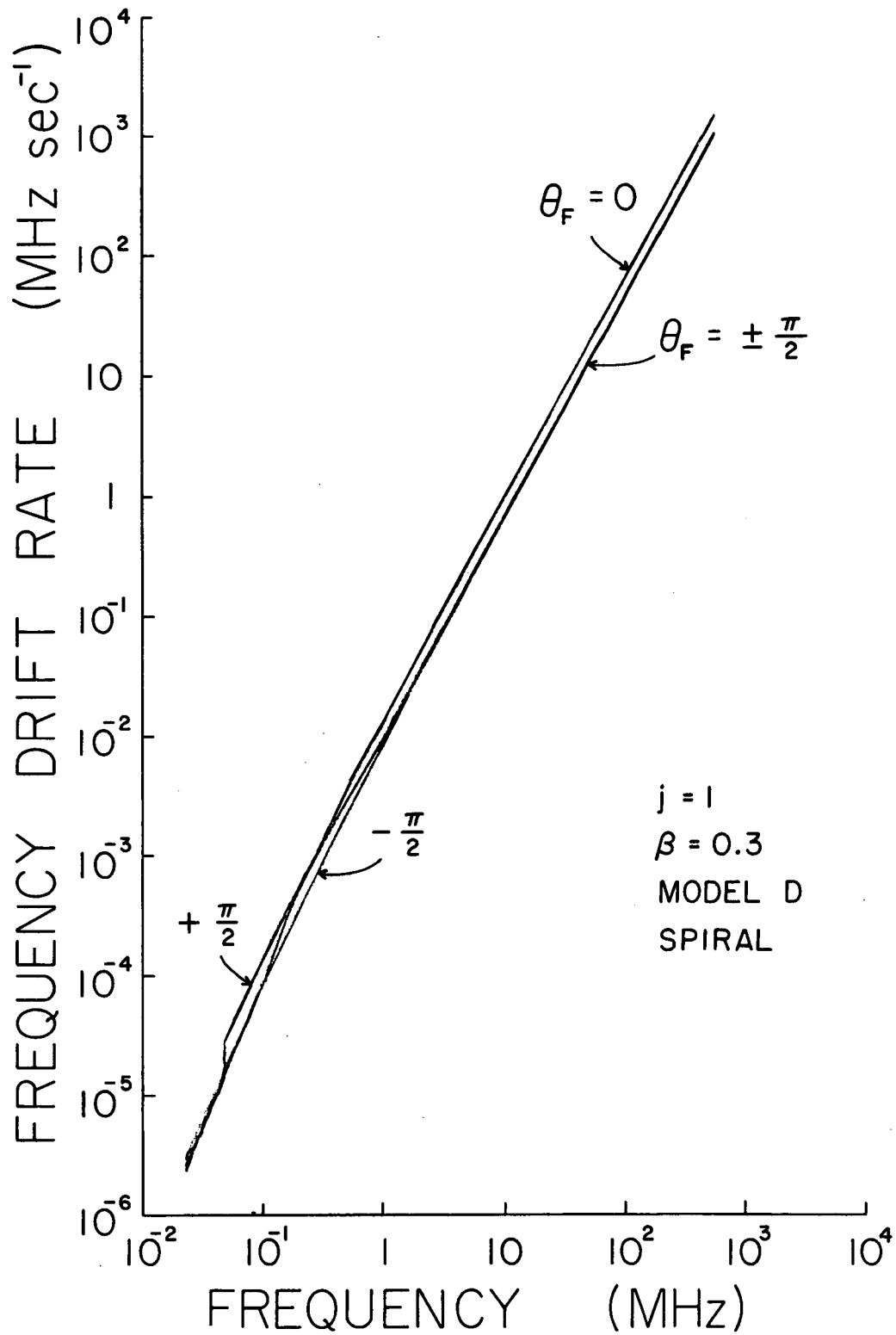
FIG. 4.10  EFFECT OF THE ORIENTATION OF THE TRAJECTORY ON THE

PREDICTED FREQUENCY DRIFT RATE CURVES.
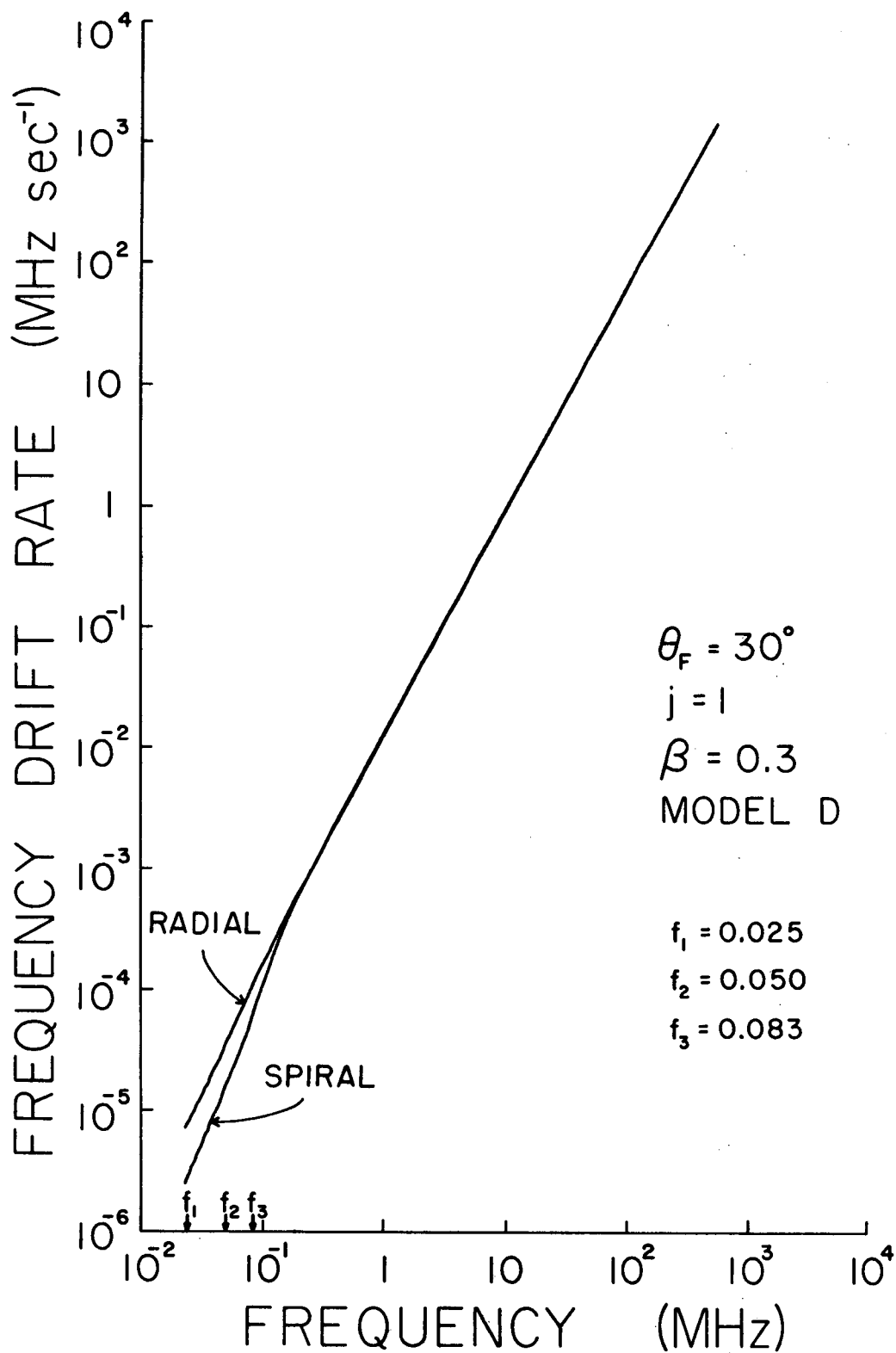
FIG. 4.11 EFFECT OF THE SHAPE OF THE TRAJECTORY ON THE PREDICTED FREQUENCY DRIFT RATE CURVES.
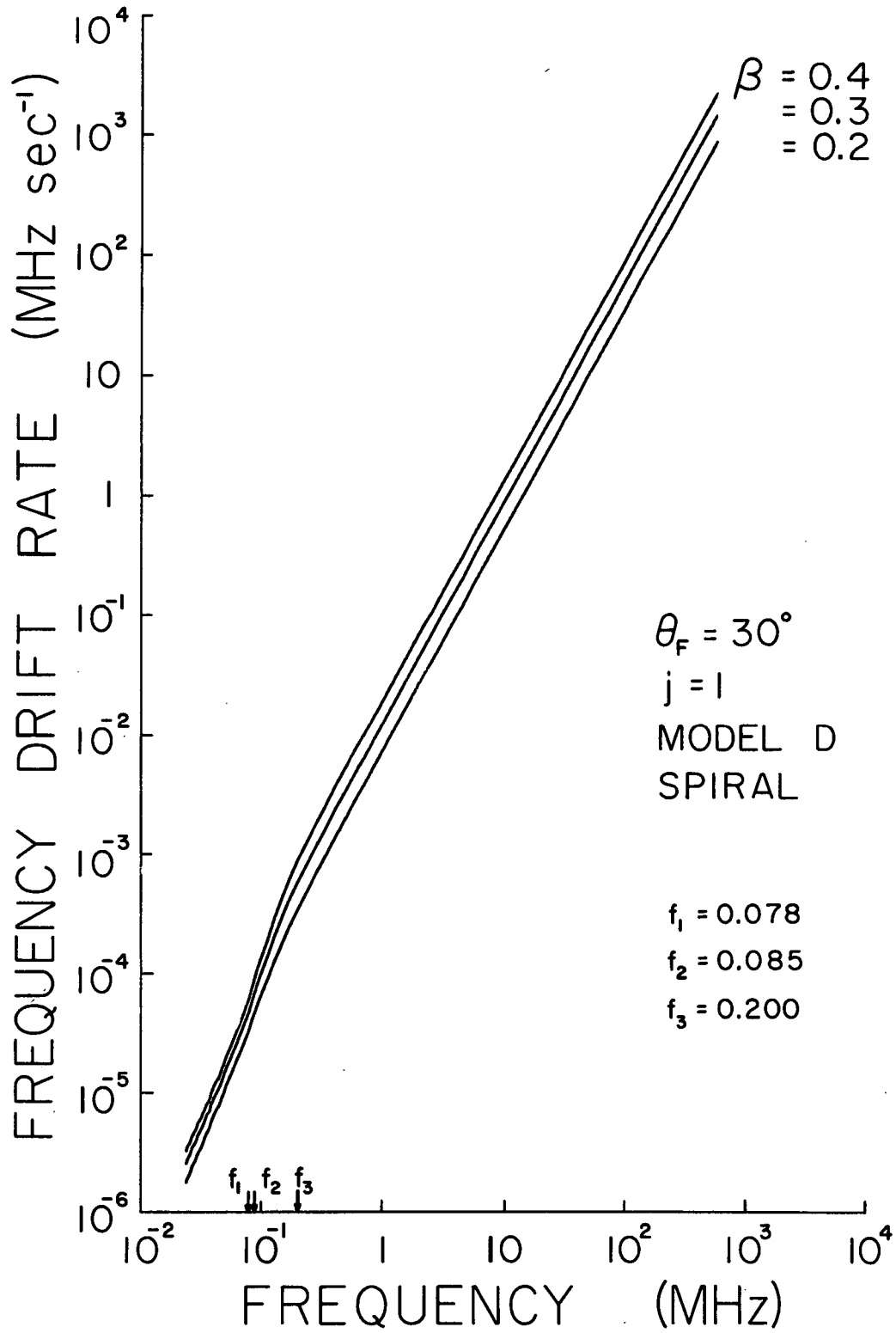
FIG. 4.12 EFFECT OF THE VELOCITY OF THE EXCITER PARTICLES ON THE

PREDICTED FREQUENCY DRIFT RATE CURVES.
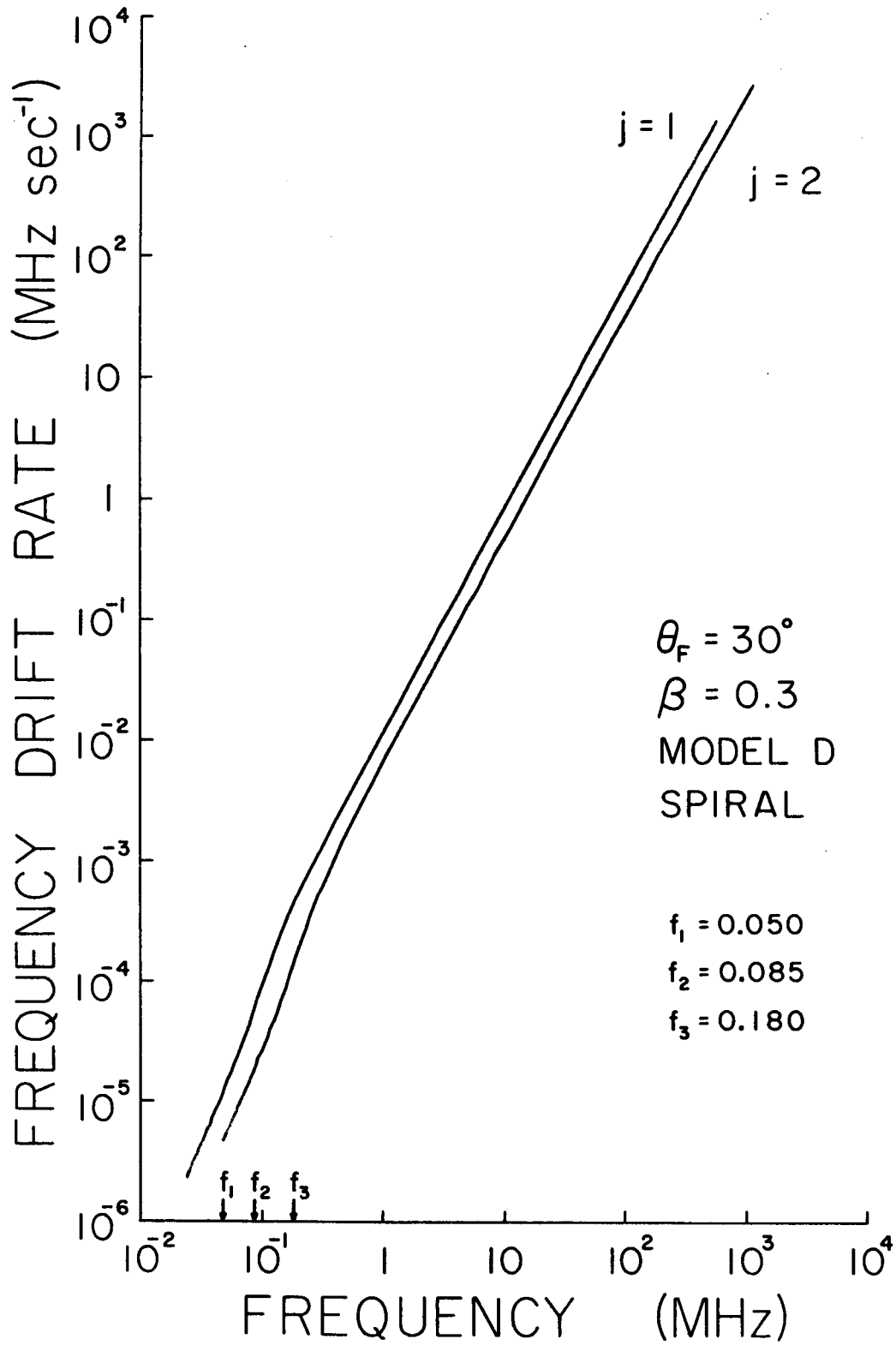
FIG. 4.13 EFFECT OF THE MODE OF EMISSION ON THE PREDICTED FREQUENCY
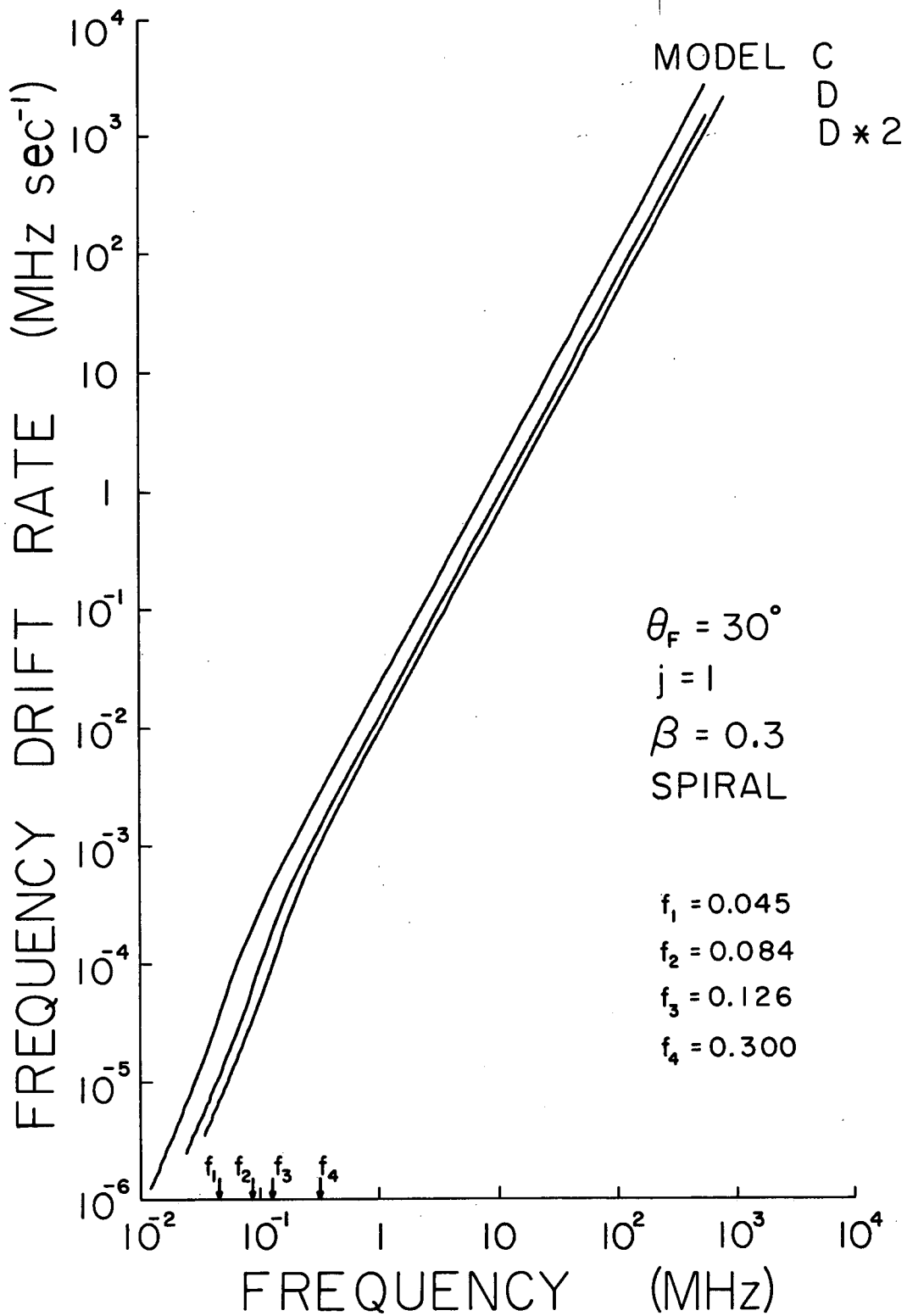
DRIFT RATE CURVES.

FIG. 4.14   EFFECT OF THE ELECTRON DENSITY MODEL ON THE PREDICTED

FREQUENCY DRIFT RATE CURVES.

are fairly straight except at the lower frequencies where a change

in shape occurs. This effect is due partly to the proximity of the

source of the burst to the Earth. For the case illustrated in this

figure the trajectory for $\Theta_F = \pi/2$ passes, by construction, through

the Earth and because of the model chosen the 0.05 MHz as fundamental

occurs at 215 $R_\odot$. For this particular case there is a sudden discontin-

uity in the FDR because when the exciter particles pass through the

Earth the term $\Delta$ in Eq. (A.27) changes sign. Physically this is due

to the fact that before the particles go through the Earth with a

vectorial velocity $\vec{v}$ the radio waves that we observe propagate in a

direction very close to $\vec{v}$ but just after the particles pass the Earth

the radio waves that we observe are those propagating in the direction

$-\vec{v}$. This is discussed in the Appendix No. 3. The sharpness of the

discontinuity depend on how close to the Earth the trajectory passes.

The possibility of observing this effect is low because the large size of the

source, in which we would be immersed, would smear out the time of

arrival. It is of interest to notice that the separation of the

curves shown is small considering the wide range of values of $\Theta_F$,

between $-\pi/2$ and $+\pi/2$. We recall that for OGO-V bursts one standard

deviation in the distribution of $\Theta_F$ in heliocentric longitude is only 51°.

Figure 4.11 illustrates the effect of varying the shape of the

trajectory. Under equality of the other conditions the radial and

spiral paths are coincident down to approximately 0.2 MHz. If we

extrapolate the straight line defined in the high frequency range and

use it as a reference then we can have a quantitative idea of the

amount of bending of the computed curves. We will define $f_{1/2}$ as the

frequency at which the drift rate drops by a factor of 1/2 from the straight line extrapolation. For the conditions of the figure the frequencies $f_{1/2}$ for the spiral and radial models are 0.083 MHz and < 0.025 MHz, respectively. The drift rates predicted at 0.05 MHz differ by a factor of 2.2. This effect might be detected by observations obtained with high time resolution.

Figure 4.12 illustrates how the velocity affects the drift-rate curves. Above 0.2 MHz they are fairly straight and parallel. As we could expect the larger the velocity the higher the curve. We observe that the amount of curvature in the low-frequency range depends also on the velocity. For the conditions of the figure the frequencies $f_{1/2}$ are, in order of increasing velocities, 0.078, 0.085, and 0.100 MHz.

Figure 4.13 shows the effect of the mode of the emission. We should note that the frequency scale is the same for both curves but the corresponding distance scale is not. In fact, for the conditions of the figure the fundamental radiation at 0.05 MHz occurs at 215 $R_\odot$ while the same frequency as second harmonic occurs at about 390 $R_\odot$. The amount of departure from a straight line is about the same for both except that the curve corresponding to the second harmonic starts bending down at a higher frequency. For the conditions of the figure the $f_{1/2}$ values for the fundamental and second harmonic are 0.085 and 0.180 MHz, respectively. It is of interest to notice that the two curves are practically parallel, the lower one corresponding to the second harmonic; consequently, in fitting observations this mode leads to higher velocities, as expected. We will come back to this point when we discuss the phenomenon of the prevalence of the second harmonic radiation.

Finally, Figure 4.14 illustrates how the overall density affects the FDR curves. As expected, the denser the model the higher the frequency at which the curves bend down. The $f_{1/2}$ values for the conditions of the figure, in order of increasing densities, are 0.045, 0.084 and 0.126 MHz. The curves are fairly parallel and are all practically straight lines above 0.300 MHz. The figure shows the effect of doubling the electron density of model D. For reference we recall that for distances corresponding to frequencies less than 25 MHz model C is four times less dense than Model D.

In Section 4.2.1 (Table 4.3) we found that the scatter of the observational points in Fig. 4.5 from the least-square fit line has a standard deviation $\sigma = 0.13$ in log $|df/dt|$ (a factor of 1.35 in the drift rate). It is interesting to express the effects on the FDR curves resulting from the variation of the different parameters in terms of this standard deviation. This information is contained in Table 4.12. $A_D$ is the coefficient A in Eq. (4.12) corresponding to Model D. We observe that the position of the curves in the plot is more sensitive to changes in the velocity than in the other parameters. For comparison we note that the parameters j, A and $\beta$ were doubled.

When we adopt a density model we can select combinations of trajectories, orientations and velocities to compute the FDR curves for the fundamental and second harmonic. Since we generally know the position of the associated flare of our bursts, we could find by trial and error the set of other parameters for which a computed curve best fits the observations. If the observations are adequate we could obtain the velocity, the trajectory and the modes. However, this method would apply only to

Table 4.12

Effects of the Variation of Parameters on the FDR Curves Expressed

Approximately in Terms of $\sigma$

| Parameter | Range of Parameters | Approximate Separation of Curves | Approximate Frequency Range of Validity (MHz) | Figure |
|---|---|---|---|---|
| $\theta_F$ (Orientation) | $+\frac{\pi}{2}$ , $-\frac{\pi}{2}$ | $2\sigma$ | all | 4.10 |
| $\epsilon$ (Trajectory) | $0 - \frac{\pi}{2}$ (radial - spiral) | $< 2\sigma$ | $> 0.10$ | 4.11 |
| j (Mode) | $1 - 2$ | $2\sigma$ | $\gtrsim 0.50$ | 4.13 |
| A (Model) | $A_D - 2\,A_D$ | $1\sigma$ | $\gtrsim 0.50$ | 4.14 |
| $\beta$ (Velocity) | $0.2 - 0.4$ | $\leq 4\sigma$ | all | 4.12 |

those bursts for which there is no uncertainty about the measured drift rates. This restriction limits considerably its applicability because it is indirect; it involves derived quantities (FDR) obtained from measurements (times of arrival). A more direct method is to fit directly the times of arrival. This has the advantage that it can be applied to complicated cases containing mixtures of fundamental and second harmonic emission modes. This approach was used and it will be discussed in Section 4.2.5.

Summary

We have found a mathematical expression to represent a coronal electron density model that has the following properties:

(a)  It is of simple form,

(b)  It contains only three parameters that can be determined from the density gradient and the number density at any two distances,

(c)  It can be fitted to individual sets of optical observations by an adequate choice of parameters,

(d)  A selection of the appropriate parameters produced models that are consistent with optical observations near the Sun, with measurements in the Earth neighborhood, with radio observations of Type III bursts, and with direct measurements of the height of Type III sources,

(e)  Its gradient at large distances agrees with those predicted by theoretical models, and

(f)  A derivation of the frequency drift rates of Type III bursts predicts some effects that may allow testing of some of the assumptions made in this study.

Electron Density Distribution--Other Forms. A function that resembles Eq. (4.12) in its behavior is

$$N = \frac{A}{r^p - b} \ .$$

$$(4.14)$$

A comparison of the series expansion of Eqs. (4.12) and (4.14) reveals that under the normal conditions $r^p > b$ and $p > 1$, the latter function decreases faster at small r, otherwise the behavior of Eq. (4.14) and (4.12) are very much the same. The function Eq. (4.14) was not used in this work.

In general the theoretical models predict a decrease in density slower than that given by Eq. (4.12). (See for example Table 4.7.) A modification of Eq. (4.12) to obtain this effect, at the expense of increasing the complexity, is:

$$N = \frac{A}{r^p - mr^q - b} \ ,$$

where $m > 0$ and $p > q$. This form was not used either.

4.2.5  Determination of Velocities and the Second Harmonic Phenomenon.

Introduction. In the preceding two sections we have discussed the electron density models evolved from the present study. We have explained the deficiencies of Form 1 and how this led to Form 2 which was finally accepted.

Because it was developed first and because under appropriate conditions it provided reasonable electron density distributions,

Form 1 was used in the next chronological stage of our research. This consisted in predicting the times of arrival of the bursts at the different frequencies and comparing them with the observations. Later, after Form 2 was developed, we found that the early model used in the prediction of the times of arrival and based on Form 1 was numerically close to Model C (Form 2), at least within 1 astronomical unit. We estimated then that the use of any of the two models would not modify appreciably the deduced velocities and that the presence and characteristics of the second harmonic phenomenon, described shortly, would be unchanged. Based on these considerations we decided that it was not necessary to repeat the work using a new model. We will start then by discussing briefly the model used.

The Electron Density Model. We used Eq. (A.14). The selection of the parameters was done as follows: The parameters $\alpha$ and a, related to p and D by Eqs. (A.11) and (A.12), were chosen from an earlier fit of a straight line through the observational points in Fig. 4.5. These points consisted of the November 18, 1968 event observed by OGO-V, and of the observations of other bursts made by various workers. The values adopted were $\alpha = 1.89$ and a = -1.97.

Comparing them with those in Table 4.3, we see that they are close to values determined subsequently in a more precise way. The adopted $\alpha$ leads to p = 2.25 that should be compared with p = 2.38, Eq. (4.13).

We computed models for j = 1 and j = 2.

The trajectories selected were spiral and radial with $\epsilon$ equal to $\pi/2$ and 0, respectively, in Eq. (A.5). Equation (A.10) gives the explicit form of s for $\epsilon > 0$. For $\theta_F$, the orientation of the trajectories,

which appears in the term x in Eq. (A.4), we selected $\pi/2$ and 0. We

applied the boundary condition at $r_o = 1$ assuming that $N_o = 3 \times 10^8$ cm$^{-3}$.

The fact that this density is not high enough to produce a plasma

frequency of 550 MHz does not invalidate our results because we use

the model only in connection with the OGO-V data corresponding to much

lower frequencies.

Finally we let $\beta$ be a running parameter. We proceeded as follows:

We computed $N = N(r)$ for different $\beta$ but for a given set of $N_o$, $r_o$, $\theta_F$,

j and trajectory. Since $N_o$ was fixed the result was a set of curves

converging at $r = 1$ and that could be pivoted about this point by

varying $\beta$. By controlling the position of the curve with $\beta$ in this

fashion we selected a value of $\beta$ such that the corresponding curve gave

a good fit to the optical observation out to 20 $R_\odot$ and to the spacecraft

observations near the Earth. By hypothesis the model is consistent

with the drift rates of radio observations. Figure 4.15 shows curves

for $N_o = N(1) = 3 \times 10^8$ cm$^{-3}$, $j = 2$, $\beta = 0.30$ and a spiral trajectory.

This figure illustrates also the effect of the orientation of the spiral.

In order to select one model we made a rough average of the two curves.

This is equivalent to choosing a $\theta_F$ probably somewhere between 30° and

50°. We will see in Section 4.5.1 that 65 percent of our events were

associated with solar flares on the western hemisphere. The electron

distribution adopted is shown in Fig. 4.16. For comparison we include

some observations. The dashed part of it was not used because it

corresponds to plasma frequencies > 3.5 MHz. Due to the relatively low

density this distribution corresponds to a background corona rather than to a

streamer. This model is comparable to model C of Fig. 4.8, based on Form 2.
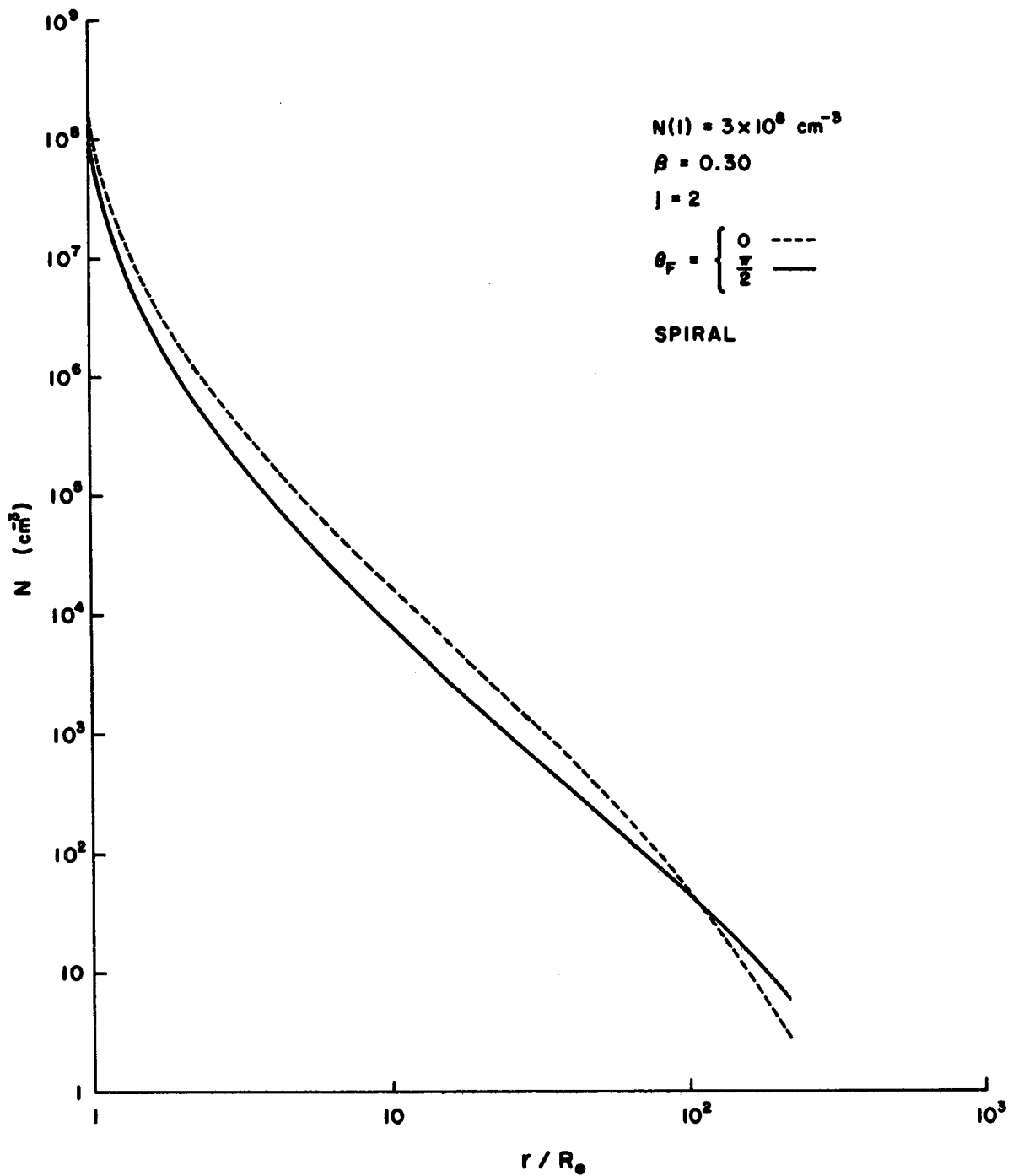
FIG. 4.15   ELECTRON DENSITY MODEL BASED ON FORM 1.   SPIRAL

TRAJECTORY.
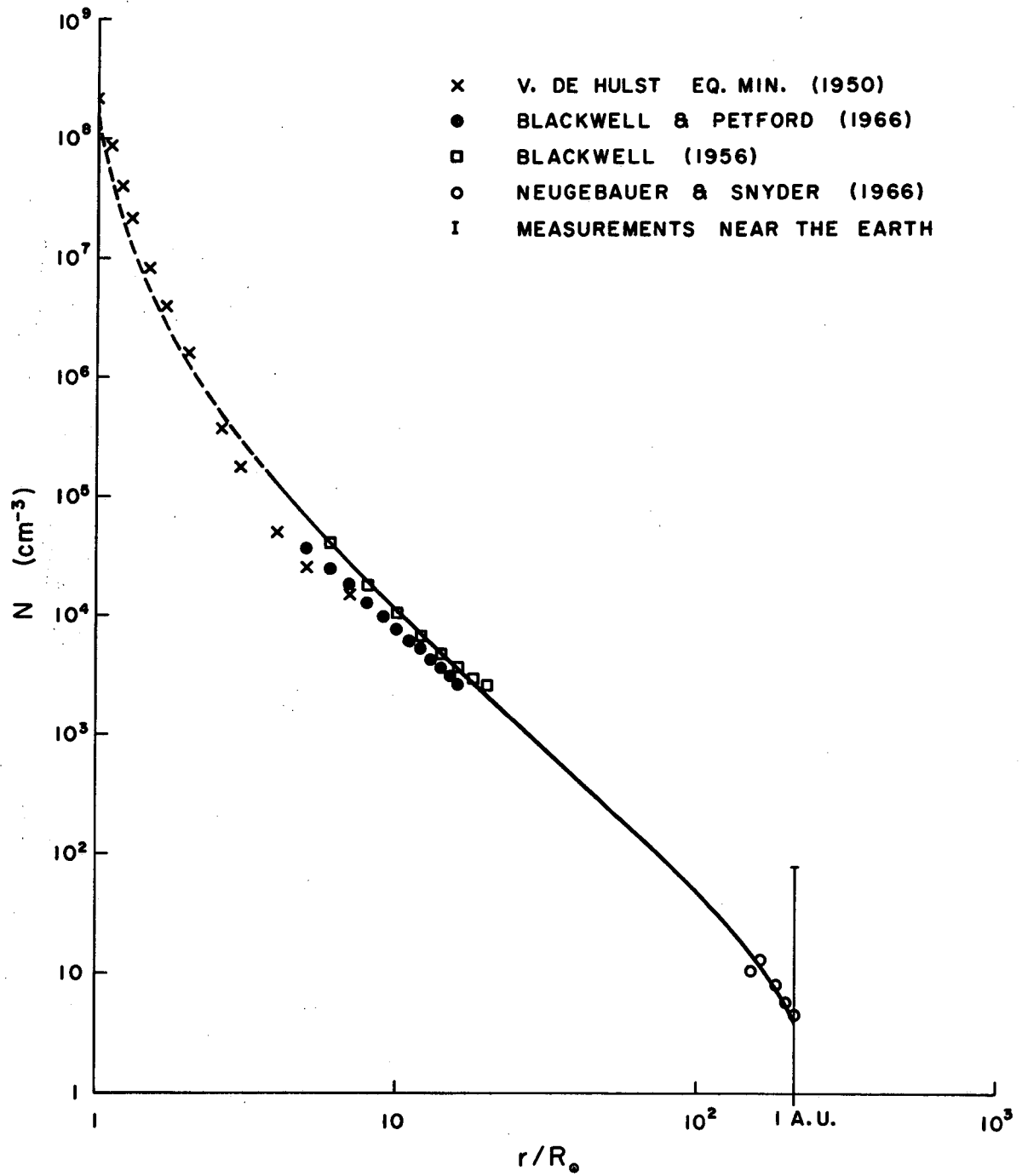
FIG. 4.16  ELECTRON DENSITY MODEL ADOPTED TO COMPUTE TIMES OF

ARRIVAL.

We also computed electron distributions assuming a radial trajectory but we made little use of it. For the sake of completeness we show in Fig. 4.17 models corresponding to the same conditions as those in Fig. 4.15, except for the trajectory.

Prediction of the Times of Arrival. Once we adopted an electron density distribution it was straightforward to compute the times of arrivals of the bursts at the Earth. For this we used the same basic assumptions discussed in Section 4.2.2. We assumed that the particles travel with constant speed along a spiral trajectory (with $\epsilon = \pi/2$ in Eq. 4.8) contained in the plane of the ecliptic. We also assumed that at a particular level the plasma frequency and its second harmonic are emitted simultaneously from the same point with the same propagation velocity in a straight line toward the Earth. The expected sequence of events is as follows: The first burst to arrive at the Earth is the one emitted at 3.5 MHz as a fundamental; its second harmonic at 7.0 MHz falls outside the range of our radiometer. As the particles proceed in their motion they reach the 1.8 MHz fundamental level; its second harmonic at 3.6 MHz is not observed because the bandwidth of the radiometer channel centered at 3.5 MHz is only 10 kHz. The process continues similarly at higher levels. Table 4.13 shows the levels that, according to the adopted model, contribute with emission at frequencies observable with our instrument. Subscript F refers to fundamental and H to second harmonic emission.
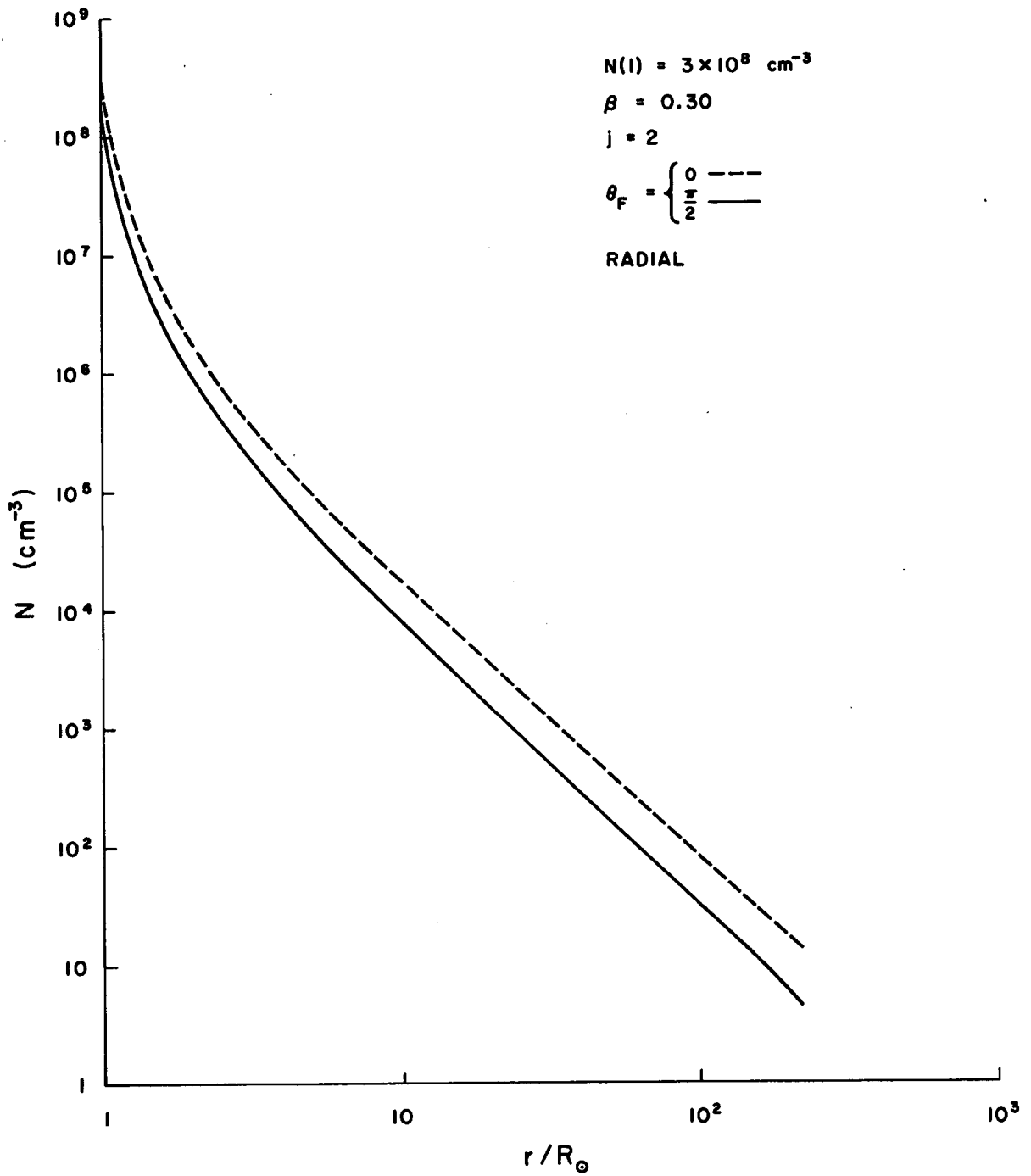
FIG. 4.17  ELECTRON DENSITY MODEL BASED ON FORM 1.  RADIAL
TRAJECTORY.

Table 4.13

Levels that Contribute with Radiation

Observable in OGO-V Radiometer

| $r(R_\odot)$ | $f_F$ (MHz) | $f_H$ (MHz) |
|---|---|---|
| 3.75 | 3.5 | -- |
| 5.95 | 1.8 | -- |
| 6.00 | -- | 3.5 |
| 10.3 | 0.9 | 1.8 |
| 14.9 | 0.6 | -- |
| 19.0 | -- | 0.9 |
| 23.6 | 0.35 | -- |
| 27.0 | -- | 0.6 |
| 38.1 | 0.2 | -- |
| 42.4 | -- | 0.35 |
| 68 | 0.1 | 0.2 |
| 114 | 0.05 | 0.1 |
| 178 | -- | 0.05 |

According to our definition we see that the only levels from which we can observe a fundamental and a second harmonic at the same frequency are at distances of 10.3, 68 and 114 $R_\odot$ corresponding to a fundamental of 0.9, 0.1 and 0.05 MHz, respectively.

Let us refer to Fig. 4.6. Equation (A.10) gives the distances along the spiral between the center of the Sun and a point at a radial distance r. The distance x is given by Eq. (A.4). Then the time elapsed since the exciters leave the surface of the Sun with constant

velocity $\beta$ until the fundamental emission at frequency $f_F$, excited at the level r, is received at the Earth is:

$$t(f_F) = \left\{ \left[ \frac{s(f_F) - 1}{\beta} \right] + x(f_F) \right\} \frac{R_\odot}{c} \quad , \tag{4.15}$$

where $t(f_F)$ is in sec, $R_\odot$ in Km and c in Km sec$^{-1}$. The relationship between r and $f_F$ is given in Table 4.13. A similar expression can be obtained for the second harmonic at the same frequency by replacing F by H. Since the first frequency observed in our radiometer under the above conditions is 3.5 MHz emitted as fundamental, we will take its time of arrival as reference and work with time delays.

We computed and plotted time delays versus frequency for different $\theta_F$ and $\beta$. We varied $\theta_F$ between $-90°$ and $+130°$ in steps of $10°$. For each $\theta_F$ we varied $\beta$ between 0.10 and 0.60 in steps of 0.02 and sometimes 0.01. An example of predicted times of arrival is shown in Fig. 4.18.

In what follows we will use the notation fF or fH to identify points in this plot. f will be the frequency in MHz of a channel of our radiometer. F and H have the same meaning as before.

The Second Harmonic Phenomenon. In Section 4.2.1 we described the technique used first in order to determine the frequency drift rates. This consisted of drawing a smooth curve through the observed points in a frequency versus time of arrival plot and then measuring the slop of this curve. We explained that this method produced FDR curves that could be separated into several groups according to their shapes (see Fig. 4.2). Except for those curves that were a straight line, the shapes were difficult to explain in terms of reasonable physical arguments.
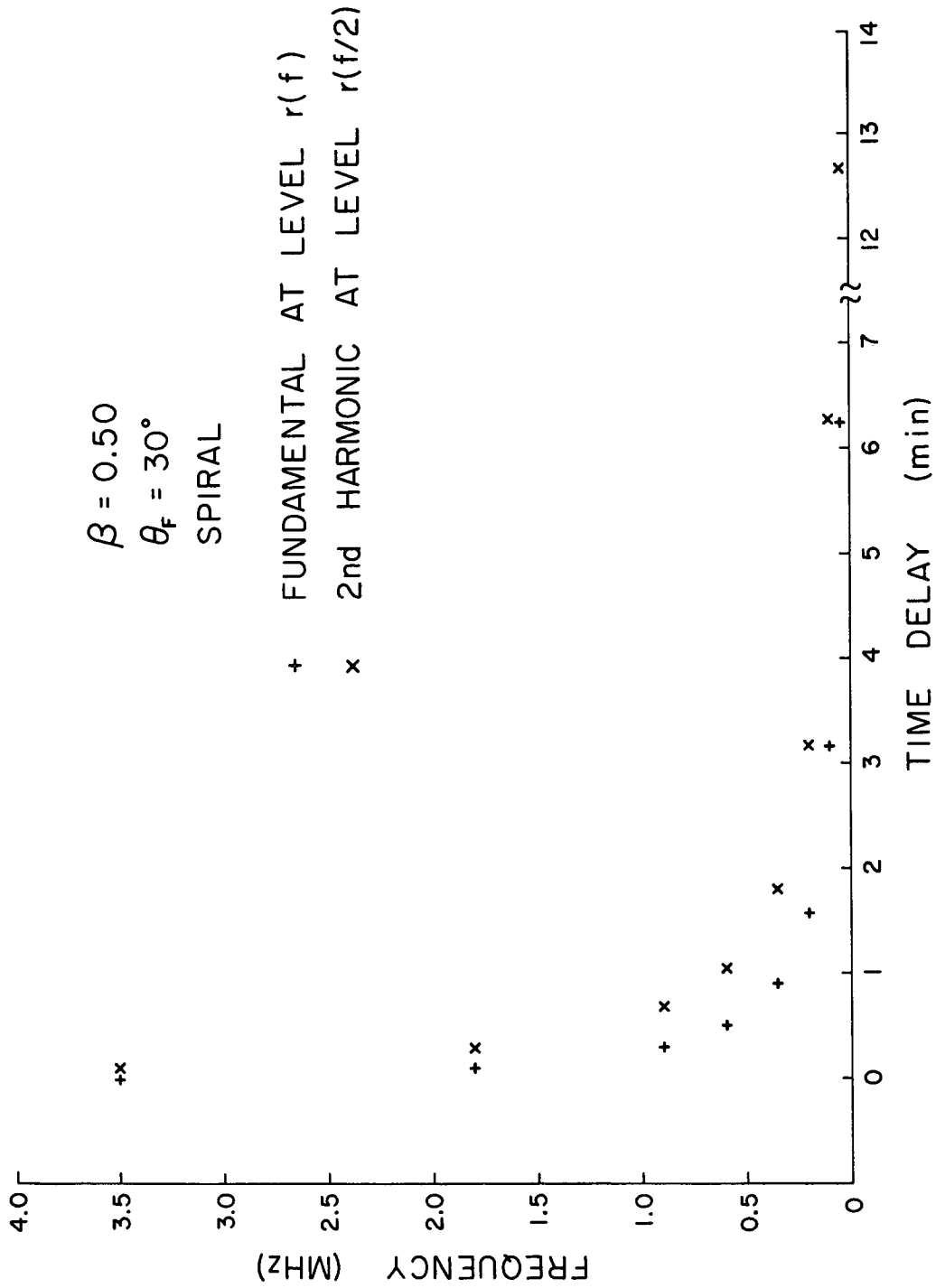
FIG. 4.18 PREDICTED ARRIVAL TIMES.

The second technique that we devised consisted of comparing directly
the observed times of arrival with the predicted ones.  For this we
selected the set of predicted plots corresponding to the $\theta_F$ of the
associated flare of the burst under study and by overlapping with the
observational plots (Fig. 4.1) we selected the $\beta$ within the set that would
give the best fit.  Note that in this way we determine the modulus of the
velocity and not the radial component.

We first used this technique by applying it to the time of start of
the first burst of each event. In some cases the observed points would fall
on the positions predicted for either the fundamental (F) or second
harmonic (H).  In other cases the observations would fall on the (F) above
a certain frequency and on the (H) points below that frequency.  Figure 4.19
shows a typical example in which curves have been drawn through the predicted
points.  We can see that the observations at 3.5, 1.8, 0.9 and 0.6 MHz
fit the predicted arrival of fundamentals while the 0.35 MHz fits the
arrival of the second harmonic at this frequency.  This pattern gave the
clue to the peculiar shapes of the spurious FDR curves obtained by the
first technique, that is, that we were indiscriminately passing a curve
through points that corresponded to emission in two different modes and
produced at two different levels in the corona:  a fundamental and a second
harmonic at the same frequency.  The disappearance of the observed fundamental
and the emergence of the second harmonic emission at the same frequency has
been called by us "the second harmonic phenomenon."

A completely developed single burst observed in our eight channels
would give a 16-point plot.  In general, however, some of them may be
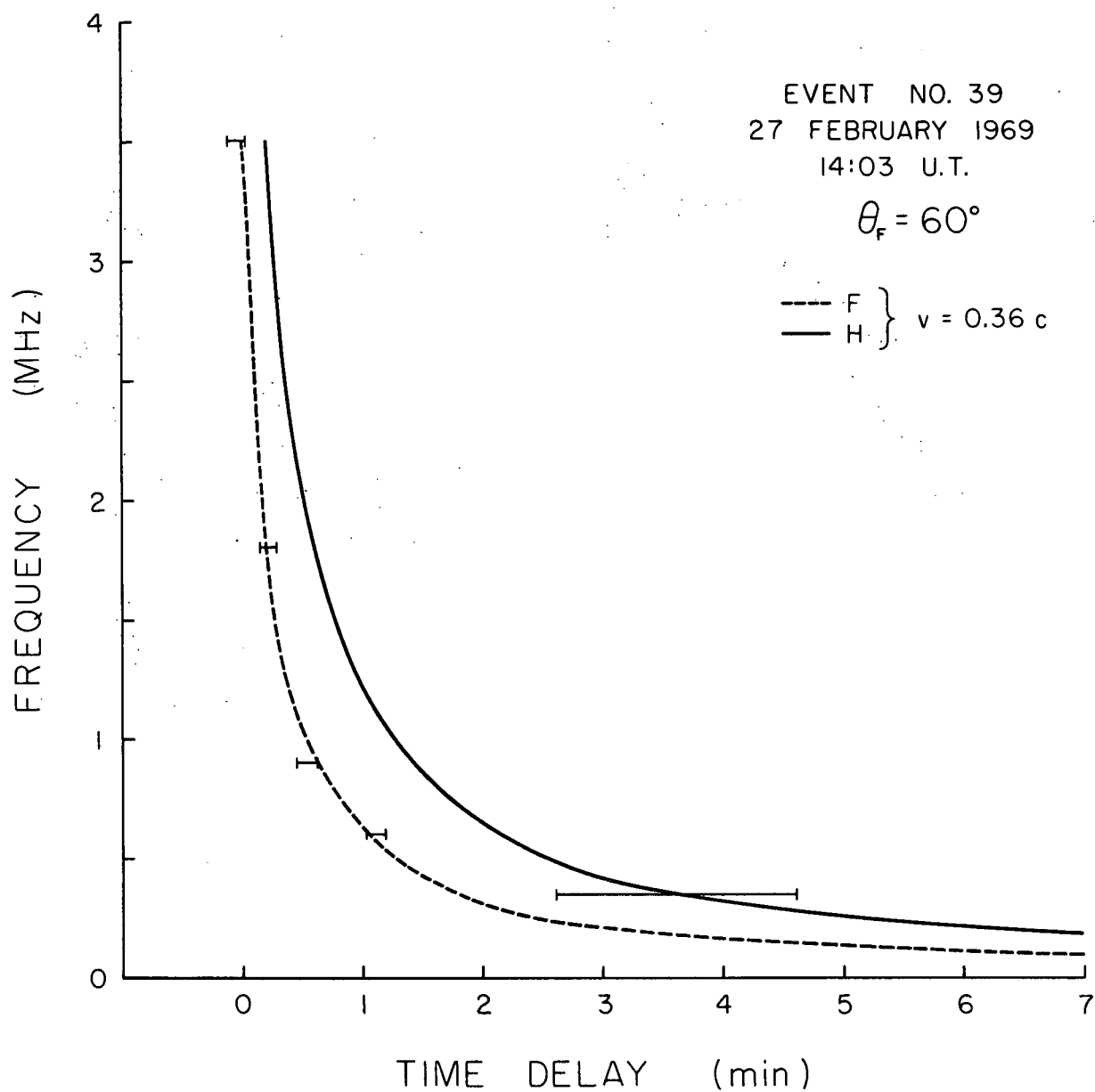
FIG. 4.19  COMPARISON OF THEORETICAL AND OBSERVATIONAL ARRIVAL

TIMES OF A TYPE III BURST.

missing either because the corresponding emission was too weak for

physical reasons, or because of instrumental reasons (interference,

data gaps, etc.) Figure 4.20 shows a case in which the 1.8-MHz

fundamental point is missing and so are the other fundamentals below

0.6 MHz. The combination of a few missing points would evidently

produce very peculiar FDR curves by the first technique. In fact, we

recall that there was a group of bursts that could not be classified

because no simple curve could be passed through the observed arrival

times of the leading edge of the time profile at the different frequencies.

The bursts that produced a fairly complete set of either F or H points

would have a FDR that is a straight line: those are the ones that we

classified earlier at Type A. Now, we find that the drift rates derived

from the fundamental and from the second harmonic curves are practically

straight lines with the same slope in the classical log-log plot (Fig.

4.13), regardless of the value of $\theta_F$. However, the value of the apparent

drift rate $\Delta f/\Delta t$ is smaller for a west limb flare than for a center disc

flare because of the propagation time of the electromagnetic radiation.

This means that when we draw a straight line segment through the drift

rate measured in this range of frequencies it is going to be steeper

for the larger $\theta_F$. This indeed was found.

We have mentioned in Section 4.2 of this work that most of the

events studied (if not all) were extremely complex. At each frequency

they were made up of numerous burst components that in general could not

be separated mainly because of lack of time resolution. We explained then

that for each event we made a chart displaying frequency versus time of

arrival for all the components that were unequivocally present or whose
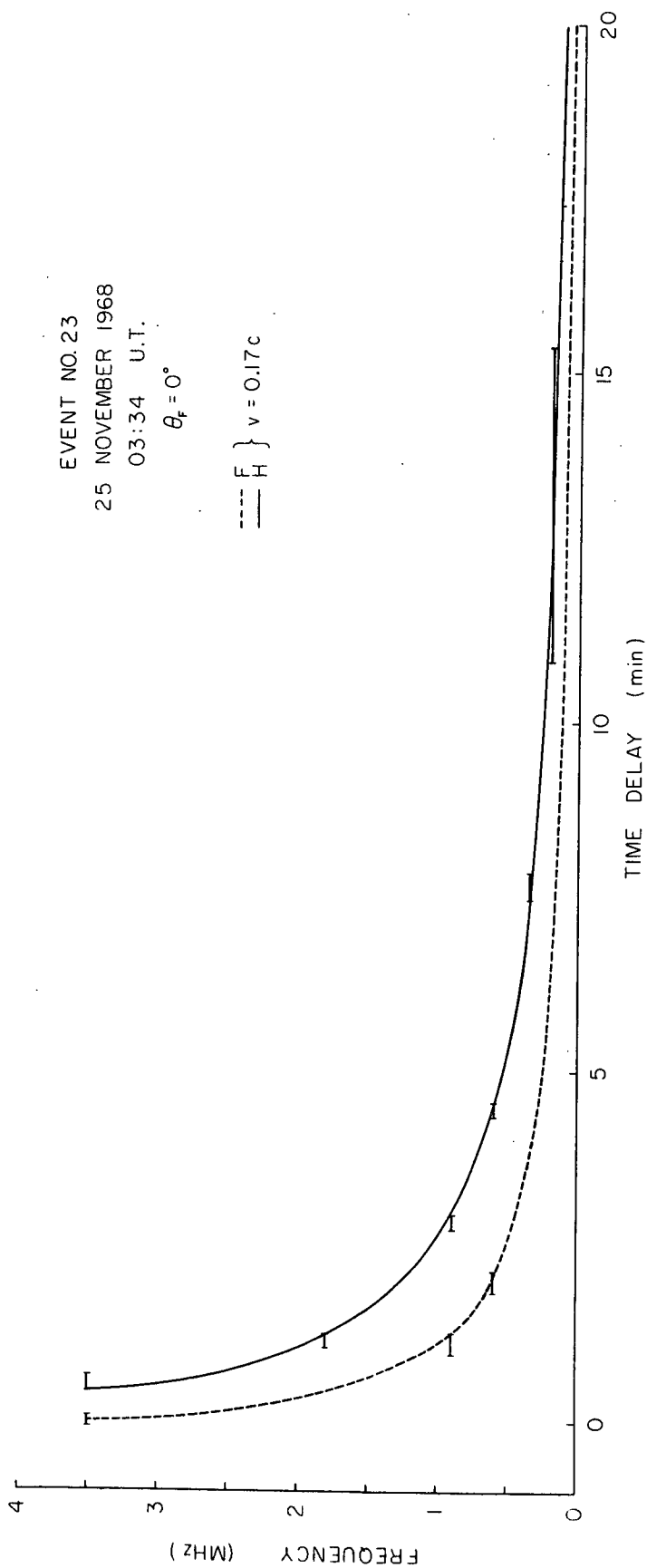
FIG. 4.20  COMPARISON OF THEORETICAL AND OBSERVATIONAL ARRIVAL

TIMES OF A TYPE III BURST.

existence was suspected on good grounds. When using the second technique

there exists then the possibility of confusion in the sense that at a

certain frequency the fundamental of a late component can be  misinterpreted

as the harmonic of an earlier component. The situation is complicated

when some observational points are missing.

. The first step in the use of the new technique was to apply it

only to the beginning of the events. The second step was to apply it to

all the components of each event, as already explained. We identified

the components of an event by Roman numerals according to the chronological

order of arrival. The operating procedure (based on the overlapping)

was as follows: We first fit the earliest times of arrival of an .event

at the different frequencies to predicted F or/and H points. For example,

we labeled  points as IF and IH to indicate that they belonged to the

first component and were identified, respectively, as fundamental and

second harmonic. We wrote down the corresponding $\beta$. We moved in time

and took the next set of points to arrive within the same event; we

repeated the same fitting operation except that these points were labeled

II. The process was continued until we reached the last points to arrive

in the events.

In an ideal situation all the observed points of an event would

be accounted for in the fitting and a velocity would be determined for

each component. However in practice several things can happen to introduce

confusion:

    (a)  Some points of a component may be missing,

    (b)  There may be data gaps,

(c)  A point can be assigned to one or more components as either F or H if the velocities of adjacent components are so different that the curves cross each other,

(d)  When the uncertainties in time of arrival are large the predicted points for different velocities and components fall within the error bar and therefore are indistinguishable.

Table 4.14 shows an actual example of the way in which we tabulated our results.  For this event we determined 9 components.  The first is uncertain and it was assigned only one point at 3.5 MHz; this could not be fitted with the rest into a single component.  Component II starts as F and then goes to H; it is not seen below 0.9 MHz.  For large velocities the separation in time between 3.5 F and 3.5 H is of the same order of magnitude or less than our uncertainty in time resolution, therefore, the predicted F and H may fall within the time error bar.  This happened to component III at 3.5 MHz.  At 1.8 MHz the same observed point can be accounted for as III 1.8 H or IV 1.8 F.  This is indicated by encircling and connecting them as shown.  In component V we can fit a point to 3.5 F and another to 3.5 H.  The predicted F at 1.8 MHz falls in a calibration cycle therefore its existence cannot be either accepted or rejected.

What we have called the structure of the F-H pattern is a combination of the sequence, number and mode of the observational points assigned to a component.  If we do not impose some criteria on this we may  have a large amount of possible fits for the points of an event. The main criterion was to find fits using the least number of components

Table 4.14

Example of Tabulation Resulting from the Fitting of Times of Arrival  (Event No. 1)

| Component | β | f (MHz) | | | | | | | |
|---|---|---|---|---|---|---|---|---|---|
| | | 3.5 | 1.8 | 0.9 | 0.6 | 0.35 | 0.2 | 0.1 | 0.05 |
| I | ? | ? | | | | | | | |
| II | 0.36 | F | H | H | H | | | | |
| III | 0.36 | F and/or H | (H)—(F) | (H)—(F) cal  or/and  (H) cal | H | (H)—(H)—(F) | (H)—(H)—(F) | (H)—(H) | |
| IV | 0.36 | F | | F | F | | | | |
| V | 0.34 | F | F cal | (H)—(F) | (H)—(F) | | | | |
| VI | 0.34 | H | H | H | H | | | | |
| VII | 0.34 | F | | (H)—(F) | (H)—(F) | | | | |
| VIII | 0.34 | H | | (H)—(F) | (H)—(F) | | | | |
| IX | 0.34 | F | | H | H | | | | |

with the smallest spread in the velocities. This last requirements seems reasonable if the components come from the same flare within a few minutes of time; but there is no guarantee that it is always true however. In deciding to what component to assign the observation corresponding to ambiguous points (those encircled and connected in Table 4.14) we tried to avoid those resulting sequences in which the modes alternates between fundamental and harmonic as the frequency decreases, and also those that were too incomplete. In selecting a representative velocity for the whole event we gave more weight to the velocities of the components fitting the lower frequencies. For the event No. 1 illustrated in Table 4.14 we selected $\beta = 0.36$.

The above conditions usually lead to a more or less unique solution for each event. However there are some cases that admit two solutions. This is due to the fact that the predicted times of arrival of the second harmonics for a burst with an associated velocity $\beta$ are very close to the times of arrival of the fundamentals with a velocity approximately equal to $\beta/2$, the other parameters being the same. An example of this is shown in Fig. 4.21, where at the higher frequencies there is practically an overlap between the H curve for $\beta = 0.31$ and the F curve for $\beta = 0.18$ leading to ambiguity in the velocity. At the lower frequencies where the coincidence starts to fail, the lack of time resolution prevents us from resolving the ambiguity. The structure of these cases is a sequence of F points with an assigned velocity $\beta/2$ or a sequence of H points with a velocity close to $\beta$. We called these cases "ambiguous" and we will discuss them shortly. Not surprisingly we found that most of the ambiguous cases had been classified earlier as Type A.
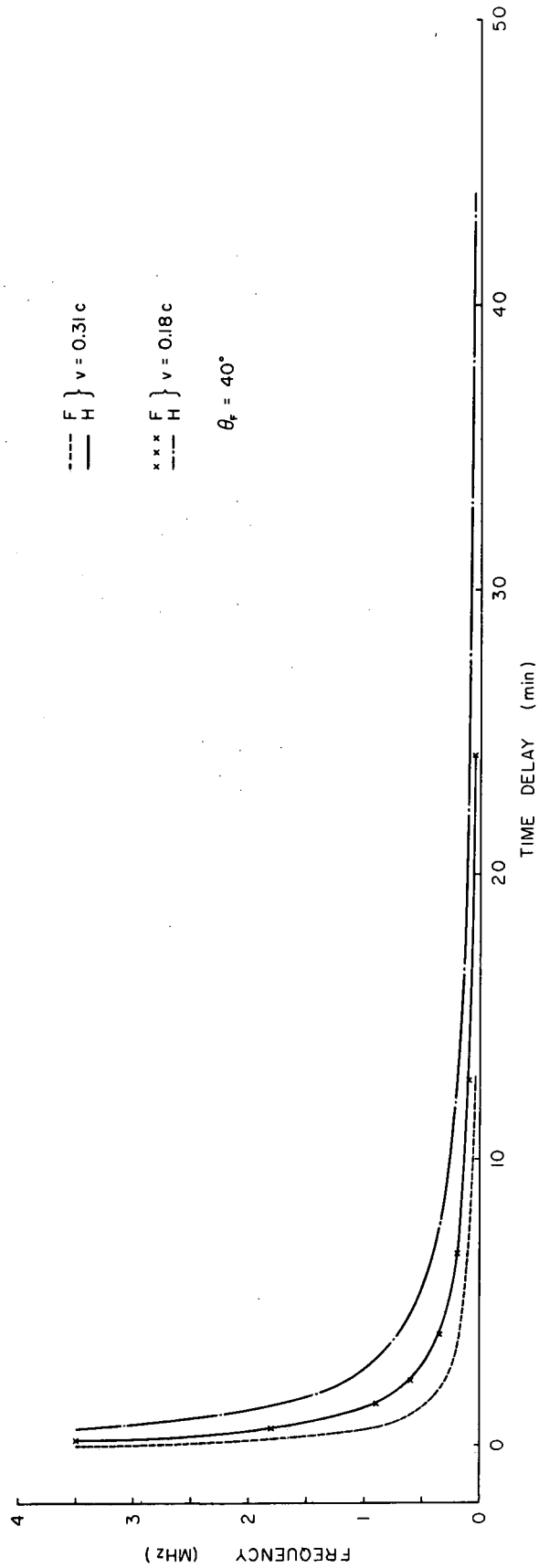
FIG. 4.21   THEORETICAL ARRIVAL TIME OF A TYPE III BURST FOR

FUNDAMENTAL AND SECOND HARMONIC EMISSION.   CASE

OF AMBIGUITY.

The method explained above is not completely objective. In order to reduce subjectivity, the fits were performed by two persons. The results were not significantly different initially and the cases of discrepancy were discussed until an agreement was reached.

In order to have quantitative information with respect to the second harmonic phenomenon we treated the F-H distribution of the events on statistical bases. For this we counted at each frequency of observation, the number of points in all the unambiguous events that were fitted either as F or H, then we analyzed the result according to two criteria. Following the first and less rigorous criterion we counted only the F and H points that presented no major uncertainties in their identification. The count was done regardless of the F-H structure except subjected to the condition that a point, to be counted, should belong to a component with at least 3 points. The second criterion consisted of counting the points of only well defined components with at least 4 points.

Calling F and H the number points counted as fundamental or harmonic, respectively, the results were expressed in terms of the fractional content of components fitted as second harmonic:

$$\frac{H}{H + F} \; .$$

Figure 4.22 shows this quantity as a function of frequency for the two criteria (see note No. 7 of Table A.3). The data on second harmonic obtained from ground-based observations are very limited and we estimate that the fractional harmonic content in the range about 40 to
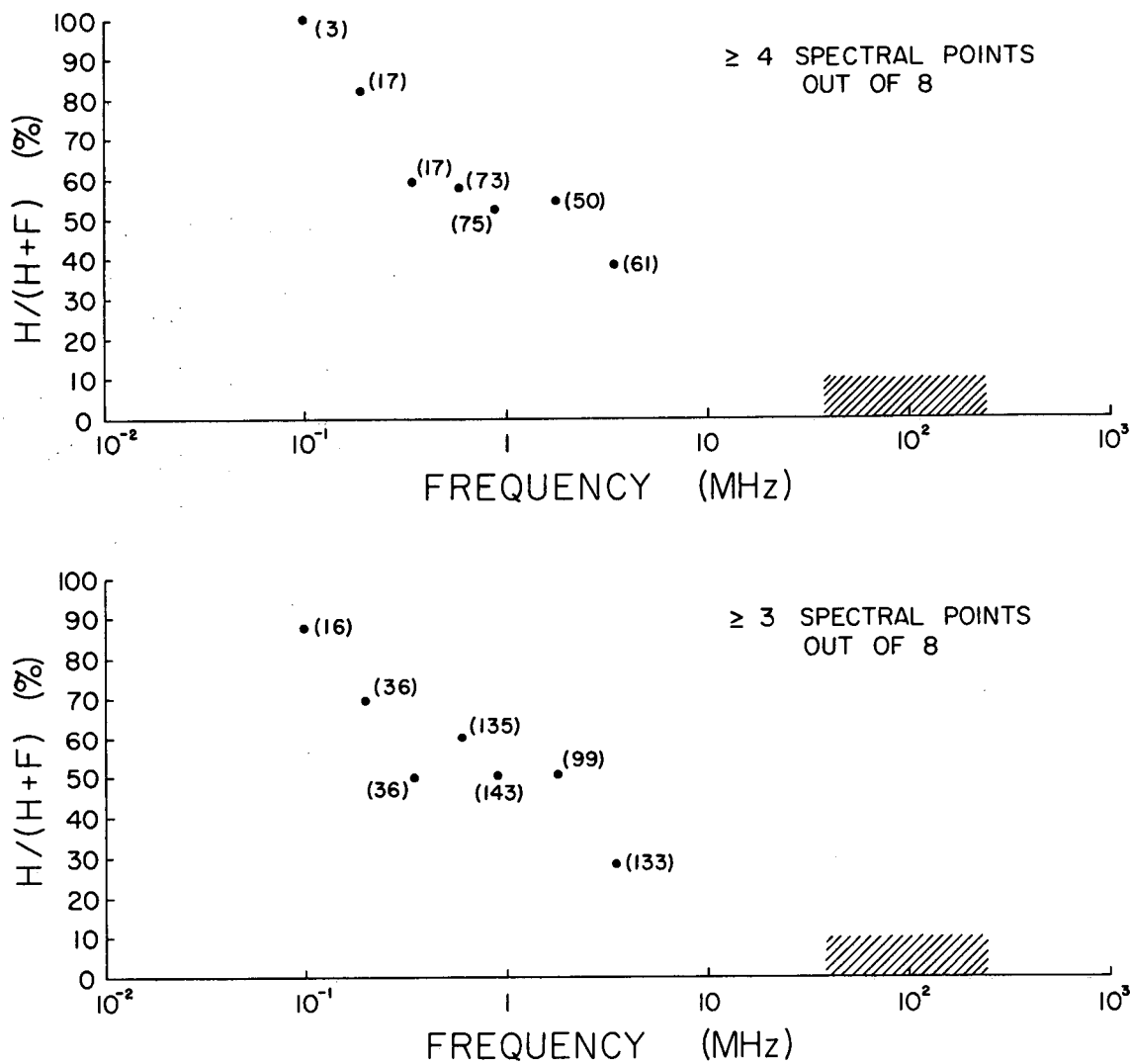
FIG. 4.22   FRACTION OF SECOND HARMONIC COMPONENTS IN UNAMBIGUOUS

TYPE III EVENTS.

240 MHz is not larger than 10% (Wild et al. 1954) or less (Smerd et al. 1962). With regard to this subject we think that Kundu's interpretation of the paper by Wild, Murray and Rowe (1954) data is misleading. His statement is: "The harmonics occur in about 60 percent of the bursts observed in the 40-240 Mc/sec range." (Kundu, 1965, p. 282). The statement of Wild et al. is: "Of the several hundred Type III bursts observed during the year, the recognition of harmonics was considered certain on 20 ocassions. In addition there were many doubtful cases. Certain recognition is often made difficult owing to the combination of wide bandwidth and rapid frequency drift, which may result in the merging of the two bands. In cases where the bursts show tails, however, it is possible to decide without ambiguity whether or not the two bands are present. Of 19 such cases recorded, 12 were found to have the two bands. If it is assumed that the cause of harmonic production is independent of the cause of tail production, this result suggests that the proportion of bursts in which fundamental and harmonic are both of detectable magnitude may exceed 50 per cent." Kundu's statement apparently refers to the 12 out of 19 (or 20) special cases. We can estimate approximate upper and lower bounds to the ratio H/(H+F) from the above statement by Wild et al. It thus appears that during special rare periods the fraction of harmonics to total Type III bursts components H/(H+F) can approach 37% but over a year the average H/(H+F) ~ 20/several hundreds, or < 10%. A statement similar to Kundu's has been made by Boischot (1967a). On Fig. 4.22 the number in parentheses indicates the number of counts. We observe a clear tendency of increase in the harmonic fractional contents as the frequency decreases. This is the quantitative expression of the second

harmonic phenomenon. The 50% frequency seems to be around 1 MHz. We observe that the use of different criteria does not change the results appreciably. It should be emphasized that these results were derived from very intense and complex radio events.

In order to explain this phenomenon we cannot use current theories of the emission mechanism of Type III bursts because they have been derived for the metric range of wavelengths that is $10^2$ and $10^3$ times shorter than OGO-V's. (Smith, 1969; Melrose, 1970; Zheleznyakov and Zaitsev, 1970; Yip, 1970). These theories require observational data on the size of the source, on the density of the exciter particles, on the distribution of their energies, on the ratio of intensities of the fundamental emission and the second harmonic on the temperature of the ambient coronal plasma, etc. Most of these parameters are partially or completely unknown at very low frequencies.

To explain the second harmonic phenomenon several possibilities could be considered:

(a) Directionality effect due to the radiation pattern of the source, or to focusing by the ambient plasma or both. In any of these cases there should be a dependence on the position of the associated flare. In Fig. A.2 in Appendix No. 4, we plotted the distribution in position of the associated flares for ambiguous and unambiguous cases. Since the last ones were in general those in which the fundamentals disappear within the frequency range of our radiometer we could expect them to have a different distribution than the ambiguous. As we will show shortly there is no evidence that the two groups differ with respect to the positions of the associated flares.

(b) The fundamental radiation at level r(f) may be actually much weaker than the second harmonic at level r(f/2).

(c) The two radiations in (b) may be of the same order of magnitude but scattering and refraction effects of the intervening medium would tend to attenuate the fundamental more than the second harmonic at the same frequency because the first is emitted at a point further away from the Earth and because the ambient conditions at the two levels are different.

As we will discuss in Sections 4.3 and 4.4 the second harmonic phenomenon will have important implications in the interpretation of the bursts' spectra and in the determination of the electron temperature of the ambient corona.

The Distribution of Velocities. The determination of the modulus of the velocity of the exciter particles associated with a burst is a direct consequence of the fitting of the observed data to the predicted times of arrival, together with the recognition of the second harmonic phenomenon. As we have explained, we selected a representative value for the whole event from the velocities of the burst components. For some events we could get a unique velocity but for others we could obtain a fit to two solutions with velocities related by a factor near two: One solution corresponding to second harmonic radiation associated with certain velocity $\beta$ and the other corresponding to fundamental radiation associated with a velocity close to $\beta/2$. These cases were called ambiguous. Table A.3 in Appendix No. 1 contains the list of events and their corresponding velocities. $\beta_H$ and $\beta_L$ stand for the high and low alternatives of the ambiguous velocities. These values depend on several

assumptions, particularly on the electron density model shown in Fig. 4.16. There are 32 unambiguous and 31 ambiguous cases, that is, both types are common.

In an attempt to resolve the ambiguity we plotted the distribution of velocities for the unambiguous and ambiguous cases. The first case (unambiguous) is shown in Fig. 4.23 and we denote the velocity $\beta$ without subscript. (See Note No. 7 of Table A.3). In the second case for each event there is a choice between the high velocity and the low velocity that we will call $\beta_H$ and $\beta_L$ respectively. We decided arbitrarily to consider only the alternatives of all velocities high or all low. The resulting distributions are shown in Fig. 4.24. The average velocity and standard deviation $\sigma$ of each of the three distributions are shown in Table 4.15 where n is the number of cases. (See Note No. 7 of Table A.3).

Table 4.15

Parameters of the Velocity Distributions

| Case | n | $\bar{\beta}$ | $\sigma$ | $\bar{\beta} \pm \sigma$ |
|------|---|------|------|------|
| Unambiguous | 32 | 0.32 | 0.09 | 0.32 (1 $\pm$ 0.3) |
| Ambiguous High | 31 | 0.33 | 0.05 | 0.33 (1 $\pm$ 0.2) |
| Ambiguous Low | 31 | 0.18 | 0.03 | 0.18 (1 $\pm$ 0.2) |

It is interesting that the averages of $\beta$ and $\beta_H$ are practically the same however the spread in individual values is larger in $\beta$ than in $\beta_H$ by a factor of 1.8. Also the average of $\beta_H$ is about twice that of $\beta_L$, in fact the ratio is $\bar{\beta}_H/\bar{\beta}_L = 1.83$ but the spread in percent is the same. This could have been expected because of the following: In Eqs. (A.26)
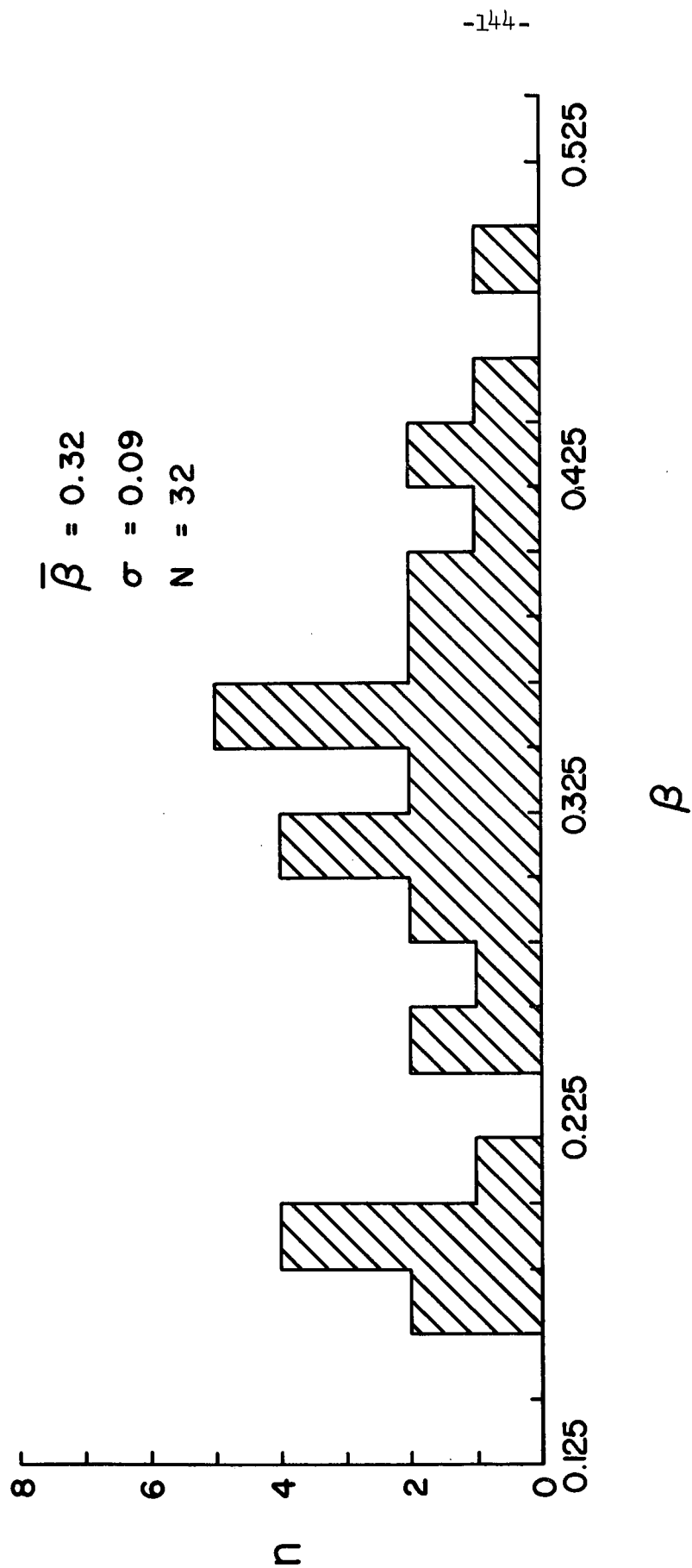
FIG. 4.23  DISTRIBUTION OF VELOCITIES FOR 32 UNAMBIGUOUS CASES.
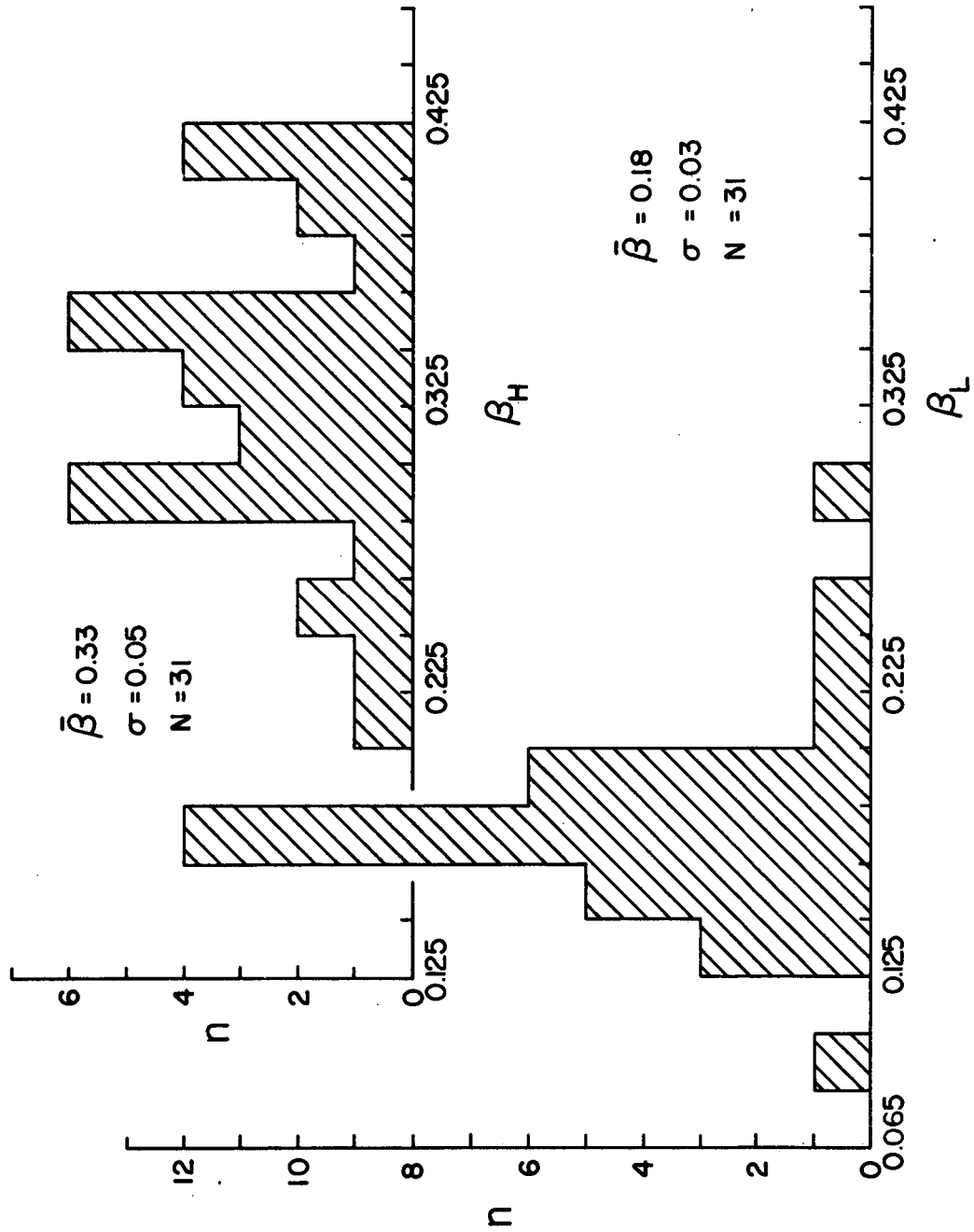
FIG. 4.24   DISTRIBUTION OF VELOCITIES FOR 31 AMBIGUOUS CASES.

and its equivalent Eq. (A.27) let us neglect the correction term $\Delta$
that in the range of frequencies of our interest does not contribute
with more than 20%. The only term left that depends on the velocity is
the first term in the right-hand side of these equations. The velocity $\beta$
and the mode of emission $j$ enter in this term in the ratio $\beta/j^{2/p}$ whose
value is not altered when we take $j = 1$ with the corresponding velocity
$\beta_F$ or $j = 2$ with the corresponding $\beta_H$. In any case,

$$\frac{\beta_H}{\beta_L} = 2^{2/p}$$

which equals 1.85 with $p = 2.25$ (used in the model). This is close to
1.83 obtained from Table 4.15.

It is interesting to notice in Fig. 4.23 that the unambiguous cases
show a narrow distribution around $\beta = 0.19$, which make the distribution
look bimodal. The implication could be that there may exist two ranges
of velocities that center approximately around 0.19c and 0.36c, and
this would account in part for the distribution of the ambiguous cases.
However we have not observational evidence to support this hypothesis and
we know of no theoretical prediction of the phenomenon either.

In trying to find a clue that would allow us to resolve the
ambiguity in velocity we ran some statistical tests on the distributions
obtained and also searched for possible correlations that would
characterize the unambiguous cases. The details of this work are given
in the Appendix No. 4, here we will only mention it.

(a) We applied a $\chi^2$ test to the unambiguous, ambiguous-high and ambiguous-low distribution in order to estimate the likelihood of the hypothesis that each of them came from a normal population with the parameters shown in Table 4.15. The probabilities obtained range between 0.40 and 0.64 and indicate that there is no reason to suspect the hypothesis.

(b) We did a more detailed study of the unambiguous distribution by computing its moments up to the fourth order. The calculated skewness is -0.91; that it is negative can be seen in Fig. 4.23. The calculated amount of flattening is 2.22, that is, the distribution is more flattened than a normal distribution (3.00).

(c) We applied an F-test to test the hypothesis that the unambiguous and ambiguous-high distributions came from two normal populations with the same variance (not necessarily the same mean). The probability is 0.01 therefore the hypothesis is unlikely.

(d) We studied the frequency of occurrence versus $\theta_F$ in unambiguous and ambiguous cases. We applied a Student's Test and concluded that it is likely that the two distributions found are samples of a same normal parent population. The probability at the 20% level is 0.10.

(e) We tried to find correlations involving the ambiguous and unambiguous cases. For example, we studied the relationship $\beta$ versus $\theta_F$ for each distribution. These are shown in Fig. A.3 and A.4. There may be a weak indication of absence of low $\beta$ at $\theta_F \geq 60°$ in the unambiguous cases, however, the results are considered inconclusive.

In conclusion, the tests performed gave no statistical evidence that would help us to resolve the ambiguity.

Before we discuss the velocities determined by us we will review
the results of other workers. Most of them obtained their values by
assuming different coronal electron density models and other different
assumptions; therefore it is almost meaningless to compare individual
results. Table 4.16 and Fig. 4.25 show data found in the literature. In
this figure the numbers in parenthesis refer to the authors listed in
Table 4.16. In some cases the data has been interpreted by the authors
in two different ways with completely different values of velocity.
For those cases we kept the same author number. It is interesting to
observe in Fig. 4.25 that the values of $\bar{\beta}$ concentrate in two regions: from
0.10 to 0.20 and from 0.30 to 0.50. The fact that we have found the
tendency to our velocities to concentrate about 0.18c and 0.36c could be
the same effect. Our velocities were obtained by assuming a model for the
electron density distribution. Had we used a denser solar wind model
within the limitations, we would have obtained higher average velocities
and the form of the distributions would have been different. We will
discuss this soon.

An advantage of our method of velocity determination is that the
fitting for each burst was done in a frequency range of more than a decade,
corresponding to a range of distances of about 100 $R_\odot$.

Other distributions of velocities have been given by Wild et al.
(1959), Malville (1962a), Stewart (1965), Alexander et al. (1969), and
Haddock and Graedel (1970). The distribution observed by Wild et al.
(1959) corresponds to radial velocities determined independently of a

Table 4.16

Velocities of Exciter Particles

| | Velocity Range | $\bar{\beta}$ | f (MHz) | N(r) Model | Instrument | Observer |
|---|---|---|---|---|---|---|
| 1 | 0.2-0.8 | 0.45 | 70-40 | None | Sweep Freq. Interf. | Wild et al. (1959) |
| 2 | 0.05-0.60 | 0.24 | 41-8 | Newkirk's Streamer | Sweep Freq. Interf. | Melville (1962a) |
| 3 | 0.30-0.50 | 0.38[1] | 400-25 | 10 x (B.A.) | Sweep Freq. | Hughes and Harkness (1963) |
| 3 | 0.34-0.53 | 0.43[2] | 400-25 | 10 x (B.A.) | Sweep Freq. | Hughes and Harkness (1963) |
| 4 | | 0.17 | 30-24 | Newkirk's Streamer | Sweep Freq. | Riihimaa (1963) |
| 5 | 0.10-0.15 | 0.125 | 10-1.5 | B.A. and v.DeHulst | Sweep Freq. | Hartz (1964) |
| 6 | 0.17-0.50 | 0.33 | 70-42.5 | Newkirk | Sweep Freq. | Stewart (1965) |
| 7 | 0.27-0.41 | 0.31[3] | 30-10 | B.A. | Sweep Freq. Interf. | Boischot (1967b) |
| 7 | 0.10-0.14 | 0.12[4] | 12-4 | B.A. | Sweep Freq. Interf. | Boischot (1967b) |
| 8 | 0.4-0.5 | 0.45[5] | 1.0-0.20 | None | Step. Freq. (?) | Slysh (1967a) |
| 9 | | 0.13[6] | 23-0.985 | Hartz and N(215) | Step Freq. (?) | Slysh (1967b) |
| 10 | | 0.35 | 15-0.6 | Hartz | Sweep Freq. | Hartz (1969) |
| 11 | 0.10-0.55 | 0.30 | 3.0-0.45 | Alexander et al I | Step Freq. | Alexander et al. (1969) |
| 11 | 0.05-0.30 | 0.15 | 3.0-0.45 | Alexander et al II | Step. Freq. | Alexander et al. (1969) |

(cont.)

Table 4.16 (cont.)

| | Velocity Range | β̄ | f(MHz) | N(r) Model | Instrument | Observer |
|---|---|---|---|---|---|---|
| 12 | | 0.38 | 2.8-0.7 | (7) | Step. Freq. | Fainberg and Stone (1970) |
| 13 | 0.05-0.25 | 0.11 | 4-2 | Hartz | Sweep Freq. | Haddock and Graedel (1970) |
| 14 | | 0.18 | 10-2 | Mean Corona | Sweep Freq. | Bradford and Hughes (1970) |
| 14 | | 0.50 | 10-2 | 10 x (Mean Corona) | Sweep Freq. | Bradford and Hughes (1970) |
| 15 | 0.18-0.49 | 0.32 | 3.5-0.05 | Fig. 4.16 of this work | Step. Freq. | OGO-V data of this work |

Notes:

(1)  Derived assuming all fundamental radiation.

(2)  Derived assuming all second harmonic radiation.

(3)  Derived from fundamental radiation.

(4)  Derived from second harmonic radiation.

(5)  Determined from angular distance of source from the Sun.

(6)  It used also ground base observation at 23 MHz.

(7)  Results are only weakly dependent on an electron density model.
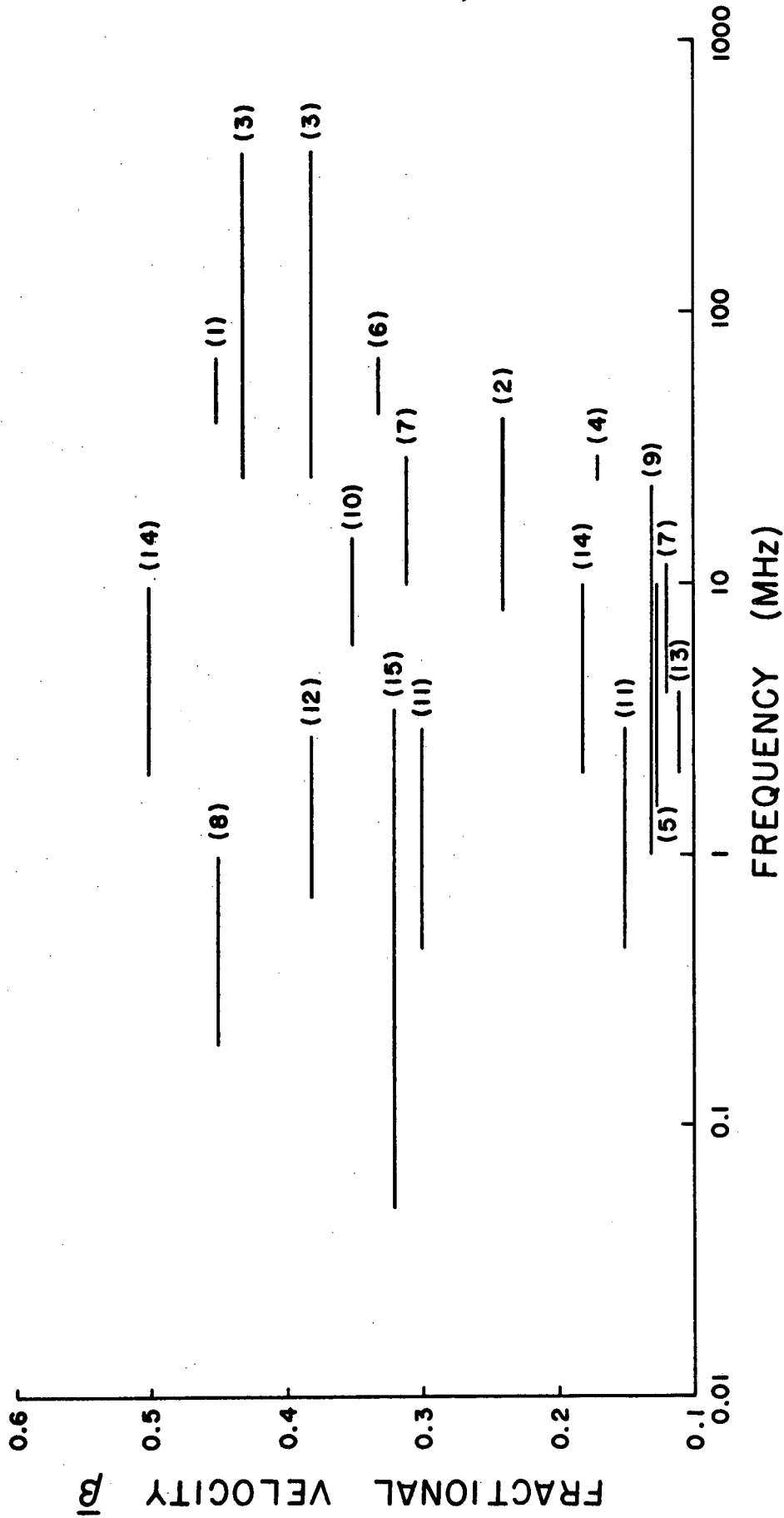
FIG. 4.25   AVERAGE VELOCITIES DETERMINED BY VARIOUS OBSERVERS.
NUMBERS REFER TO TABLE 4.16.   BARS INDICATE FREQUENCY
RANGE.

coronal model. The distribution shows an abrupt decline in the number

of bursts for velocities between about 0.35c and 0.20c and it shows no

cases of velocities less than 0.20c. This apparent cutoff in velocity

has been discussed by de Jaeger (1960a), Malville (1962a), Sturrock (1964),

Takakura (1966), Melrose (1970). They offer explanations of cutoffs

between 0.13c and 0.20c assuming that the exciter particles are

electrons. The distributions obtained by Malville (1962a) and by

Haddock and Graedel (1970) show a faster decline in the low frequencies

and the cutoff occurs at 0.05c. Alexander et al.'s distributions do

not show an abrupt decline; using their Models I and II they do not

deduce velocities lower than 0.01c or 0.05c, respectively.

Effects of the Assumptions on the Deduced Velocities. The

velocities derived in this section rest upon the validity of the

assumptions made in the computation of the times of arrival from Eq.

(4.15). We will discuss them in the rest of this section.

(a) Electron Density

In order to have an estimate of the effect of a denser solar

wind model on the velocities determined by our method we computed

times of arrival using a model about eight times denser than that of

Fig. 4.16, and fitted a few events. We selected the events at the extremes

of the unambiguous distribution of Fig. 4.23. The results are shown

in Table 4.17.

Table 4.17

Velocities β Obtained from Different Models

| Event No. | Model Fig. 4.16 | 8 x Model Fig. 4.16 |
|:---:|:---:|:---:|
| 8 | 0.18 | 0.38 |
| 36 | 0.18 | 0.38 |
| 11 | 0.19 | 0.38 |
| 23 | 0.19 | 0.38 |
| 64 | 0.19 | 0.39 |
| 28 | 0.20 | 0.41 |
| 3 | 0.43 | 0.80 |
| 32 | 0.49 | 0.70 |

As expected the velocities corresponding to the denser model are higher. Except for event No. 32 the ratio of velocities is about two. The distribution is shifted up to range between 0.38 and 0.80, and the average could be expected to be somewhere around 0.60. These values appear too high. Also it is suspicious not to obtain velocities lower than 0.38. At the higher velocities the errors in fitting are larger because the time delays are smaller than the time resolution of the radiometer.

(b) Trajectory

In our treatment we assumed that the trajectory of the particles lies in the plane of the ecliptic. A three dimensional trajectory needs to take into account not only the heliographic latitude of the associated optical flare but also the position of the Earth with respect to the solar equator. The geometry is shown in Fig. 4.26 where:
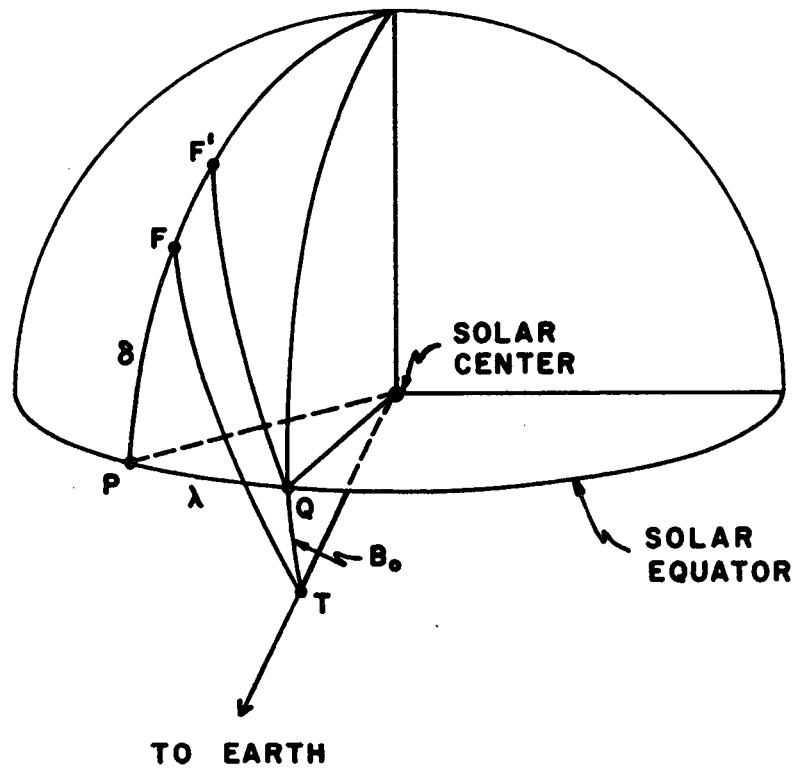
FIG. 4.26   RELATIVE POSITION OF THE EARTH AND Hα FLARES.

QP = $\lambda$ = heliographic longitude of a flare at F,

PF = $\delta$ = heliographic latitude of a flare at F,

QT = $B_o$ = heliographic latitude of the solar disk center and

FT = $\psi$ = angular distance between the radius at the center of the flare and the Sun-Earth line.

Approximating angles by integer degrees, the amplitude of $B_o$ is never larger than $7°$. From Table A.2 we note that the absolute values of $\delta$ are not larger than $25°$. Because $\delta$ and $B_o$ are not too large we have made an approximation that will allow us to estimate the effect on arrival times for trajectories out-of-the-ecliptic. If the exciter particles are ejected radially from F and if the Earth is on the plane of the solar equator then it is simple to calculate the time delays of the bursts observed at the Earth. The approximation we have made is to assume that $\psi$ equals F'Q rather than FT, that is, we have assumed the Earth on the solar equator and we have increased the declination PF by FF' = $B_o$. Let us estimate how good the approximation is. When $\lambda = 0$ the situation corresponds to the exact case. When $\lambda = 90°$ we have calculated, for $\delta = +25°$ and $B_o = -7°$, that FT = $93°$ and F'Q = $90°$. For our purposes the difference is negligible, especially when we recall that the uncertainties in the flare position is of the same order or larger.

Table 4.18 shows delays based on the electron density model of Fig. 4.16 and assuming a radial path for the exciter particles. We recall that the time resolution of our radiometer is of 0.15 min. Let us take as an example a burst originating at a flare located at $\lambda = 0$,

Table 4.18

Time Delays in Minutes Predicted at the Earth and Between the

Indicated Plasma Frequencies

| $\beta$ | $\lambda°$ | $\delta°$ | Fundamental | | Second Harmonic | |
|---|---|---|---|---|---|---|
| | | | 3.5-1.8 (MHz) | 3.5-0.05 (MHz) | 3.5-1.8 (MHz) | 3.5-0.05 (MHz) |
| 0.30 | 0 | 0 | 0.20 | 10.0 | 0.59 | 15.81 |
| | 0 | 30 | 0.21 | 11.09 | 0.63 | 18.54 |
| 0.32 | 0 | 0 | 0.18 | 9.11 | 0.54 | 14.40 |
| | 0 | 30 | 0.19 | 10.20 | 0.58 | 17.30 |
| 0.34 | 0 | 0 | 0.17 | 8.32 | 0.49 | 13.15 |
| | 0 | 30 | 0.18 | 9.41 | 0.53 | 15.89 |

$\delta = +25°$, and assume that $B_o = -7°$. Using our approximation we can consider an equivalent $\delta$ equal to $32°$. If the particles are traveling with a velocity of $0.34c$ we observe a delay of approximately 15.89 min. between the arrivals of the 3.5- and 0.05-MHz bursts, assuming second harmonic emission. However, the original assumption that the trajectory lies in the plane of the ecliptic is equivalent to take $\delta = 0$. For this condition the delay closest to 15.89 min. in our table is of 15.81 min. and it is associated with a velocity of approximately $0.30c$ only. Then according to the above conditions we have underestimated a velocity by about 12%. It may be expected that for a spiral trajectory the error is of the same order.

In Fig. 4.27 we have plotted $\beta$ versus $|\delta - B_o|$ for the unambiguous cases in an attempt to detect the effect of neglecting the third dimension. There is no obvious correlation that would indicate the existence of such an effect.

## (c) Propagation of Radio Waves

The neglect of the effect of the solar plasma on the propagation of the electromagnetic waves results in an underestimation of the velocities. The correction for the bending of the rays due to refraction would make the path longer than we assumed (see Section 4.2.2) and the correction for group retardation would make the time delays shorter. It is difficult to evaluate these errors. From Fig. 15 in the paper of Wild et al., (1959), we can grossly estimate that an apparent velocity of $0.35c$ should be about $0.40c$ when this correction is made. The error is approximately of 12% in this velocity range.
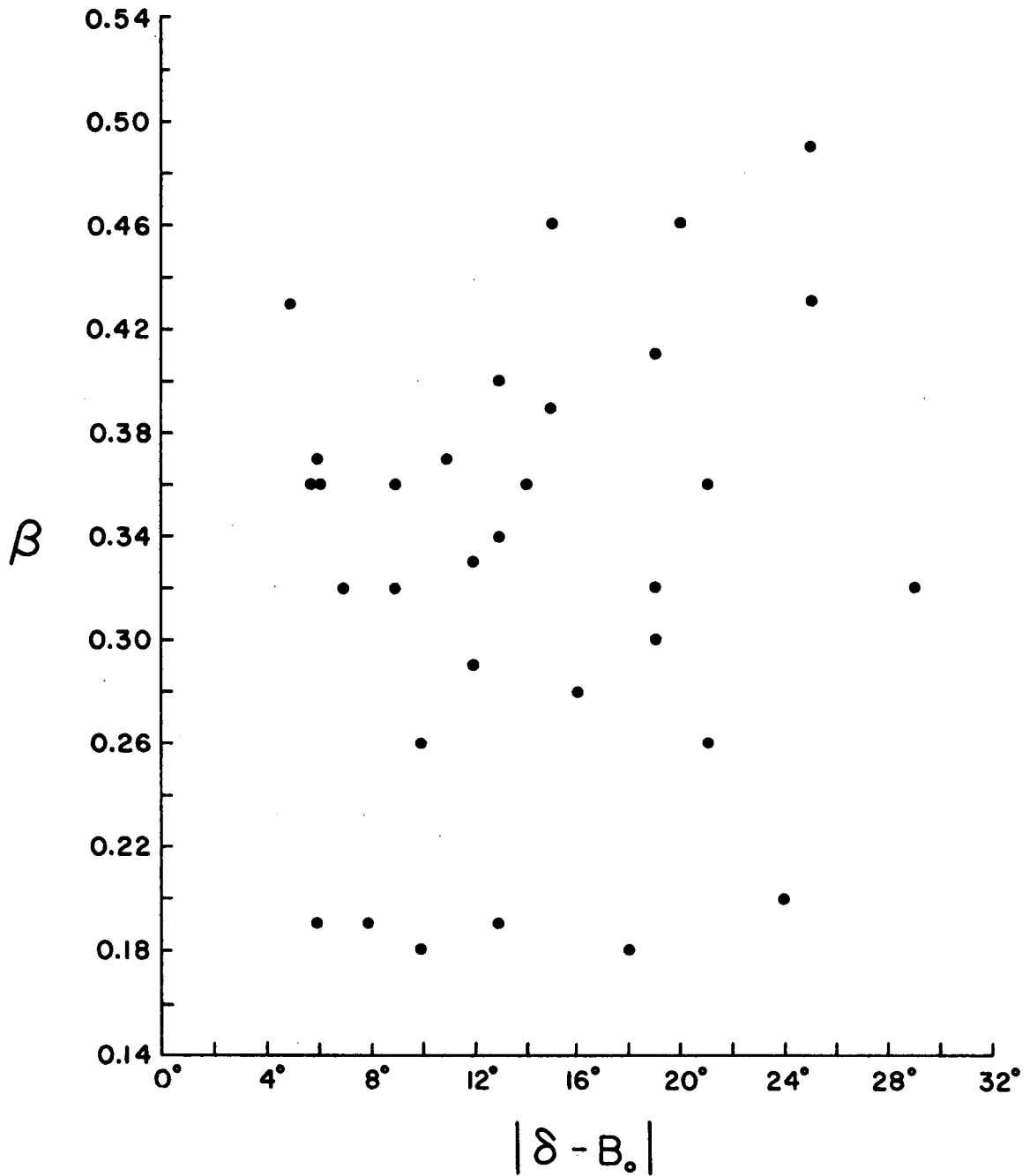
FIG. 4.27  SEARCH FOR OUT-OF-PLANE EFFECTS ON THE VELOCITIES OF
THE UNAMBIGUOUS CASES.

The estimated errors given above should be taken with caution and they could be considered perhaps as lower limits. They can be tentatively used in discussing coronal models. For example, let us take the event No. 32 that has the following parameters (Table A.2): $\lambda = -2°$, $\delta = +18°$, $B_o = -7°$. From Table 4.17 we see that if the true distribution actually corresponds to the denser model then $\beta \approx 0.70$. If we further assume that we have underestimated the velocity by 24% because of effects (b) and (c) then the corrected value would rise to $\beta \approx 0.87$. This value is high but not impossible. Wild et al. (1959) reported bursts with velocities between 0.8c and 0.9c. However, the assumed correction factor of 24% would exclude any coronal model that would give $\beta \geq 0.81$ because then the corrected velocities would exceed the speed of light in vacuum.

## 4.3 Spectra

### 4.3.1 Introduction.

As was shown in Section 2.1.5, the output of the OGO-V radiometer gives a quantity RT that is proportional to the incoming flux density, see Eq. (2.8).

The concept of the power spectrum of Type III solar bursts is different from that of galactic or extragalactic radio sources where, due to the fact that the source size scale is small compared to their distances from the Earth, it is assumed that the power emitted at the different frequencies come from a common region.

For solar Type III sources the situation is different for several reasons:

(a) The emission at different frequencies originates at different levels of the corona,

(b) The physical conditions of the ambient coronal plasma and of the exciter streams are different at different distances from the Sun,

(c) Radiation at a particular frequency may originate from two different levels, from one level as fundamental and from an outer level as second harmonic. It is necessary then to deal with two spectra,

(d) The sources at very low frequencies may originate close to the Earth,

(e) The directivity pattern of the electromagnetic radiation at the source, for both fundamental and second harmonic, will affect the observed flux density depending on the shape and orientation of the trajectory of the exciter particles.

(f) The effect of the coronal plasma on the propagation of the electromagnetic waves to the Earth can modify drastically the received radiation from its origin,

(g) In general the position of the source changes during the lifetime of the burst.

The factors listed above added to the complexity of our data makes it very difficult to interpret the measured intensities especially since little is known about these factors. The identification of harmonic and fundamental emission is possible. However the presence of both modes may require very strong events, but this condition then makes the separation of components more difficult. In fact, we have

seen that the time profiles of strong events are highly complex and that the components usually merge into one big burst.

The anisotropy of the plasma waves and the directivity of electromagnetic waves at the source of Type III bursts has been theoretically investigated, for example by Smith (1969), by Melrose (1970), and especially by Smerd, Wild, Sheridan (1962), by Zheleznyakov and Zaitsev (1970a,b) and by Yip (1970a,b).

The patterns given by Zheleznyakov and Zaitsev for the fundamental and second harmonic emission are quite directive. There is some loss of directivity in the second harmonic when the reflected emission is taken into consideration, but in general the orientation of the radiation diagram with respect to the Earth should influence the observed intensity, particularly in the fundamental mode.

All the theories however have been developed for a range of frequencies extending down only to about 20 MHz, and it is not obvious that they are still valid at frequencies 10 to $10^3$ times lower.

The effects of the refractive, reflecting and absorbing properties of the corona on the propagation of Type III bursts is not fully known. These effects and the directivity of the emission are related to the physical properties of the exciter streamer and of the local coronal plasma in which the burst originates.

In order to search for directivity effects we grouped the OGO-V kilometric wavelength events according to the lowest frequency $(f_L)$ at which they were observed. We defined four groups corresponding to $f_L$ equal to 0.35, 0.2, 0.1, and 0.05 MHz. Within each group we plotted

the distribution of the bursts in angular distance ($\theta_F$) of the associated flare from the Sun's central meridian. The results are shown in Fig. 4.28. They indicate that the eastern tail of the distribution is displaced to the west as the lowest frequency decreases. This can be attributed to directivity effects at the emission and during propagation.

The effect of the OGO-V radiometer system on the measured flux densities can be attributed to the antenna radiation pattern and to the receiver response profile. The receiver response and mismatch at each of the observing frequencies is taken into account by the preflight calibration curves and by the correction factors computed in Section 2.1.5; the antenna system can be assumed to be that of a short dipole, as was discussed in Chapter II. In Section 2.2.2 we saw that the direction of the nulls of the antenna rotates slowly in a plane that is approximately normal to the Sun-Earth line. If a burst occurs when the axis of the nulls is almost contained in the ecliptic then the source of the bursts at about 0.05 MHz or below may be close to the direction of a null. This depends on the trajectory of the exciter particles, on the mode of the emission and on the electron density distribution. Figure 4.29 is an idealized picture of two trajectories of exciter particles viewed from the north ecliptic pole. The circles shown are the fundamental plasma level corresponding to Model D in Table 4.9. The figure shows also a $\cos^2 \theta$ dipole pattern centered at the Earth when the nulls axis is passing through the ecliptic. The direction of 0.5 and 0.1 of the maximum gain are also indicated. The trajectories SA and SB correspond to a west-limb and center-limb flare, respectively.

C.4
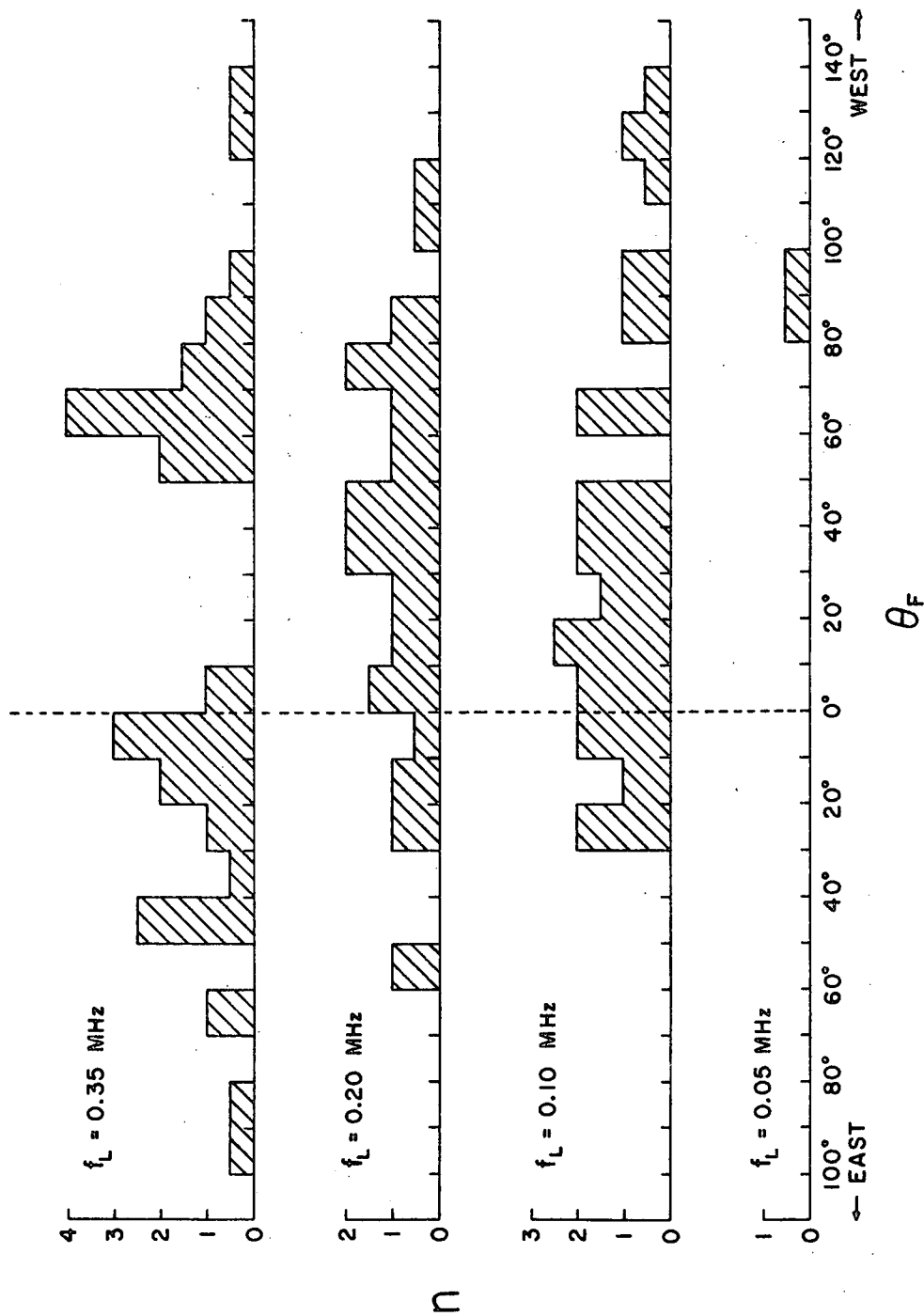
FIG. 4.28  POSITIONAL DISTRIBUTION OF BURSTS FOR DIFFERENT LOWEST

FREQUENCIES OF OBSERVATION, $f_L$.
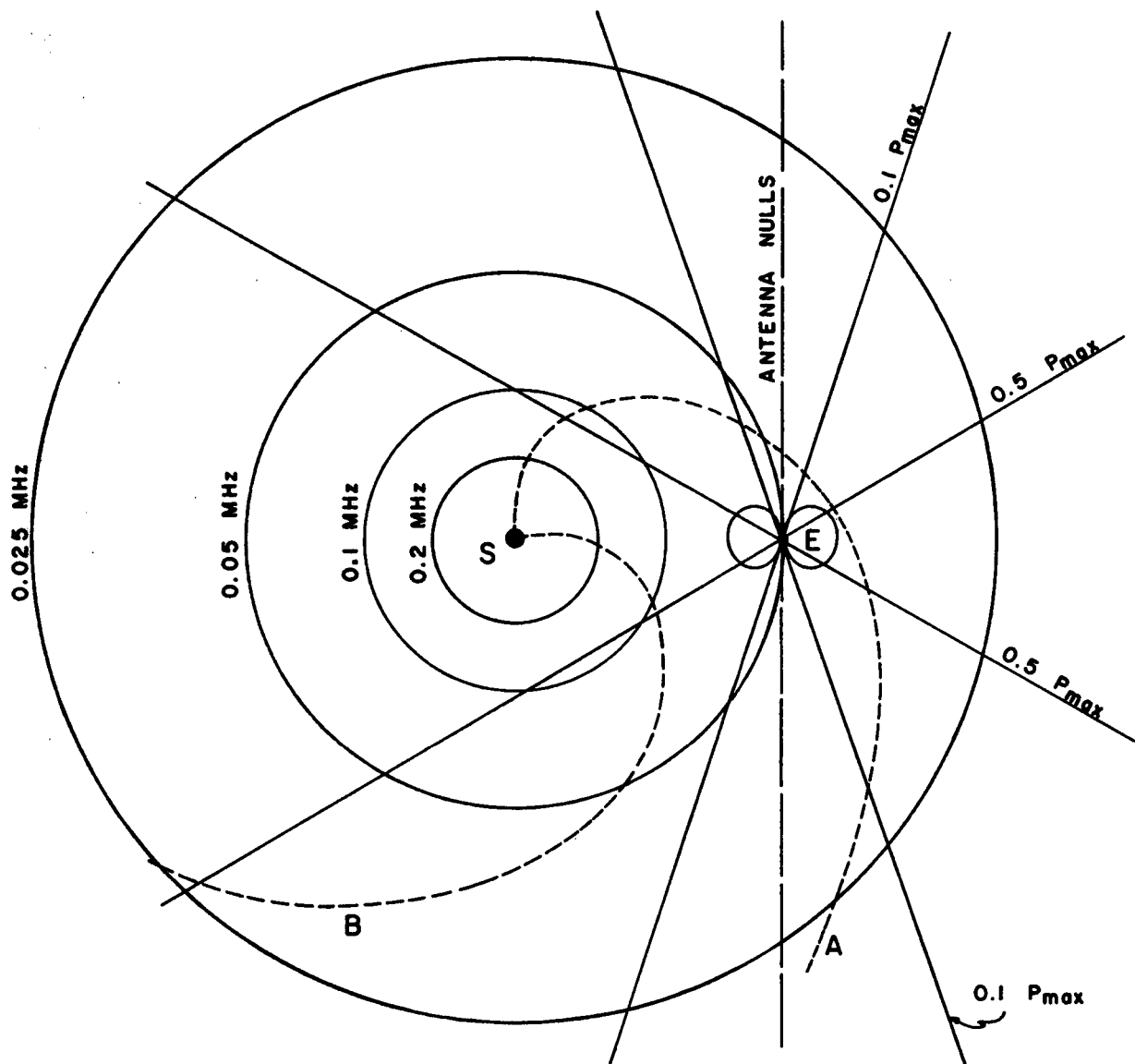
FIG. 4.29  TWO TRAJECTORIES OF EXCITER PARTICLES AND A cos² θ DIPOLE PATTERN
WHEN THE NULLS DIRECTION LIES ON THE ECLIPTIC.

The position of the antenna with respect to the planes (F) and (Q) in Fig. 2.9 is known at any time from the values of the angles ⁂ TEU and ⁂ SEU, listed as θ and ⌀, respectively, in the OR 3/A predictions. When ⌀ = 0° or 180° the direction of the nulls is contained in the ecliptic; when θ = 0° the direction is normal to that plane. The values of θ and ⌀ at the times of the events analyzed in this work are listed in Table A.1 of Appendix 1.

4.3.2 Power Spectra. The fact that the source of a Type III burst moves outward through the corona introduces the concept of a composite spectrum. When excited a uniform and homogeneous plasma emits a spectrum of radio waves at and above the corresponding plasma frequency. This is called by us local spectrum. Assume that the passage of the exciter particles through the corona produces a local spectrum at each level. Then as the exciter particles travel outwards they produce a continuous succession of local spectra. Because of the negative electron density gradient in the corona the successive local spectra are shifted toward lower frequencies. At any instant there will be many local spectra excited at a different stage of development because of the finite velocity of the exciter particles. The local spectra are also different in form because of the different local conditions, expecially the electron-ion collision frequency. The incident spectrum at the observer at a given instant is formed by the superposition of the incoherent radiation from a continuous sequence of local spectra. This superposition of local spectra is a function of the exciter particles trajectory orientation with respect to the observer because of the different distances from the source to the observer and because

of propagation effects, such as scattering and refraction. The main
fact known about the local spectrum is that the radiation at the
fundamental and the second harmonic of the plasma frequency are
prominent. In the earliest attempt to study theoretically the local
spectrum Jaeger and Westfold (1949) considered the problem of transients
in an ionized medium. Their treatment did not consider the second
harmonic. Modern theories have been developed that start by investi-
gating the spectrum of the emitted plasma waves, Smith (1969), Melrose,
(1970), Zheleznyakov and Zaitsev (1970a,b), Yip (1970a,b).

In connection with the above discussion it is interesting to
mention the so-called "instantaneous" bandwidth "which is defined as the
instantaneous frequency extent at any given time," Kundu (1965, p. 280).
The instantaneous bandwidth is measured directly on dynamic spectro-
grams. It lies between 10 and 100 MHz in the metric range, Wild, (1959),
Elgaroy and Rodberg (1963). Hughes and Harkness (1963) measured 100 MHz
bandwidth at 100 MHz; using the same definition we can estimate from
the event shown by Graedel (1969) in his Fig. 7 that in the range between
2 and 4 MHz the instantaneous bandwidth is about 2 or 3 MHz. If we
call $\Delta f$ the instantaneous frequency bandwidth these numbers suggest a
relationship of the form:

$$\frac{\Delta f}{f} \approx 1$$

The OGO-V radiometer obtains only limited samples of the incident
spectrum at the 8 channel frequencies, each with a 10 KHz band, whose
output levels are only recorded sequentially every 9.2 seconds. From

these samples a plot is made of peak power level against frequency.
These will be referred to hereafter simply as power spectra of Type III
bursts.

When dealing with lengths at the different plasma frequency levels,
especially if the frequencies are very low, it is convenient to have
a reference length scale.  If we assume that the electron density
varies as $r^{-p}$ then it can be shown that the distance $\Delta r$ between levels
with plasma frequencies f and $\rho f$, where $\rho < 1$, is

$$\Delta r = \frac{2}{p} (1 - \rho)r \quad .$$

Adopting p = 2.38, see Table 4.9, and a 10% drop in frequency we
obtain:

$$\Delta r = 0.08 \; r$$

where $\Delta r$ and r are in solar radii.

Perhaps a quantity more significant for the interpretation of
our results is the distance $\Delta r$ between plasma frequency levels
corresponding to the extremes of the receiver bandpass (10 KHz).  Using
model D in Table 4.9 it can be shown, for the frequency range of the
OGO-V observations, that:

$$\Delta r = 2.8 \times 10^{-4} \; r^{2.19} \quad ,$$

where $\Delta r$ and r are in solar radii.  We will call $\Delta r$ the "frequency
length-scale."  Table 4.19 contains the numerical results.

Table 4.19

Frequency Length-Scale for Model D

and for the OGO-V Radiometer

| f (MHz) | 3.5 | 1.8 | 0.9 | 0.6 | 0.35 | 0.2 | 0.1 | 0.05 |
|---|---|---|---|---|---|---|---|---|
| $\Delta r$ ($R_{\odot}$) | $\approx 0.014$ | 0.055 | 0.19 | 0.39 | 2.0 | 2.8 | 9.9 | 36 |

The energy emitted at any one level in the corona is a function of the size and shape of the packet of exciters and of the time elapsed since their passage through the level. We will make the important assumption that the extension of the source at any frequency is very small, compared to the frequency length-scale. Preliminary report of the IMP-VI satellite data indicates that the apparent size of the sources at low frequencies are large if they are close to the ecliptic, Haddock (1971).

In spite of the fact that the fundamental and second harmonic emissions are not separable in our spectra the discussion that follows will only be for the fundamental; a similar treatment can be made for the second harmonic.

We can express the flux density by the functional dependence:

$$S = S(f,t) \quad . \qquad\qquad (4.16)$$

For a fixed frequency this equation represents the time profile of the burst at that frequency. To investigate the amplitude of time profiles we can plot quantities of interest versus frequency. A one such plot is the maximum flux density versus frequency. To correct

for the changing distance of the source from the Sun we can reduce
the observed flux densities to a common distance such as 1 astronomical
unit. To compensate for the inverse distance-squared reduction, the
flux density of radiation observed at a frequency f and emitted at a
distance x from the Earth should be multiplied by a factor:

$$q = \left[\frac{x(f)}{\ell}\right]^2 \quad,$$

where $\ell$ is the Sun-Earth distance. See Fig. 4.6. This factor ignores
the effects of the corona on the direction of propagation of the
radio waves and also depends on the electron density model assumed.
q can be computed from the Eqs. (A.4) and (A.17). Table 4.20 shows
values of q for different conditions. It is observed that the values
on some columns reverse their trend as the frequency decreases. This
happens when the sources start receding from the Earth.

Table 4.20

Values of the Correction Factor q for a Spiral Trajectory

| f (MHz) \ $\theta_F$ | Model C | | | | Model D | | | |
|---|---|---|---|---|---|---|---|---|
| | Fundamental | | Second Harmonic | | Fundamental | | Second Harmonic | |
| | $\pi/2$ | 0 | $\pi/2$ | 0 | $\pi/2$ | 0 | $\pi/2$ | 0 |
| 3.5 | 1.00 | 0.96 | 1.00 | 0.94 | 1.00 | 0.94 | .99 | .89 |
| 1.8 | 1.00 | 0.94 | 0.99 | 0.90 | .99 | .90 | .98 | .82 |
| 0.9 | 0.99 | 0.90 | 0.98 | 0.83 | .98 | .82 | .94 | .71 |
| 0.6 | 0.99 | 0.86 | 0.97 | 0.76 | .96 | .76 | .89 | .63 |
| 0.35 | 0.97 | 0.79 | 0.92 | 0.66 | .92 | .66 | .75 | .52 |
| 0.2 | 0.93 | 0.69 | 0.80 | 0.54 | .80 | .54 | .44 | .60 |
| 0.1 | 0.80 | 0.54 | 0.45 | 0.60 | .44 | .60 | .00 | 2.03 |
| 0.05 | 0.45 | 0.60 | 0.00 | 2.01 | .00 | 2.03 | 3.08 | 7.63 |

4.3.3 Energy Spectra. In deriving equation (2.8) that relates
the measured RT product and incident flux density we assumed that the
radiation was randomly polarized. The assumption was implicit in the
definition of the flux density $S_f$ that refers only to one state of
polarization. This assumption is not always valid in the case of
Type III bursts. Komesaroff (1958) observing in the range 40 to 240 MHz
found that half of the 500 bursts exhibited the characteristics of
fairly strong circular polarization. Takakura (1964) states that "most
of Type III bursts at 200 Mc/s seem to be unpolarized or weakly
circularly polarized." Kai (1970) observing at 80 MHz found that the
bursts showed weak circular polarization or were unpolarized while
Harvey and McNarry (1970) examples illustrates the full range of variation
in ellipticity in the polarization of bursts observed at 74 MHz. In
view of this we will assume that the radiation of the bursts under
study was unpolarized, especially since the linear dipole will receive
one-half of the incident flux density for circularly polarized signals.

If we integrate S(f,t) over the duration $\Delta$ of a burst we obtain
the energy density received per unit bandwidth centered at the frequency
f. Assuming that the radiation is emitted into $\pi$ steradians and that
it comes from a small source, the total energy emitted by the burst in
one polarization and per unit bandwidth is:

$$E(f) = \pi x^2(f) \int_{\Delta(f)} S(f,t) \, dt \quad , \quad \text{jóule m}^{-2} \text{ Hz}^{-1} \quad , \qquad (4.17)$$

where x is the distance from the source to the Earth.

Finally the total energy emitted by the radio event in the
range of the frequencies of observation is

$$E_T = \int_{f_1}^{f_2} E(f) \, df \quad , \quad \text{joule m}^{-2} \quad . \quad (4.18)$$

This result applies to the spectrum of either the fundamental or
second harmonic emission.  The addition of their contributions gives the
total of energy of the burst in one state of polarization.  This is in
theory because in practice we did not separate them.

4.3.4  The OGO-V Observations.  As we have seen there are many
factors that contribute to the spectrum of the observed flux densities
and any interpretation has to be considered very provisional.    Before
we realized the prevalence of the second harmonic emission below 1 MHz
we selected those events having a strong component that was recorded on
the eight frequencies.  We assumed that these components corresponded to
the same burst and to the fundamental.  Their peak-flux density was
computed from Eq. (2.8a).  The correction factor q for inverse square of
distance effect was based on a coronal model about 20% less dense than
that of Fig. 4.16.  As a consequence q was close to unity in most cases.

In the following flux densities the contribution from the
background noise level has been subtracted.    Considering the shape of
these peak-power spectra we can distinguish two basic types: single
and double peaked.  They are illustrated in Fig. 4.30.  Usually the
amplitude of the maximum fluctuates between $3 \times 10^{-13}$ and $3 \times 10^{-12}$
w m$^{-2}$ Hz$^{-1}$.  These measurements are about seven orders of magnitude
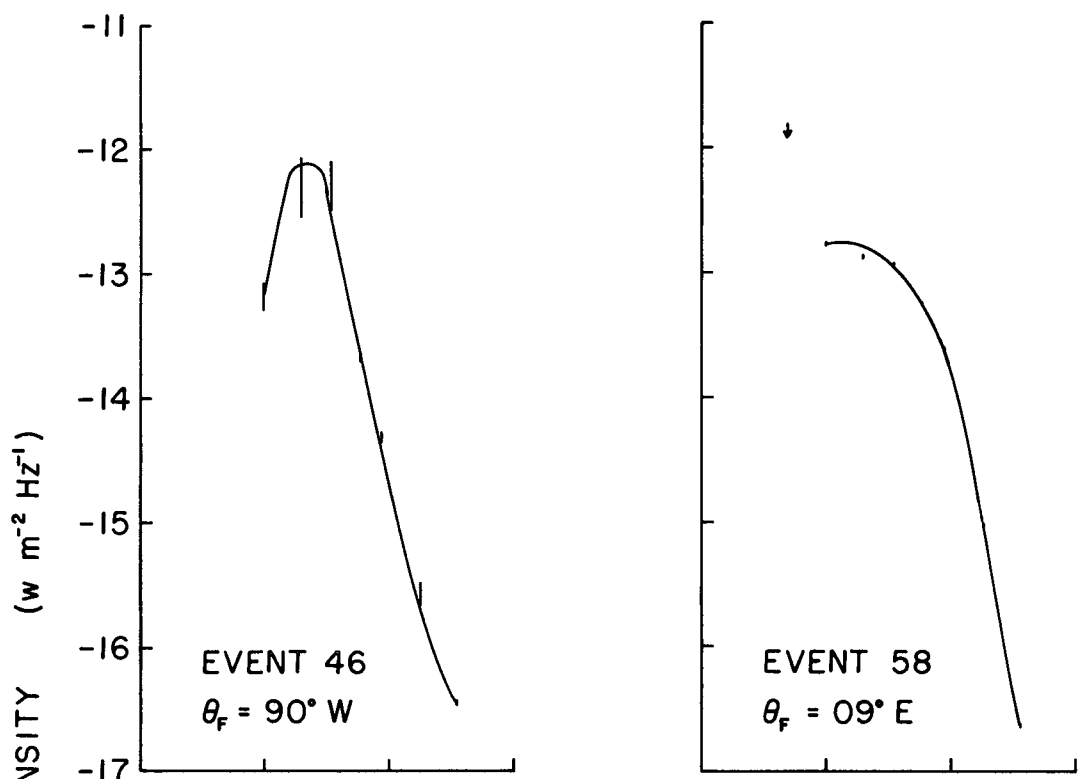
(a) SINGLE PEAKED SPECTRA
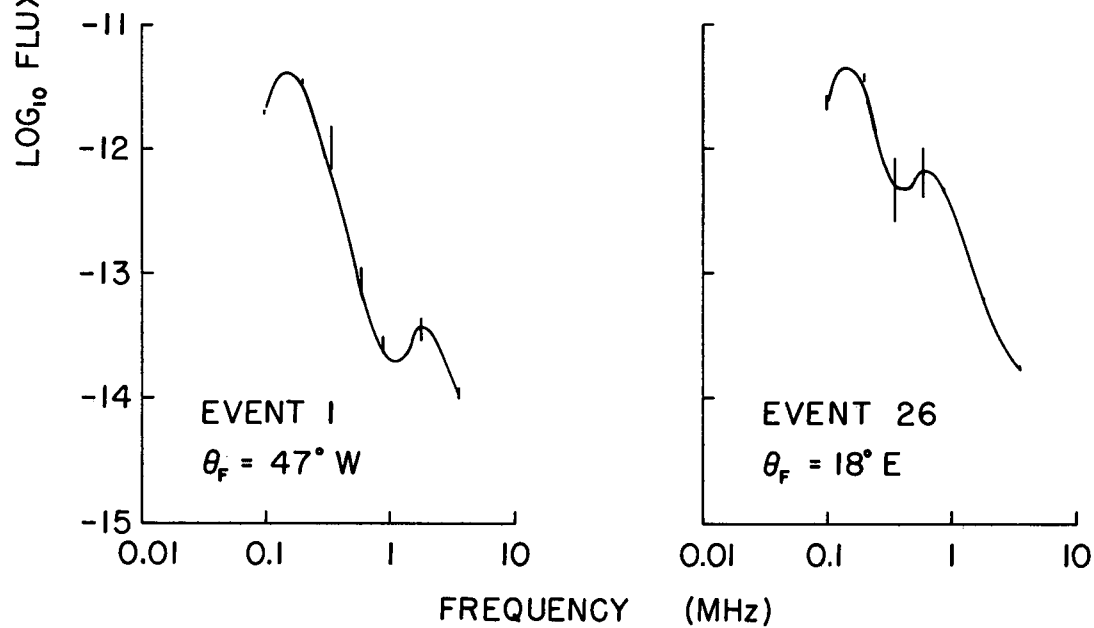
(b) DOUBLE PEAKED SPECTRA

FIG. 4.30 TYPICAL PEAK-POWER SPECTRA.

larger than the ones obtained from ground-based observations at frequencies above 10 MHz.  This could be partly due to the closeness of the burst sources to the Earth but from Table 4.20 we see that the correction, even at 0.2 MHz emitted as second harmonic, is small and practically independent of the orientation of the trajectory of the exciter particles.  However for the combination of model D, second harmonic and $\theta_F = \pi/2$ the 0.1-MHz flux density should be much affected. In Fig. 4.30 we include the orientation $\theta_F$ of the trajectory.  We observed that the flux density at 0.1 MHz of event No. 26 is very large in spite of the fact that it originated 18° East of the Sun's central meridian.

An unequivocal identification of modes and possible correlations of spectral shapes with the position of the associated flares would help to learn more about double peaked spectra.  In particular the trough could be produced by the onset of the second harmonic with increasing intensity.

We measured the energy spectrum E(f) for eight events (Nos. 13, 16, 24, 31, 32, 33, 34, and 46) which were selected because of the simplicity of their time profiles.  To obtain E(f) we measured the area under the time profile at each frequency without regard to mode separation.  The results are shown in Fig. 4.31 where the symbol x in our OGO-V data indicates the average over the different events.  The error bars represent the extreme values measured.  The number of events taken at 3.5, 1.8, 0.9, 0.6, 0.35, 0.2 and 0.1 MHz were 8, 8, 8, 8, 3, 3 and 2, respectively.  At 0.1 MHz the bar represents one case and the arrow the lower bound of another case.  We notice that the
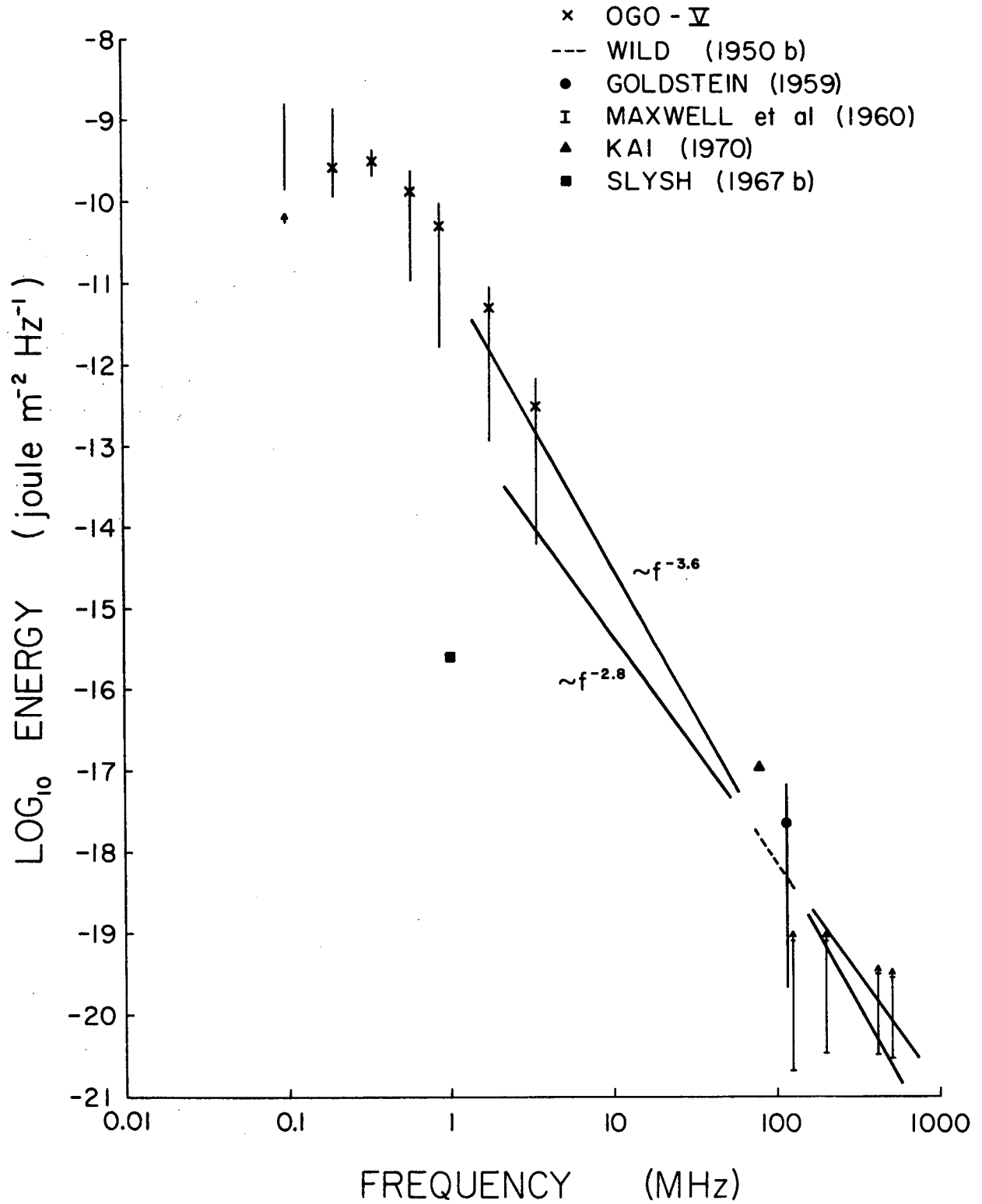
FIG. 4.31 AVERAGED ENERGY SPECTRUM. ALL VALUES EXCEPT WILD'S AND OGO-V's WERE DEDUCED FROM THE REFERENCES.

extremes can fluctuate by a factor of $10^2$, however, they indicate a

definite trend with frequency.  In particular the average follows a

smooth curve that seems to peak about 0.3 MHz.  In the same figure

we show similar data obtained by Wild (1950b) between 70 and 130 MHz.

He found that a curve of the form $f^{-n}$ well fitted his observations

and that the best fit is obtained with n = 3.25.  Plausible values of

n lie between 2.8 and 3.6.  We found that the equation of his best

fit curve is:

$$E(f) \ = \ 10^{-11.65} \, f^{-3.25}$$

where f is in MHz.

The exponent in Wild's functional form was misprinted on page

279 of Kundu's book (1965) as -3.50 instead of -3.25, as given by

Wild.  This error has been propagated by Melrose (1970) and by

Graedel (1969).  Graedel also misinterprets Wild's equation as referring

to flux density rather than to energy.  In Fig. 4.31 we plotted Wild's

curve for n = 2.8 and n = 3.6.  We found that the agreement for n = 3.6

with the OGO-V values is good but n = 3.8 would be better.  The rest

of the data included in Fig. 4.31 was deduced from the references

indicated and it should be taken cautiously.  The increase in flux

density with decreasing frequency observed by Wild was also noticed

by Slysh (1967b) who compared a burst at 0.985 MHz with the associated

Type III burst  detected from ground.  Values as low or lower than that

deduced from Slysh's publication can be expected since it is a matter

of the weakness of the event and the capability of the radiometer to

detect it.  We wish to remark again that the OGO-V data corresponds to

a selected group of events characterized by high intesnity.

In order to estimate the total energy in the spectrum defined in the low frequency range by the OGO-V average values, we fitted it to a function of the form:

$$E(f) = E_m \left( \frac{f_M}{f} \right)^n \exp \left[ \frac{n}{p} \left\{ 1 - \left( \frac{f_M}{f} \right)^p \right\} \right] , \qquad (4.19)$$

where n and p are constants,

$E_M$ = energy of the peak of the spectrum, and

$f_M$ = frequency at which $E_M$ occurs.

For large values of f the function behaves as $f^{-n}$, as required by Wild's observations. Our observations of the eight events plotted in Fig. 4.31 suggest the following approximate values:

$$E_M = 3 \times 10^{-10} , \quad \text{joule m}^{-2} \text{ Hz}^{-1}$$

$$f_M = 0.3 , \quad \text{MHz} .$$

We found that with p = 1 and n = 3.8 to 4.2, the function Eq. (4.19) gives a good fit to the data. The curves are shown in Fig. 4.32. For the purpose of computing the total energy, both curves are satisfactory.

The definite integration of Eq. (4.18) using (4.19) can be achieved by the following change of variable:

$$\zeta = \frac{n}{p} \left( \frac{f_M}{f} \right)^p ,$$

which transforms the integrand into the form of an incomplete gamma function. The difference between two incomplete gamma functions gives
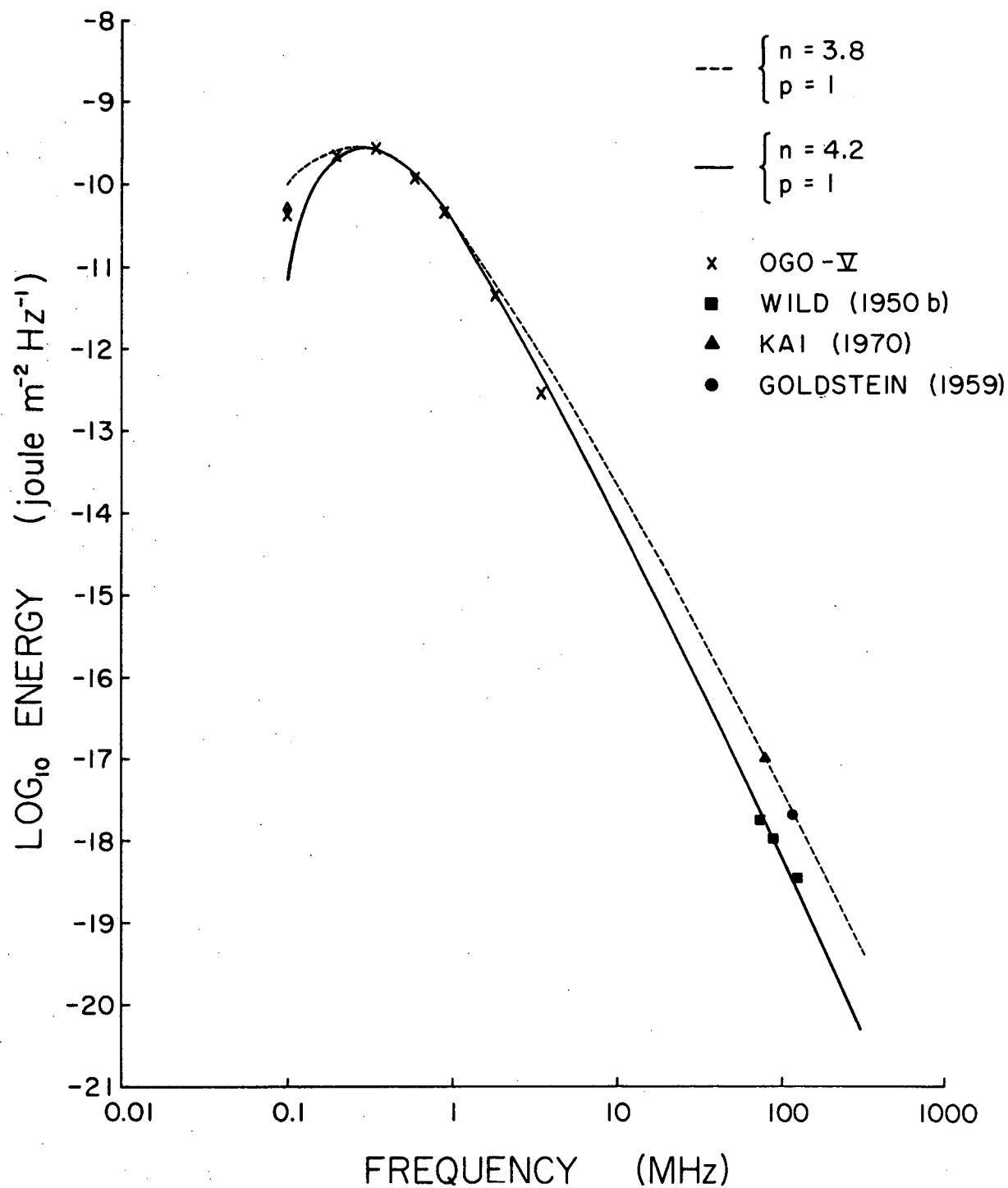
FIG. 4.32 FIT OF EQUATION 4.19 TO AVERAGED ENERGY SPECTRUM.

the result. We found that the spectral energy density received at the Earth in the band between 0.1 and 300 MHz, using n = 4.2, is of $1.5 \times 10^{-4}$ joule $m^{-2}$.

We can deduce the total energy produced by this "average" radio event, assuming that the source is at 1 A.U., that it is small and that it radiates into $\pi$ stereoradian. The result is $E_T = 7 \times 10^{18}$ joule. This value could be used to estimate the number of particles involved if we knew the kind of particles, the efficiency of the transformation of the kinetic energy of the exciter into plasma waves and the efficiency of the coupling between plasma and electromagnetic waves. The nature of the exciters is not known and electrons and protons have been proposed. Since the average speed of the particles is 0.32c this corresponds to 30-KeV electrons or 54-MeV protons. We have not found explicit information in the literature about the loss of kinetic energy to plasma waves.

Little is known about the effectiveness of the coupling of plasma waves into electromagnetic waves; to complicate the problem, it is necessary to differentiate between coherent and noncoherent processes. The results also depend on the mechanism invoked and on whether the emission is at the fundamental or the second harmonic frequency. Ginzburg and Zheleznyakov (1958a, 1958b) have derived an approximate expression for the efficiency Q of the conversion of incoherent plasma waves into electromagnetic waves. An upper value of Q is about $3 \times 10^{-6}$, while a mean value is $< 10^{-7}$. This subject is complex and uncertain and we consider any attempt we make to estimate the number of particles involved almost meaningless. This situation

is further aggravated by the fact that we do not know how applicable
are the current theories in the kilometric range of wavelength.

To estimate the number of electrons involved Melrose (1970)
computed the total energy $E_T$ from Wild's (1950b) data, in a way similar
to ours. His calculations assumed however a low-frequency cutoff near
35 MHz. He arrived at a total energy of $10^{11}$ - $10^{12}$ joules. (The
actual values he gives are $10^{13}$ - $10^{14}$ joules due to an error in the
exponent of f in his equation 8, Paper II. The error originates from
a misprint in Kundu's book (1965) where the exponent appears as
-3.5 when it should have been -3.25.) Notice that the total energy
derived by us is about $10^7$ times larger. We present in Table 4.21
the total number N of particles estimated by different authors. The
subscript e and p refer to electrons and protons, respectively.

Table 4.21

Number of Exciter Particles for Type III Bursts Estimated by Various

Authors

| $N_e$ | $N_p$ | Energy/Particle | Authors |
|---|---|---|---|
| $10^{35}$ | | | Wild (1964,1969) |
| $9 \times 10^{29}$ | | 30 KeV | Smith (1969) |
| | $5 \times 10^{25}$ | 50 MeV | Smith (1970) |
| $10^{33}$ - $10^{34}$ | | | Melrose (1970) |
| $\approx 3 \times 10^{33}$ | | > 40 KeV | Lin (1968) |

The 18 November 1968 Event. This event, No. 21, deserves special consideration because it is the only one analyzed that was observed down to 0.05 MHz, see Fig. 3.2. It was the radio component of a complex solar proton event associated with a west-limb flare. We recall that in our analysis of velocities we used a coronal model close to Model C, and that the event No. 21 is ambiguous, having the alternatives $\beta = 0.18$ radiating at the fundamental or $\beta = 0.36$ radiating at the second harmonic. (Table A.3 Appendix No. 1). We assume that the second harmonic is most likely because of the results shown in Fig. 4.22. Figure 4.33 shows the peak-power spectrum of this event without the distance correction. From Table 4.20 we see that for Model C a correction due to the inverse square of the distance would change the 0.1-MHz flux density by a factor of 0.80 or 0.45, depending on the mode. This is not much considering the uncertainties and the high power level of the whole spectrum. We decided to present the spectrum without the distance correction although this correction is not negligible at 0.05 MHz. In the same figure we include also the available ground-based data. The event occurred at a time, 1026.5 U.T., in which the major solar radio observatories were at night.

A comprehensive report on the phenomena associated with this important event has been published by the World Data Center A, Report UAG-9, 1970. The observations of the Weissenau Observatory are not included there.

The event was observed over 6 decades between 36 GHz and 0.05 MHz, which makes it the most extensive frequency coverage of any radio event
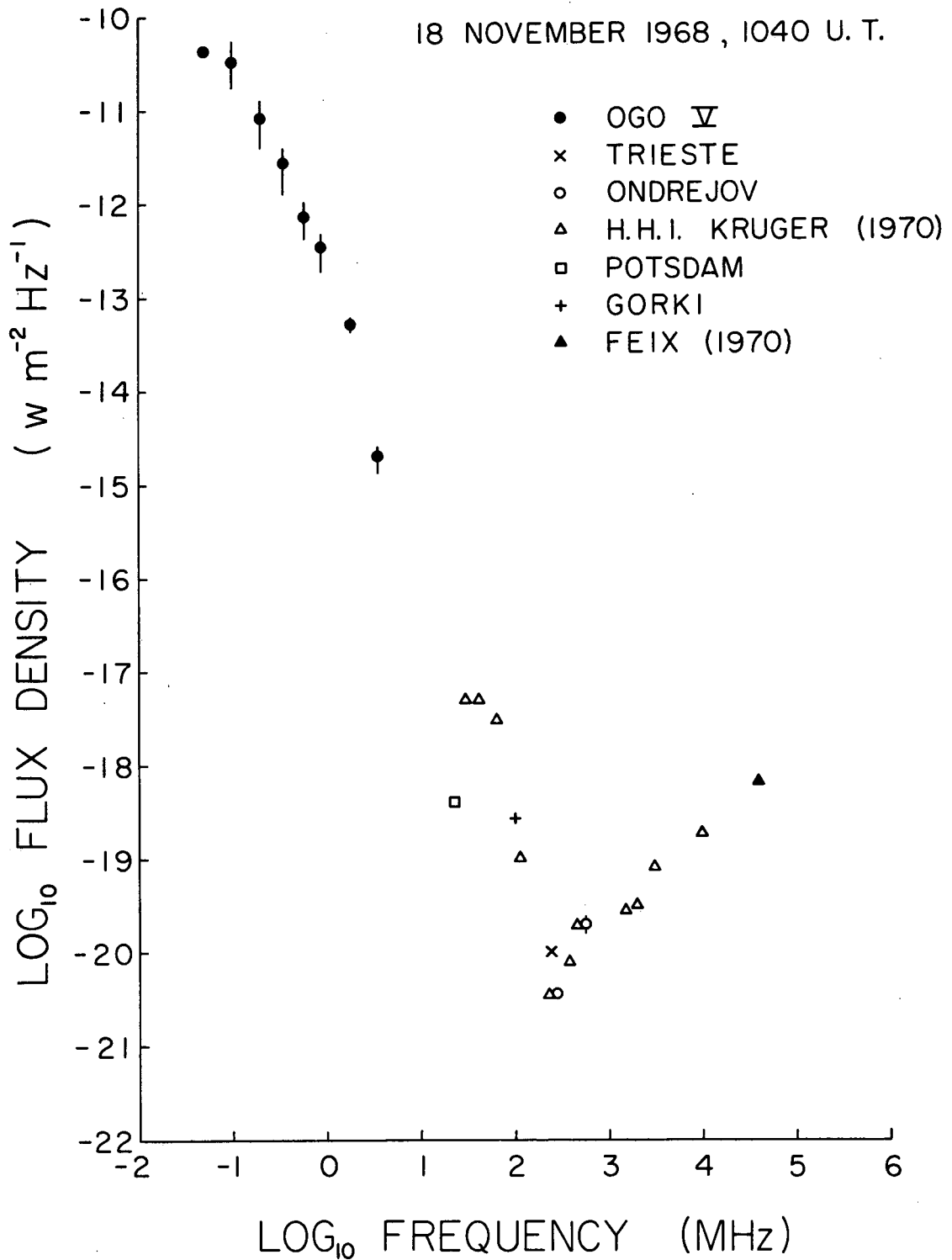
FIG. 4.33 PEAK-POWER SPECTRUM OF THE 18th NOVEMBER 1968 EVENT.
BURSTS GROUP STARTING AT 1040 U.T. NO DISTANCE
CORRECTION APPLIED TO OGO-V DATA.

so far reported. The data shown in Fig. 4.33 correspond to the group

of bursts that started at 1040 U.T. at 3.5 MHz. Previous to this

strong group there was a weak group starting at 1026.5 U.T. at 3.5 MHz,

that is, at the time of the optical flare. See Fig. 3.2b and Table A.2.

The radio event was extremely complex in the entire frequency range.

Urbarz (1969) reports bursts of at least Types II, III and IV in his

spectral observations between 30 and 965 MHz. Thus, it is difficult

to establish what part of the single-frequency ground-based observations

used in Fig. 4.33 corresponds to the Type III group. Above about 100 MHz

the spectrum follows the same pattern found by Castelli et al., (1967)

in other proton events.

Because of the typical starting frequency observed in the Type III

bursts (Malville, 1962a, 1967) we could say that the spectrum below

260 MHz (and certainly below 23 MHz) belong to the Type III group. The

shape of the spectrum between 0.05 and 260 MHz suggests a double peak

as those shown in Fig. 4.30b . It is observed that the main peak seems

to occur at 0.05 MHz or below.

Figure 4.34 shows the energy spectrum of this event, not corrected

for distance, which is more striking than the power spectrum because,

instead of turning over at 0.05 MHz as in Fig. 4.31, this spectrum

continues to rise at a rate approximately proportional to $f^{-3}$. At 0.1

MHz the spectral energy density received at the Earth is between two

and three orders of magnitude higher than typical strong events observed

by OGO-V. An estimate indicates that the total integrated energy

involved is about 40 times larger than that in a typical strong event.
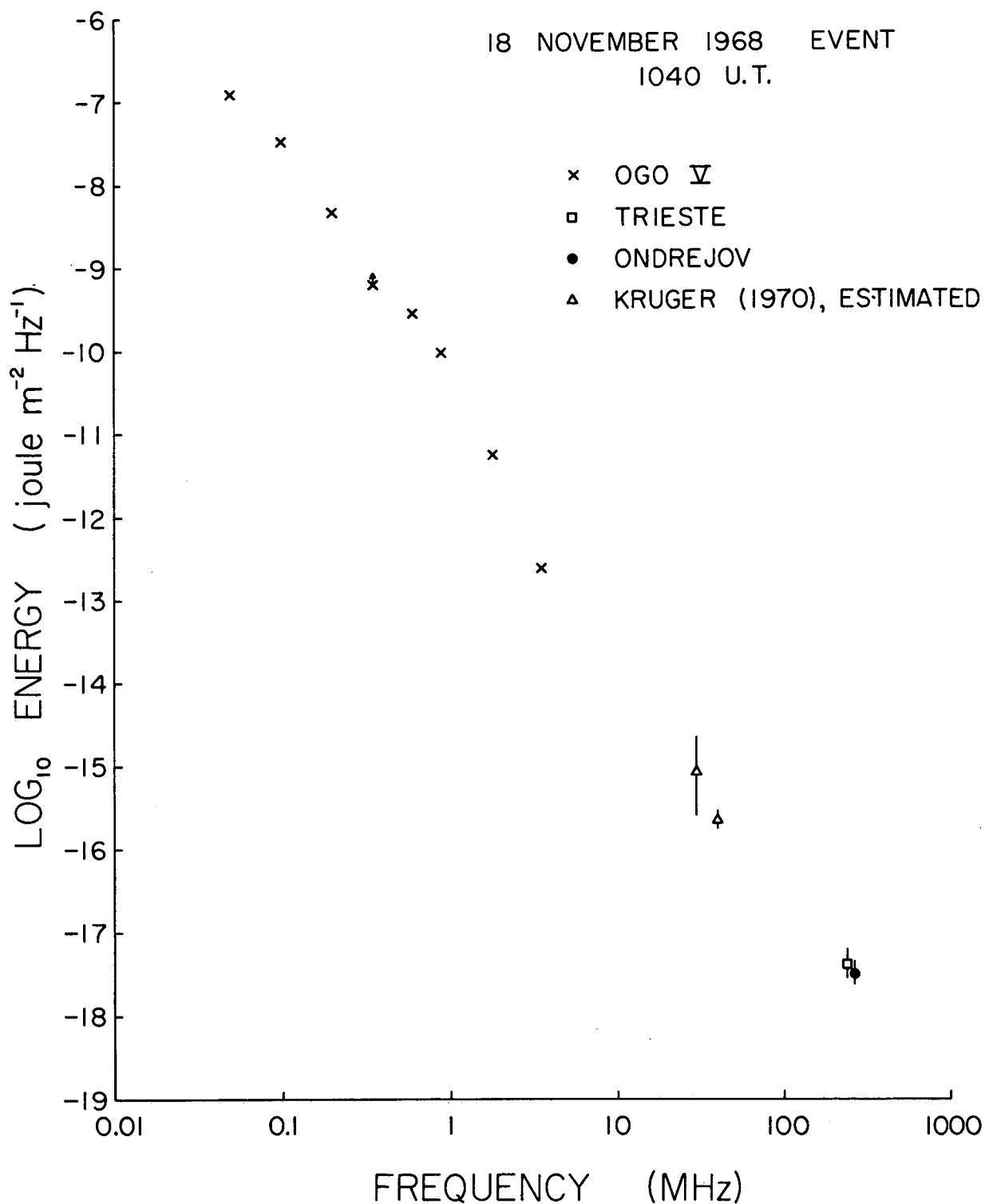
FIG. 4.34   ENERGY DENSITY SPECTRUM OF THE 18th NOVEMBER 1968 EVENT.

BURSTS GROUP STARTING AT 1040 U.T.   NO DISTANCE

CORRECTION APPLIED TO OGO-V DATA.

Theoretical Implications. If we accept the flux densities from the OGO-V observations we find that they exceed by several orders of magnitude the values obtained at higher frequencies from ground-based stations. This should be useful information in any theory developed to explain the emission mechanism of Type III bursts. The fact that we have selected the more intense events is interesting because, as Smith (1969) recognizes, "the explanation of the most intense burst is likely to present the most stringent test of a model." Smith considered $3.2 \times 10^{-19}$ w $m^{-2}$ $Hz^{-1}$ as a maximum possible peak value and applied his model to a frequency as low as 20 MHz. The theory developed by Zheleznyakov and Zaitsev (1970) is not applicable to bursts with a flux density exceeding $2 \times 10^{-17}$ w $m^{-2}$ $Hz^{-1}$ at 100 MHz and, as they indicate, the generation of bursts that violated this condition deserves a special investigation.

The average peak-value observed by us is $10^{-12}$ w $m^{-2}$ $Hz^{-1}$. We conclude that our observations may represent a severe test to theories on the generation of Type III bursts although the highest frequency observed by OGO-V is at least one decade below the lowest frequency to which theories have been applied.

Another aspect in which our observations should influence theory refers to the second harmonic emission. The relative abundance of one of the two modes in Type III bursts as a function of the strength of the bursts has been pointed out by Zheleznyakov and Zaitsev (1970) and by Melrose (1970). Our results contradict the prediction of the Soviet authors that the "intensity ratio of the fundamental and second harmonic should increase as the concentration $N_s$ in the stream decreases,

and thereby as the power of the burst decreases. One would expect in this connection that the percentage of bursts where the fundamental and second harmonics are simultaneously present would also increase as the intensity of the burst decreases." Our results, on the other hand, support Melrose's (1970) model that predicts that "the more intense the burst the higher should be the ratio of the intensity at the second harmonic to that at the fundamental." None of the proposed emission mechanisms predict the increase of the relative content of the harmonic with decreasing frequency found by us and illustrated in Fig. 4.22, however, the second harmonic prevalence may be due to phenomena affecting the radiation during propagation.

Malville (1962b) predicted a turn-over in the energy spectrum, but he placed it at 50 MHz. Smith (1969) accounts for the increase of flux density at lower frequencies by invoking a decrease in the width of the velocity distribution function of the exciter stream.

## 4.4 Time of Decay of Time Profiles

4.4.1 The Observations. The time profile of a burst at a frequency f is defined by Eq. (4.16) with f constant. The output from each of the channels of the OGO-V Radio Astronomy receiver constitutes a time profile. Figure 3.2a shows the eight profiles for the 18 November 1968 event.

The shape of a time profile depends on many factors, for example the size, shape and energy of the bunch of exciters particles, the temperature and density of the local plasma, and the modifying effect of the receiver bandwidth. In this respect it is interesting to calculate

the time of transit of the exciters particles between the two plasma
levels corresponding to the frequency extremes of the bandpass of the
OGO-V radiometer for the different frequencies. It depends on many
uncertain factors (velocity of exciters particles, coronal model etc.,)
however we can obtain representative values from the empirical drift-
rate law, Eq. (4.2), adopting the parameters corresponding to "all data"
shown in Table 4.3. If $\Delta f$ is the receiver bandwidth of 10 kHz then
the transit times $\Delta t$ are given by:

$$\Delta t = f^{-1.84} \text{ sec} ,$$

where f is in MHz. The $\Delta t$ calculated for the OGO-V frequencies are
shown in Table 4.22.

### Table 4.22

Typical Transit Times Through the Eight OGO-V Bandpasses

| f (MHz) | 3.5 | 1.8 | 0.9 | 0.6 | 0.35 | 0.2 | 0.1 | 0.05 |
|---|---|---|---|---|---|---|---|---|
| $\Delta t$ (sec) | 0.10 | 0.34 | 1.21 | 2.56 | 6.9 | 19.2 | 69 | 246 |

As was stated in Chapter II, the receiver time constant is 0.21
seconds, but each channel is sampled every 9.2 seconds, therefore down
to about 0.35 MHz we are limited in time resolution by the sampling
rate. On the other hand at frequencies equal or less than 0.2 MHz
the transit time through the bandpass prevents measurements with an
accuracy better than $\Delta t$.

One of the most important characteristics of a time profile
is the rate of amplitude decay. We observe the decay of the

electromagnetic radiation that, according to the local plasma hypothesis, depends on the decay of the plasma oscillations set up by the passage of the exciter particles through the corona.

Jaeger and Westfold (1949) developed the thoery of transients in homogeneous ionized medium. They concluded that the oscillations set up by a pulsed excitation decay with time according to an exponential law

$$\sim \ e^{-\nu t}$$

where $\nu$, the ion-electron collision frequency (Coulomb collisions) is given by:

$$\nu \ = \ 4.2 \times 10^{-5} \ NT^{-3/2} \ \ \sec^{-1} \tag{4.20}$$

where $N$ = electron density, $m^{-3}$ and

$\quad\quad T$ = electron kinetic temperature, K.

They proposed that Eq. (4.20) could be applied to bursts of solar noise produced in the solar corona. Evidence found by Williams (1948) and Payne-Scott (1949) suggested that the decay in intensity of the bursts was approximately exponential; but they did not compute temperatures. Further study was reported by Jaeger and Van't Verr (1957) and Boischot et al. (1960). These last authors used Eq. (4.20) in the range of 15 to 38 MHz assuming the local plasma hypothesis and computed temperatures in agreement with that obtained from optical observations. Malville (1962a) using a similar formula given by Spitzer obtained good agreement also in the derived temperature at 25 MHz.

Boischot (1967) found that the temperatures obtained from observations at 36, 18 and 8 MHz showed a decrease with frequency, as expected from pure collisional damping. The first measurements from an artificial earth satellite reported by Hartz (1964) also showed this trend between 10 and 2 MHz that agreed with Slysh's value at 0.985 MHz. However, Hartz (1969) first pointed out that the temperatures obtained in the range of 9 to 0.7 MHz were "substantially below those expected for the solar wind." Further studies of Type III bursts at lower frequencies have confirmed this disagreement. Haddock and Graedel (1970), Alexander et al. (1969).

Criticisms of this determination of temperature has been raised by Hughes and Harkness (1963). They argue that the time decay of a burst is also affected by the increase in the size of the exciter packet by dispersion and by contamination of the Type III burst with Type V and with second harmonic radiation of the same Type III. If these factors are taken into account the deduced temperatures would be even lower thus increasing the discrepancy.

We believe that it is necessary to ascertain that the burst decay is in fact exponential before using Eq. (4.20) or its equivalent. However, to present the OGO-V results we have measured the time $\tau$ that it takes a burst to drop from its peak to $e^{-1}$ of that value regardless of whether the decay is exponential or not. Besides the factors that affect the time profile mentioned by Hughes and Harkness we should add the impossibility of resolving individual components in the extremely complex time profiles of the events we have analyzed. All these effects

become worse in our data as the frequency of observation decreases. In many of those cases affected by saturation and telemetry quantization (see Chapter II) we were reduced to drawing an idealized curve through the observed profile. Because of all the reasons discussed our measurements of $\tau$ are upper limits of the times of decay expected from collisional damping. This is supported by the fact that in bursts that exhibit saturation the decaying portion, after the saturation terminates, decreases at a faster rate than the ideal profile. This decay could be closer to the free relaxation after the exciter particles have passed through the appropriate plasma level. Figure 4.35 shows the measured decay times. The sybmols x indicate the averages, the length of the error bar is $2\sigma$ centered at the average. The number in parenthesis indicates the number of cases considered. At 0.05 MHz we have used the data of the radio burst that occurred on the 6th of April, 1971 at 0915 U.T., observed by OGO-V but not included in our analysis. We see that in spite of the crudeness of the measurements the decay times follow a definite increase with decreasing frequency. In Fig. 4.36 we have gathered all the information we could find in the literature. It is interesting to observe that the observations fall approximately on a straight line, except for a few points. The points obtained by Boischot et al. (1960) that depart the most were considered perhaps erroneously high by Kundu (1965, p. 329).

In this plot we can fit approximately a straight line whose equation is

$$\tau f^{0.97} = 10^{7.75} \quad , \tag{4.21}$$
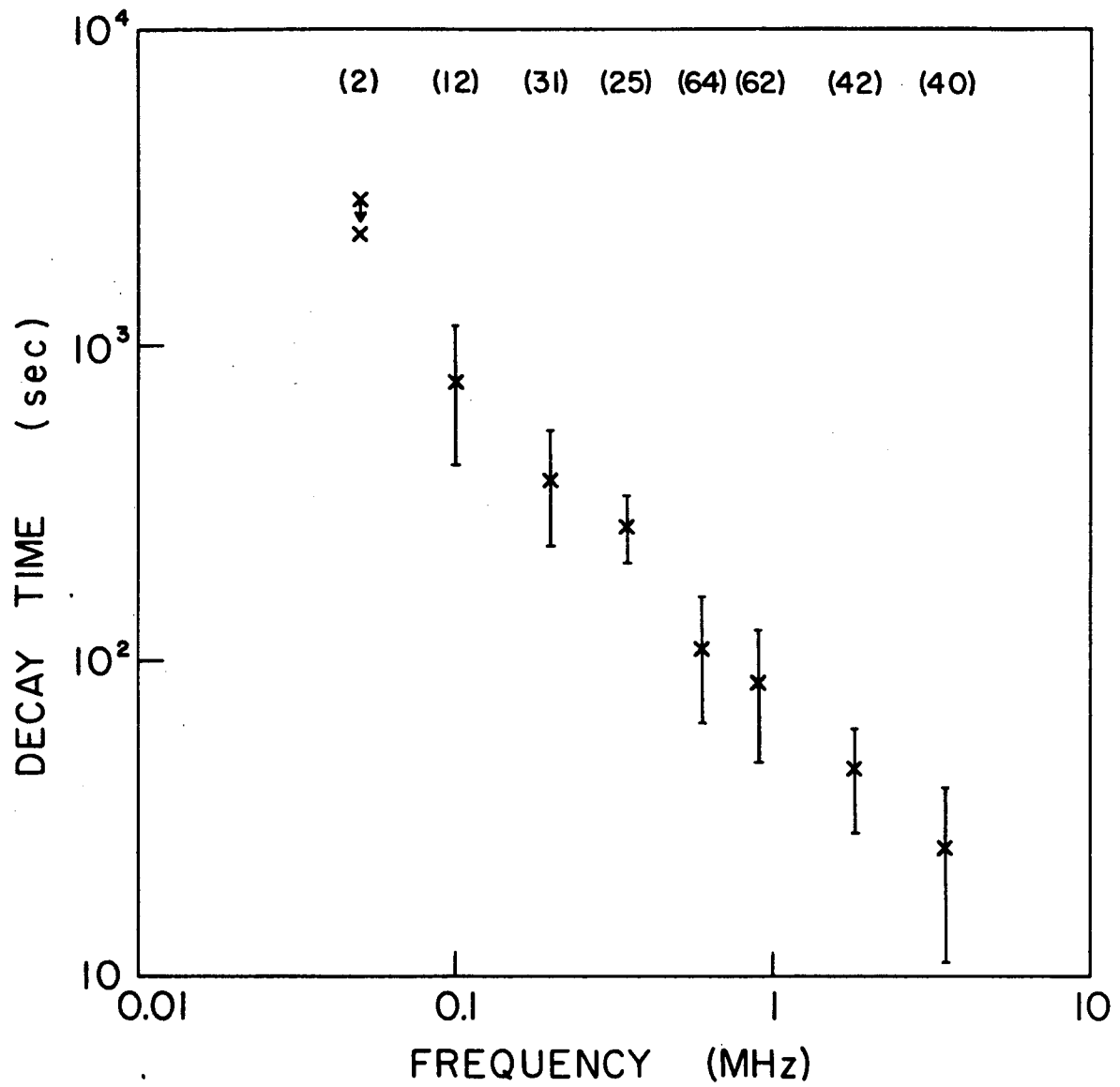
FIG. 4.35 DECAY TIMES OF TYPE III BURSTS OBSERVED BY OGO-V.
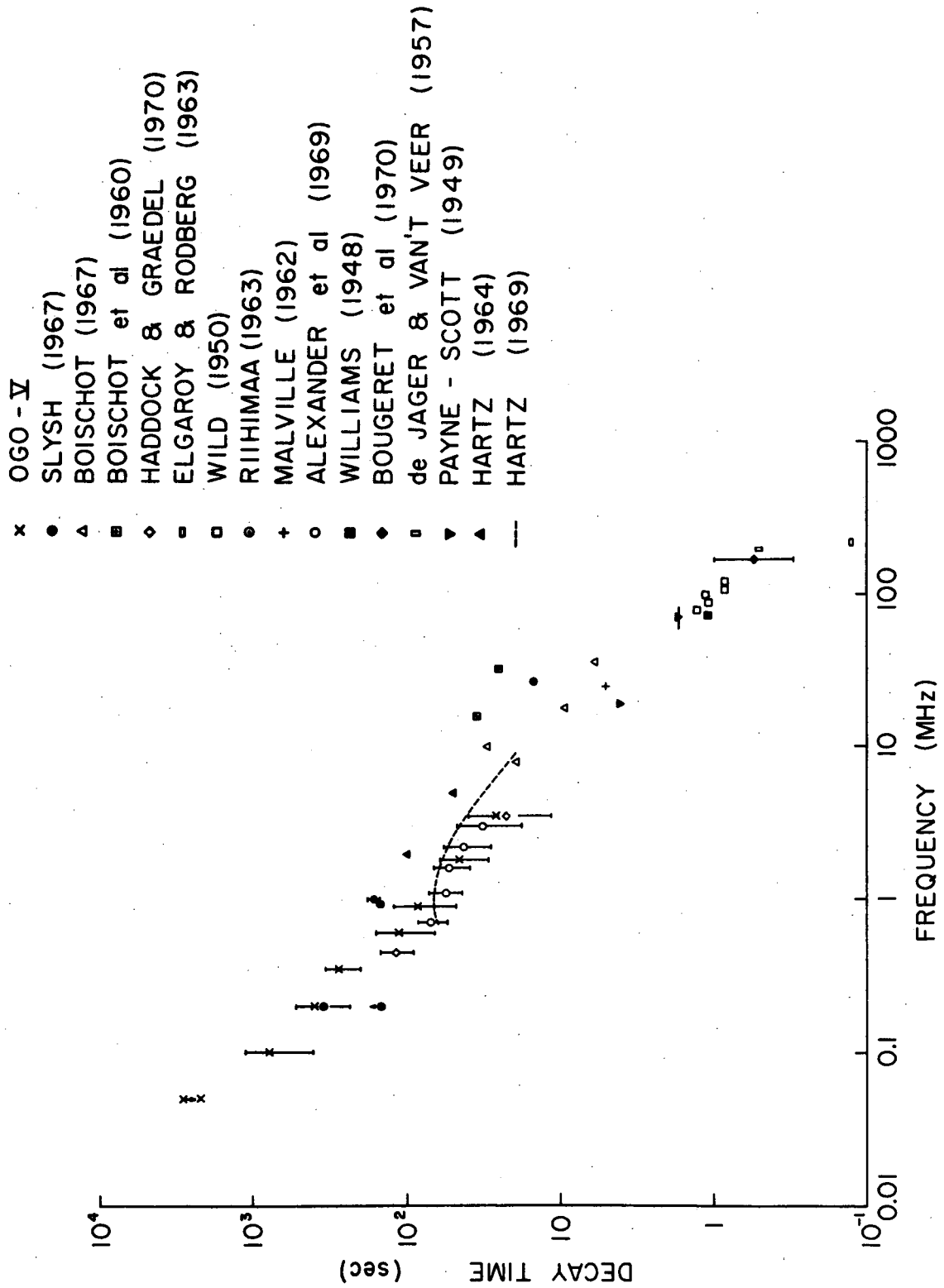
FIG. 4.36 DECAY TIMES OF TYPE III BURSTS.

where $\tau$ is in seconds and $f$ in Hz. It is interesting to note that Wild (1950b), observing between 80 and 120 MHz, fitted a line

$$\tau f = 10^8 \quad ,$$

that is, practically the same. As Bracewell pointed out in the discussion of the paper by Alvarez and Haddock (1971), this means that it requires $10^8$ cycles of the radiated waves for damping to occur, independently of frequency or plasma density.

In order to study the experimental results, we have obtained the decay times $\tau_c$ due to Coulomb ion-electron collisional damping derived from some theoretical solar wind models. $\tau_c$ is defined by

$$\tau_c = \frac{1}{\nu} \tag{4.22}$$

and $\nu$ is given by Eq. (4.20). Figure 4.37 shows $\tau_c$ for two solar wind models and one solar streamer model; it also shows the measured $\tau$ that, as we said, constitutes at best upper limits. The increase in the disagreement with diminishing frequency is obvious and at 1 MHz the difference is of one order of magnitude. It is interesting to observe that the variation of $\tau_c$ with frequency is similar in the three theoretical models in spite of the fact that Pneuman and Kopp's streamer (core) is very thin. We realize that actual Type III bursts may not occur in media given by these models. However, at the lowest frequencies, where the discrepancy is larger the bursts may occur in the solar wind rather than in well-defined streamers.

At 1 A.U. Whang et al. model gives $\tau_c = 18.4$ hours and Hartle and Sturrock's give an even longer time. This large disagreement could
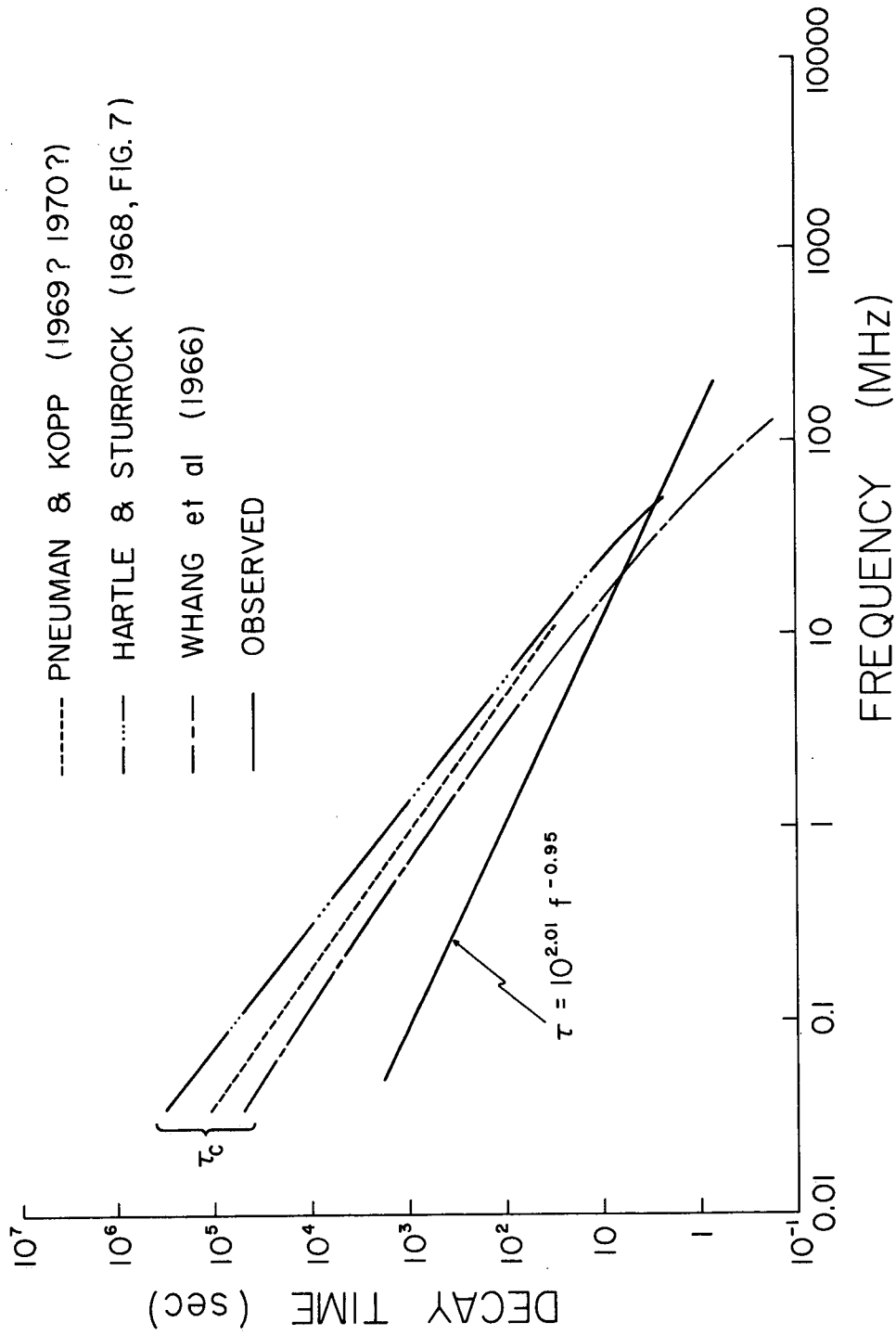
FIG. 4.37 COLLISIONAL DECAY TIMES OBSERVED AND CALCULATED FROM
THEORETICAL MODELS.

be explained by invoking additional damping to the ion-electron collisions

contribution (we will see shortly that this is what the solar wind

theoreticians have assumed.) We can think for example, of the dissi-

pative effect of turbulence in the local plasma of either a permanent

nature or a transient character and perhaps produced by the passage

of the exciter particles. The time profile may be sensitive to the

efficiency of the coupling between plasma waves and electromagnetic

waves. This efficiency could perhaps be altered by the passage of the

exciters particles. Figure 4.37 indicates that whatever the source

of the additional damping, it increases with decreasing frequency. It

would be important to measure the times of decay with better time

resolution in well identified fundamental and second harmonic emission.

4.4.2 The Temperature of the Corona. The problem of the

determination of the coronal temperature has proven to be more complex

than that of the coronal density. Like density, the temperature has

only been measured near the Sun and near the Earth. It has been well

established that the temperature near the base of the corona ranges

between $7.5 \times 10^5$ and $4.5 \times 10^6$ K, and the values are evidently

influenced by the method used for the determination, Billings ( 1966),

Zirin (1966), Rosh (1967).

The temperature near the Earth has been measured from

artificial satellites and space probes. The information from these

experiments has brought the necessity to modify some concepts that were

hitherto applied to the solar wind. For example, the solar wind cannot

be considered any more as a one-component fluid rotating and expanding

quietly but rather as a turbulent multiple-component fluid having important discontinuities and being continuously crossed by plasma waves.

The temperature of the protons was measured first. Due to the interplanetary magnetic field their random motions are not isotropic and it is necessary to speak of "transverse" ($T_{\perp}$) and "longitudinal" ($T_{11}$) temperatures; the so-called thermal anisotropy. Its magnitude is expressed by the ratio $T_{11}/T_{\perp}$ that is found to be near 2. Usually the proton temperature is given as a weighted mean $T = 1/3 \ (T_{11} + 2T_{\perp})$. The generally accepted value for the proton temperature in the "quiet" solar wind is $4 \times 10^4$ K. Values as high as $8 \times 10^5$ K have been obtained at times when the solar wind velocity was above its quiet value, Hundhausen (1968). The important point is that the assumption of isotropic Maxwellian distributions is not valid for the solar wind protons, Hundhausen (1968, 1970).

The problems involved in the observation of thermal electrons have been solved only recently. The electrical neutrality of the solar wind and the equality of flow speeds of electrons and protons are well established. The thermal anisotropy of the electrons is small, and much less than that of protons. Here again, the velocity distribution function of the electrons is not Maxwellian and seems to fit a bi-Maxwellian distribution except for a high-velocity tail that is usually present. The accepted mean electron temperature of the "quiet" solar wind is between $10^5$ and $1.5 \times 10^5$ K, Hundhausen (1970). Variations between $7 \times 10^4$ and $5 \times 10^5$ K have been observed in a two-month period,

Kavanagh et al. (1970). Usually the temperature of the electrons is about four times higher than that of the protons.

The theoretical treatment of the solar wind started with one-fluid models, for example, Noble and Scarf (1963) and Whang et al. (1966), and continued with two-fluid models, Hartle and Sturrock (1968), Cuperman and Harten (1971), and Wolff et al. (1971). The last three predict, to a different extent, electron temperatures higher than proton temperatures.

Because of these circumstances it seems logical to expect that the use of Eq. (4.21) to determine electron temperatures from radio observations at low frequencies would not give accurate values because the derivation of Eq. (4.20) assumes a Maxwellian distribution of velocities of electrons and colder protons. There are other arguments against this formula. For example, the ratio of the mean collision time for protons (or electrons) to the scale time for the coronal expansion, although very small near the Sun, becomes unity at about 0.13 A.U. (28 $R_\odot$). The ratio continues to increase with distance and beyond approximately 0.13 A.U. the plasma is essentially collisionless, Hundhausen (1968). Thus near 1 A.U. the electrons make about one collision per $10^5$ sec, for $N \approx 5$ $cm^{-3}$ and $T = 10^5$ K, while it takes the solar wind $3 \times 10^5$ sec to travel from about 0.1 to 1 A.U. The importance of the plasma-wave-particle interaction in the physical state of the coronal plasma has been discussed by solar wind theoreticians. This interaction produces plasma turbulence that in turn "provides a very local effective dissipation mechanism because the wave-particles scattering leads to an anomalous (low) electrical conductivity,"

Scarf (1970). This may be the way to increase the Coulomb collision frequency. Our results support this suggestion. As can be seen in Fig. 4.37 the predicted decay times are longer than the observed ones, that is, the predicted Coulomb collision frequencies are too small. This effect was considered in the two-fluid model of Cuperman and Harten (1971), who introduced an enhanced noncollisional coupling between the proton and the electrons to bring the theory into agreement with the observations near the Earth. This was expressed by taking, ad hoc, an effective collision frequency 30 times larger than the classical Coulomb collision frequency. Nishida (1969) had earlier used a factor of 10. The latest solar wind model, by Wolff et al. (1971), introduces a distance dependent coefficient to increase the collisional energy exchange between electrons and protons. Figure 4.38 shows Hartle and Sturrock's temperature model based on collisional coupling and that of Wolff et al. including enhanced noncollisional coupling. Observations are also included; the temperature near the Sun was arbitrarily placed at r = 1.

In Fig. 4.37 we can draw approximately a straight line through the low-frequency portion of the curve derived from the Hartle and Sturrock's model. Its equation is $\tau_c = 10^{12.71} f^{-1.58}$, where $\tau_c$ is in sec and f in Hz. If we call $\tau$ the observed decay time given by Eq. (4.21) then we can write the discrepancy in the following functional form:

$$\frac{\tau_c}{\tau} = 10^{5.00} f^{-0.63} . \qquad (4.23)$$
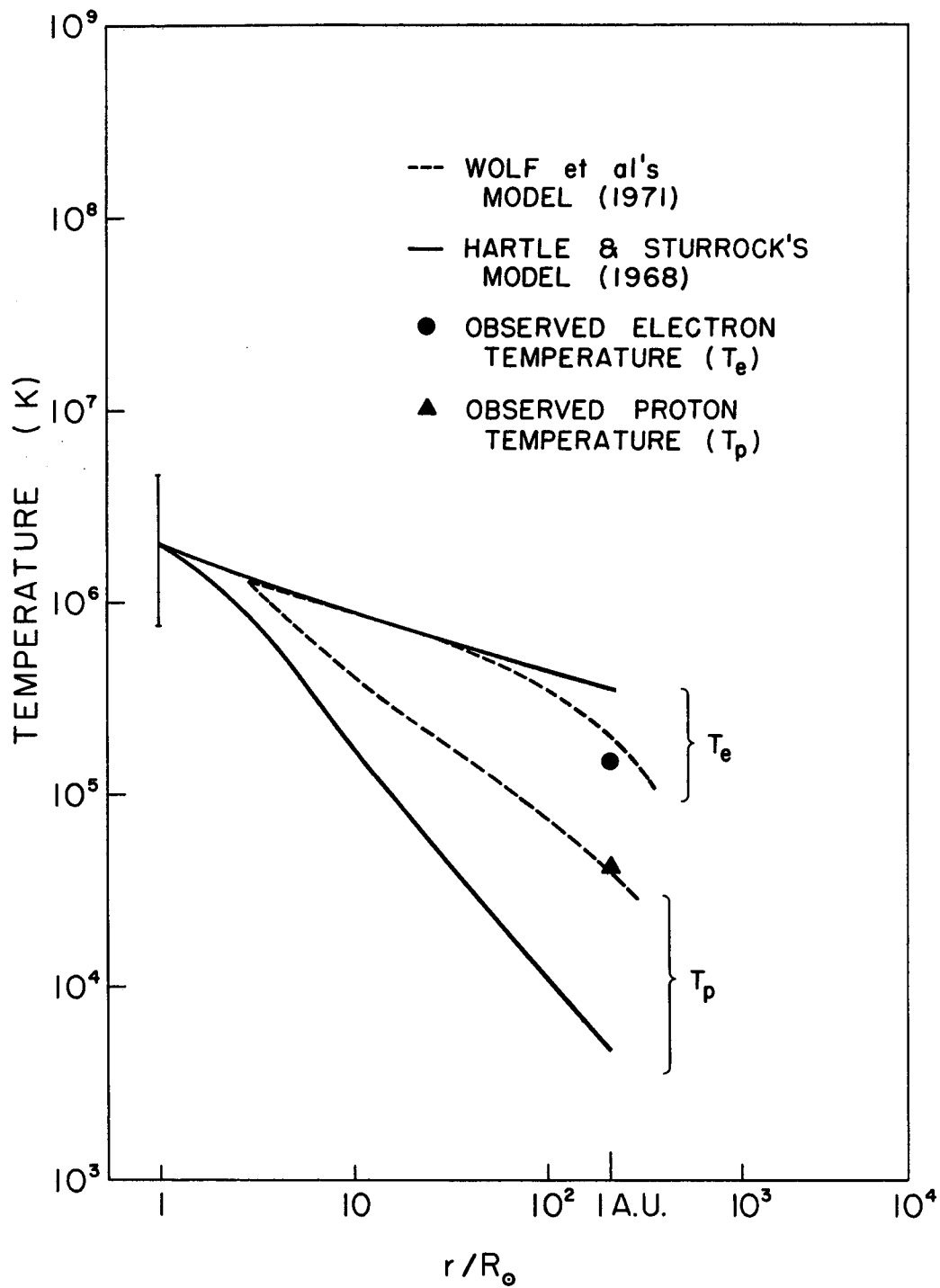
## SOLAR WIND TEMPERATURES

FIG. 4.38   OBSERVATIONS AND THEORETICAL MODELS OF SOLAR WIND

TEMPERATURE.

Using the local plasma hypothesis, Eq. (4.7), this equation can be rewritten as:

$$\frac{\tau_c}{\tau} = 10^{4.40} \, N^{-0.315} \, j^{-0.63} \quad , \tag{4.24}$$

where N is in $cm^{-1}$ and $j = 1,2$ for fundamental and harmonic, respectively. The distance dependence is determined by the electron density model chosen. Using for N the fitting given in Table 4.6 for Hartle and Sturrock's model we can write explicitly:

$$\frac{\tau_c}{\tau} = 3.3 \, r^{-0.71} \quad , \quad \text{for } j = 1 \quad , \tag{4.25a}$$

and

$$\frac{\tau_c}{\tau} = 2.1 \, r^{-0.71} \quad , \quad \text{for } j = 2 \quad . \tag{4.25b}$$

In their model Wolff et al (1971) increase the ion-electron energy exchange by assuming that the electrom mean free path is proportional to the reciprocal of the distance raised to an arbitrary power. This power was chosen so as to give the best agreement between the theory and the observations at the Earth, particularly of the proton temperature. In terms of our notation their law can be written as:

$$\frac{\tau_c}{\tau} = r^{-0.73} \quad . \tag{4.26}$$

Considering the uncertainties in the measurements of temperatures and in our determination of decay times we believe that the agreement

between Eqs. (4.25) and (4.26) is good. The comparison of Equation
(4.25) based on Hartle and Sturrock's model with Eq. (4.26) based on
Wolff et al. is valid because Wolff et al. reduces practically to
Hartle and Sturrock's when no corrections are made.

We observe that the second harmonic gives better agreement.

To summarize Section 4.4 we can say that we have shown in a
conclusive way, the failure of the pure collisional damping hypothesis
to explain the decay times of Type III bursts. Our results are consistent
with those found by solar wind theoreticians independently and by
completely different means. Both results complement each other because
one is valid near the Sun and at the Earth while ours is valid in a
continuous range of distance in between.

## 4.5  The Association with Other Solar Phenomena

The Type III solar bursts are usually associated, to a different
degree, with other manifestations of the solar activity. We will
briefly examine the association of the bursts analyzed in this work
with optical flares (Hα), x-ray flares, solar cosmic rays and radio
bursts observed from ground-based stations. Other correlations with
terrestrial effects, i.e., ionospheric disturbances, geomagnetic storms,
etc., will not be discussed.

### 4.5.1  Optical Flares (Hα). The association of Type III bursts
with Hα flares has special importance because, except for appropriate
radio observations, it is the only means known so far to establish
the approximate location of the exciter particles origin.

The association of enhancements of solar radio emission with solar flares was established by Appleton and Hey (1946). Specifically, an association of flares with Type III bursts was pointed out by Wild, Roberts and Murray (1954); afterwards it has been studied by several authors.

The subject can be studied in at least two respects: time of occurrence and position of the flare on the disk.

Temporal Association. In the study of the temporal association it is important to define the criterion of coincidence, especially the phase of the optical event considered as time reference. This is confusing in the literature because the different authors use a variety of phase references and not all flares exhibit the same phases. For example, the following terminology occurs in connection with this subject: puff, surge, spray, flash phase, explosive phase, flash-explosive phase, etc....

In order to study the correlation of our data with solar flares we used the tables of Confirmed Solar Flares compiled by the ESSA Research Laboratories (now NOAA) and published in the Solar-Geophysical Data. In only two cases (events No. 4 and 16) we used the Unconfirmed List. Reports of the same flare from different observatories are listed together in a group and average values for the group are given.

The time reference for the Type III bursts analyzed by us is the start time at 3.5 MHz. In most cases we found that a flare occurred close to our radio events. We compared the time of start of the radio event with two times associated with a flare: (a) with the closest

time of start within the group of observations and (b) with the average time of start of the group. The times in the ESSA lists are given to within one minute. We rounded the OGO-V data (usually measured to one-tenth of a minute) to the closest minute. The differences of time of start $t_{3.5} - t_{H\alpha}$ are then an integral number of minutes. In plotting their distribution we centered the one minute intervals of the histograms on integer numbers. Figures 4.39 and 4.40 show the distribution of the differences in time of start according to criteria (a) and (b), respectively.

Of the 64 radio events studied eight were not considered in Fig. 4.39; five occurred behind the limb (43, 53, 54, 55, 56), two (27, 47) did not have a reported flare during these hours and one (63) occurred 38 minutes after the closest flare. Two events (30, 46) were probably associated with $H\alpha$ flares already in progress when they were first observed. Evidence from x-ray flares supports the association so we decided to keep these two cases adopting the minimum value of the time difference. In Fig. 4.40 ten events were not included: The eight excluded from Fig. 4.39 and two (30, 46) for which the average of time of start of the $H\alpha$ flares was not available. Event No. 4 is probably wrongly associated because it is the one that departs the most from the general trend both in temporal (Fig. 4.39) as well as in positional association (Fig. 4.41). In addition, it is associated with an unconfirmed flare.

The statistics obtained from these figures are summarized in Table 4.23. We observe that most of the bursts occur after the optical
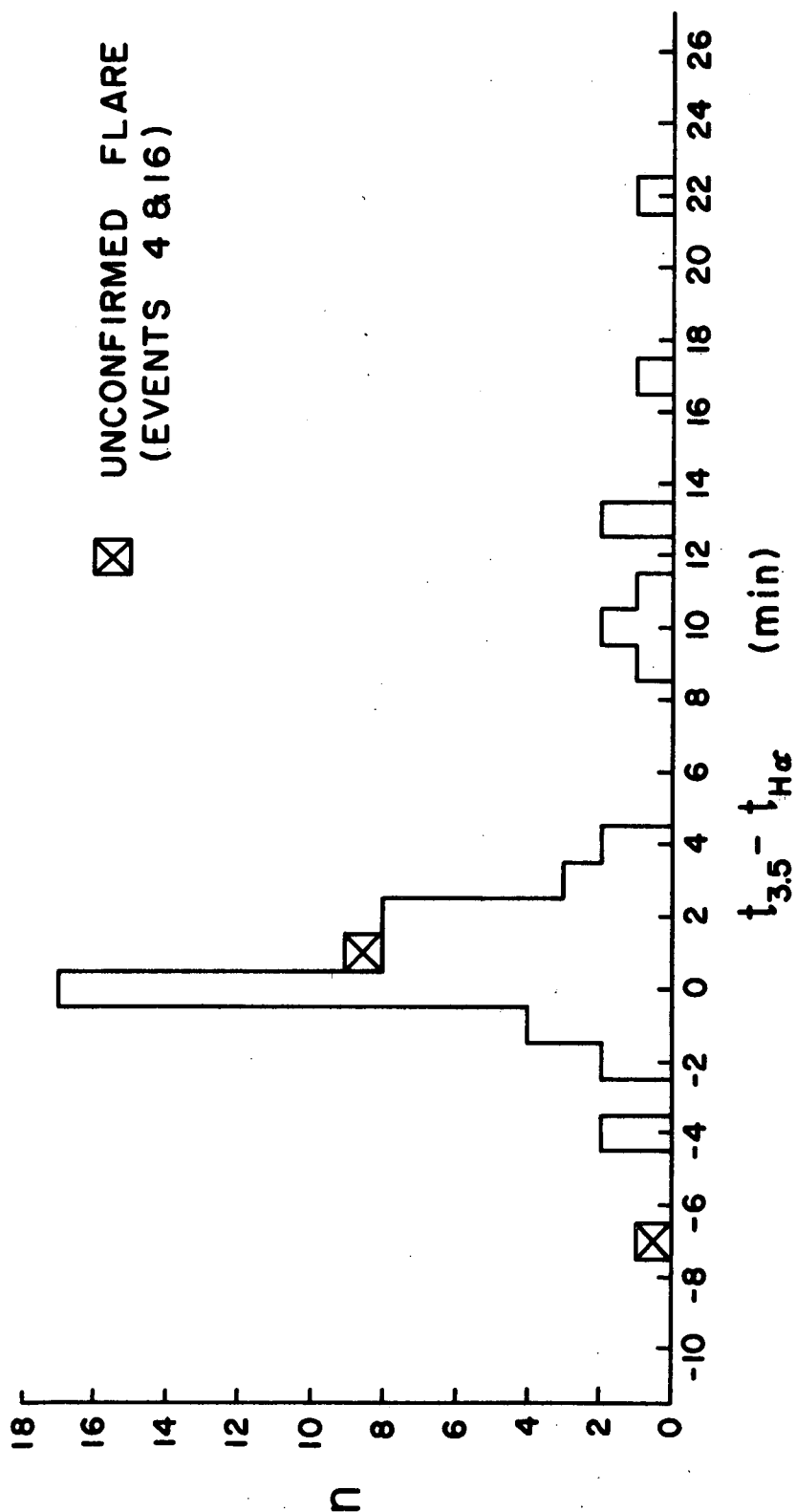
FIG. 4.39  ASSOCIATION OF TYPE III BURSTS OBSERVED BY OGO-V

WITH Hα FLARES WHICH OCCURRED WITHIN 25 min.

CRITERION (a).
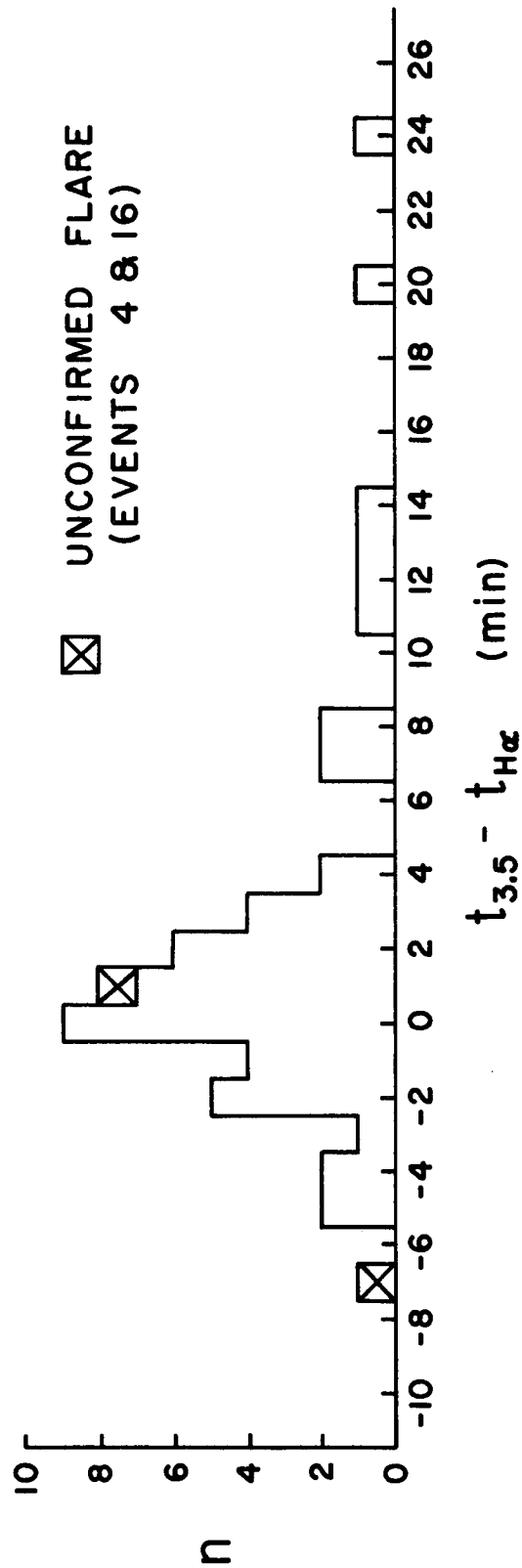
FIG. 4.40 ASSOCIATION OF TYPE III BURSTS OBSERVED BY OGO-V

WITH Hα FLARES WHICH OCCURRED WITHIN 25 min.

CRITERION (b).

flare and that a large percentage occur within 4.5 minutes of the

optical event.  The use of criterion (a) or (b) does not affect

appreciably the results.

Table 4.23

Temporal Association of the Type III Bursts Observed

by OGO-V with Hα Flares

(Number of Occurrence Are Expressed in Percentage)

| Criterion | $t_{3.5} - t_{H\alpha}$ (min) | | | | |
| --- | --- | --- | --- | --- | --- |
| | -8 to 0 | 0 to 25 | -2 to 0 | 0 to +2 | -4.5 to +4.5 |
| a | 31.3 | 68.7 | 24.1 | 38.4 | 83.0 |
| b | 36.1 | 63.9 | 20.4 | 28.7 | 76.0 |

For comparison we gathered in Table 4.24 the results of other

observers.  We should stress the fact that our results refer to very

intense radio events.  The data of at least three references relate

also to major radio events (Swarup et al., Boorman et al., Riihimaa).

Because of the different criteria used for coincidence it is

difficult to compare our results with those of other investigators.

Malville's criterion of Start ±2 min seems to be the closest to ours.

He found that 50% of the bursts were associated with flares.  Our

results for the condition Start ±2 min (Table 4.23 columns 4 and 5) give

62.5% and 49.1%, depending on the criterion used.

The observed proportion of bursts preceding or following the

flare varies for different authors.  From Malville's figure 5 (1962c)

we see that 45% of the bursts preceded the onset of the flash phase

Table 4.24

Temporal and Positional Association of Type III Bursts with Hα Flares

| Type III Bursts Assoc. with Flares (%) | Flare Assoc. with Type III Bursts (%) | Criterion for Coincidence | Asymmetry (Preferred Half Disk) λ* | Asymmetry (Preferred Half Disk) δ | Remarks | Freq. Range (MHz) | Period of Observation | Author |
|---|---|---|---|---|---|---|---|---|
| 60 to 70 | 23 to 30 | Flare period ±2 min | E | -- | | 40-240 | Nov. 1955-July 1956 | Loughead et al. 1967 |
| | 67 | Time of "puff" ±2 min | -- | -- | | 40-240 | 1956-1957 | Giovanelli, 1958,59 |
| 92 | 20 to 22 | Lifetime ±5 min | E | none | | 48-165 | Oct. 1958- | Rabben 1960a,b |
| 72 | 20 to 22 | Lifetime ±0 min | | | | 48-165 | Dec. 1958 | |
| 20 to 30 | 25 | Flare period ±0 min | E | -- | Groups of strong bursts | 100-580 | Oct. 1956 Sept. 1957 | Swarup et al. 1960 |
| | | | none | N | Major radio events | 25-210 | Sept. 1952-Sept. 1960 | Boorman et al. 1961 |
| 97 50 36 | | Flash phase ±2 min Start ±2 min Maximum ±2 min | none | | | 8-40 | Aug. 1959-Jan. 1961 | Malville 1962c |
| | 30-57 | Flare Lifetime | | | | | | |
| 16-27 | 13.7 | Growing phase ±2 min | -- | -- | | 169, 100-580 | Mar. 1959 June 1960 | Simon 1962 |
| | 37 | Flare lifetime | E | ? | Major radio events | 27 | Oct 1960-Nov 1961 | Riihimaa 1963 |
| 70 | | Flare maximum ±10 min | -- | -- | | 2-4 | June 1966-Sept 1967 | Graedel 1970 |

λ* = longitude

δ = latitude

at most by 1.5 minutes while 37% followed it within 1.5 minutes.  This agrees with Graedel (1970) who found that on the average a burst preceded the reported flare maximum by 1.45 minutes.  Our data indicate, that on the average a burst follows a flare (column 3 of Table 4.23, Figs. 4.39 and 4.40).  This agrees with Swarup et al. (1960) who found that most of the bursts occur after the flare start, and also with Riihimaa  (1963) who found that 7 out of 11 radio bursts occurred between the onset and maximum of the flare.

Positional Association.  Before solar bursts were classified into different types Hey, Persons and Phillips (1948) found that radio bursts at 73 MHz had a tendency to be associated with flares occurring on the eastern half of the solar disk.   Hey and Hughes (1955) gave evidence that not only the radio but also the Hα radiations were more intense on the eastern than on the western half of the disk.  This effect is referred to as the East-West Asymmetry.  Table 4.24 shows the results of all the studies we could find in the literature regarding the association of Type III bursts with the position of the flares.  The asymmetry in the distribution of the burst-associated flares may be only an effect due to the asymmetry in the distribution of flares.

In order to analyze the OGO-V data we plotted the frequency distribution of burst-associated flares with respect to their central meridian distances.  We expressed this coordinate in degrees and grouped the events in intervals of 10° starting from 0°.  Flares for which any coordinate was a multiple of 10° were divided into two, each half being assigned to adjacent intervals.

We adopted three criteria for the selection of the radio events:

(A) We excluded all events not associated with a flare within 25 minutes of the radio burst and the five events (Nos. 43, 53, 54, 55 and 56) suspected to be associated with flares behind the West limb. (See Notes to Table A.2, Appendix 1.)

(B) The same as (A) except that we did not exclude the behind-the-limb events.

(C) We excluded those cases in Fig. 4.39 for which $|t_{3.5} - t_{H\alpha}| >$ 4.5 minutes or that were behind the limb. This rejected not only events No. 25, 47 and 63, but also Nos. 43, 53, 54, 55 and 56 (behind the limb) and Nos. 4, 15, 18, 24, 30, 39, 40, 41 and 52. See Fig. 4.41.

The radio data cover the periods 14 March to 25 April 1968 and 18 June 1968 to 19 February 1970. During this time there were 15 radio events observed down to or below 0.35 MHz that we did not analyze because they were processed after our stop date. During the above mentioned periods there occurred approximately 4600 Hα flares. The statistical results of the asymmetry found according to the different criteria are shown in Table 4.25.

Table 4.25

Hα Flares Occurred on the Western Hemisphere of the Sun

| Burst-Associated Hα-Flare* | | | All Hα Flares |
|---|---|---|---|
| Criterion A | Criterion B | Criterion C | |
| 65.2% | 68.1% | 65.0% | 48.7% |

*The association refers to Type III bursts observed by OGO-V.
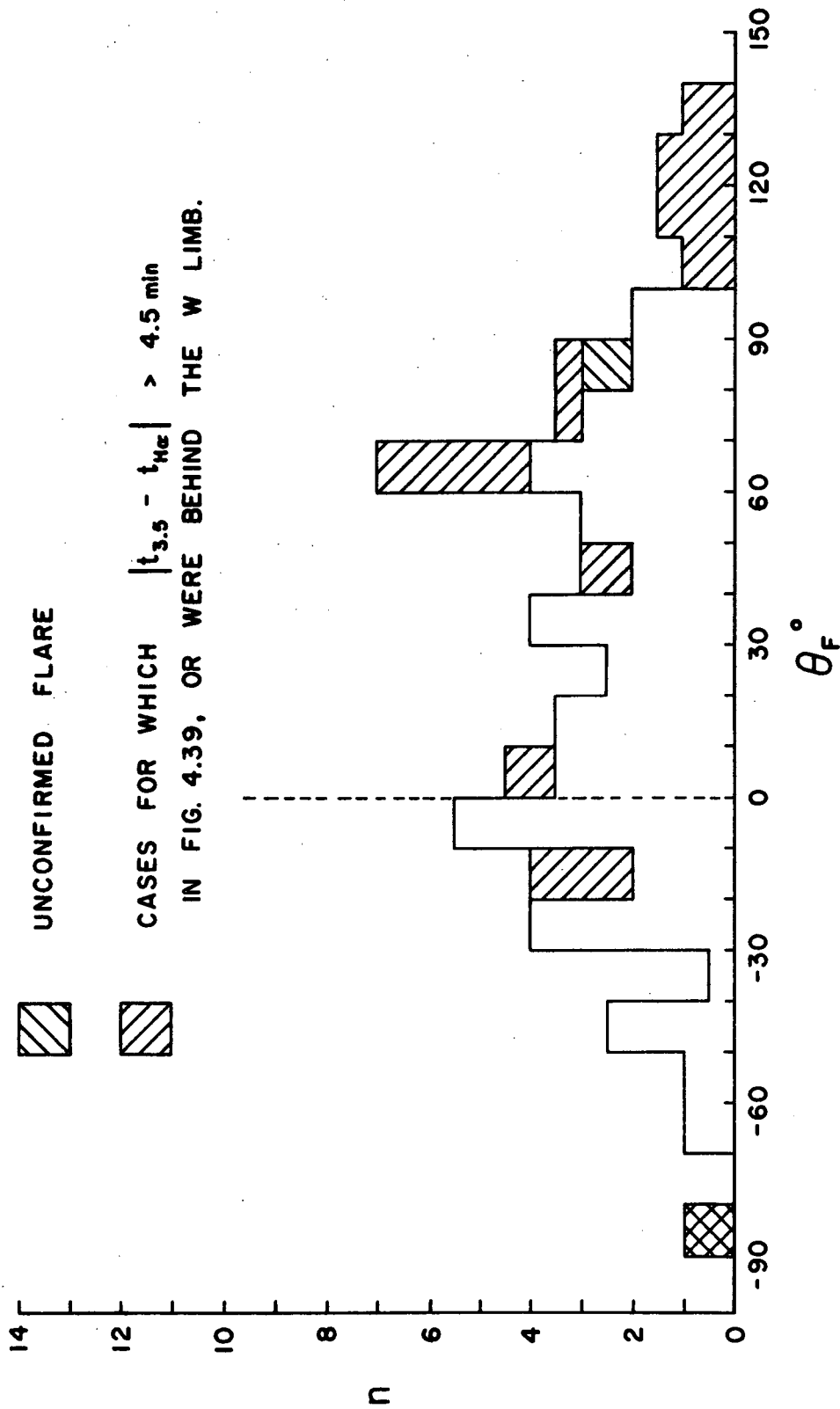
FIG. 4.41   DISTRIBUTION IN LONGITUDE OF Hα FLARES KNOWN OR SUSPECTED
TO BE ASSOCIATED WITH TYPE III BURSTS OBSERVED BY OGO-V
WITHIN 25 min.

The burst-associated Hα flares exhibit a predominance on the western hemisphere even though the total number of Hα flares shows a slight deficit in that hemisphere. We observe that the use of different criteria of choice practically does not affect the results.

The average $\bar{\theta}_F$ and standard deviation σ of the distribution of the burst-associated flares in longitude of Fig. 4.41 are given in Table 4.26.

### Table 4.26

Distribution in Longitude of Burst-Associated Hα-Flares

| Criterion | $\bar{\theta}_F^{\circ}$ | $\sigma^{\circ}$ |
|-----------|------|------|
| B | 30 W | 51 |
| C | 22 W | 43 |

These results are the opposite of what has been found from ground-based observations, as can be seen in Table 4.24. To explain this difference it could be argued that the OGO-V results refer only to very strong events and therefore are not directly comparable with the others, however, the asymmetry found by Swarup et al.(1960) and Riihimaa (1963) refer also to major radio events.

The effect also seems to be independent of the phase of the solar cycle. In fact the ground-based observations reported in Table 4.24 were obtained during the cycle N°19 that began as a minimum on April 1954 and reached the maximum around December 1958. We do not have an explanation for this western hemisphere predominance.

A north-south asymmetry seems to exist also, but it has been less studied. Figure 4.42 and Table 4.27 show our results that indicate
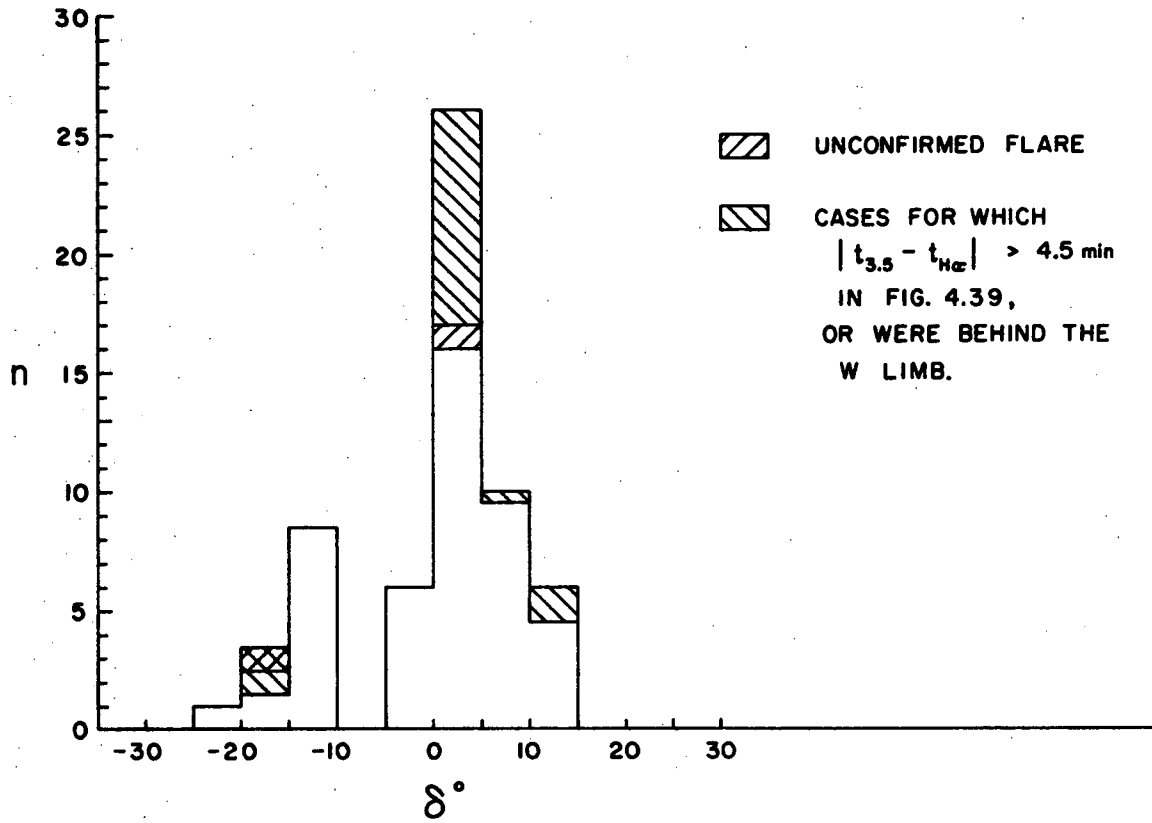
FIG. 4.42 DISTRIBUTION IN LATITUDE OF Hα FLARES KNOWN OR SUSPECTED TO BE ASSOCIATED WITH TYPE III BURSTS OBSERVED BY OGO-V WITHIN 25 min.

a high concentration of burst-associated Hα flares on the northern
hemisphere. During the same period the predominance of all Hα flares
was also high there. The concentration of the burst-associated Hα flares
in two bands of latitude as seen in Fig. 4.42 is not unexpected because
the same phemonenon is characteristic of sun spots.

The data of Boorman et al. (1961) indicates a northern
predominance of burst-associated Hα flares but we do not know the
distribution of all flares during the period of observation. Riihimaa
(1963) reports north-south asymmetry without mentioning which hemisphere
was the preferred one.

This north-south asymmetry was observed also by Harvey and
Bell (1968), who found that the percentage of microwave bursts associated
with the northern hemisphere exceeded substantially what was expected
from the asymmetric distribution of all flares. The data analyzed by
them covered the period June 1957 to December 1960.

We searched unsuccessfully for a correlation between the
distribution in latitude of the burst-associated flares and the position
of the Earth with respect to the solar equator.

Table 4.27

Hα Flares Occurred on the Northern Hemisphere of the Sun

| Burst-Associated Hα-Flare* | | | All Hα Flares |
|---|---|---|---|
| Criterion A | Criterion B | Criterion C | |
| 76.8% | 78.7% | 78.7% | 63.0% |

*
The association refers to Type III bursts observed by OGO-V.

4.5.2 X-Ray Flares. In order to study the association of our Type III events with x-ray flare events we have used the data on Outstanding Events observed from a spacecraft by the University of Iowa (UI) or by the National Research Laboratory (NRL) when the first were not available. These data are published in the Solar-Geophysical Data, ESSA (now NOAA). The list of outstanding x-ray events is given in Table A.4, Appendix No. 1.

The time reference for the Type III bursts is again the onset of the 3.5 MHz burst. The reference for the x-ray flares is their time of start. The distribution of the differences in time of start is shown in Fig. 4.43, where we have considered only differences with absolute value less than 25 minutes. The results indicate that out of 64 radio events 40 (62.5%) were associated with x-ray flares. In approximately 31 of these 40 cases (77.5%) the radio bursts followed the x-ray, and the most frequent delay was between 1.5 and 2.5 minutes. This was close to the results of Teske et al. (1971) who found that on the average the soft x-ray rise began 1.4 minutes before the Type III bursts in the metric and decametric range. In 25 out of the 40 cases (62.5%) the radio bursts and the x-ray flares were separated by 4.5 minutes or less.

We have studied the positional association of x-ray flares with our Type III bursts. For this we have had to use the association of Hα-flare with the Type III bursts as an intermediate step.
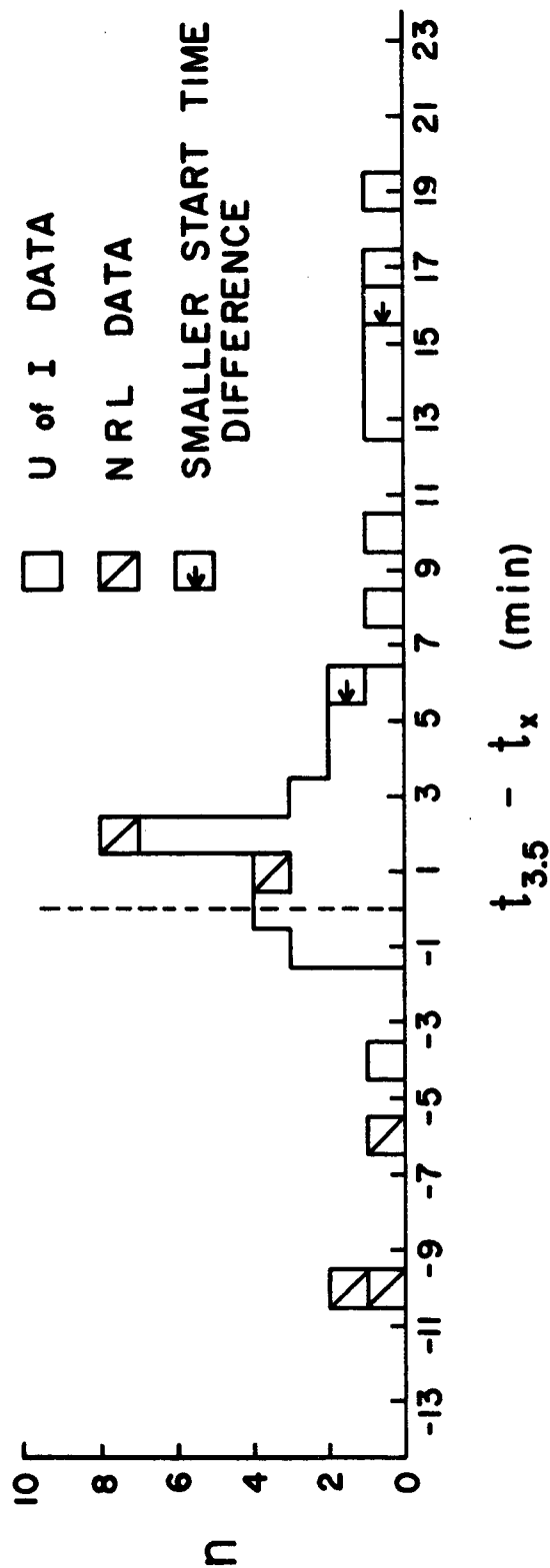
FIG. 4.43 ASSOCIATION OF TYPE III BURSTS OBSERVED BY OGO-V WITH X-RAY FLARES

WHICH OCCURRED WITHIN 25 min.

In order to have two degrees of reliability in the temporal association we have adopted the criteria (A) and (C) used in the analysis of Hα flares, Section 4.5.1. Figures 4.44 and 4.45 show the results according to criterion (A) and (C), rexpectively. We observed that some of the Hα flares did not have an associated x-ray flare and, conversely, that two x-ray flares are not accompanied by Hα flares. In these last two cases the active regions of origin were behind the west limb. It is interesting that the radiation in the optical range was not visible when the flare was behind the limb but the x-ray radiation was detectable. The explanation is that the source of x-ray must be high enough over the photosphere. Teske et al. (1971) have studied the occurrence of Type III bursts accompanied by soft x-radiation in the absence of Hα flares. They considered it as a phenomenon resulting from a physical process and not from the geometry of behind-the-limb events. The real situation may probably involve both.

The presence of an asymmetry in Figs. 4.44 and 4.45 is obvious. The results of the analysis are shown in Table 4.28 and 4.29.

Table 4.28

Type III Bursts Associated with X-Ray Flares

Occurred on the Western Hemisphere of the Sun

| Criterion A | Criterion C |
|---|---|
| 70.0% | 73.2% |
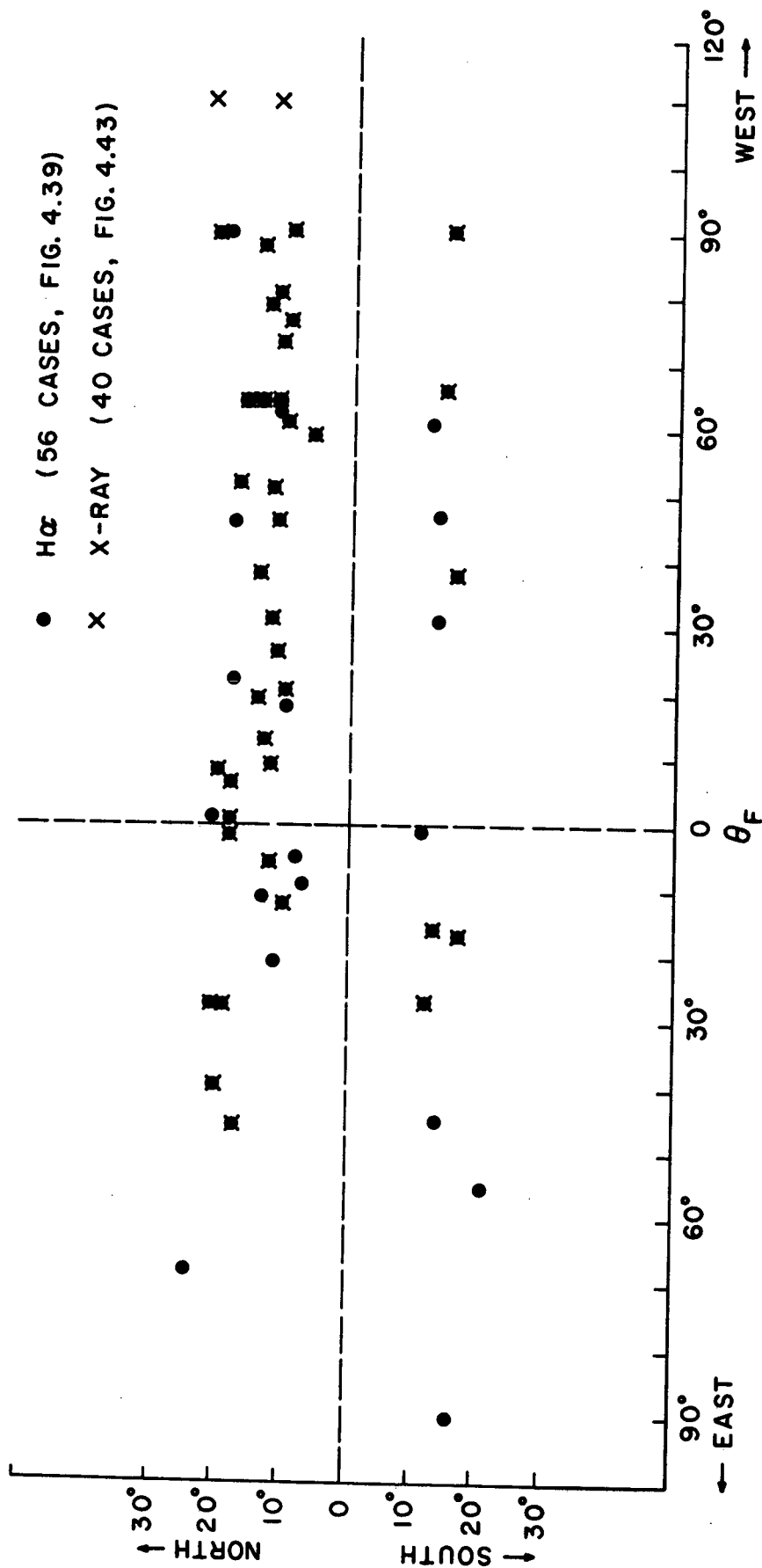
FIG. 4.44  POSITIONAL DISTRIBUTION OF SOLAR FLARES STARTING WITH

25 min FROM THE 3.5 MHz BURSTS.  CRITERION A.
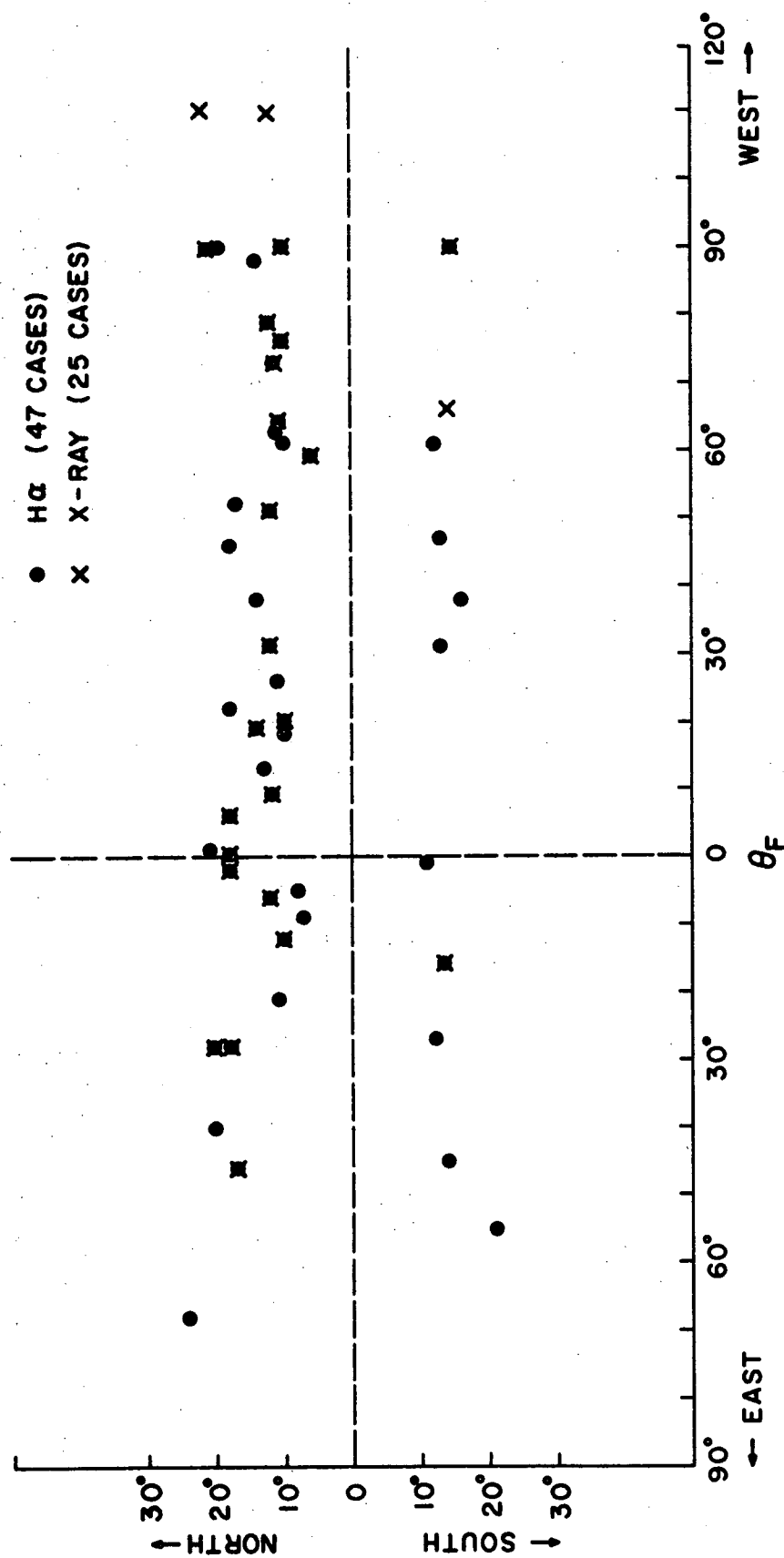
FIG. 4.45  POSITIONAL DISTRIBUTION OF SOLAR FLARES STARTING WITH

4.5 min FROM THE 3.5 MHz BURSTS.  CRITERION C.

Table 4.29

Type III Bursts Associated with X-Ray Flares

Occurred on the Northern Hemisphere of the Sun

| Criterion A | Criterion C |
|:---:|:---:|
| 84.0% | 85.0% |

Comparing these results with those in Table 4.25 and 4.27 we observe that the preference for the west and for the north seems to be more marked for the x-ray flares than for the Hα flares, however we cannot make a definite statement because we do not know the distribution in position of all the x-ray flares. As in the case of Hα flares, a change in criterion does not appreciably change the statistical results for the x-ray flares. The more rigorous conditions tend to accentuate the asymmetry slightly.

4.5.3 High-Energy Particles. These particles are generated during or after Hα flares and fall under the general designation of solar cosmic rays. The main components are protons and electrons with energies of approximately $\gtrsim 1$ MeV and $\gtrsim 40$ KeV, respectively. These particles have been classified in the literature according to their energy E as cosmic rays or relativistic particles ($E > mc^2$) and as subcosmic or nonrelativistic ($E < mc^2$). The latter have been in turn subdivided into "fast" and "slow."

The association of solar bursts in the metric range with energetic solar particles seems to have been first recognized in connection with radio bursts of Types II and IV (Maxwell et al., 1964). With the advent

of artificial satellites in the last decade it has been possible to detect these particles directly. This is of special interest to the understanding of the mechanism of generation of Type III bursts because, as we have seen in Section 4.3.4, the nature of the exciter particles is not definitely known. It is generally accepted however, that they are either protons or electrons. The ranges of their energy correspond to the ranges of velocity determined for the exciters particles. A velocity range between 0.05 and 0.87 c corresponds to protons with energies between 1 MeV and 1 GeV, and to electrons between 1 KeV and 400 KeV.

The observations of the solar cosmic rays have shown that they are guided by the interplanetary magnetic field. It seems logical to assume then that the field also guides the Type III exciter particles, therefore they would be expected to travel along a spiral path. Observations of Type III bursts at very low frequencies ($\leq$ 50 KHz) are especially important because the sources may be close to 1 Astronomical Unit and the times of arrival of the bursts can be compared directly with those of the energetic particles detected at the Earth. If the exciter particles are identified in a particular instance then their velocities would be known. Ideally we could then work a fitting process similar to the one described in Section 4.2.5 to determine velocities except that now it would be inverted: instead of having the electron density model fixed and the velocity as a variable parameter we could have the predictions of times of arrival for fix velocities and variable electron density models. In practice we should

be warned against delays in time of arrival due to propagation effects that can make the identification uncertain, McCracken (1969).

The fact that Type III bursts can be continuously followed as soon as they leave the Sun, makes them valuable to settle questions regarding the origin of the two species of particles and the difference in the characteristics of their propagation, as discussed by Lin and Anderson (1967). As a consequence they should be valuable also in the study of flare mechanisms or post-flare particle acceleration mechanism.

In this section we will briefly study the correlation of particles events with Type III bursts observed by OGO-V.

Solar Protons. The phenomenon of interest here is the arrival at the Earth of clouds of energetic solar protons. We will refer to them as "solar proton enhancements" to differentiate from the so-called "Solar Proton Events." This latter name has been given in the literature to extremely complex solar events involving the occurrence of a wide range of phenomena, solar and terrestrial. During the period analyzed here the Solar-Geophysical Data, ESSA, (now NOAA), gives provisional data for four Solar Proton Events:  31 October to 3 November 1968; 18-20 November 1968; 25 February to 1 March 1969; 30 March to 2 April 1969. We shall not study these events in detail.

In the study of solar cosmic ray protons we have used the data of the experiment that John Hopkins University and the Goddard Space Flight Center had on Explorer 34 and have on Explorer 35. The detector has three windows with energies greater than 60, 30 and 10 MeV. The information is also published in the Solar-Geophysical Data.

The data are given in the form of hourly averages and thus are not accurate enough to study differences in times of arrival. Our criterion for association is necessarily a loose one. We rounded the time of start of the radio event to the closest hour, and then selected those radio events that preceded the particle event by at most 3 hours, or that occur while the particle event was in progress. It takes these enhancements hours or days to decay and this makes it more difficult to establish an association. The solar proton cosmic ray events selected in this way correspond to what the solar particle investigators call "prompt" event, Lin and Anderson (1967). The length of the spiral path between the Sun and the Earth orbit that we have adopted (see Section 4.2.2) is approximately 1.3 A.U. This distance is traveled in about 22.0 and 12.5 minutes by particles with velocities of 0.05c and 0.89c, respectively. During the time between events No. 44 and 59, there were no solar proton observations. Out of the 48 radio events that occurred during proton-monitoring time 27 (56%) were temporally associated with proton enhancements: 13 (27%) preceded them and 14 (29%) occurred while the particle event was in progress. The positional distribution of the radio events possibly associated with proton enhancements is shown in Fig. 4.46. From this figure we deduce that 29.5 out of 43 (65.6%) Hα flare-associated radio events occurred on the western hemisphere while 29 out of the 27 (74.0%) radio events associated with solar protons occurred on that hemisphere. With respect to the north-south distribution the situation is as follows: 32 out of 43 (74.5%) Hα flare-associated radio events occurred on the North

C.5
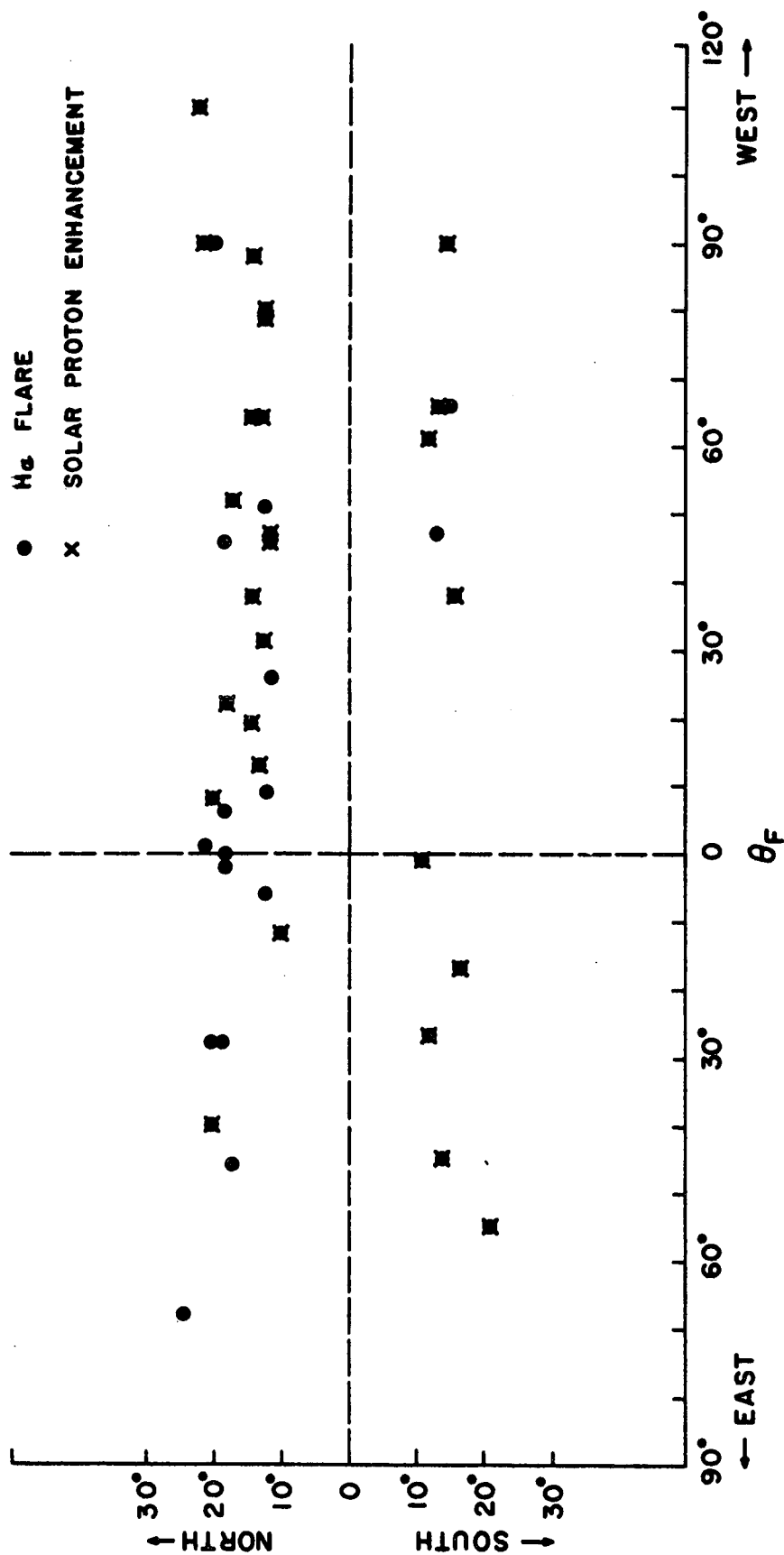
FIG. 4.46  POSSIBLE ASSOCIATION OF TYPE III BURSTS OBSERVED BY OGO-V

WITH SOLAR PROTON ENHANCEMENTS.

while 18 out of the 27 (64.2%) radio events associated with solar

proton enhancements occurred on that hemisphere. We do not know

what was the distribution of all solar proton enhancements.

Solar Electrons. Anderson and Winckler (1962) detected an

important x-ray event, and though they did not measure high-energy

electrons, they implied that electrons associated with the x-ray flare

were also responsible for the Type III radio bursts. Direct

measurements of the solar cosmic ray electrons with $E \gtrsim 40$ KeV

supported the idea but in connection with solar radio bursts in general

(van Allen and Krimigis, 1965; Anderson and Lin, 1966).

The fact that flares producing solar electrons are usually

associated with Type III bursts was established by Lin and Anderson

(1967). However the influence of the association of solar electron

events with Type I bursts, on the distribution on the solar disk,

asserted by these authors, has been questioned by McCracken and Rao

(1970). Lin (1968) proposed an identification of solar electrons as

the exciter particles of Type III bursts. He found that out of 24

electron events with observational radio coverage, 20 (83%) were

associated with Type III bursts. The radio bursts were assumed to be

associated with the flare if they occurred within $\pm 2$ minutes of the

period between the start and maximum of the flare. He noticed that

the associated Type III bursts tended to be exceptionally intense

bursts. In a subsequent series of papers Lin found that the emission

of ~40 KeV electrons is a distinct phenomenon from the emission of

energetic protons and relativistic electrons. He proposed that low-energy

electrons ($E < mc^2$) are correlated with Type III bursts while protons are correlated with Type II and IV radio bursts (Lin, 1970a,b).

There are no systematic publications of data on solar cosmic ray electrons. The data that follow were obtained from a letter from R. P. Lin to F. T. Haddock (March 31, 1971). Lin examined the observations of electron events made from Explorer 35 and IMP-5 during the time covered by the 64 radio events analyzed in this work. In spite of the fact that he worked with preliminary radio data there are very few differences when using the final data. The final results are shown in Fig. 4.47. His criteria were as follows:

(a) A Type III burst was considered associated with an Hα flare if the burst occurred within $\pm 3$ minutes of the flare start to maximum.

(b) An electron event was considered to be associated with a Type III burst if the electron onset at 1 A.U. was within 40 minutes of the burst.

(c) The background radiation was considered too high and the comparison invalid if a flux of 10 electrons $cm^{-2}$ $sec^{-1}$ $sr^{-1}$ could not be observed above the background.

Out of 55 Hα flare-associated radio events, 26 (47.3%) were associated with electron events. Out of these 55, 38.5% occurred in the western hemisphere; 100% of the ratio bursts associated with electron events occurred on that hemisphere. The north-south distribution was such that 45 out of the 55 (81.8%) Hα flare-associated radio events occurred in the north while 24 out of the 26 (92.3%) radio bursts associated with electron events occurred on that hemisphere.
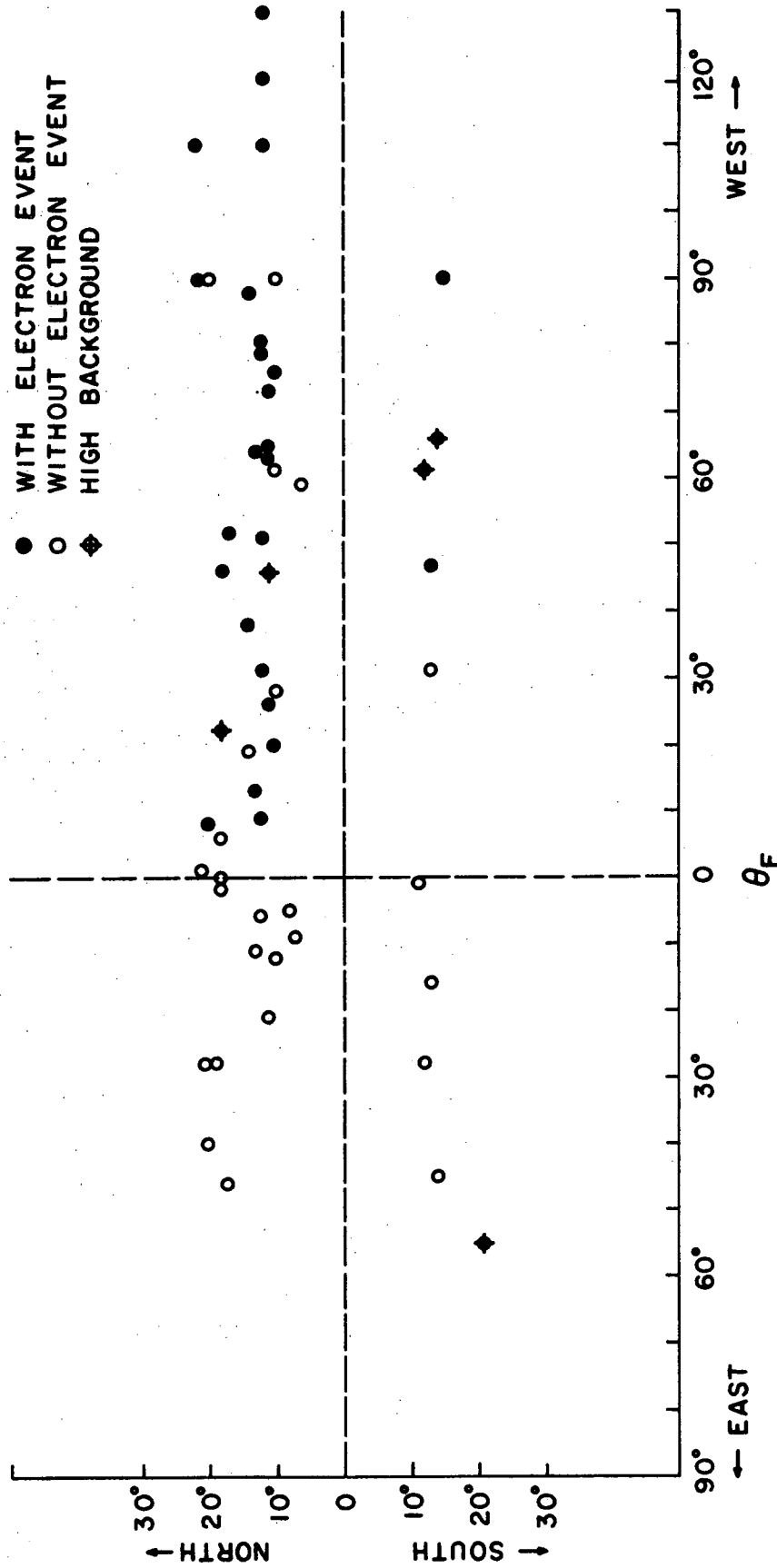
FIG. 4.47 ASSOCIATION OF TYPE III BURSTS WITH SOLAR COSMIC RAY ELECTRONS.

(ELECTRON DATA FROM LIN, 1971)

It is interesting to observe that all of the electron-associated bursts originated on the western hemisphere. This general effect could have been expected because of the guidance of the particles by the interplanetary magnetic field. In Fig. 4.47 we may interpret that the electrons produced in flares to the East of approximately 7° West of the solar central meridian are guided away from the Earth by the spiral field that does not hinder the radio emission. This limiting angle depends evidently on the tightness of the spiral and on the angular width of the cone of emission of the particles.

Of special interest is the association of four cases with origin located behind the limb. We saw in Section 4.5.1 that the two of them that were just over the limb (Nos. 43 and 53) were associated with x-ray flares. The one (No. 43) that occurred during time of solar proton monitoring was indeed associated with a proton enhancement.

4.5.4 <u>Ground-Based</u> <u>Radio</u> <u>Observations</u>. In order to find what type of radio emission accompanied our Type III bursts, we have used the information on spectral radio observations published in the Solar-Geophysical Data, ESSA; in the Geophysics and Space Data Bulletin, or in data sheets provided by Weissenau Observatory. The burst types as defined in the Solar-Geophysical Data are:

I: Storm bursts.

II. Slow-drift bursts.

III. Fast-drift bursts.

IV. Prolonged continuum.

V. Brief continuum (normally following Type III bursts).

CONT: Continuum in close association with Type III burst

storms, often with reverse drift bursts and often,

but not always, associated with noise storms on metric

wavelength (used by Boulder and Sagamore Hill).

UNCLF: Unclassified activity.

The sysbol U stands for a U-shaped burst of Type III.

The Table A.5 Appendix 1 shows the individual association of 60

out of the 64(93.8%) bursts observed by OGO-V that occurred during

ground-based patrol. Out of those 60 events 57 (95.0%) were accompanied

by activity observed from ground. Table 4.30 summarizes the results.

Table 4.30

Association of 57 Bursts Observed by OGO-V

with Ground-Based Radio Observations

| Ground-Based Observations | OGO-V Observations (%) |
|---|---|
| Type I | 15.8 |
| Type II | 38.6 |
| Type III | 98.3 |
| Type IV | 24.6 |
| Type V | 36.9 |
| CONTINUUM | 21.1 |
| UNCLASSIFIED | 15.8 |

The fact that 95% of the 60 events with ground-based coverage were

found to have high frequency counterparts is not surprising because

of the selection criterion.

We believe that the events No. 55 and 56 were not accompanied by activity observed from ground because they originated at about 120°, or further, west of the central meridian. The events No. 43, 53, and 54 are also believed to originate behind the limb but closer to it than the events No. 55 and 56. This may explain the fact that they were accompanied by high-frequency bursts observed from ground. From Table 4.30 we see that the most frequent type of the associated bursts is the type III, as could be expected.

# CHAPTER V.   DISCUSSION OF THE RESULTS

The purpose of this research was to analyze the data on solar radio bursts obtained by the OGO-V satellite. Since the wavelengths corresponding to our three lowest frequencies of observations exceed one kilometer, we have designated the bursts detected in those channels as kilometer-waves.

The data search covers approximately 9200 hours between March 1968 and February 1970. This period includes the maximum of solar cycle No. 20.

Our data have shown that the Type III bursts reach frequencies as low as 0.05 MHz. The high level of radio interference limited the number of events observed at that low frequency to one. The detection of this event has far reaching implications because it allowed for the first time the probing of the interplanetary space between the Sun and the Earth's orbit in an almost continuous way.

We concentrated on the study of 64 Type III solar radio events reaching frequencies equal or lower than 0.35 MHz. This selection criterion appears to have led to the choice of the most intense radio events. We measured times of start, times of decay and amplitudes of these 64 events. We also investigated various solar phenomenon associated with them.

The analysis of the frequency drift-rate led us to a simple empirical expression relating frequency drift-rate and frequency. In connection with this relationship we introduced the concept of

frequency drift-rate index. Combining our results with those of other observers we showed that the expression is valid between 550 and 0.075 MHz. Our formula is a generalization of that proposed earlier by Wild.

We developed a new technique to study the arrival times of the bursts. This consists in the prediction of arrival times at the Earth and the comparison with the observations. The predictions are based on several fundamental assumptions of which we will mention the most important. First, we have assumed that the bursts are emitted at the fundamental and/or second harmonic of the local plasma frequency. We considered that at present this is the best assumption. Second, we assumed that the exciter particles travel with constant velocity along an Archimedes spiral situated on the plane of the ecliptic. The constancy of the velocity seems to us the most tenable hypothesis at the present time; we have not found evidence strong enough to reject it. The adopted shape of the trajectory seems reasonable in view of the results of studies of solar high-energy particles and the solar wind. For simplicity we assumed that the trajectory lies in the ecliptic. We have found no evidence in favor or against this. The lack of good time resolution in the lowest frequency channels prevented us from detecting out-of-plane effects. Third, to have a self-consistent model we adopted an electron density distribution derived from the frequency drift-rate expression mentioned above and from some of the assumptions now under discussion. Also, the electron density distribution was chosen to fit the observations near the Sun and near the Earth. In this assumption we depart from the

current belief that the Type III bursts occur in dense solar streamers
and we assume that they occur in the solar wind itself, at least for
these low-frequency bursts. These two propositions may not be
incompatible because our results refer to distances from the Sun
larger than about 20 solar radii and the others refer to distances
in general less than that. Fourth, we disregarded the effects of
the coronal plasma on the propagation of the radio waves. This may
be the most debatable of our assumptions. We adopted it because of its
simplicity and because the changes in arrival times stemming from it
would be undetectable in our data due to the lack of good time resolution.
Finally, we did not consider the effects of magnetic fields except
for the guiding of the exciter particles along a spiral trajectory but
not spiraling about it. Again, this assumption was made to simplify
the analysis.

The use of the technique for determining the exciter particles
velocity revealed an unexpected preponderance of the second harmonic
emission below about 1 MHz. We found that as the frequency of
observation decreases the times of arrival of the bursts fits better
the arrival time of the second harmonic than that of the fundamental
emission. At 0.05 MHz about 100% of the radiation seems to be emitted
as second harmonic. This phenomenon practically doubles the distances
from the Sun at which the observed radiation was supposed to originate
and it places the source of the 0.05 MHz burst near the Earth's orbit.
The recognition of this phenomenon led us to derive velocities of the
same order as those measured from ground-based observations by direct
methods, without requiring models several times denser than the solar

wind. The distribution of the velocities has an average of 0.32c and a standard deviation of 0.09c. There is some suggestion in the distribution for two preferred ranges of velocities centered approximately at 0.18c and 0.36c.

We found a simple three-parameter formula to express the electron density of the solar corona as a function of distance from the Sun between approximately a few solar radii and the Earth's orbit. The parameters can be determined from the coronal electron densities near the Sun and the Earth, and from the measured frequency drift-rate index of Type III bursts. Incidentally, the formula can be used also with good approximation to fit optical determinations of electron densities in individual streamers.

The OGO-V Radio Astronomy experiment was not designed to measure absolute flux density values. However, by making certain approximations we attempted a study of the burst spectra. The basic assumptions were that the antenna-spacecraft structure behaves like a short center-fed dipole and that the bursts' radiation is unpolarized.

We found that, in general, the derived flux densities increase with decreasing frequency. The peak-power spectra usually exhibit one or two peaks. We suspect that the double peaks may be associated with the presence of second harmonic emission at lower frequencies and with directional effects at the emission or during propagation. We computed energy densities and found a function that fits approximately the average energy density spectra observed. This function is a generalization of that proposed previously by Wild. The measured flux densities and energies exceed by several orders of magnitude the

values obtained from ground-based instruments at higher frequencies.
The main peak of the few events studied appears to occur on the average
at about 0.3 MHz.

We measured the times of decay of selected bursts. The
measurements were made in idealized curves drawn through their complex
time profiles, without an attempt to separate fundamental from second
harmonic emission. We defined the time of decay at a certain frequency
as the time between the peak of the burst and one e-th of it,
regardless of whether the decay was exponential or not. Combining our
observations with others obtained at frequencies up to about 200 MHz
we established an empirical relationship between decay time and
frequency. This is practically the same that Wild found earlier in
the limited range between 80 and 120 MHz. At 100 MHz it takes a burst
about one second to decay while at 0.05 MHz it takes it about 1000
seconds. Our results confirmed the inadequacy of the proton-electron
collisional damping mechanism to explain the decay time of Type III
bursts at these low frequencies. Using radio observations in the
full frequency range available and our electron density models we
established an empirical expression according to which an _effective_
collision frequency must increase with distance to produce the observed
burst durations. This is approximately the same relationship that
theoreticians have required to make the theory fit the temperature
observations of solar wind protons and electrons near the Earth.

We studied the association of the kilometric-wave bursts
with Hα flares, X-ray flares, solar proton enhancements, solar electron
events, and ground-based observations. The two most interesting

results are: first, all of the bursts associated with solar cosmic ray electron events originated on the western solar hemisphere and second, the Type III solar bursts observed from OGO-V were associated with the flares occurring predominantly in the western solar hemisphere. This last result is opposite to the asymmetry found from ground-based observations at higher frequencies.

Our data indicate that the lowest frequency reached by a burst depends on the position of the exciter particles origin with respect to the Sun's central meridian. The further westward from the east limb that a flare occurs the lower is the lowest frequency observed. We have interpreted this either as a directional effect at the emission or as refractive effect during the propagation of the radio waves.

Our results on the prevalence of second-harmonic emission, on the times of decay, and on the flux densities may have important implications for theories of the emission mechanism of Type III bursts and of the propagation of the radio waves through the corona.

The consistency of our results, within the accuracy of the measurements, lends support to some of the assumptions made for the analysis, notably, the validity of the local plasma hypothesis, the contancy of the exciter particles velocity, and the spiral shape of their trajectory.

CHAPTER VI.   RECOMMENDATION FOR FUTURE ANALYSIS

The analysis of the kilometric-wave bursts observed by OGO-V suggests several topics for future investigation.   Some are refinements of the research presented in this work, others are new areas of study.

Except for problems of theoretical character most of the rest would require new instrumentation.   We estimate that a stepping radiometer like the one used in this research has much to offer yet, therefore we will not discuss other types.   We will assume that the instrument would be aboard a spacecraft stabilized in the same way as OGO-V.

The emphasis in a new instrument should be laid upon the following topics that will be discussed subsequently:

(a)   Higher time resolution,

(b)   A less noisy spacecraft,

(c)   Higher system sensitivity,

(d)   Selection of observing frequencies,

(e)   Bandwidth requirements,

(f)   Internal functions.

Conditions (a) and (b) would allow a better identification of the components of an event at the different frequencies especially with regard to the nature of the emission: fundamental at a certain frequency or second harmonic at that frequency.   A higher time resolution is needed mainly in the high frequency end, near 3.5 MHz,

-235-

where the time scale of the burst is still short. The accuracy in the measurements of the times of arrival could help in establishing whether the exciter particle trajectories are radial or spiral.

Conditions (b) and (c) would permit the detection of a large number of weak events down to the lowest frequencies. As we have shown, the spectrum drops rapidly below 0.1 MHz. It would be of interest to know to what extent, if any, the selection criterion used for OGO-V data affected our conclusions. Of special importance would be the possibility of working with less complex burst events, if the weaker bursts are indeed simpler. In our analysis complexity was a major source of confusion in the identification of components and modes of emission. Of particular interest would be the measurement of decay time of the radiation in the fundamental mode at a certain frequency and in the second harmonic mode at the same frequency.

Conditions (a) through (d) would allow a more accurate determination of the range of frequencies in which the predominance of the second harmonic sets in. It would be of interest to investigate if there is a correlation between these frequencies and the position of the associated flares. This might result in information regarding the directivity pattern at the emission or regarding refractive effects on the propagation of the radio waves.

The selection of frequencies, (d), may depend on the main objective of the experiment. For example, if we want to study the second harmonic prevalence we may want to have several channels more or less closely spaced in the upper half of the range, from 3.5 MHz to 0.35 MHz. Otherwise we may want to have them concentrated in other ranges.

Condition (e) refers to the possible need of a narrower receiver bandwidth at the lower frequencies, below about 0.1 MHz, if the time scale of the events at those frequencies is less than the time it takes the exciters particles to traverse the range of plasma frequencies determined by the extremes of the receiver bandpass. Measurement of the rise time of the bursts may give information about the ambient solar plasma and/or the spatial distribution of the exciter packet.

We could search for the possibility that the frequency drift rate depends on the intensity of the burst, as suggested by Rabben (1960b). We could test whether the lowest frequency observed in a burst is a function of the position of the associated Hα flare, as suggested by our results, and whether the suggestion of bimodality in the distribution of exciter particles velocities is real or not.

The most important function included in (f) is the inflight calibration. The OGO-V radiometer stability was better than expected, therefore a similar instrument would not need such frequent calibration which would reduce the probability of coincidence with a burst.

An improved radiometer would probably make it necessary to incorporate in the analysis refinements related to the effect of the solar plasma on the propagation of the radio burst radiation. This would improve upon the accuracy of the deduced velocities and would test the validity of the ideas proposed by other workers, for example, the "echo hypothesis."

So far we have assumed that the lowest frequency of observation is 0.05 MHz. A lower frequency would be better, especially if conditions (b) and (c) are fulfilled. In this range the bandwidth could become a problem because it should be narrow enough not to smear the time profiles.

Of special importance would be the study of those Type III events that reach 0.05 MHz or lower, and are associated with energetic solar particle events observed near the Earth by space instruments. A precise knowledge of the mode of emission, of the particle velocity and trajectory would allow the calculation of times of arrival of the particles at the Earth and the comparison with the direct detection of solar energetic particles. This would answer the question about the nature of the particles.

In dealing with individual events it would also be of interest to undertake a joint study of selected Type III bursts with a ground-based radio observatory that has the capability of measuring directly the velocities. This would give information about the coronal electron density distribution. For similar reasons it would be of interest to study individual events observed by OGO-V and other spacecraft that may provide supplementary information, for example, IMP-6.

The analysis in this study points out the need of theoretical work, especially in two areas. The first is an extension of the theory of Type III mechanisms down to very low frequencies. The theories should account for the second harmonic phenomenon and for the high intensities observed at very low frequencies. Of special importance

for the theories would be experimental measurement of the size of
the Type III sources, the scattering of the radiation, the absolute
or relative intensities of the radiation at the different frequencies
and modes, the energy  distribution of the exciter particles, etc.
The second area is the study of the mechanisms that shorten the decay
time of the bursts.  We have given quantitative information on an
effective collision frequency.  This should be combined with other
observations that give information concerning the size of the electron
density inhomogeneities or the state of turbulence of the solar wind.
For example, studies based on the occultation of radio sources by the
solar corona, on the observation of pulsars, and on radar observations.
As far as we know radio observations and deep space probes provide the
only means available today to study the corona between the Earth and
a few solar radii from the Sun.

Table A.1

List of Events Observed by OGO-V Below 0.6  MHz

| Event No. | Date | Time[1] (U.T.) | Lowest Frequency (MHz) | Spacecraft[2] Distance ($10^3$ km) | $\emptyset°$ | $\theta°$ | Note |
|---|---|---|---|---|---|---|---|
| 1 | 28 Mar. 1968 | 0321.0 | 0.1 | 54 | 253 | 54 | |
| 2 | 14 Aug. 1968 | 1323.0 | 0.35 | 140 | 173 | 31 | |
| 3 | 6 Sept. 1968 | 0916.6 | 0.35 | 149 | 143 | 39 | |
| 4 | 13 Sept. 1968 | 1302.2 | 0.35 | 109 | 120 | 50 | (3) |
| 5 | 26 Sept. 1968 | 1925.1 | 0.2 | 131 | 115 | 45 | |
| 6 | 27 Sept. 1968 | 1033.8 | 0.35 | 149 | 126 | 35 | (3) |
| 7 | 29 Sept. 1968 | 0929.6 | 0.1 | 129 | 112 | 46 | |
| 8 | 29 Sept. 1968 | 1621.4 | 0.35 | 145 | 118 | 41 | |
| 9 | 4 Oct. 1968 | 0000.7 | 0.1 | 47 | 52 | 60 | |
| 10 | 4 Oct. 1968 | 2122.0 | 0.35 | 145 | 113 | 41 | |
| 11 | 6 Oct. 1968 | 1723.8 | 0.2 | 72 | 77 | 57 | |
| 12 | 11 Oct. 1968 | 0306.3 | 0.1 | 113 | 123 | 22 | |
| 13 | 17 Oct. 1968 | 0816.4 | 0.2 | 106 | 85 | 51 | (3) |
| 14 | 23 Oct. 1968 | 2001.4 | 0.1 | 136 | 105 | 28 | |
| 15 | 27 Oct. 1968 | >1312.8 <1313.6 | 0.35 | 77 | 58 | 56 | (4) |
| 16 | 29 Oct. 1968 | 0953.9 | 0.2 | 103 | 107 | 19 | |
| 17 | 1 Nov. 1968 | 1659.7 | 0.35 | 69 | 46 | 58 | |
| 18 | 2 Nov. 1968 | 0949.6 | 0.35 | 141 | 82 | 42 | |
| 19 | 4 Nov. 1968 | 0518.0 | 0.35 | 51 | 23 | 60 | |
| 20 | 13 Nov. 1968 | 1246.4 | 0.1 | 142 | 83 | 30 | |
| 21 | 18 Nov. 1968 | 1027.7 | 0.05 | 148 | 73 | 55 | |

(cont.)

Table A.1 (cont.)

| Event No. | Date | Time[1] (U.T.) | Lowest Frequency (MHz) | Spacecraft[2] Distance ($10^3$ km) | $\phi°$ | $\theta°$ | Note |
|---|---|---|---|---|---|---|---|
| 22 | 23 Nov. 1968 | >0531.5 <0540.5 | 0.1 | 142 | 62 | 42 | (4) |
| 23 | 25 Nov. 1968 | 0334.6 | 0.35 | 76 | 28 | 57 | (3) |
| 24 | 9 Dec. 1968 | 0622.7 | 0.2 | 148 | 52 | 35 | |
| 25 | 20 Dec. 1968 | 1546.3 | 0.35 | ~113 | 60 | 10 | |
| 26 | 24 Dec. 1968 | 2227.7 | 0.1 | 147 | 37 | 33 | |
| 27 | 3 Jan. 1969 | 0316.4 | 0.35 | 68 | 342 | 60 | |
| 28 | 6 Jan. 1969 | 0907.3 | 0.2 | 137 | 15 | 43 | |
| 29 | 17 Jan. 1969 | 1704.7 | 0.35 | 133 | 18 | 26 | |
| 30 | 24 Jan. 1969 | 0717.0 | 0.1 | 116 | 348 | 49 | |
| 31 | 8 Feb. 1969 | 0415.3 | 0.35 | 50 | 15 | -5 | |
| 32 | 9 Feb. 1969 | 1431.9 | 0.35 | 147 | 347 | 36 | |
| 33 | 9 Feb. 1969 | 1724.7 | 0.2 | 146 | 349 | 33 | |
| 34 | 10 Feb. 1969 | 0343.8 | 0.35 | 130 | 355 | 24 | |
| 35 | 23 Feb. 1969 | 0440.9 | 0.1 | 128 | 342 | 23 | |
| 36 | 24 Feb. 1969 | 1427.2 | 0.2 | 123 | 319 | 48 | |
| 37 | 24 Feb. 1969 | 2308.1 | 0.2 | 142 | 327 | 40 | (3) |
| 38 | 25 Feb. 1969 | 0909.7 | 0.1 | 145 | 334 | 32 | |
| 39 | 27 Feb. 1969 | 1403.8 | 0.35 | 143 | 325 | 40 | |
| 40 | 27 Feb. 1969 | 1412.0 | 0.35 | 143 | 325 | 40 | |
| 41 | 12 Mar. 1969 | 1752.1 | 0.35 | 145 | 314 | 37 | |
| 42 | 13 Mar. 1969 | 2117.7 | 0.35 | 72 | 335 | 1 | |
| 43 | 30 Mar. 1969 | 0249.6 | 0.1 | 88 | 267 | 57 | |

Table A.1 (cont.)

| Event No. | Date | Time[1] (U.T.) | Lowest Frequency (MHz) | Spacecraft[2] Distance ($10^3$ km) | $\phi°$ | $\theta°$ | Note |
|---|---|---|---|---|---|---|---|
| 44 | 3 May 1969 | 1942.5 | 0.2 | 145 | 264 | 36 | |
| 45 | 4 May 1969 | 0719.8 | 0.1 | 133 | 271 | 25 | |
| 46 | 6 May 1969 | 0639.5 | 0.1 | 143 | 250 | 39 | |
| 47 | 11 May 1969 | 1820.3 | 0.2 | 144 | 258 | 33 | |
| 48 | 25 May 1969 | 0641.5 | 0.35 | 122 | 253 | 20 | |
| 49 | 28 May 1969 | 2310.2 | 0.1 | 91 | 209 | 58 | |
| 50 | 29 May 1969 | 0020.8 | 0.2 | 99 | 214 | 55 | |
| 51 | 29 May 1969 | 1451.5 | 0.2 | 141 | 235 | 40 | |
| 52 | 29 May 1969 | 1938.4 | 0.2 | 144 | 238 | 36 | |
| 53 | 31 May 1969 | 2101.5 | 0.2 | 124 | 224 | 48 | |
| 54 | 1 June 1969 | 1700.1 | 0.1 | 141 | 240 | 30 | (3) (4) |
| 55 | 2 June 1969 | 0854.2 | 0.35 | 91 | 251 | 8 | |
| 56 | 2 June 1969 | 0914.5 | 0.1 | 89 | 252 | 7 | |
| 57 | 11 June 1969 | 1619.8 | 0.1 | 142 | 223 | 39 | |
| 58 | 18 June 1969 | 2109.5 | 0.1 | 106 | 198 | 54 | |
| 59 | 18 June 1969 | 2338.5 | 0.1 | 116 | 203 | 51 | |
| 60 | 5 July 1969 | 1225.0 | 0.2 | 140 | 207 | 29 | |
| 61 | 25 Oct. 1969 | 1534.9 | 0.1 | 126 | 102 | 20 | |
| 62 | 7 Nov. 1969 | 0346.0 | 0.1 | 140 | 82 | 33 | (3) (4) |
| 63 | 25 Nov. 1969 | 1303.4 | 0.2 | 137 | 66 | 30 | |
| 64 | 19 Feb. 1970 | 0801.2 | 0.2 | 137 | 338 | 29 | |

(cont.)

Table A.1 (cont.)

Notes:

(1)  Time of start of the event at 3.5 MHz.

(2)  Approximate values taken from the OR/3A.  The distance is geocentric.
     $\emptyset$ is the angle from Earth-Sun line to the projection of earth-
     spacecraft line onto ecliptic plane.  $\Theta$ is the angle between Earth-
     spacecraft line and ecliptic plane.  In Fig. 2.9, $\emptyset$ = ⚥ SEU, $\Theta$ = ⚥
     TEU.

(3)  Burst probably observed also in next channel below.

(4)  Event No. 15 - Calibration at the beginning of the burst.
     Event No. 22 - Data gap at the beginning of the burst.
     Events No. 54 and 62 - Time corresponds to the start of the
        event at 0.9 MHz.  The event was not observed at the two higher
        frequencies.

APPENDIX NO. 1

Table A.2

Association of OGO-V Events with Hα Flares.[*] Heliographic Latitude $B_o$

of the Solar Disk Center[**] at the Time of the Events

| Event No. | Position of the Associated Flare δ(°) | λ(°) | McMath Plage No. | Flare Start Time (U.T.)(†) | Range of Flare Importance | $B_o$(°) | Note |
|---|---|---|---|---|---|---|---|
| 1 | S 13 | W 47 | 9273 | 0321 | 1N, 1B | -6.72 | |
| 2 | N 12 | W 79 | 9567 | 1322 | 1B | +6.62 | |
| 3 | N 12 | W 51 | 9630 | 0917 | -N, 2B | +7.25 | |
| 4 | S 16 | E 90 | 9668 | 1309 | -F | +7.22 | (1),(2) |
| 5 | S 21 | E 55 | 9692 | 1925 | -F, 1N | +6.91 | |
| 6 | N 10 | E 12 | 9687 | 1033 | -B | +6.87 | |
| 7 | N 13 | W 13 | 9687 | 0930 | 1N, 2B | +6.78 | |
| 8 | N 17 | W 52 | 9678 | 1619 | 1N, 2B | +6.78 | |
| 9 | S 16 | W 38 | 9692 | 2357 | 2N, 3B | +6.54 | (3) |
| 10 | N 20 | E 40 | 9705 | 2120 | 2B | +6.54 | |
| 11 | N 14 | W 19 | 9700 | 1722 | 1N, 1B | +6.43 | |
| 12 | N 18 | W 46 | 9705 | 0304 | 1N | +6.12 | |
| 13 | N 21 | W 01 | 9726 | 0816 | -N, -B | +5.68 | |
| 14 | N 20 | W 90 | 9726 | 2001 | -N, -B | +5.18 | |
| 15 | S 17 | E 17 | 9740 | 1300 | 2N | +4.81 | |
| 16 | N 14 | W 88 | 9733 | 0953 | -N, -B | +4.62 | (1) |
| 17 | S 12 | W 61 | 9740 | 1656 | -N | +4.32 | (2) |
| 18 | S 14 | W 66 | 9740 | 0940 | 2B | +4.22 | |
| 19 | S 15 | W 90 | 9740 | 0515 | 1B, 2B | +4.01 | |
| 20 | N 18 | W 22 | 9760 | 1246 | -N, 1B | +3.02 | |

(cont.)

Table A.2 (cont.)

| Event No. | Position of the Associated Flare δ(°) | λ(°) | McMath Plage No. | Flare Start Time (U.T.)(†) | Range of Flare Importance | $B_o$(°) | Note |
|---|---|---|---|---|---|---|---|
| 21 | N 21 | W 90 | 9760 | 1026 | 1B | +2.43 | |
| 22 | S 12 | E 27 | 9780 | 0538 | -N | +1.82 | (2) |
| 23 | S 11 | E 01 | 9780 | 0335 | -N | +1.57 | |
| 24 | N 11 | W 46 | 9798 | 0613 | 3F, 1N | -0.21 | |
| 25 | S 19 | W 12 | 9829 | -- | -- | -1.61 | (4) |
| | N 22 | W 100 | 9821 | | | | |
| 26 | N 19 | E 28 | 9842 | 2228 | 1B, 2B | -2.11 | |
| 27 | N 24 | E 68 | 9855 | 0320 | -N | -3.30 | |
| 28 | N 20 | E 28 | 9855 | 0907 | 1B | -3.64 | |
| 29 | N 17 | E 46 | 9873 | 1704 | -B, 1B | -4.79 | |
| 30 | N 20 | W 08 | 9879 | 0706 | 3N, 2B | -5.42 | (5) |
| 31 | N 12 | E 06 | 9911 | 0415 | -N | -6.50 | |
| 32 | N 18 | E 02 | 9918 | 1431 | -N, -B | -6.55 | |
| 33 | N 18 | E 00 | 9918 | 1723 | -B | -6.55 | |
| 34 | N 18 | W 06 | 9918 | 0343 | -N, -B | -6.61 | |
| 35 | N 12 | W 09 | 9946 | 0441 | -N, 1B | -7.11 | |
| 36 | N 11 | W 26 | 9946 | 1432 | -N, 1B | -7.14 | |
| 37 | N 12 | W 31 | 9946 | 2310 | 2B | -7.14 | |
| 38 | N 14 | W 38 | 9946 | 0909 | 2N, 2B | -7.16 | |
| 39 | N 13 | W 64 | 9946 | 1355 | 1N, 2B | -7.19 | (6) |
| 40 | N 13 | W 64 | 9946 | 1355 | 1N, 2B | -7.19 | (6) |
| 41 | N 12 | W 80 | 9966 | 1739 | 2B, 3B | -7.21 | |
| 42 | S 14 | E 45 | 9988 | 2117 | -N, -B | -7.20 | |
| 43 | N 09 | E 50 | 10114 | -- | -- | -6.63 | (4) |
| | N 22 | W 110 | 9994 | | | | |

(cont.)

Table A.2 (cont.)

| Event No. | Position of the Associated Flare δ(°) | λ(°) | McMath Plage No. | Flare Start Time (U.T.)(†) | Range of Flare Importance | $B_o$(°) | Note |
|---|---|---|---|---|---|---|---|
| 44 | N 06 | W 59 | 10057 | 1945 | 1N | -3.94 | |
| 45 | N 10 | W 61 | 10057 | 0720 | -F, 1N | -3.83 | |
| 46 | N 10 | W 90 | 10057 | 0637 | --F | -3.63 | (2),(5) |
| 47 | -- | -- | -- | -- | -- | -3.08 | (4) |
| 48 | N 11 | E 21 | 10109 | 0640 | -F, 1F | -1.47 | |
| 49 | N 11 | W 63 | 10109 | 2310 | 1N | -1.11 | |
| 50 | N 11 | W 64 | 10109 | 0020 | 1B | -0.99 | |
| 51 | N 11 | W 73 | 10109 | 1452 | 1B | -0.99 | |
| 52 | N 10 | W 76 | 10109 | 1938 | 1B | -0.99 | |
| 53 | N 12 | W 110 | 10109 | -- | -- | -0.75 | (4) |
| 54 | N 12 | W 120 | 10109 | -- | -- | -0.63 | (4) |
| 55 | N 12 | W 130 | 10109 | -- | -- | -0.51 | (4) |
| 56 | N 12 | W 130 | 10109 | -- | -- | -0.51 | (4) |
| 57 | N 10 | W 20 | 10134 | 1620 | 2N, 3B | +0.57 | |
| 58 | N 07 | E 09 | 10148 | 2109 | -N, -B | +1.41 | |
| 59 | N 08 | E 05 | 10148 | 2337 | -N, -B | +1.41 | |
| 60 | S 13 | E 16 | 10181 | 1226 | 1N, 2B | +3.34 | |
| 61 | N 10 | W 18 | 10381 | 1535 | -N | +5.02 | |
| 62 | N 13 | E 11 | 10406 | 0324 | 1F, 2N | +3.72 | |
| 63 | N 11 | W 47 | 10432 | 1225 | 1N | +1.60 | (4) |
| 64 | S 13 | W 31 | 10579 | 0802 | -F, 1N | -6.99 | |

(cont.)

Table A.2 (cont.)

* From Solar-Geophysical Data, Environmental Science Services Administration (ESSA), now National Oceanic and Atmospheric Administration (NOAA).

** From the American Ephemeris and Nautical Almanac.

(†) Time closest to the start of the 3.5 MHz burst.

Notes:

(1) Unconfirmed.

(2) Only one observation reported.

(3) Time corresponds to previous day.

(4) Because of the selection criterion all the radio events studied were extremely strong and except in very few cases they were always related to intense and complex optical flares. Usually there were several flares from the same McMath plage, starting within a few minutes of our radio events. The times given here indicate how close the group of flares was to the radio event. Unless we had no choice we did not consider flares that were already in progress for times longer than about 10 minutes since our radio events started. The Importance is given as a range when there were discrepancies in its estimation. The minus (-) sign indicates a subflare. The position corresponds to the average of the group.

Event No. 25 -- Unconfirmed flare -F at S 19 W 12. At 1501 it was in progress. The McMath plage region No. 9821 was very active from December 16 until December 19 when it disappeared behind the limb. The longitude 100°W is extrapolated.

Event No. 43 -- Unconfirmed flare -B N 09 E 50 starting before 02 49. Ground base radio observations give evidence that the flare occurred at the McMath plage No. 9994 behind the limb (V. L. Badillo, J. E. Salcedo, 1969). The longitude 110°W is extrapolated.

Event No. 47 -- No flares between 1711 and 2056 hrs. No flare patrol between 1900 and 1905. All confirmed flares on the day of this event and on the previous day came from the eastern hemisphere the Sun, almost all of them from McMath. No. 10088. The estimated average position is E 50.

Events No. 53, 54, 55, 56 -- No flare occurred near the time of these events except 3 unconfirmed weak subflares on June 2, starting between 0845 and 0850 and ending before 0915, at N 12 E 79. Evidence given

Table A.2   (cont.)

in the text suggests that these four events originated at the McMath plage No. 10109 when it was behind the limb and that they belong a sequence started with event No. 49.  This has been supported later on by solar electrons observations by R. P. Lin (1971).  He found correlations with these four events.  Longitudes are extrapolated.

Event No. 63 -- This confirmed flare continued after 1246.

(5)   Earliest time of observation.  At this time the flare was in progress.

(6)   Same flare.

Table A.5

Velocities Derived from the Model of Fig. 4.16

| Event No. | Unambiguous | Ambiguous | | |
| --- | --- | --- | --- | --- |
| | $\beta$ | $\beta_L$ | $\beta_H$ | $\beta_H/\beta_L$ |
| 1 | 0.36 | | | |
| 2 | | 0.17 | 0.33 | 1.94 |
| 3 | 0.43 | | | |
| 4(1) | -- | -- | -- | -- |
| 5 | | 0.20 | 0.40 | 2.00 |
| 6 | | 0.14 | 0.35 | 2.50 |
| 7 | 0.36 | | | |
| 8 | 0.18 | | | |
| 9 | | 0.19 | 0.36 | 1.90 |
| 10 | | 0.20 | 0.42 | 2.10 |
| 11 | 0.19 | | | |
| 12 | | 0.21 | 0.41 | 1.95 |
| 13 | 0.39 | | | |
| 14(7) | 0.46 | | | |
| 15 | | 0.20 | 0.34 | 1.70 |
| 16 | 0.32 | | | |
| 17 | | 0.13 | 0.28 | 2.15 |
| 18 | | 0.17 | 0.30 | 1.76 |
| 19(2) | | 0.29 | 0.40 | 1.38 |
| 20 | | 0.17 | 0.29 | 1.71 |
| 21(3) | | 0.18 | 0.36 | 2.00 |
| 22 | | 0.18 | 0.34 | 1.89 |
| 23 | 0.19 | | | |
| 24 | | 0.24 | 0.36 | 1.50 |
| 25(2,4) | | 0.17 | 0.30 | 1.76 |
| 26 | | 0.16 | 0.30 | 1.88 |
| 27 | | 0.18 | 0.36 | 2.00 |

(cont.)

Table A.3  (cont.)

| Event No. | Unambiguous $\beta$ | Ambiguous $\beta_L$ | $\beta_H$ | $\beta_H/\beta_L$ |
|---|---|---|---|---|
| 28 | 0.20 | | | |
| 29 | | 0.20 | 0.42 | 2.10 |
| 30 | | 0.15 | 0.24 | 1.60 |
| 31 | | 0.20 | 0.32 | 1.60 |
| 32 | 0.49 | | | |
| 33 | 0.43 | | | |
| 34 | | 0.25 | 0.41 | 1.64 |
| 35 | 0.32 | | | |
| 36 | 0.18 | | | |
| 37 | 0.30 | | | |
| 38 | 0.26 | | | |
| 39 | 0.36 | | | |
| 40 | 0.46 | | | |
| 41 | 0.41 | | | |
| 42 | | 0.10 | 0.26 | 1.63 |
| 43(4) | 0.32 | | | |
| 44 | 0.26 | | | |
| 45 | 0.36 | | | |
| 46(2) | | 0.18 | 0.36 | 2.00 |
| 47(5) | | 0.13 | 0.22 | 1.69 |
| 48(2) | 0.33 | | | |
| 49 | 0.29 | | | |
| 50 | | 0.16 | 0.32 | 2.00 |
| 51 | | 0.18 | 0.25 | 1.39 |
| 52(2) | 0.37 | | | |
| 53(6) | | 0.18 | 0.37 | 2.05 |
| 54(6) | 0.34 | | | |
| 55(6) | | 0.15 | 0.30 | 2.00 |
| 56(6) | 0.40 | | | |
| 57 | | 0.18 | 0.30 | 1.67 |
| 58 | 0.57 | | | |
| 59 | 0.32 | | | |

Table A.3   (cont.)

| Event No. | Unambiguous $\beta$ | Ambiguous | | |
|-----------|---------------------|-----------|---|---|
| | | $\beta_L$ | $\beta_H$ | $\beta_H/\beta_L$ |
| 60 | 0.28 | | | |
| 61 | | 0.18 | 0.34 | 1.89 |
| 62 | 0.36 | | | |
| 63 | | 0.16 | 0.32 | 2.00 |
| 64 | 0.19 | | | |

Notes:

(1)  Useless to determine velocity.

(2)  Somewhat large spread in the velocities of the components.

(3)  November 18, 1968 event.

(4)  Two possible associated flares.  For event No. 25 we accepted $\theta_F = 100°$; for event No. 43 we accepted $\theta_F = 110°$.  See Table A.2.

(5)  The velocity was determined assuming an average $\theta_F = -50$. See Table A.2.

(6)  The associated flares were assumed to be behind the west limb. See Table A.2.

(7)  Almost at the end of this work we found that due to mistake in the date this event was misidentified.  The position of the wrongly associated Hα flare was S 12 E 60 while the correct one was N 20 W 90. This error leads to a velocity of 0.22c.  The wrong information was used in Figs. 4.23, 4.24 and A.2 from which the computational results contained in Tables 4.15, A.6 and A.7 were obtained.  We estimated that the use of the correct values would not change the result appreciably therefore we did not modify them.

Table A.4

Outstanding X-Ray Events[1] Associated with the  Radio Events Observed

by OGO-V

| Radio Event No. | X-Ray Event | | | |
|---|---|---|---|---|
| | Start U.T. | Max. U.T. | End U.T. | Observer[2] |
| 1 | 0349 | | 0522 | N.R.L. |
| 2 | 1324 | 1352 | | U.I. |
| 3 | 0917 | 0921 | | " |
| 6 | 1033 | 1039 | | " |
| 7 | 0925 | 0942 | | " |
| 8 | 1616 | 1624 | | " |
| 9 | 0010 | | 0011 | N.R.L. |
| | 2324(3) | 0011 | | U.I. |
| 10 | 2132 | | 2133 | N.R.L. |
| | -- | 2155 | | U.I. |
| 11 | 1721 | 1736 | | " |
| 15 | 1307 | 1341 | | " |
| 16 | 0944 | 0959 | | " |
| 18 | 0947 | 1005 | | " |
| 19 | 0520 | | 0540 | N.R.L. |
| | 0518(4) | 0529 | | U.I. |
| 21 | 1026 | 1057 | | " |
| 22 | 0538 | 0543 | | " |
| 24 | 0613 | | 0711 | N.R.L. |
| | 0610 | 0620 | | U.I. |
| 26 | 2227 | | 2240 | N.R.L. |
| 28 | 0907 | | 0918 | N.R.L. |
| | 0906 | 0913 | | U.I. |
| 29 | 1704 | | 1711 | N.R.L. |
| | 1705 | 1706 | | U.I. |

(cont.)

Table A.4 (cont.)

| Radio Event No. | X-Ray Event | | | |
|---|---|---|---|---|
| | Start U.T. | Max U.T. | End U.T. | Observer[2] |
| 30 | 0709 | | 1031 | N.R.L. |
| | 0658 | 0740 | | U.I. |
| 31 | 0413 | 0418 | | " |
| 32 | 1432 | | 1438(6) | N.R.L. |
| | 1430 | 1435 | | U.I. |
| 33 | 1724 | | 1736 | N.R.L. |
| | 1723 | 1726 | | U.I. |
| 34 | 0343 | 0346 | | " |
| 35 | 0440(5) | | 0508 | N.R.L. |
| | 0442 | 0451 | | U.I. |
| 36 | 1433 | | 1445 | N.R.L. |
| 37 | 2330 | | 0112 | N.R.L. |
| | 2306 | 2322 | | U.I. |
| 38 | 0856 | 0918 | | " |
| 39 | 1400(5) | | 1735 | N.R.L. |
| | 1356 | 1412 | | U.I. |
| 40 | 1400(5) | | 1735(6) | N.R.L. |
| | 1356 | 1412 | | U.I. |
| 41 | 1739(5) | | 1954 | N.R.L. |
| | 1737 | 1745 | | U.I. |
| 43 | 0257(5) | | 0904 | N.R.L. |
| | 0246 | 0302 | | U.I. |
| 44 | 1959(5) | | 2016 | N.R.L. |
| | 1947 | 2006 | | U.I. |
| 45 | 0730 | | 0744 | N.R.L. |
| 46 | 0638 | | 0716 | " |
| | 0636 | 0648 | | U.I. |
| 50 | 0019 | | 0031(6) | N.R.L. |
| | 0019 | 0027 | | U.I. |
| 51 | 1449 | | 1518(6) | N.R.L. |
| | 1449 | 1500 | | U.I. |

(cont.)

Table A.4 (cont.)

| Radio Event No. | X-Ray Event | | | |
|---|---|---|---|---|
| | Start U.T. | Max. U.T. | End U.T. | Observer[2] |
| 52 | 1939 | | 2013 | N.R.L. |
| | 1938 | 1946 | | U.I. |
| 53 | 2057 | | 2300(6) | N.R.L. |
| | 2103 | 2126 | | U.I. |
| 57 | 1617 | | 1834 | N.R.L. |
| | 1616 | 1630 | | U.I. |
| 60 | 1229 | | 1244(6) | N.R.L. |
| | 1225 | 1238 | | U.I. |

Notes:

(1) Published in Solar-Geophysical Data, E.S.S.A.

(2) N.R.L. stands for Naval Research Laboratories and U.I. stands for University of Iowa.

(3) Flare started in the day previous to the day of the maximum.

(4) Start time given corresponds to rapid rise. Onset occurred at 0458.

(5) The flare was in progress when observation started.

(6) The flare was in progress when observation ended.

Table A.5

Association of Ground-Based Radio Observations with the Radio Events

Observed by OGO-V

| Event No. | I | II | III | IV | V | CONT. | UNCLF |
|---|---|---|---|---|---|---|---|
| 1 | | √ | √ | | √ | | √ |
| 2 | | | √ | | √ | √ | |
| 3 | | | √ | | | | |
| 4 | No activity recorded. | | | | | | |
| 5 | | | √ | | | | |
| 6 | | | √ | | √ | | |
| 7 | | | √ | √ | √ | | |
| 8 | | √ | √ | | | √ | |
| 9 | | √ | √ | | | √ | |
| 10 | | | √ | | | √ | √ |
| 11 | | √ | √ | | | | |
| 12 | | | √ | | | | |
| 13 | | | √ | | √ | | |
| 14 | √ | | | | | | |
| 15 | | | √ | √ | | | |
| 16 | | | √ | | √ | | |
| 17 | | √ | √ | √ | | | √ |
| 18 | | √ | √ | √ | | | √ |
| 19 | | √ | √-U | | √ | √ | |
| 20 | | | √ | | | | |
| 21 | | √ | √ | √ | | | |
| 22 | | | √-U | | √ | | |
| 23 | √ | | √ | | √ | | √ |
| 24 | | | √-U | | √ | | |
| 25 | | | √ | | | | |
| 26 | | √ | √ | √ | √ | | √ |

(cont.)

Table A.5 (cont.)

| Event No. | I | II | III | IV | V | CONT. | UNCLF |
|---|---|---|---|---|---|---|---|
| 27 | No spectral observations available. | | | | | | |
| 28 | | | √ | | | | |
| 29 | | √ | √ | √ | √ | √ | |
| 30 | No spectral observations available. | | | | | | |
| 31 | | √ | √-U | | √ | | √ |
| 32 | √ | √ | √ | | √ | | |
| 33 | | √ | √ | √ | √ | | |
| 34 | | | √ | | √ | | |
| 35 | | √ | √ | | √ | | |
| 36 | | | √ | | | | |
| 37 | | √ | √ | √ | √ | √ | √ |
| 38 | | | √ | √ | | | |
| 39 | | √ | √ | √ | | | |
| 40 | | √ | √ | √ | | | |
| 41 | √ | √ | √ | √ | | √ | |
| 42 | | √ | √ | | | | |
| 43 | | √ | √ | | | | |
| 44 | √ | | √ | | | √ | √ |
| 45 | No spectral observations available. | | | | | | |
| 46 | | | √ | | | | |
| 47 | | | √ | | | | |
| 48 | | | √ | √ | | | |
| 49 | | | √ | | | | |
| 50 | | √ | √-U | | √ | | |
| 51 | | | √ | | | √ | |
| 52 | | | √ | | | √ | |
| 53 | | | √ | | | √ | |
| 54 | | | √ | | | | |
| 55 | No activity recorded. | | | | | | |
| 56 | No activity recorded. | | | | | | |
| 57 | | √ | √-U | √ | √ | | |
| 58 | √ | | √ | | | | |

Table A.5 (cont.)

| Event No. | I | II | III | IV | V | CONT. | UNCLF |
|---|---|---|---|---|---|---|---|
| 59 | √ | | √-U | | √ | | |
| 60 | | | √ | | | | |
| 61 | √ | | √ | | | | |
| 62 | No spectral observations available. | | | | | | |
| 63 | √ | | √ | | | | |
| 64 | | | √ | | | | |

APPENDIX NO. 2

Derivation of the Electron Density Distribution Function, Form 1

The assumption made in the following derivation were discussed in Section 4.2.2 and they will be briefly reviewed here. With reference to Fig. 4.6, S represents the Sun and E the Earth. Exciter particles are ejected from a point on the Sun located at an angular distance $\theta_F$ from the central meridian. The particles travel along a spiral path with constant velocity v and produce a burst at frequency f at a point P. These radio waves travel along a straight trajectory to the Earth with a velocity equal to the velocity of light in vacuum. At a later time a burst at frequency $f - \Delta f$ is produced at point $P_1$, and it propagates to the Earth in the same conditions as the burst at P. The burst from $P_1$ is observed at the Earth with a time delay respect to the burst coming from P.

We want to find a differential equation of the form

$$\frac{dN(r)}{dr} + Q(r) = 0 .$$

We start by using the chain law and write:

$$\frac{dN}{dr} = \frac{dN}{df} \frac{df}{dt} \frac{dt}{dr} . \tag{A.1}$$

We will proceed to find these derivatives.

For convenience we reproduce here the following equations:

$$\frac{df}{dt} = -10^a \, f^\alpha \quad , \tag{4.2}$$

$$f = j \, \Omega \, N^{1/2} \quad , \tag{4.7}$$

$$\Theta = \Theta_F - \epsilon \, \frac{r}{\ell} \quad , \tag{4.8}$$

$$v = \frac{ds}{dt} \quad , \tag{4.10}$$

$$\beta = \frac{v}{c} = \text{constant} \quad . \tag{4.11}$$

Let:

   $t'$  =  time at which the particles reach point P,

   $t$  =  time at which the radio waves emitted from point P reach

the Earth,

   $t_1$  =  time at which the radio waves emitted from point $P_1$ reach

the Earth and

   $c$  =  velocity of light in vacuum.

Then:

$$t = t' + \frac{\overline{PE}}{c} \quad ,$$

$$t = t' + \frac{\overset{\frown}{PP_1}}{v} + \frac{\overline{P_1 E}}{c} \quad .$$

The delay in arrival at the Earth is then:

$$dt = t_1 - t$$

$$= \frac{\overset{\frown}{PP_1}}{v} + \frac{\overline{P_1 E} - \overline{PE}}{c} \quad .$$

Let us call

$$\widehat{PP}_1 = ds \quad ,$$

$$\overline{PE} = x \quad ,$$

$$\overline{P_1E} - \overline{PE} = dx \quad .$$

Then

$$dt = \frac{ds}{v} + \frac{dx}{c} \tag{A.2}$$

and

$$\frac{dt}{dr} = \frac{ds}{vdr} + \frac{dx}{cdr} \quad . \tag{A.3}$$

From the cosine law:

$$x^2 = r^2 + \ell^2 - 2\ell r \cos \theta \quad .$$

Using Eq. (4.8) we can write:

$$x^2 = r^2 + \ell^2 - 2\ell r \cos \left(\theta_F - \epsilon \frac{r}{\ell}\right) \tag{A.4}$$

so (dx/dr) can be obtained.

Also in polar coordinates

$$ds^2 = (r\, d\theta)^2 + dr^2$$

and from Eq. (4.8):

$$ds = \left(\frac{r^2\epsilon^2}{\ell^2} + 1\right)^{1/2} dr \quad . \tag{A.5}$$

Next, from Eq. (4.7) we have:

$$\frac{df}{dN} = \frac{9}{2} j N^{-1/2} \quad .$$

(4.6)

Substituting Eq. (4.7) into (4.2) we have:

$$\frac{df}{dt} = -10^a (9 j N^{1/2})^\alpha \quad .$$

(A.7)

Therefore substituting Eqs. (A.3), (A.6), (A.7) and (4.11) into (A.1) we have:

$$\frac{dN}{dr} = -\frac{2 \cdot 10^a}{c} \left( 9 j \right)^{\alpha-1} N^{(\alpha+1)/2} \left( \frac{dx}{dr} + \frac{1}{\beta} \frac{ds}{dr} \right)$$

(A.8)

We can next perform a definite integration:

$$\int_{N(r_o)}^{N(r)} N^{-(\alpha+1)/2} \, dN = -\frac{2}{c} 10^a (9j)^{\alpha-1} \left( \int_{x(r_o)}^{x(r)} dx + \frac{1}{\beta} \int_{s(r_o)}^{s(r)} ds \right) \quad .$$

(A.9)

The quantity x is given by Eq. (A.4). From Eq. (A.5), except for an integration constant:

$$s = \frac{\epsilon}{2\ell} \left\{ r \left[ r^2 + \left( \frac{\ell}{\epsilon} \right)^2 \right]^{1/2} + \left( \frac{\ell}{\epsilon} \right)^2 \ln \left[ r + \left( r^2 + \left( \frac{\ell}{\epsilon} \right)^2 \right)^{1/2} \right] \right\} \quad .$$

(A.10)

The limit $r_0$ depends on where we want to apply the boundary condition
on the electron density $N(r_0) = N_0$.

Let us also define

$$p = \frac{2}{\alpha - 1} \qquad \text{(A.11)}$$

and

$$D = \left( \frac{c \quad 10^{-a}}{(\alpha - 1)(9j)^{\alpha-1}} \right)^{2/(\alpha-1)} . \qquad \text{(A.12)}$$

Then we can rewrite the result of the integration of Eq. (A.9) as
follows:

$$N^{-1/p} - N_0^{-1/p} = D^{-1/p} \left[ \frac{1}{\beta}\left(s(r) - s(r_0)\right) + x(r) - x(r_0) \right] . \qquad \text{(A.13)}$$

The meaning of $s(r) - s(r_0)$ is the length of the
trajectory of the particles between points at distances $r$ and $r_0$ while
$x(r) - x(r_0)$ is the difference in paths along which the radio waves
propagate from those points to the Earth. This equation is perfectly
general in two dimensions in the sense that it is valid for any trajectory
and for any form of propagation. For the case of the radial trajectory
the limit $\epsilon = 0$ should be taken in Eq. (A.5) before the integration rather
than at Eq. (A.10).

Finally we can rearrange Eq. (A.13) and write:

$$N = \frac{D}{\left[ \left(\frac{D}{N_0}\right)^{1/p} + \frac{1}{\beta}\left(s(r) - s(r_0)\right) + x(r) - x(r_0) \right]^p} , \qquad \text{(A.14)}$$

where $p$ is defined by Eq. (A.11), $D$ by Eq. (A.12), $\beta$ by Eq. (4.11), $x$ by
Eq. (A.4) and $s$ by Eq. (A.5).

## APPENDIX NO. 3

## Derivation of the Frequency Drift Rate from the

## Electron Density Distribution, Form 2

We start from Eq. (A.1) that we write now in a different form:

$$\frac{df}{dt} = \frac{\frac{dN}{dr}}{\frac{dN}{df}\frac{dt}{dr}} \cdot \qquad (A.15)$$

We will find these derivaties as functions of f.

From Eq. (4.12)

$$\frac{dN}{dr} = -p\frac{A}{(r-b)^{p+1}} \cdot \qquad (A.16)$$

Equating N in Eqs. (4.7) and (4.12) we have

$$\frac{A}{(r-b)^p} = \frac{f^2}{(9j)^2} \cdot \qquad (A.17)$$

After solving for (r - b) and substituting in Eq. (A.16) we can write:

$$\frac{dN}{dr} = -p \quad A\left[\frac{f^2}{9^2j^2A}\right]^{(p+1)/p} \cdot \qquad (A.18)$$

From Eq. (4.7)

$$\frac{dN}{df} = \frac{2f}{9^2j^2} \cdot \qquad (A.19)$$

Using Eq. (4.11) we write Eq. (A.3) as follows:

$$\frac{dt}{dr} = \frac{1}{c}\left[\frac{1}{\beta}\frac{ds}{dr} + \frac{dx}{dr}\right] \quad , \qquad (A.20)$$

where ds/dr is given by Eq. (A.5) and dx/dr can be derived from Eq. (A.4).
Let us define two functions as follows:

$$H_1[r(f)] = \frac{ds}{dr}$$

and

$$G_1[r(f)] = \frac{dx}{dr} \quad . \qquad (A.21)$$

Then

$$H_1[r(f)] = \left[\frac{\varepsilon^2 r^2}{\ell^2} + 1\right]^{1/2}$$

and

$$G_1[r(f)] = \frac{r - \varepsilon\, r\sin\left[\theta_F - \frac{\varepsilon r}{\ell}\right] - \ell\cos\left[\theta_F - \frac{\varepsilon r}{\ell}\right]}{\left[r^2 + \ell^2 - 2\ell r\cos\left[\theta_F - \frac{\varepsilon r}{\ell}\right]\right]^{1/2}} \quad . \qquad (A.22)$$

From Eq. (A.17) we could express r in terms of f and then substitute in Eq. (A.22). However this would make the equation too complicated therefore we will only indicate this dependence by defining two new functions:

$$G(f, \varepsilon, \theta_F) = G_1[r(f)]$$

and

$$H(f, \varepsilon, \theta_F) = H_1[r(f)] \quad . \qquad (A.23)$$

Now we can write Eq. (A.20) as follows:

$$\frac{dt}{dr} = \frac{1}{c}\left[\frac{1}{\beta}H(f,\,\varepsilon,\,\theta_F) + G(f,\,\varepsilon,\,\theta_F)\right] \quad . \tag{A.24}$$

Replacing Eqs. (A.18), (A.19) and (A.24) into Eq. (A.15) we have:

$$\frac{df}{dt} = -\frac{pc}{2}\cdot\frac{f^{(p+2)/p}}{\left[A\,9^2 j^2\right]^{1/p}\left[\frac{1}{\beta}H(f,\,\varepsilon,\,\theta_F) + G(f,\,\varepsilon,\,\theta_F)\right]} \quad . \tag{A.25}$$

If we express N in $(cm^{-3})$, r in $R_\odot$, and f in MHz and take logarithms of the modulus in both sides of Eq. (A.25) we can write:

$$\log\left|\frac{df}{dt}\right| = \log\left[\frac{pc\beta}{2R_\odot(81\,10^{-6}\,j^2\,A)^{1/p}}\right]$$

$$+ \left(\frac{p+2}{p}\right)\log f - \log\left[H(f,\,\varepsilon,\,\theta_F) + \beta G(f,\,\varepsilon,\,\theta_F)\right] \quad . \tag{A.26}$$

This is of the form:

$$\log\left|\frac{df}{dt}\right| = a + \alpha\log f + \Delta \quad . \tag{A.27}$$

Except for the term $\Delta$, the equation is the same as Eq. (4.1). The relationship between p and $\alpha$ is the same as in Eq. (A.11). $\Delta$ represents the departure of Eq. (A.27) from a straight line in a log-log plot and we could call it a correction term. It is interesting to note that the constant "a" depends on the density model through A and p, on the mode of emission j and on the velocity $\beta$. The constant $\alpha$ depends only on the density model through p. The correction term $\Delta$ depends on

all the parameters: velocity, geometry of trajectory ($\varepsilon$ and $\theta_F$) model and mode.

The function $G_1$ in Eq. (A.22) has a singularity when the numerator and denominator approach zero simultaneously. This happens whenever the trajectory of the exciter particles passes through the Earth and when $r = \ell$.

A series expansion of the numerator and denominator about $r = \ell$ shows that the function $G_1$ approaches a limit whose sign depends on whether $r$ approaches $\ell$ from larger or smaller values. This phenomenon introduces a jump discontinuity in the predicted drift rates whenever particles go through the Earth.

APPENDIX NO. 4

Statistical Tests and Correlations Related to the Exciter Particles Velocity

(a) $\chi^2$ Test

We wanted to know the likelihood that the observed distributions of velocities (Figs. 4.23 and 4.24) came from normal distributions. We divided the normal curve into six categories in such a way that to each one there would correspond a theoretical frequency equal to or larger than five (Dixon and Massey, 1951, p. 190). The degrees of freedom (D.F.) turn out to be three. Figure A.1 shows the percentage of areas in each category. The term n is the total number of cases and P is the probability that $\chi^2 \geq \chi^2_{obs}$. The estimates of the parameters were taken from Table 4.15. The results are shown in Table A.6. (See Note No. 7 of Table A.3.)

Table A.6

Results of the $\chi^2$ Test with 3 D.F.

| Distribution | n | $\chi^2_{obs}$ | P |
|---|---|---|---|
| Unambiguous | 32 | 1.743 | 0.62 |
| Ambiguous-High | 31 | 1.645 | 0.64 |
| Ambiguous-Low | 31 | 2.925 | 0.40 |

For example for the Unambiguous distribution the test says that in 62 "of the cases out of 100 we should expect a fit as poor as this or poorer" (Mode, 1961, p. 208). According to Fisher (1958, p. 80), "if P is between 0.1 and 0.9 there is certainly no reason to
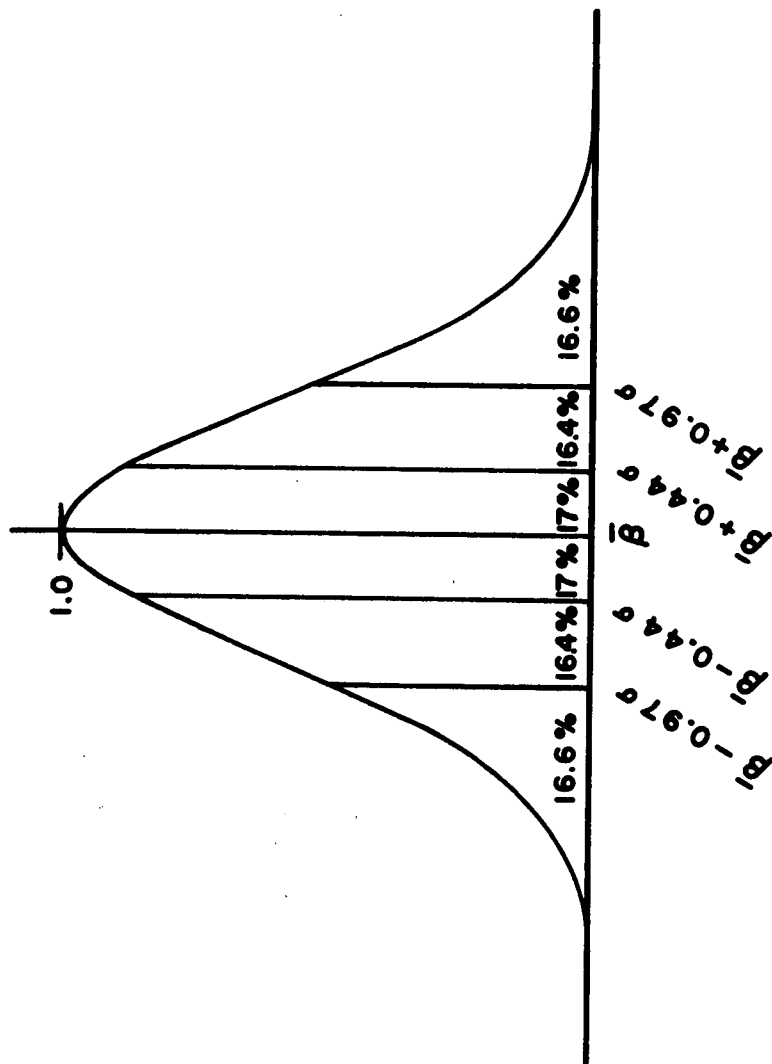
FIG. A.1   SELECTION OF CATEGORIES IN THE NORMAL DISTRIBUTION.

suspect the hypothesis tested," therefore we can accept that the three distributions may be samples from normal populations. The P for the Ambiguous-High is higher than that of the Ambiguous-Low, however this is not enough justification to accept it in favor of the Ambiguous-Low.

(b) Detailed Study of the Unambiguous Distribution

In order to study more the Unambiguous distribution we calculated its moments $m_i$ up to the fourth (i = 4).

The amount of skewness and flattening are given respectively by the parameters $\xi_1$ and $\xi_2$ where (Aitken, 1952):

$$\xi_1 = \frac{m_3^2}{m_2^3} \cdot (\text{sign } m_3)$$

and

$$\xi_2 = \frac{m_4}{m_2^2} \; .$$

The values obtained are:

$$m_1 = 0.320 \; ,$$

$$m_2 = 0.734 \; ,$$

$$m_3 = -6.0 \times 10^{-5}$$

and

$$m_4 = 12.0 \times 10^{-5} \; .$$

Therefore:

$$\xi_1 = -0.91$$

and

$$\xi_2 = 2.22 \; .$$

$\xi_1$ is negative because $m_3 < 0$. From Fig. 4.23 it is obvious that the distribution has negative skewness. The normal distribution has $\xi_2 = 3$ therefore our distribution is platykurtic, that is, flattened at the center as compared to the normal distribution.

(c) F-Test

Next, following the extreme alternatives of velocity chosen, we compared the $\beta_H$ and $\beta_L$ distributions with the $\beta$ (Unambiguous) distribution. For this we ran an F-test to test the hypothesis that the two distributions came from two normal parent distributions with the same variance (but not necessarily the same mean). Calling $\sigma^2$ and $\sigma_H^2$ the variances of the Unambiguous and Ambiguous-High distributions respectively, the F-test gave:

$$ F = \left[ \frac{\sigma}{\sigma_H} \right]^2 = 2.64 $$

and
$$ \text{Prob} (0.39 < F < 2.63) = 0.01 \ . $$

That is, the differences in $\sigma^2$ and $\sigma_H^2$ are large enough to be considered a rare event, it happens in less than 1% of the cases. We may conclude that the $\beta$ and $\beta_H$ distributions are unlikely to be samples from the same normal population under the stipulated conditions. This does not contradict the conclusions from the $\chi^2$ test that says that each of distributions is likely to come from different but normal populations.

Because the $\beta_L$ distribution departs from the $\beta$ distribution even more than the $\beta_H$ we decided not to test it.

It is probably possible to select from the ambiguous velocities some high and some low in such a way as to mimic the Unambiguous distribution, considered as true, however we do not feel confident about this method of resolving the ambiguity.

(d) Frequency of Occurrence Versus Position of Associated Flare

In another attempt to find an indication that the Ambiguous and Unambiguous events could belong to different populations we studied the distribution of the associated flare position. The histograms of Fig. A.2 illustrate the distributions. (See Note No. 7 of Table A.3.) We found that 70.4% of the 32 unambiguous cases and 64.5% of the ambiguous cases occur on the western hemisphere. The statistical parameters of the two distributions are shown in Table A.7 where n is the number of cases.
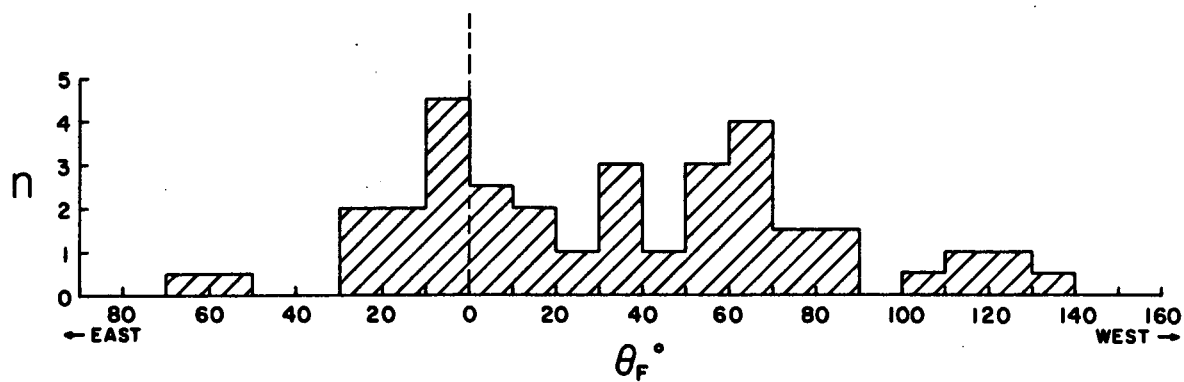
Table A.7

Parameters of the Distributions in $\theta_F$

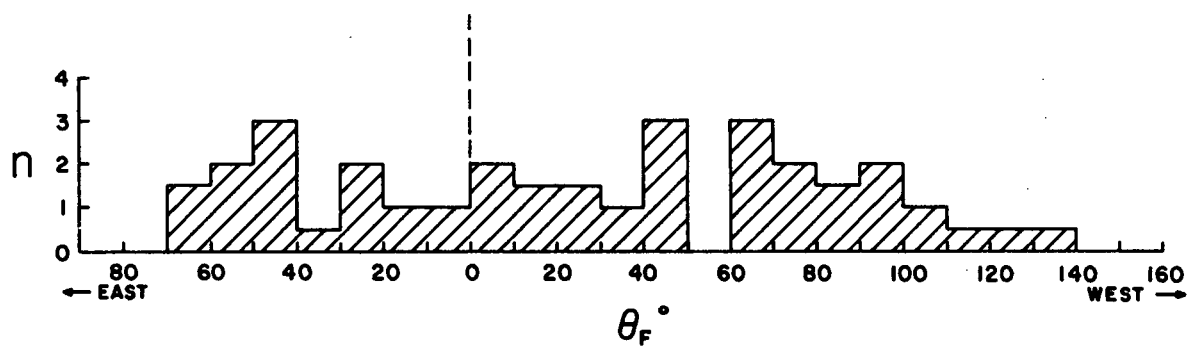| Distribution | n | $\bar{\theta}_F^\circ$ | $\sigma$ |
|---|---|---|---|
| Unambiguous | 32 | 33.8 | 44.8 |
| Ambiguous | 31 | 26.2 | 55.7 |

We used the F-test to test the hypothesis that the variances are equal. From Table A.7 we obtained F = 1.51 and from statistical tables (Wine, 1964), we found:

$$\text{Prob } (F \geq 1.61) = 0.10$$

$$\text{Prob } (F \leq 0.62) = 0.10$$

(a)   UNAMBIGUOUS   CASES   (32)



(b)   AMBIGUOUS   CASES   (31)

FIG. A.2   LONGITUDE DISTRIBUTION OF THE Hα FLARES ASSOCIATED WITH
TYPE III BURSTS HAVING AMBIGUOUS AND UNAMBIGUOUS VELOCITIES.

so that at the 20% confidence level there is no reason to doubt the hypothesis. By general standards this level is considered high.

Next, we applied the Student's t-test and obtained $t = 0.58$. Then from the tables of Johnson and Jackson (1959) and for 61 D.F. we find:

$$\text{Prob } (|t| \geq 0.58) = 0.56 \ .$$

That is, we can accept the hypothesis that the distribution in position of both the ambiguous and unambiguous bursts came from the same normal population.

(e) Search for Correlations

In pursuit of the same goal we tried to find correlations that would characterize the unambiguous cases. For example in order to look for a possible effect of the position of the associated flare on the velocity we plotted $\beta$ versus $\theta_F$ for the unambiguous cases. The plot is shown in Fig. A.3. The data seems to suggest a depletion of high velocities on the eastern half of the disk and a depletion of low velocities on the western half. Figure A.4, shows a plot of $\beta_H$ and $\beta_L$ versus $\theta_F$. If the suggested correlation existed it would permit the resolution of some cases for $\theta_F$ larger than about $60°$, however, the effect is not strong enough as to provide a discrimination. Besides, if it were, it could mean that some of our assumptions are not correct because the velocity of the exciter particles is unlikely to depend on the angular position of the Earth with respect to the associated flare. Figure 4.27 was also studied in the search for possible correlations. Again, the result was not significant.
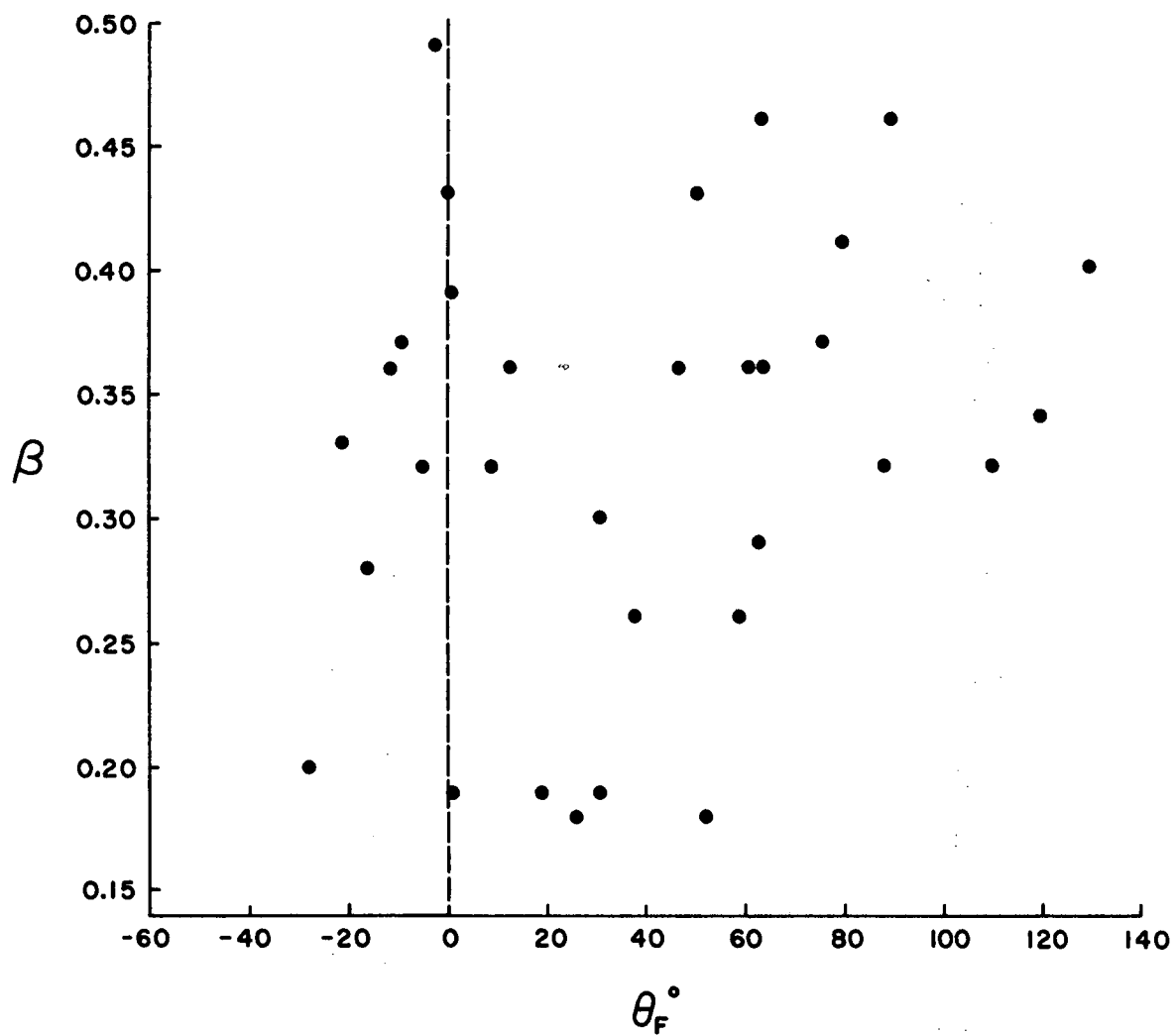
FIG. A.3  EXCITER PARTICLES VELOCITY VERSUS LONGITUDE OF THE ASSOCIATED
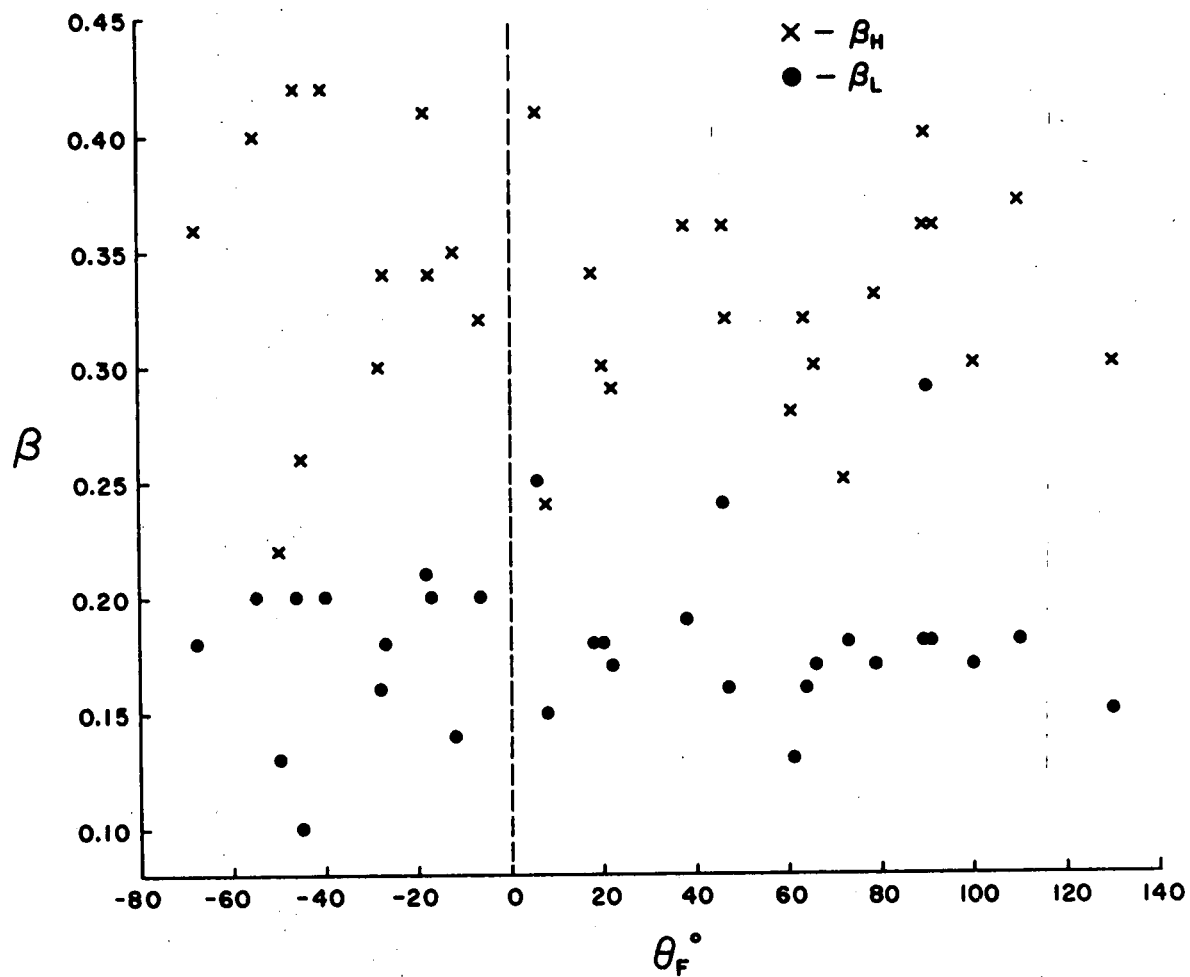
Hα FLARE.   UNAMBIGUOUS CASES.

FIG. A.4  EXCITER PARTICLES VELOCITY VERSUS LONGITUDE OF THE ASSOCIATED

Hα FLARE.  AMBIGUOUS CASES.

# BIBLIOGRAPHY

Aitken, A. C.: Statistical Mathematics, Seventh Edition, Oliver and Boyd, Ltd., 1952.

Alexander, J. K., Malitson, H. H., Stone, R. G.: Solar Phys. 8, 388, 1969.

Allen, C. W.: M.N.R.A.S. 107, 426, 1947a.

Allen, C. W.: M.N.R.A.S. 107, 386, 1947b.

Alvarez, H.: UM/RAO OGO-E Memo No. 179, 1971.

Alvarez, H., Haddock, F. T.: URSI Meeting, Washington, D.C., April 1970.

Alvarez, H., Haddock, F. T.: A.A.S. Meeting, Boulder, June 1970.

Alvarez, H., Haddock, F. T.: URSI Meeting, Los Angeles, September 1971.

Anderson, K. A., Winckler, J. R.: J. Geophys. Res. 67, 4103, 1962.

Anderson, K. A., Lin, R. P.: Phys. Rev. Lett. 16, 1121, 1966.

Appleton, E. V.: Nature 156, 534, 1945.

Appleton, E., Hey, J. S.: London Phil. Mag. Ser. 7, 37, 73, 1946.

Badillo, V. L., Salcedo, J. E.: Nature 224, 503, 1969.

Baselyan, L. L., Sinitsin, V. G.: Solar Phys. 17, 129, 1971.

Baumbach, S.: Astr. Nachr. 263, 121, 1937.

Billings, D. E.: A Guide to the Solar Corona, p. 256, Academic Press, 1966.

Blackwell, D. E.: M.N.R.A.S. 116, 56, 1956.

Blackwell, D. E., Ingham, M. F.: M.N.R.A.S. 122, 129, 1961.

Blackwell, D. E., Petford, A. D.: M.N.R.A.S. 131, 399, 1966.

Bohlin, J. D., Simon, M.: Solar Phys. 9, 183, 1969.

Bohlin, J. D.: Solar Phys. 13, 153, 1970.

Boischot, A.: in Rendiconti della Scuolla Internazionale di Fisica "E. Fermi." XXXIX Corso, 1967a.

Boischot, A.:  Ann. Astrophy. $\underline{30}$, No. 1, 85, 1967b.

Boischot, A., Lee, R. H., Warwick, J. W., Ap. J. $\underline{131}$, 61, 1960.

Bonnetti, A., Moreno, G., Cantarano, S., Egidi, A., Marconero, R., Palutan, F., Pizzela, G.:  Nuovo Cim. Serie X, $\underline{64}$, B, 307, 1969.

Boorman, J. A., McLean, D. J., Sheridan, K. V., Wild, J. P., M.N.R.A.S. $\underline{123}$, 87, 1961.

Bourgeret, J. L., Caroubalos, C., Mercier, C., Pick, M.:  Astr. and Astrophys. $\underline{6}$, 406, 1970.

Bowles, K. L.: Science $\underline{139}$, 389, 1963.

Bracewell, R. N., Preston, G. W.:  Ap. J. $\underline{123}$, 14, 1956.

Bradford, H. M., Hughes, V. A.: J. Roy. Astron. Soc. Canada $\underline{64}$, 185, 1970.

Brandt, J. C.:  Science $\underline{146}$, 1971, 1964.

Breckenridge, S.: UM/RAO Tech. Report, March 1969.

Bridge, H. S., Lazarus, A. J., Snyder, C. W., Smith, E. J., Davis, L., Jr., Coleman, P. J., Jr., Jones, D. E.:  Science $\underline{158}$, 1669, 1967.

Campbell, D. B., Muhleman, D. O.:  J. Geophys. Res. $\underline{74}$, 1138, 1969.

Castelli, J. P., Aarons, J., Michael, G. A.:  J. Geophys. Res. $\underline{72}$, 5491, 1967.

Chapman, S.:  Smithson. Contr. Astrophys. $\underline{2}$ , 1, 1957.

Cuperman, S., Harten, A.: Ap. J. $\underline{163}$, 383, 1971.

Denisse, J.: Revue Scientifique, $\underline{84}$, 259, 1946.

Dessler, A. J.: Rev. Geophys. $\underline{5}$, 1, 1967.

Dixon, W. J., Massey, F. J., Jr.:  Introduction to Statistical Analysis, First Edition, McGraw Hill, 1951.

Dulk, G. A., Clark, T. A.: quoted by T. R. Hartz, 1969.

Elgaroy, O., Rodberg, H.:  Astrophys. Norw. $\underline{8}$, 271, 1963.

Elsasser, H.:  Planet. Space Sci. $\underline{11}$, 1015, 1963.

Erickson, W. C.: J. Geophys. Res. $\underline{68}$, 3169, 1963.

Erickson, W. C.: Ap. J. $\underline{139}$, 1290, 1964.

Fainberg, J., Stone, R. G.:   Solar Phys. 15, 433, 1970.

Fainberg, J., Stone, R. G.:   Solar Phys. 17, 392, 1971a.

Fainberg, J., Stone, R. G.:   Ap. J. 164, Part 2, 123, 1971b.

Fan, C. Y., Pick, M., Ryle, R., Simpson, J. A., Smith, D. R.:
     J. Geophys. Res. 73, 1555, 1968.

Feix, G.:   J. Geophys. Res. Space Phys. 75, 211, 1970.

Ferencz, Cs., Tarcsai, Gy.,: Planet. Space Sci. 18, 1213, 1970.

Fisher, R. A.:   Statistical Methods for Research Workers, Thirteenth
     Edition, Revised, Hafner Publishing Co., 1958.

Gillet, F. C., Stein, W. A., Ney, E. P.:   Ap. J. 140, 292, 1964.

Ginzburg, V. L., Zheleznyakov, V. V.:   Soviet Astron. 2, 653, 1958a.
     (Astr. Zu. 35, 694, 1958)

Ginzburg, V. L., Zheleznyakov, V. V.:   Paris Symp. on Radio Astr.
     I.A.U. Symp. No. 9, Ed. R. N. Bracewell, p. 574, 1958b.

Ginzburg, V. L., Zheleznyakov, V. V.:   Soviet Astron. 5, 1, 1961.
     (Astr. Zu. 38, 3, 1961).

Giovanelli, R. G.:   Austr. J. Phys. 11, 350, 1958.

Giovanelli, R. G.:   Paris Symp. on Radio Astr.   I.A.U. Symp. No. 9,
     Ed. R. N. Bracewell, 214, 1959.

Gold, T.:   I.A.U. Symp. No. 6, Ed. B. Lehner, p. 275, 1958.

Goldstein, S. J., Meisel, D. D.:   Nature 224, 349, 1969.

Graedel, T. E.:   Ph.D. Thesis, The University of Michigan, 1969.

Graedel, T. E.:   Ap. J. 160, 301, 1970.

Haddock, F. T., URSI Meeting, Los Angeles, September, 1971.

Haddock, F. T., Alvarez, H.:   A.A.S. Meeting, New York, December 1969.

Haddock, F. T., Alvarez, H.:   A.A.S. Meeting, Boulder, June 1970.

Haddock, F. T., Alvarez, H.:   A.A. Meeting, Tampa, December 1970.

Haddock, F. T., Alvarez, H.:   URSI Meeting, Washington, D.C., April 1971.

Haddock, F. T., Graedel, T. E.:   Ap. J. 160, 293, 1970.

Hansen, R. T., Garcia, C. J., Hansen, S. F., Loomis, H. G.: Solar
    Phys. 7, 417, 1969.

Hartle, R. E., Sturrock, P. A.:  Ap. J. 151, 1155, 1968.

Harvey, G. A., Bell, B.:  Smithson. Contr. Astrophys. 10, No. 4, 1968.

Harvey, G. A., McNarry, L. M.:  Solar Phys. 11, 467, 1970.

Hartz, T. R.:  Ann. Astrophys. 27, 831, 1964.

Hartz, T. R., Planet. and Space Sci. 17, 267, 1969.

Hewish, A.:  Proc. Roy. Soc. A 228, 238, 1955.

Hey, J. S.:  Nature 157, 47, 1946.

Hey, J. S., Hughes, V. A.: M.N.R.A.S. 115, 605, 1955.

Hey, J. S., Parsons, S. J., Phillips, J. W.:  M.N.R.A.S. 108, 354, 1948.

Hollweg, J. V.:  Nature 220, 771, 1968.

Howard, H. T.:  Trans. Am. Geophys. Union, 49th Annual Meeting, p. 262,
    1968.

Howard, H. T., Eshleman, V. R., Barry, G. H., Fenwick, R. B.:
    Geophys. Res. 70, 4357, 1967.

Howard, H. T., Koehler, R. B.:  Intern. Symp. on Zod. Light and Interpl.
    Medium, Honolulu, p. 361, 1967.

Howard, H. T.:  Trans. Am. Geophys. Union, 49th Annual Meeting, p. 262,
    1968.

Hughes, M. P., Harkness, R. L.:  Ap. J. 138, 239, 1963.

Hundhausen, A. J.:  Space Sci. Rev. 8, 690, 1968.

Hundhausen, A. J.:  Rev. Geophys. Space Sci. 8, 729, 1970.

Ingham, M. F.:  M.N.R.A.S. 122, 45, 1961.

Jaeger, J. C., Westfold, K. C.:  Austr. J. Sci. Res. A2, 322, 1949.

Jaeger, J. C., Westfold, K. C.:  Austr. J. Sci. Res. A3, 376, 1950.

Jager, C., de:  Space Research 1, 628, 1960a.

Jager, C., de:  Radiostronomia Solare, Rendiconti-della Scuola,
    Internazionale de Fisica, 'Enrico Fermi,' Corso XII, p. 313, 1960b.

Jager, C. de., Van't Veer, F.:  I.A.U. Symp. No. 4, Ed. H. C. van de
    Hulst, 1957.

James, J. C.:  Ap. J. 146, 670, 1966.

James, J. C.: Solar Phys. 12, 143, 1970.

Johnson, P. O., Jackson, R. W. B.: Modern Statistical Methods, Rand McNally, 1959.

Jordan, E. C.: Electromagnetic Waves and Radiating Systems, Prentice-Hall, 1950.

Kai, K.: Solar Physics 11, 456, 1970.

Kaplan, S. A., Tsytovich, V. N.: Soviet Phys. Astronomy 11, 956, 1968. (Astr. Zu. 44, 1194, 1967).

Kavanagh, L. D., Jr., Schardt, A. W., Roelof, E. C.: Rev. Geophys. Space Sci. 8, 389, 1970.

Khaikin, S. E., Chikachev, B. M.: Dokl. Akad. Nauk. 58, 1923, 1947.

Koehler, R.: Geophys. Res. 73, 4883, 1968.

Komesaroff, M.: Austr. J. Phys. 11, 201, 1958.

Krauss, J. D.: Radioastronomy, McGraw-Hill, 1966.

Kruger, A.: World Data Center A, Report UAG-9, 1970.

Kuckes, A. F., Sudan, R. N.: Nature 223, 1048, 1969.

Kuckes, A. F., Sudan, R. N.: Solar Phys. 17, 194, 1971.

Kundu, M. R.: Solar Radio Astronomy, Interscience, 1965.

Kundu, M. R., Roberts, J. A., Spencer, C. L., Kuiper, J. W.: Ap. J. 133, 255, 1961.

Kundu, M. R., Erickson, W. C., Jackson, J. D., Fainberg, J.: Solar Phys. 14, 394, 1970.

Lee, R. H., Warwick, J. W.: Radio Science 68D, 807, 1964.

Lin, R. P.: Can. J. Phys. 46, S757, 1968.

Lin, R. P.: Solar Phys. 12, 266, 1970a.

Lin, R. P.: Solar Phys. 15, 453, 1970b.

Lin, R. P.: Personal communication to F. T. Haddock (March 31, 1971).

Lin, R. P., Anderson, K. A.: Solar Phys. 1, 446, 1967.

Link, F.: B.A.C. 3, 6, 1951.

Loughead, R. E., Roberts, J. A., McCabe, M. K.: Austr. J. Phys., 10, 483, 1957.

C.6

Machin, K. E., Smith, F. G.:  Nature 168, 599, 1951.

MacRae, B. D.:  UM/RAO Technical Report, September 1968.

Malville, J. M.:  Ap. J. 136, 266, 1962a.

Malville, J. M.:  Astr. J. 67, 580, 1962b, (abstract).

Malville, J. M.:  Ap. J. 135, 834, 1962c.

Malville, J. M., Solar Phys. 2, 484, 1967.

Malitson, H. H., Erickson, W. C.:  Ap. J. 144, 337, 1966.

Maxwell, A., Howard, W. E., III, Garmire, G.:  J. Geophys. Res. 65, 3581, 1960.

Maxwell, A., Defouw, R. J., Cummings, P.:  Planet. Space Sci. 12, 435, 1964.

Maxwell, A., in The Solar Spectrum, Ed. C. deJager, D. Reidel Publishing Co., 1965.

McCracken, K. G.:  J. Geophys. Res. 67, 447, 1962.

McCracken, K. G.:  Solar Flares and Space Research, North-Holland Publ. Co., Amsterdam, p. 202, 1969.

McCracken, K. G., Rao, U. R.:  Space Sci. Rev. 11, 155, 1970.

McLean, D. J.:  Austr. J. Phys. 24, 201, 1971.

Melrose, D. B.:  Austr. J. Phys. 23, 871, 1970.

Michard, R.:  Ann. Astrophys. 17, 429, 1954.

Mode, E. B.:  Element of Statistics, Third Edition, Prentice Hall, 1961.

Montgomery, M. D., Bame, S. J., Hundhausen, A. J.:  Trans. Am. Geophys. Union 49th Annual Meeting, p. 262, 1968.

Morimoto, M.:  Publ. Astr. Soc. Japan 13, 285, 1961.

Morimoto, M.:  Publ. Astr. Soc. Japan 16, 163, 1964.

Neugebauer, M., Snyder, C. W.:  The Solar Wind, ed. Mackin and Neugebauer, 1966a.

Neugebauer, M., Snyder, C. W.:  J. Geophys. Res. 71, 4469, 1966b.

Newkirk, G., Jr.:  Ap. J. 133, 983, 1961.

Newkirk, G., Jr.: A. Rev. Astr. and Astrophys. 5, 1967.

Newkirk, G., Jr., Hansen, R. T., Hansen, S.: Annals. IQSY 3, 49, 1969.

Newkirk, G., Jr., Dupree, R. G., Schmahl, E. J.: Solar Phys. 15, 15, 1970.

Ney, E. P., Huch, W. F., Kellogg, P. J., Stein, W., and Gillet, F.: Ap. J. 133, 616, 1961.

Nishida, A.: J. Geophys. Res. 74, 5155, 1969.

Noble, L. M., Scarf, F. L.: Ap. J. 138, 1169, 1963.

Papagiannis, M. D., Solar Phys. 18, 311, 1971.

Parker, E. N.: Ap. J. 128, 663, 1958.

Parker, E. N.: Res. in Geophys. 1, 99, 1964.

Parker, E. N.: Space Sci. Rev. 9, 325, 1969.

Pawsey, J. L., Payne-Scott, R., McCready, L. L.: Nature 157, 158, 1946.

Payne -Scott, R.: Austr. J. Sci. Res. Ser. A. 2, 214, 1949.

Payne-Scott, R., Yabsley, D. E., Bolton, J. G.: Nature 160, 256, 1947.

Pneuman, G. W., Kopp, R. A.: Preprint 1969?, 1970?

Rabben, H. H.: Z. Astrophys. 49, 95, 1960a.

Rabben, H. H.: "Radio Astronomia Solare," Rendiconti della Scuola Internazionale Fisica 'Enrico Fermi', Corso 12, p. 395, 1960b.

Reber, G.: Ap. J. 100, 279, 1944.

Riihimaaa, J. J.: Ann. Acad. Sci., Fennicae Series A. VI, Physica, No. 131, 1963.

Reule, A.: Z. Naturforsch 7a, 234, 1952.

Rosh, J.: Solar Physics, Ed. J. N. Xanthakis, Interscience, 1967.

Saito, K.: Ann. Tokyo Astr. Obs. 3, 3, 1950.

Scarf, F. L.: Space Sci. Rev. 11, 234, 1970.

Schmidt, M.: B. A. N. 12, 61, 1953.

Shklovskii, I. S.: Astr. Zu. 23, 333, 1946.

Shain, C. A., Higgins, C. S.:  Austr. J. Phys. 12, 357, 1959.

Simon, P.:  Ann. Astrophys. 25, 12, 1962.

Slysh, V. I.:  Cosmic Res. 3, 620, 1965 (Kosm. Issled. 3, 760, 1965).

Slysh, V. I.:  Cosmic Res. 5, 759, 1967a (Kosm. Issled 5, 897, 1967).

Slysh, V. I.:  Sov. Astron. 11, 389, 1967b, (Astr. Zu. 44, 487, 1967).

Slysh, V. I.:  Sov. Astron. 11, 72, 1967c.  (Astr. Zu. 44, 94, 1967).

Smerd, S. F., Westfold, K. C.:  London Phil. Mag. Ser. 7, 40, 831, 1949.

Smerd, S. F., Wild, J. P., Sheridan, K. V.:  Austr. J. Phys. 15, 180, 1962.

Smith, A. G., Radio Exploration of the Sun. D. Van Nostrand, 1967.

Smith, D. F.:  Solar Phys. 15, 202, 1970.

Smith, D. F.:  Institute for Plasma Research, Stanford University, Rpt. No. 309, 1969.  (Also Adv. Astr. and Astrophys. 7, 148, 1970).

Smith, W. B., Bowles, K. L., Shapiro, I. I.:  Moon and Planets II, Ed. A. Dollfus, 1968.

Southworth, G. C.:  Journ. Franklin Inst. 239, 1945.

Staff of Center for Radar Astronomy. Stanford University, J. Geophy. Res. 71, 3325, 1966.

Stelzried, C. T., Levy, G. S., Sato, T., Rusch, W. V. T., Ohlson, J. E., Schatten, K. H., Wilcox, J. M.:  Solar Phys. 14, 440, 1970.

Stewart, R. T.:  C.S.I.R.O. Radiophysics Laboratory RPR 142, February 1962.

Stewart, R. T.:  Austr. J. Phys. 18, 67, 1965.

Stone, R. G. quoted by Sky and Telescope, 281, May 1971.

Sturrock, P. A.:  A.A.S.--NASA Symp. on Phys. of Solar Flares, Ed. W. N. Ness, p. 357, 1964.

Sturrock, P. A., Smith, S. M.:  Solar Phys. 5, 87, 1968.

Swarup, G., Stone, P. H., Maxwell, A.:  Ap. J. 131, 725, 1960.

Tai, C. T.:  IRE Trans. Antennas Propagat., Vol. AP-9, 224, 1961.

Takakura, T.:  Publ. Astron. Soc. Japan, 16, 230, 1964.

Takakura, T.:  Space Sci. Rev. 5, 80, 1966.

Takakura, T.: Solar Phys. 1, 304, 1967.

Teske, R. G., Soyumer, T., Hudson, H. S., Ap. J. 165, 615, 1971.

Tsytovich, V. N., Kaplan, S. A.:  Soviet Astron. 12, 618, 1969.
     (Astr. Zu. 45, 777, 1968).

Urbarz, H.:  Personal Communication (1969).

Van Allen, J. A., Krimigis, S. M.:  J. Geophys. Res. 70, 5737, 1965.

Van de Hulst, H. C.:  B.A.N. 11, 135, 1950.

Vitkevich, V. V.:  Dokl. Akad. Nauk. SSSR, 77, 585, 1951.

Weber, R. R., Stone, R. G., Somerlock, C. R.:  Astr. and Astrophys.
     1, 44, 1969.

Whang, Y. C., Liu, C. K., Chang, C. C.:  Ap. J. 145, 255, 1966.

Wilcox, J. M.:  Space Sci. Rev. 8, 258, 1968.

Wild, J. P.:  Austr. J. Sci. Res. A3, 399, 1950a.

Wild, J. P.:  Austr. J. Sci. Res. A3, 541, 1950b.

Wild, J. P.:  AAS-NASA Symp. on the Physics of Solar Flares, Ed. W. N.
     Hess, 161, 1964.

Wild, J. P.: in Plasma Stabilities in Astrophysics, Ed. D. A. Tidman
     and D. C. Wentzel.  Gordon and Breach, 1969.

Wild, J. P., McCready, L. L.:  Austr. J. Sci. Res. A3, 387, 1950.

Wild, J. P., Murray, J. D., Rowe, W. C.:  Austr. Phys. 7, 439, 1954.

Wild, J. P., Roberts, J. A., Murray, J. D.:  Nature 173, 532, 1954.

Wild, J. P., Sheridan, K. V., Neylan, A. A.:  Austr. J. Phys. 12,
     369, 1959.

Wild, J. P., Smerd, S. F., Weiss, A. A.:  Ann Rev. Astr. and Astrophys.
     1, 291, 1963.

Williams, S. E.:  Nature 162, 108, 1948.

Wine, R. L.:  Statistics for Scientists and Engineers, Prentice-Hall,
     1964.

285-

Wolfe, J. H., Silva, R. W., McKibbin, D. D.:  Int. Symp. on Zod. Light
    and Interpl. Medium, Honolulu, 1967.

Wolff, C. L., Brandt, J. C., Southwick, R. G., Ap. J. 165, 18, 1971.

Yip, W. K.:  Austr. J. Phys. 23, 161, 1970a.

Yip, W. K.:  Planet. Space Sci. 18, 479, 1970b.

Yip. W. K.:  Planet. Space Sci. 18, 867, 1970c.

Yorks, R. G., UM/RAO OGO-E Memo No. 144, September 23, 1968.

Young, C. W., Spencer, C. L., Moreton, G. E., Roberts, J. A.:  Ap. J.
    133, 243, 1961.

Zheleznyakov, V. V.,  Radio Emission of the Sun and Planets, Pergamon,
    1970.

Zheleznyakov, V. V., Zaitsev, V. V.:  Soviet Astr. 14, 47, 1970a,
    (Astr. Zu. 47, 60, 1970).

Zheleznyakov, V. V., Zaitsev, V. V.:  Soviet Astr. 14, 250, 1970b,
    (Astr. Zu. 47, 308, 1970).

Zirin, H., The Solar Atmosphere, p. 178, Blaisdell, 1966.